NUMERICAL SIMULATION OF

FATIGUE CRACK GROWTH

Xiaobin Lin, *B. Sci., M. Sci.*

A thesis submitted for the degree of

Doctor of Philosophy at the University of Sheffield

Summary

This thesis describes the advances made by the author on the direct modelling of the fatigue growth of planar cracks. A versatile step-by-step 3D finite element technique has been developed, which calculates the stress intensity factors at a set of points on the crack front according to linear elastic fracture mechanics principles and then applies a fatigue crack growth law to this set of points to obtain a new crack profile. The software DUCK developed has a good capability of automatic remeshing so that the fatigue propagation of arbitrary shaped cracks can be conveniently followed.

The stress intensity factor calculation using the 3D finite element method has been improved and widely verified to be of good accuracy generally, which provides an important guarantee for the fatigue growth prediction. Several major problems associated with the stress intensity factor calculation, such as crack front definition, free surface layer and mesh abutting the crack front, as well as J-integral path independence, have been discussed.

A variety of cracked geometries of either theoretical or practical significance have been modelled by the numerical technique, including internal defects in infinite solids, surface cracks in finite thickness plates, round bars and pressure vessels, and initially multiple surface small cracks. Many results useful for the fatigue assessment of each kind of crack, such as stress intensity factor variations, fatigue shape changes and fatigue lives, have been obtained. By comparing with existing numerical methods and some limited experimental data found in the literature, it is shown that the numerical simulation technique is reliable and can predict the fatigue propagation of complex crack configurations, which is seldom possible for methods with assuming crack front configurations. Meanwhile, due to the highly automated procedure of the technique, it has become straightforward to model the fatigue growth of practical cracked components, as demonstrated by the computations in this thesis. It is believed that such a numerical simulation technique has a great potential and will play an useful role in the area of fatigue study and assessment.

To my wife Hailan and my parents

CONTENTS

Acknowledgements

Xiaobin Lin

December 1994

Certificate

This research has been carried out in the Department of Mechanical and Process Engineering at the University of Sheffield between December 1990 and December 1994. The contents of this thesis are original and are solely the work of the author except where otherwise stated. No part of this thesis has been submitted to any other university.

References

References are listed alphabetically at the end of the chapters in which they appear.

Keywords

aspect ratio; bending; crack shape change; crack coalescence; crack interaction; defect assessment; embedded crack; fatigue crack growth; finite element method; finite thickness plate; infinite solid; J-integral; linear elastic fracture mechanics; multiple crack; pressure vessel; round bar; stress intensity factor; surface crack; tension; virtual crack extension.

Abbreviations

DOB	degree of bending
EDI	equivalent dominant integral
FE	finite element
IVCE	infinitesimal virtual crack extension
NIIT	no interaction and immediate transition
PPP	preferred propagation path

SIF	stress intensity factor
VCE	virtual crack extension
2D	two-dimensional
3D	three-dimensional

Nomenclature

a	crack size, or crack depth
a_f	final crack size
a_o	initial crack size, or initial crack depth
b	crack surface half arc-length
c	crack surface half-length
c_o	initial crack surface half-length
ds	increment along J-integral contour
m	Paris growth law exponent used in Chapter 2
n	Paris growth law exponent, or number of corner nodes along crack front
(r, θ)	polar coordinates
r_M	crack radius of surface crack in round bar
$r_{(1/4)}$	distance away from crack tip at 1/4-points
s	distance between two adjacent cracks
t	plate thickness, or wall thickness of pressure vessel
(t, n, z)	coordinate axes
(x, y, z)	coordinate axes
u	displacement component in x direction
u_z	displacement component along z direction (*out of crack plane*)
$u_{z(1/4)}$	displacement along z direction at 1/4-points
$\mathbf{u}$	displacement vector
v	displacement component in y direction
C	Paris growth law constant, or J-integral contour
C_a	Paris growth law constant at crack depth point
C_c	Paris growth law constant at crack surface point

C_f, C_m	Paris growth law constant, used in Chapter 2
D	diameter of round bar
E	Young's modulus
E_i	relative residual
F_a	dimensional stress intensity factor at crack depth point
F_P	dimensional stress intensity factor by the present author
F_{NR}	dimensional stress intensity factor by Newman and Raju (1981)
G	energy release ratio
H	plate half-height
J	J-integral, fracture parameter
J_c	critical J-integral, material property
K	Mode I stress intensity factor
K_I, K_{II}, K_{III}	Mode I, II and III stress intensity factors
K_{Ic}, K_c	Mode I fracture toughness
K_{max}	maximum stress intensity factor along crack front
K_{min}	minimum stress intensity factor along crack front
N	number of fatigue loading cycles
N_0	initial number of elapsed fatigue loading cycles, or constant
N_f	number of elapsed fatigue loading cycles when crack reaches a given size
N_{fr}	reference number of elapsed fatigue loading cycles
P	internal pressure of pressure vessel
Q	Φ^2
R	stress ratio, defined by $\sigma_{min}/\sigma_{max}$
R_i	internal radius of pressure vessel
R_0	external radius of pressure vessel
S_r	relative standard deviation
$\mathbf{T}$	stress vector acting on the contour
U	potential energy
W	plate half-width, or strain energy density
(X, Y, Z)	coordinate axes
ε	tolerance for controlling numerical calculation accuracy
ε_{ij}	strain tensor

ϕ	parametric angle defining position on crack front
μ	shear modulus
ν	Possion's ratio
θ	parametric angle defining position on crack front
θ_i	parametric angle at ith nodal position of surface crack in round bar
θ_B	parametric angle at surface point of surface crack in round bar
σ_b	remote bending stress
σ_{max}	maximum fatigue stress
σ_{min}	minimum fatigue stress
σ_t	remote tension stress
σ_x, σ_y	normal stress component in x and y direction
σ_{ij}	stress tensor
σ_θ	hoop stress along vessel wall in Chapter 6
$\overline{\sigma_\theta}$	average hoop stress along vessel wall
$\sigma_{\theta max}$	maximum hoop stress along vessel wall
$\sigma_{\theta min}$	minimum hoop stress along vessel wall
τ_{xy}	shearing stress
Δa_i	crack growth increment at ith node along crack front
Δa_{max}	maximum crack growth increment along crack front
ΔK	stress intensity factor range
ΔK_a	stress intensity factor range at crack depth point
ΔK_c	stress intensity factor range at crack surface point
ΔK_{eff}	effective stress intensity factor range
ΔK_{th}	threshold stress intensity factor range
Φ	complete elliptic integral of second kind

Chapter 1

INTRODUCTION

This chapter introduces the phenomena of fatigue, and briefly describes the progress made in assessing the fatigue crack propagation in the "long" crack field. The principal objective of this thesis and the fatigue growth problems modelled together with several important aspects associated with the technique are outlined. The arrangement of the following chapters is also described.

1.1 Introduction

Fatigue is rather like a disease of metal. Many structural failures are due to its consequences. Fatigue essentially is a process of gradual failure of a structure at alternating loads below the ultimate strength of a particular, not a sudden event, like brittle fracture, even though the final appearance of fatigue is likely to be sudden and catastrophic.

Fatigue failure is a consequence of crack initiation and growth. When a structure is subject to a periodical varying load, some cracks are formed at the site of some material imperfections such as voids, inclusions and crack-like defects, which usually are of microscopically small size. As fatigue cycles accumulate, these short cracks may continue to grow and coalesce, and gradually evolve to be a dominant crack, eventually reaching a critical size, beyond which catastrophic failure will happen. However, the initial further propagation of certain defects may be arrested at grain boundaries or within grains, which often occurs at low fatigue loads below a threshold.

The study of fatigue can be traced back to the last century. The establishment of Wohler's empirical findings of stress range/life relationship and the concept of a fatigue limit at the end of the last century was a start of understanding of fatigue knowledge, even though quantitative assessments were still lacking and the mechanisms of fatigue remained a mystery. There were many papers published on further attempts to understand the fatigue phenomenon of both micro and macro crack sizes, which were reviewed by Smith (1984) in the title of "Thirty years of fatigue crack growth - a historical review". The paper written by Paris and Erdogan (1963) must be mentioned here, in which the quantitative framework of fracture mechanics was constructed by introducing the concept of stress intensity factor range into the relationship of the fatigue growth rate and the applied fatigue load, instead of the stress range used earlier. A great explosion of literature followed over the next two decades, largely adding detail and practical expertise to this simple idea. The acceptance of the stress intensity factor parameter took perhaps ten years to become almost universal. During present studies of the fatigue growth of the so-called "long" cracks, the Paris law has predominated, although many factors, such as stress ratio, mean stress and loading frequency, which may influence the fatigue propagation, were not taken into account in this law.

The validation of the prediction of fatigue growth of practical complicated cracks, which often are in complex stress states and possess irregular shape, is the target of engineers and

researchers in the fatigue area. Lots of efforts have been devoted to various typical cracks in practice, such as 2D cracks under I-II mixed mode loading, surface cracks in finite plates or round bars subjected to mode I fatigue load and more complicated inclined surface cracks in plates under tension. The Paris law has been widely applied and extended to practical structures and components, and its applicability has also been examined in most of the publications.

One of the main difficulties in using the Paris law is that the practical cracks usually experience significant shape change or even orientation change if the tip of original cracks is in a mixed mode stress, and the stress intensity factor at the crack tip (*for 2D crack*) or along the crack front (*for 3D crack*) varies with crack growth. Due to the unavailability of the stress intensity factor variations, a widely used method of dealing with these propagating cracks is to assume that a certain crack shape is maintained during the fatigue process and then to calculate the stress intensity factors for a series of cracks of different size. A typical example is the fatigue growth prediction of surface cracks in plates subjected to mode I loading. On the basis of many experimental observations, the shape of a surface crack is assumed to be always semi-elliptical, which permits the use of the Paris law at the two extremities of the surface crack front, the surface and depth points (Newman and Raju, 1981). Recently, Carpinteri (1993) also used a part-elliptical assumption, together with his stress intensity factor solutions, in estimates of shape change of surface cracks in round bars under cyclic tension. Lotsberg and Bergan (1979) made an effort to model the shape development of an embedded fatigue crack using the energy release rate calculated by the finite element method. They defined the crack front by three elliptical half axes to simplify their calculations. The shape assumption method, in spite of probably being valid for certain cracks, obviously, is too simple to predict more precisely the fatigue growth of initially irregular defects, and interacting and coalescing defects.

To overcome the difficulty in assessing fatigue cracks, caused by the crack shape change during the fatigue process, a numerical technique has been proposed initially by Smith and Cooper (1989). This technique can follow the fatigue shape development of a crack by directly establishing a 3D finite element model for each crack front and applying an appropriate fatigue crack growth law at a set of points along the crack front. Obviously, the assessment method of following fatigue crack growth has a great advantage for practical engineering cracked structures and can provide more accurate predictions not only for crack

shape developments but for fatigue lives, compared with the shape assumption method mentioned above.

1.2 Scope of The Thesis

This thesis mainly reports the progress made by the author on the versatile numerical technique in aspects of both accuracy and efficiency, and also clarifies several important problems in estimates of stress intensity factors using the finite element method. Various planar cracks of theoretical and practical interest, including internal defects in infinite solids, surface cracks in finite thickness plates, round bars and pressure vessels, and initially multiple surface small cracks, are modelled both to examine the accuracy and capability of the modelling technique and to investigate the fatigue growth behaviours of theses cracked geometries. A wide range of predictions made by the numerical technique, such as crack shape changes, stress intensity factor variations, fatigue lives are compared with the experimental observations or the numerical approximate results available in the literature.

However, the numerical technique currently only considers linear elastic material although plasticity near the crack tip probably occurs. The cracked structures modelled should only contain planar cracks either in their initial state or in their propagation process, i.e. cracks cannot be allowed to change their initial orientation. The fatigue crack growth relation planted in the technique at present is the well-known Paris law, but it is not difficult to include a more complex relation considering, for example, the threshold and rapid growth stages.

1.3 Thesis Layout

Chapter 2 of this thesis describes the theoretical background and the technical details of numerical simulation of planar defects, including both the finite element automatic mesh generation procedure and the principles of linear elastic fracture mechanics together with discussion on three key points in estimates of stress intensity factors by using the displacement and *J*-integral methods. The accuracy of the simulation technique is mainly demonstrated in its practical applications. Subsequent chapters (*3 to 7*), each dealing with certain types of defects, are as self-contained as possible. The literature review appropriate to a particular fatigue crack geometry is arranged to appear in it relevant chapter in order to ensures that each chapter is as clear and complete as possible.

Chapter 3 models the fatigue growth of irregular embedded defects within infinite solids subjected to remote tension. The results obtained are compared with some available analytical solutions, and then some theoretical aspects, such as the stress intensity factor accuracy and the crack growth increment, which are very important for the technique, are discussed. A proposal of dealing with small crack problems in practical engineering structures is also made in this chapter.

Studied extensively in Chapter 4 are the fatigue growth behaviours of initially semi-elliptical surface cracks in finite thickness plates subjected to different combinations of tension and bending loads. A large number of publications involved in this area are reviewed. This chapter overall clarifies the discrepancy caused by the current widely used Newman and Raju's 'two-point plus semi-ellipse' method of prediction of aspect ratio changes, stress intensity factor variations, fatigue cycles and so on. The shape change characteristic of surface cracks is numerically revealed through proposed quantitative criteria which can effectively describe the degree of deviation of the propagating crack profiles from the semi-ellipses. The boundary layer correction considering the different stress states near the free surface is used to investigate the aspect ratio variations. This chapter reports a wide range of results that are believed to provide a further understanding of fatigue growth of surface cracks.

The focus of Chapter 5 is mainly on the investigation of the fatigue growth starting from multiple small surface cracks in finite thickness plates under different combinations of tension and bending. The crack shape development at different growth stages, i.e. pre-coalescence,

coalescence and post-coalescence, is predicted, and some crack growth behaviours particularly during coalescence are analysed.

Chapter 6 presents a variety of fatigue growth results for external surface cracks in internally pressurised cylinders, including aspect ratio changes, stress intensity factors and fatigue life predictions. These results are of very practical significance for the study of LBB (*Leak-Before-Break*) and further for the safety assessment of pipes or pressure vessels.

The shape change of surface cracks in round bars under tension is predicted in Chapter 7 by the numerical simulation technique after a detailed literature review. Comparison is also performed between the predicted results and experimental observations.

In addition to the conclusions included in each individual chapter, Chapter 8 summarises some principal conclusions of this research. Further directions and applications of this modelling technique are also indicated and discussed in this final chapter.

1.4 References

Carpinteri, A. (1993) *Shape change of surface cracks in round bars under cyclic axial loading.* **Int. J. Fatigue 15**(1), 21-26.

Lotsberg, I. and Bergan, P. G. (1979) *Calculation on fatigue growth of internal cracks by the finite element method.* **Engng Fract. Mech. 12**, 33-47.

Newman, J. C., Jr. and Raju, I. S. (1981) *An empirical stress intensity factor equation for the surface crack.* **Engng Fract. Mech. 15**, 185-192.

Paris, P. C. and Erdogan, F. (1963) *Critical analysis of crack propagation laws.* Trans. ASME, Ser. D, **J. Basic Engng 85**(4), 528-534.

Smith, R. A. (1984) *Thirty years of fatigue crack growth - an historical review.* Proceedings of a Conference on Fatigue Crack Growth, Fatigue Crack Growth, 20 September, 1984, Cambridge, UK, 1-16.

Smith, R. A. and Cooper, J. F. (1989) *A finite element model for the shape development of irregular planar cracks.* **Int. J. Pres. Ves. Piping 36**(4), 315-326.

Chapter 2

NUMERICAL TECHNIQUE OF SIMULATING FATIGUE GROWTH OF PLANAR CRACKS UNDER MODE I LOADING

This chapter reviews the development of the finite element simulation technique proposed initially by Smith and Cooper (1989). The theoretical background pertinent to the fatigue crack growth simulation, the subject in this dissertation, is described. This includes the linear elastic fracture mechanics principles and several major fatigue growth laws as well as numerical methods of estimating stress intensity factors by the finite element method. New software developed by the present author, which can automatically simulate the fatigue growth of initially arbitrary shaped planar cracks under Mode I loading, is also detailed in this chapter. Many developments have been added to the new software, such as the cubic spline definition for a crack front, the technique of correcting the fatigue growth rate at free surfaces, the significantly enhanced capability of automatic remeshing and dealing with boundary conditions, and so on. Furthermore, the sensitivity of SIF results to crack shape, the effect of mesh orthogonality and the J-integral path independence, which are three key problems in the SIF evaluations by the finite element method, are discussed and clarified. It is shown that the SIF results are sensitive to the crack front shape, that the cubic spline approximation to a crack front can eliminate the oscillation of SIFs around the crack front defined by the polyline and consequently greatly increase the SIF accuracy, and that the J-integral path independence is usually maintained but is lost at the free surface if a slightly non-orthogonal intersection exists between the free surface and the crack front.

2.1 Introduction

As indicated in Chapter 1, the prediction of fatigue crack growth has mostly employed the shape assumption method to assist in simplifying the fatigue calculation. However, the possible crack shape during the fatigue process usually varies with the crack geometry and loading condition as well as the material properties. It is obviously very difficult, sometimes even impossible, to describe properly the propagating crack profiles as a unique shape, particularly for cracks contained in practical complex structures and components with residual stresses or for multiple crack configurations. The shape assumption method, therefore, needs to be firmly supported by experimental studies for the cracked components under consideration before it can be used, and is very likely to be invalidated due to failing to establish such a crack shape throughout the fatigue growth process.

A novel and more precise technique has been proposed initially by Smith and Cooper (1989) for simulating the shape development of planar defects under Mode I fatigue loading. The technique was based on the Finite Element Method coupled with Linear Elastic Fracture Mechanics concepts, and equipped an automatic remeshing capability to follow the crack growth, which greatly saved the time in generating finite element meshes during the fatigue process. Compared with the early methods of predicting fatigue crack growth mentioned above, the technique was a great progress since it directly calculated the stress intensity factor variations along a propagating crack front, rather than assuming a certain crack configuration ahead, and then used the Paris law to establish a new crack front. Using their technique, Smith and Cooper succeeded in investigating the effect of local brittle zones upon the Mode I fatigue growth of planar defects.

The technique was used subsequently by Kishimoto *et al.* (1989) and Soboyejo *et al.* (1989) to investigate the interaction and coalescence of twin coplanar initially semi-elliptical cracks subjected to tension. The experimental tests were also made and compared by them with the numerical results. The comparison showed that the significant crack shape change experienced during the coalescing stage of the two adjacent cracks, can be successfully simulated by the direct finite element technique. The coalescing stage has been neglected in the fatigue analysis procedures suggested by the ASME XI (1977) and BSIPD 6493 (1980) codes.

Chipalo (1990) also used the same software to examine further the tension fatigue growth of cracked geometries of engineering significance, including an embedded elliptical crack near a free surface, and semi-elliptical cracks in both round bars and finite thickness plates. The crack growth behaviours during the transitions from an internal crack to a surface crack and from surface cracks to through cracks were numerically revealed.

The work of Chipalo was extended by Gilchrist (1991) to more detailed investigations on tension fatigued defects in finite thickness plates. Gilchrist's focus was on the investigation of the effect of different fatigue loads with components of tension and bending upon fatigue crack growth. He also made some minor improvements on the original software developed by Smith and Cooper (1989), such as incorporating the function of dealing with non-uniform tension loads and adding an extra layer of elements to the cracked block to attempt to increase the SIF calculation accuracy.

A similar numerical technique for predicting the fatigue crack growth by directly tracing the crack front progress, has also been reported by Remzi *et al.* (1990), who described a new supplementary addition to the BERSAFE program. This program used Linear Elastic Fracture Mechanics to model the fatigue crack propagation with the mesh modified locally and automatically. The infinitesimal virtual crack extension (IVCE) method was used to obtain stress intensity factors. The new 3D finite element mesh was created according to the actual increments of crack growth along a crack front, but the actual increments were designed to satisfy that maximum growth increment does not exceed 4% of the element size normal to the plane of the crack in order to facilitate automatic remeshing. However, this mesh-dependent remeshing technique makes its general application very difficult. Especially when the amounts of crack growth along the crack profile are quite different, a larger growth increment is required to save computing-time. Remzi examined the fatigue growth of a semi-elliptical surface crack in a plate subjected to a combined axial and bending load as an example. It appeared that the obtained variation of stress intensity factors near the free surface was non-smooth, and a numerical instability was found in crack profiles during the crack growth process.

Recently, Thompson and Sheppard (1992), following the same finite element analytical procedure, also modelled the fatigue growth of surface cracks in plain and fillet notched shafts subjected to torsion and axial loads. However, it seemed that the new mesh after each crack

increment needed to be created manually, which is obviously unacceptable for practical modelling computations.

Although the software developed by Smith and Cooper (1989) and extended by Gilchrist (1991) has been employed to investigate some crack configurations, it was felt that the numerical accuracy for the stress intensity factor calculation, the applicability of the simulation technique to a variety of practical cracked geometries, and the capability of automatic remeshing should be further improved and enhanced. For this purpose, the present author has rewritten the software code. Many new features have been added to the new software, such as the cubic spline definition for a crack front, the technique of correcting the fatigue crack growth rate at free surface where a retardation often occurs, the significantly enhanced capability of remeshing and dealing with boundary conditions, and so on. In this chapter, some theoretical background associated with the numerical simulation technique, including some basic knowledge of Linear Elastic Fracture Mechanics and Finite Element Method, is first to be outlined. It is followed by a detailed description of the numerical technique. Three important problems in estimates of stress intensity factors along the front of planar cracks by finite element analyses, i.e. the SIF sensitivity to crack front shape, the influence of a non-orthogonal mesh on the SIF accuracy, and the *J*-integral path independence, are also discussed in this chapter.

2.2 Theoretical Background

This section mainly describes the theoretical background associated with the present finite element simulation technique.

2.2.1 Linear Elastic Fracture Mechanics

Fracture mechanics, which deals with a cracked structure, can be traced back to Griffith (1921), who first indicated that when a crack is introduced to a stressed plate of elastic material, a balance must be struck between the decrease in potential energy and the increase in surface energy resulting from the presence of the crack. He derived the famous Griffith
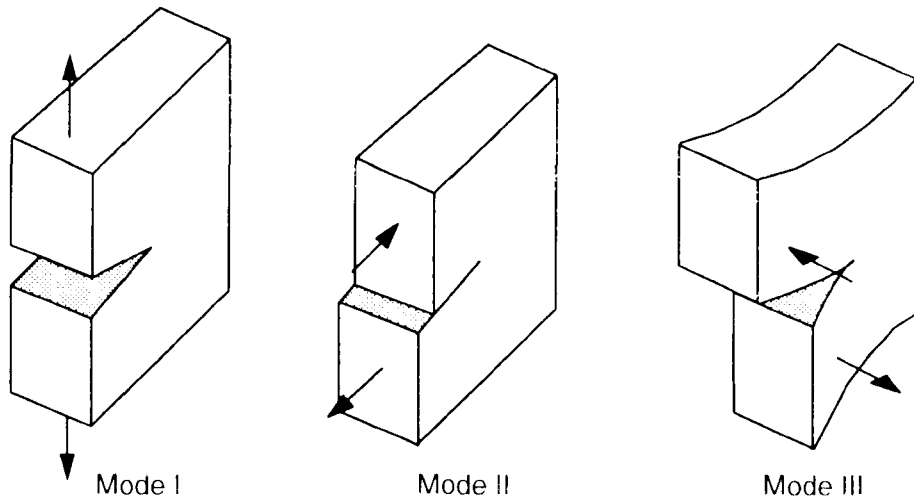
Figure 2.1   Basic modes involving different crack surface displacements

relationship between the fracture stress and the crack size, which is a basis of linear elastic fracture mechanics.

Irwin (1962), using modifications of analytical methods proposed by Westergaard (1939), obtained elastic solutions for crack tip stress distributions associated with the three major modes of loading shown in Fig. 2.1. These modes involve different motions of the top and bottom crack surfaces relative to each other:

Mode I   (Opening or tensile mode) the crack surfaces move directly apart, which occurs when the load is applied normal to the plane of the crack.

Mode II   (Sliding or in-plane shear mode) the crack surfaces slid over one another in a direction perpendicular to the leading edge of the crack.

Mode III (Tearing or anti-plane shear mode) the crack surfaces move relative to one another and parallel to the leading edge of the crack.

Any combination of these three loads is referred to as Mixed Mode.

Stress intensity factor concept

For a linear elastic material, the stresses and displacements in the vicinity of a Mode I crack, assumed to be in plane strain state, are found to be

$$\sigma = \frac{K}{\sqrt{2\pi r}} \cos\theta \left(1 + \sin\frac{\theta}{2}\sin\frac{3\theta}{2}\right)$$

$$\sigma_x = \frac{K}{\sqrt{2\pi r}} \cos\theta \left(1 - \sin\frac{\theta}{2} \sin\frac{3\theta}{2} \right)$$

(2.1)

$$\tau_{xy} = \frac{K}{\sqrt{2\pi r}} \cos\theta \left(\sin\frac{\theta}{2} \cos\frac{\theta}{2} \cos\frac{3\theta}{2} \right)$$

$$u = \frac{K}{\mu} \sqrt{\frac{r}{2\pi}} \cos\frac{\theta}{2} \left(1 - 2v + \sin^2\frac{\theta}{2} \right)$$

(2.2)

$$v = \frac{K}{\mu} \sqrt{\frac{r}{2\pi}} \sin\frac{\theta}{2} \left(2 - 2v - \cos^2\frac{\theta}{2} \right)$$

where (r, θ) defines a polar location ahead of the crack tip, as shown in Fig. 2.2, μ and v are the shear modulus and Poisson's ratio of the material respectively. Apparently, the stress field has a singularity of strength $1/\sqrt{r}$ at the crack tip and K is the magnitude of the elastic stress and displacement fields, called the Mode I stress intensity factor of the crack, K_I (*in this thesis K_I is always written as K since only Mode I loading is considered, as indicated in Chapter 1*).
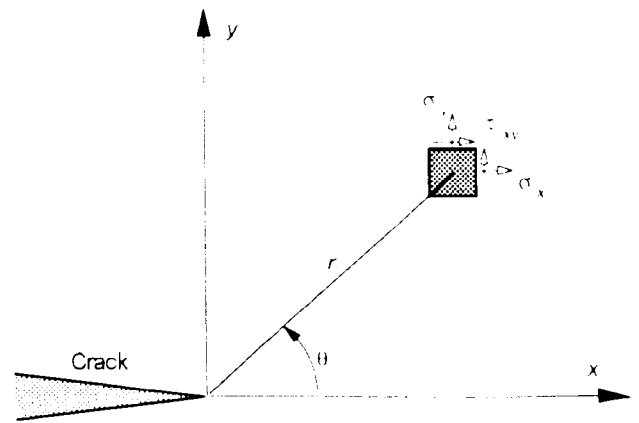
Figure 2.2   Distribution of stresses and displacements in vicinity of crack tip

An important feature of Eq. (2.1) is the fact that the stress distribution around any crack tip in a structure (*two-dimensional plane problem*) is similar and depends only on the parameters r and θ, and the difference between one cracked component and another lies in the magnitude of the stress field parameter K. The stress intensity factor K depends on the configuration of the cracked component and the manner in which the loads are applied. Such a feature leads to the establishment of linear elastic fracture mechanics which postulates that fracture occurs when K_I reaches the fracture toughness of the material, K_{Ic}, which is assumed to be a material constant.

The extension of the above framework of linear elastic fracture mechanics originated from the two-dimensional (2D) plane problem to three dimensions (3D) is due to Irwin (1962), who postulated the state of plane strain and then derived the plane strain stress intensity factor, K,
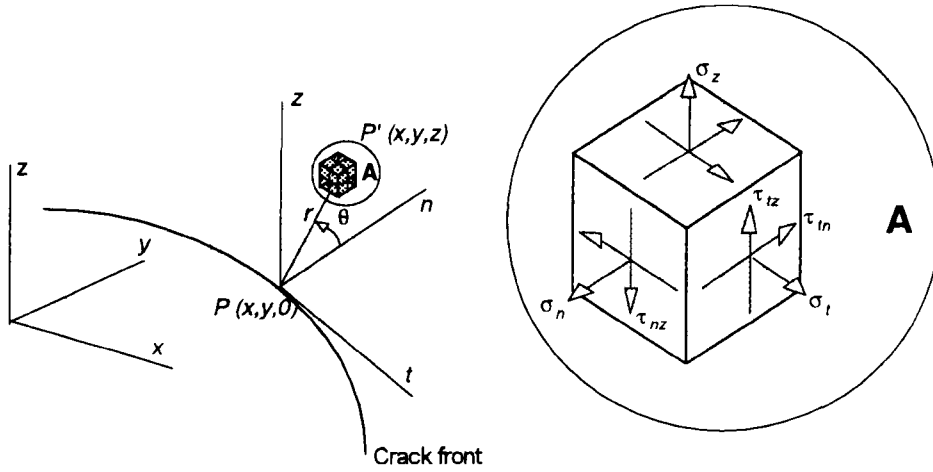
Figure 2.3 Local coordinate system for a curved crack

for an elliptical crack under tension. Irwin's postulate was later verified (Kassir and Sih, 1966; Smith *et al.*, 1967) where it was shown that the stresses and displacements near the crack tip, i.e. when $r \to 0$, can be represented in terms of a local coordinate system (t, n, z), which is tangential and normal to the crack front as shown in Fig. 2.3, as

$$\sigma_t = 2\nu \frac{K}{\sqrt{2\pi r}} \cos\theta$$

$$\sigma_n = \frac{K}{\sqrt{2\pi r}} \cos\theta \left(1 - \sin\frac{\theta}{2}\sin\frac{3\theta}{2}\right)$$

(2.3)

$$\sigma_z = \frac{K}{\sqrt{2\pi r}} \cos\theta \left(1 + \sin\frac{\theta}{2}\sin\frac{3\theta}{2}\right)$$

$$\tau_{nz} = \frac{K}{\sqrt{2\pi r}} \sin\frac{\theta}{2}\cos\frac{\theta}{2}\cos\frac{3\theta}{2}$$

$$\sigma_{tz} = 0$$

$$\sigma_{tn} = 0$$

$$u_n = \frac{K}{\mu}\sqrt{\frac{r}{2\pi}} \cos\frac{\theta}{2}\left(1 - 2\nu + \sin^2\frac{\theta}{2}\right)$$

$$u_z = \frac{K}{\mu}\sqrt{\frac{r}{2\pi}} \sin\frac{\theta}{2}\left(2 - 2\nu - \cos^2\frac{\theta}{2}\right)$$

(2.4)

13

$$u_t = 0$$

Comparison of Eqs. (2.1) and (2.2) with Eqs. (2.3) and (2.4) shows that the states of stresses and displacements in the vicinity of a curved crack front are similar to the two dimensional states.

For Mode II and III cracks, similar stress intensity factors K_{II} and K_{III} were defined according to their stress and displacement fields adjacent to the crack tip, which also have the $1/\sqrt{r}$ singularity at the crack tip.

J-integral

The *J*-integral is another key parameter which defines a line integral related to energy in the vicinity of a crack. The form of the *J*-integral is given by Rice (1968) in Eq. (2.5).

$$J = \int_c \left(W dy - \mathbf{T} \cdot \frac{\partial \mathbf{u}}{\partial x} ds \right) \qquad (2.5)$$

where x, y — rectangular coordinates normal to the crack front (*see Fig. 2.4*)

ds — increment along contour C

$\mathbf{T}$ — stress vector acting on the contour

$\mathbf{u}$ — displacement vector

W — strain energy density, $W = \int \sigma_{ij} d\varepsilon_{ij}$
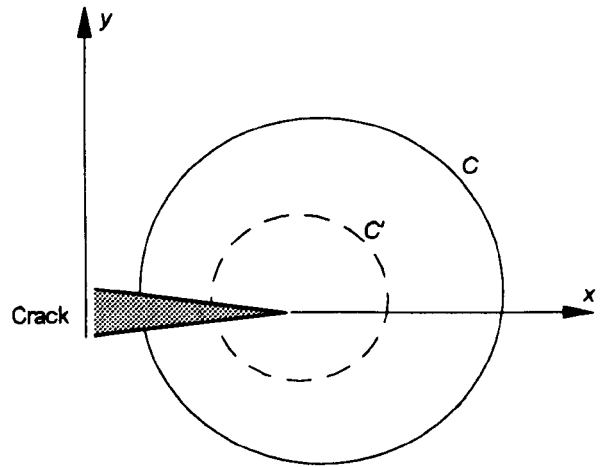
Figure 2.4   Line contour surrounding crack tip

It can be easily verified that the *J*-integral is path independent for elastic material, e.g. $J_c = J_{c'}$, as shown in Fig. 2.4, which enables the J to be calculated from σ and ε on some arbitrary contour away from a crack tip rather than at the crack tip.

The *J*-integral, actually, is an energy-related quantity. Rice (1968) has shown that the *J*-integral as defined along a contour surrounding the crack tip is the change in potential energy for a virtual crack extension da:

$$J = -\frac{dU}{da}$$

(2.6)

where U is the potential energy. For a linear elastic material $-dU/da = G$ which means that the J-integral, actually, is the energy release rate, and also has the following relationship with the stress intensity factor:

$$J = K^2/E \text{ (plane stress)}; \quad J = K^2(1 - v^2)/E \text{ (plane strain)}$$

(2.7)

From Eq. (2.7) it is easy to obtain a K value by calculating the J-integral, which will be further demonstrated later.

The J-integral was originally developed for solving two-dimensional crack problems in the presence of plastic deformation. Naturally, it is a more universal fracture criterion than K. The J-integral criterion postulates that crack growth or fracture occurs if J exceeds a critical value J_c, where J_c can be measured from experiments and is also a material property constant.

2.2.2 Fatigue crack growth laws

Fatigue crack growth laws

Whilst many different fatigue crack growth laws have been published, such as those summarised by Hoeppner and Krupp (1974), it is widely recognised that the quantitative framework of fatigue fracture mechanics, proposed by Paris and Erdogan (1963), is a major breakthrough. Paris and Erdogan indicated that the fatigue growth of a crack in a metallic material is mainly controlled by the range of stress intensity factor, ΔK.

Fig. 2.5 illustrates the experimental relation between the fatigue growth rate, da/dN, and stress intensity factor range, ΔK, on a Log vs. Log sigmoidal curve. Three regions can usually be observed. In the first region crack growth is dependent on material micro-structure with cracks propagating within grain size and possibly being arrested by grain boundaries or inclusions or other reasons. Generally, no crack growth occurs when the stress intensity factor range is below a threshold, ΔK_{th}. The second region, stable fatigue crack growth region, is represented by the linear Paris power growth law described below:

$$\frac{\mathrm{d}a}{\mathrm{d}N} = C\Delta K^n \tag{2.8}$$

Within this crack growth law the SIF range ΔK is related to the crack geometry and the applied load, whilst the C and n account for the material and environmental effects. The exponent n is dimensionless, the C is not and depends on the units used to describe crack length and SIF range. The third region represents rapid crack growth at increasing growth rate greater than that of the Paris law. Final fracture occurs when K_{max} reaches K_{c}, the fracture toughness.
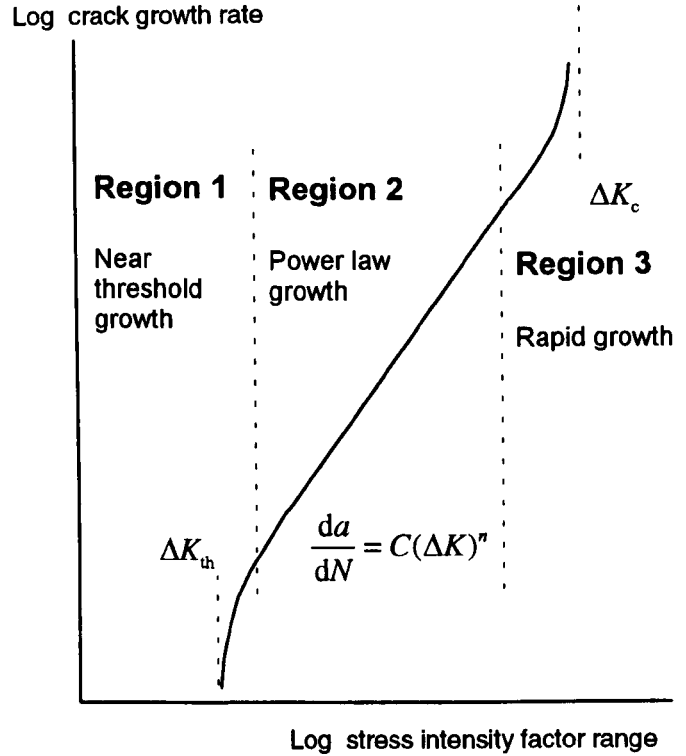
Figure 2.5   General trend of fatigue crack growth rates as a function of stress intensity factor range

A large majority of fatigue crack growth experiments have shown that in addition to the SIF range, many other factors may affect the fatigue crack growth. The stress ratio (*or the load ratio*), defined as:

$$R = \sigma_{\mathrm{min}}/\sigma_{\mathrm{max}} \tag{2.9}$$

is one of them. Walker (1970) has suggested the following empirical correction to the Paris law, according to his work on aluminium alloys

$$\frac{\mathrm{d}a}{\mathrm{d}N} = C\left(\Delta K_{\mathrm{eff}}\right)^n$$

$$\Delta K_{\mathrm{eff}} = \left(1-R\right)^{m-1}\Delta K \qquad (0 < m < 1) \tag{2.10}$$

16

A larger stress ratio generally makes the crack growth ratio tend to be greater. Pook (1975) and Rolfe and Barsoum (1977) indicated that the effect of different R ($R > 0$) is limited for steels but relatively sensitive for aluminium alloys.

Forman *et al.* (1967) and McEvily (1977) proposed corrections to the Paris law, in order to extend its range of use. Forman *et al.* presented the following crack growth equation:

$$\frac{da}{dN} = \frac{C_f \Delta K^n}{(1-R)K_c - \Delta K} \tag{2.11}$$

which, obviously, considers both the effect of stress ratio and the instability of crack growth at high SIF values. The C_f in Eq. (2.11) is different from the C in the Paris law. McEvily (1977) further extended the Paris law to cover both the higher and lower SIF ranges:

$$\frac{da}{dN} = \frac{C_m(\Delta K - \Delta K_{th})\Delta K^n}{(1-R)K_c - \Delta K} \tag{2.12}$$

where ΔK_{th} is the threshold value of applied SIF range, below which no fatigue crack growth will occur. Similarly, McEvily's correction also takes the effect of stress ratio into account, and the C_m is not the same as either C or C_f.

It is well known that scatter of experimental results is unavoidable for fatigue tests even in the most precisely controlled experiments using identical specimens, which is due to some intrinsic uncertainty of materials as well as some unknown factors affecting fatigue crack growth. In order to reduce larger scatter of fatigue predictions, it is obviously needed to establish a standard laboratory test procedure for obtaining adequate exponent, n, and coefficient, C, of the Paris law. Such a standard test procedure has been proposed in ASTM E647-88 (1988).

The complexity of actual behaviours of fatigue crack growth has led to a large number of publications which enrich greatly the fatigue knowledge. Mean stress, load ratio and frequency, random loading, multiaxial and complex stress states as well as environment such as corrosion and temperature, plastic zone sizes, microstructure all affect the manner of fatigue crack growth. But the Paris law does include the most important parameter characterising crack-tip stress field , the stress intensity factor, and provide a dominant

description of fatigue growth rate in the conceptual "long" crack low-stress regime (Brown, 1988). Throughout the present work this basic principle of fatigue crack growth will be applied to the author simulation technique.

Estimate of fatigue life

The estimate of fatigue life can be made by integrating the Paris crack growth law, Eq. (2.8), if the SIF range is within the second region, the linear region

$$\int_{N_o}^{N_f} \mathrm{d}N = \int_{a_o}^{a_f} \frac{\mathrm{d}a}{C(\Delta K)^n} \qquad (2.13)$$

The above equation can be used to determine either how many fatigue cycles, $N_f - N_o$, are required to take for the crack, a_o, to reach a certain size, a_f, or how large crack is reached for a fixed number of loading cycles.

However, it is usually difficult to obtain an analytical relation between the a_f and N_f since the ΔK is often a complicated function of both the crack geometry and stress in practical situations, thus a numerical method of solving Eq. (2.13) should be used. Eqs. (2.14) and (2.15) are two forms of Euler integration for Eq. (2.13), as shown in Fig. 2.6.

$$N_{m+1} = N_m + \frac{\Delta a}{C\left[\Delta K(a_m)\right]^n} \qquad (m = 0,1,...,n) \qquad (2.14)$$

$$a_{m+1} = a_m + C\left[\Delta K(a_m)\right]^n \Delta N \qquad (m = 0,1,...,n) \qquad (2.15)$$

In Eq. (2.14) the crack growth increment, Δa, is taken as a constant, $(a_f-a_o)/n$, during the numerical integration process, where n is the number of interval. The required integration accuracy of Eq. (2.14) can be achieved by reducing the value of Δa through the procedure shown in Fig. 2.6(a). Theoretically, when the value is taken to be infinitesimal the solution of Eq. (2.14) will converge to its correct solution, but it certainly requires a great amount of computing-time. From the numerical point of view, the iterative process in Fig. 2.6(a) can give a required numerical accuracy by specifying a certain tolerance ε. The smaller ε is chosen, the better accuracy can be achieved. Similarly, a good integration accuracy of Eq. (2.15), in which the fatigue cycle increment is specified as a constant, can also be reached.

```
      ┌─────────┐
      │  Begin  │
      └─────────┘
           │
      ┌──────────┐
      │ Chose Δa │
      └──────────┘
           │
┌───────────────────────────┐
│ Use Eq. (2.14) to calculate, Nf, │
│ the number of fatigue cycles │
│ when the crack size reaches af │
└───────────────────────────┘
           │
   ┌──────────────────┐
   │ Take the Nf as a │
   │ reference value, Nfr │
   └──────────────────┘
           │
   ┌───────────────────┐
   │ Reduce Δa to Δa/2 │
   └───────────────────┘
           │
┌────────────────────────────┐
│ Use Eq. (2.14) again to calculate, │
│ Nf, the number of fatigue cycles │
│ when the crack size reaches af │
└────────────────────────────┘
           │
        ◇ ?
   │Nf − Nfr│ ≤ ε
```

$|N_f - N_{fr}| \leq \varepsilon$

$$\Delta a = \frac{a_f - a_o}{n}$$

$$\Delta N = \frac{N_f - N_o}{n}$$

Crack size

a_f

Exact solution

Numerical solution

a_o

N_o

Number of fatigue cycles

No

Take the latest Nf as a reference, i.e. Nf → Nfr

Yes

End

(a)

(b)

Crack size

Exact solution

Numerical solution

a_o

N_o ΔN N_f

Number of fatigue cycles

Figure 2.6   Euler numerical methods of solving the fatigue growth law

In practical calculations a main difficulty arises in obtaining the ΔK value, which varies with crack growth. The analytical relation between the SIF and crack size, generally, is unavailable for complex cracked geometries and applied loads, although so many SIF solutions have been published. Some numerical methods, like the finite element method, should be used to calculate the ΔK for these crack sizes, a_m, during the crack growth. As long as these values of $\Delta K(a_m)$ are known, the number of fatigue cycles can be estimated by either Eq. (2.14) or

Eq. (2.15). It is worth indicating that the SIF values should be obtained as accurately as possible since any small errors in SIF values can cause an unacceptable error in estimates of fatigue cycles due to the exponential nature of the Paris law.

Extension of Paris law to planar defects

It is necessary to indicate that the above equations (*Eqs. (2.13), (2.14) and (2.15)*) are able to calculate the fatigue growth for 2D Mode I cracks, but not either for 2D mixed mode cracks whose crack direction probably changes when the cracks advance or for 3D planar cracks under Mode I loading because the shape of these cracks usually changes during the crack growth. Some investigators have extended the Paris law to 2D mixed mode crack problems. In this section, the focus is on the extension of the Paris law to 3D planar defects under Mode I loading.

Fig. 2.7 shows a planar crack subjected to a Mode I load. Apparently, the stress intensity factor varies along the crack front, so is a function of position. As indicated previously, the SIF along a curved crack front is defined in terms of a local coordinate system (t, n, z), as shown in Fig. 2.3. The SIF direction, according to the stress field in the vicinity of crack tip, is normal to the crack front. If the influence of the stress and strain states along the tangential direction of a crack front, which actually vary with crack shape and are usually between plane stress and plane strain states, on fatigue crack growth is neglected, the Paris law can be used at any points along the crack front as follows:

$$\frac{da}{dN}\bigg|_i = C(\Delta K)^n\big|_i \qquad (2.16)$$

Local increment at any point along crack front :

$$\Delta a_i = \left(\frac{\Delta K_i}{\Delta K_{max}}\right)^n \Delta a_{max}$$
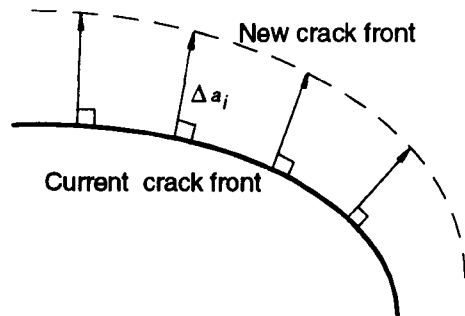
$$\frac{da}{dN} = C(\Delta K)^n$$

New crack front

Δa_i

Current crack front

Figure 2.7   Local fatigue crack growth along a curved crack front

where da_i is a local normal crack growth increment at an arbitrary point i.

It is extremely difficult to solve analytically Eq. (2.16) if the crack shape always changes during the fatigue growth process. However, it is definitely feasible to obtain a numerical solution by calculating local normal increments of propagation at a set of points through the crack front, as shown in Fig. 2.7. If an increment of fatigue cycles, ΔN, is specified, the local increment of crack growth at each point can be estimated by the following Euler's formulation:

$$\Delta a_i = C(\Delta K)^n\big|_i \Delta N \qquad (i = 1, 2, ...) \qquad (2.17)$$

As stated previously, when the ΔN is taken as an infinitesimal the numerical result of Eq. (2.17) will obviously approach a correct solution. Once these local increments Δa_i ($i = 1, 2, ...$) have been obtained a new crack front, as shown in Fig. 2.7, can be established. Repeating the calculation of Eq. (2.17) enables the fatigue growth of the crack to be followed step-by-step.

During practical computations, an adequate small increment of fatigue cycles should be chosen in order to ensure a good calculation accuracy. Smith and Cooper (1989), Chipalo *et al.* (1990) and Gilchrist (1991) did not describe the procedure of how to select an adequate ΔN value in their work. The present author suggests that throughout the crack growth process the maximum crack growth increment (*the maximum value of all* Δa_i ($i = 1, 2, ...$)), Δa_{max}, should be chosen as a constant, so that the crack shape change could be limited to a small extent. It is apparent that the maximum crack advance occurs at the point where the stress intensity factor range is the maximum over the crack front, as shown in Fig. 2.7, i.e.

$$\Delta a_{max} = C(\Delta K_{max})^n \Delta N \qquad (2.18)$$

Substituting Eq. (2.18) into Eq. (2.17) can lead to

$$\Delta a_i = \left(\frac{\Delta K_i}{\Delta K_{max}}\right)^n \Delta a_{max} \qquad (i = 1, 2, ...) \qquad (2.19)$$

Eq. (2.19) can be used to calculate the local increment of crack growth at each point along the crack front if the Δa_{max} has been specified. Ideally, a calculation loop of gradually reducing the Δa_{max} value should be followed in order to achieve a desired accuracy, as mentioned above for a 2D crack problem (*see Fig. 2.6*). The standard of accuracy can be based on some quantity, like the number of elapsed fatigue cycles when the crack reaches a given size, or a parameter characterising the crack shape change, etc. This will be further demonstrated in the following chapters.

It needs to be emphasised that the above extension of the Paris law to planar defects implies that the difference of the fatigue growth between 2D line cracks and 3D planar cracks has been ignored and the material constants, C and n, within the Paris law should be obtained from some standard small specimens subject to a regulated test procedure (like ASTM E647-88).

2.2.3 SIF calculations by FEM

According to the Paris law, it is clear that the predictions of the fatigue life, crack size and shape change of a cracked structure are principally based on the stress intensity factor. More accurate estimates of the stress intensity factor of varying crack sizes and shapes can avoid a large error in such predictions.

Estimating stress intensity factors for various crack configurations subjected to different stress states has been one of the main studies in the field of linear elastic fracture mechanics. Considerable efforts have been devoted to developing a variety of methods, ranging from exact analytical methods in terms of continuum mechanics theory to versatile numerical techniques such as alternating, weight function, body force and boundary and finite element methods. A large number of SIF solutions have been reported, and most of them have been summarised in several convenient handbooks (Rooke and Cartwright, 1976; Murakami, 1987).

Selecting the finite element method to calculate stress intensity factors in the present modelling technique is because of its versatility and generality for crack-tip stress analyses of practical complicated cracked structures. From the local distribution of crack-tip stresses, strains and displacements, obtained by the finite element analysis, along a crack front, the stress intensity factor can be estimated in terms of linear elastic fracture mechanics theory. Henshell and Shaw (1975) and Barsoum (1976) based their methods on crack opening

displacements measured at one point behind a crack front, and Blackburn and Hellen (1979) extrapolated from several points. Raju and Newman (1977) used nodal forces ahead of a crack front to estimate SIF values, and proposed empirical equations for calculating the SIF variation along the front of semi-elliptical surface cracks after a series of 3D finite element analyses (Newman and Raju, 1981). The estimate of *J*-integral (*energy release rate*), which is directly related to the stress intensity factor, has also been studied in many publications. The virtual crack extension technique for estimating the energy release rate ahead of a crack front was developed originally for 2D linear cracks by Parks (1974) and Hellen (1975), independently, and extended to 3D planar crack problems by deLorenzi (1982, 1985). Nikishkov and Alturi (1987) also presented an alternative *J*-integral concept (EDI) and developed a numerical method to calculate this parameter through finite element analysis. In addition to these methods mentioned above, there are some other methods based on finite element analyses. The interested reader can refer to the particular literature. The following sections only give a relatively detailed description of the displacement and energy release rate methods which are employed in the present simulation technique.

1/4-point displacement method

For planar cracks subject to loads normal to crack plane, the displacements out of the plane adjacent to the crack-tip has been expressed in Eq. (2.4):

$$u_z = \frac{K}{\mu}\sqrt{\frac{r}{2\pi}}\sin\frac{\theta}{2}\left(2-2\nu-\cos^2\frac{\theta}{2}\right) \qquad (2.20)$$

where μ is the shear modulus, ν is the Possion's ratio and u_z is the out of plane displacement of a point around the crack tip at polar location (r, θ), as shown in Fig. 2.3. This relationship is valid for plane strain condition and $r \rightarrow 0$. Therefore, the stress intensity factor, K, can be estimated by the out of plane displacement along the radial ray $\theta = 180°$:

$$K = \mu\sqrt{\frac{2\pi}{r}}\frac{u_z}{2(1-\nu)} \qquad (2.21)$$

Henshell and Shaw (1975) proved that the $1/\sqrt{r}$ strain singularity, which coincides with the theoretical singularity of linear elastic fracture mechanics, at the corner of an element can be exactly achieved by moving the midside nodes of the 2D standard 8-noded isoparametric element to 1/4-point positions, as shown in Fig. 2.8(a). At nearly the same time, Barsoum (1976) indicated, in addition to the same conclusion as obtained by Henshell and Shaw, that the prism elements (*degenerated from standard 20-noded isoparametric cubic elements, as shown in Fig. 2.8(b)*), if the midside nodes are relocated at the 1/4-points, also possessed the
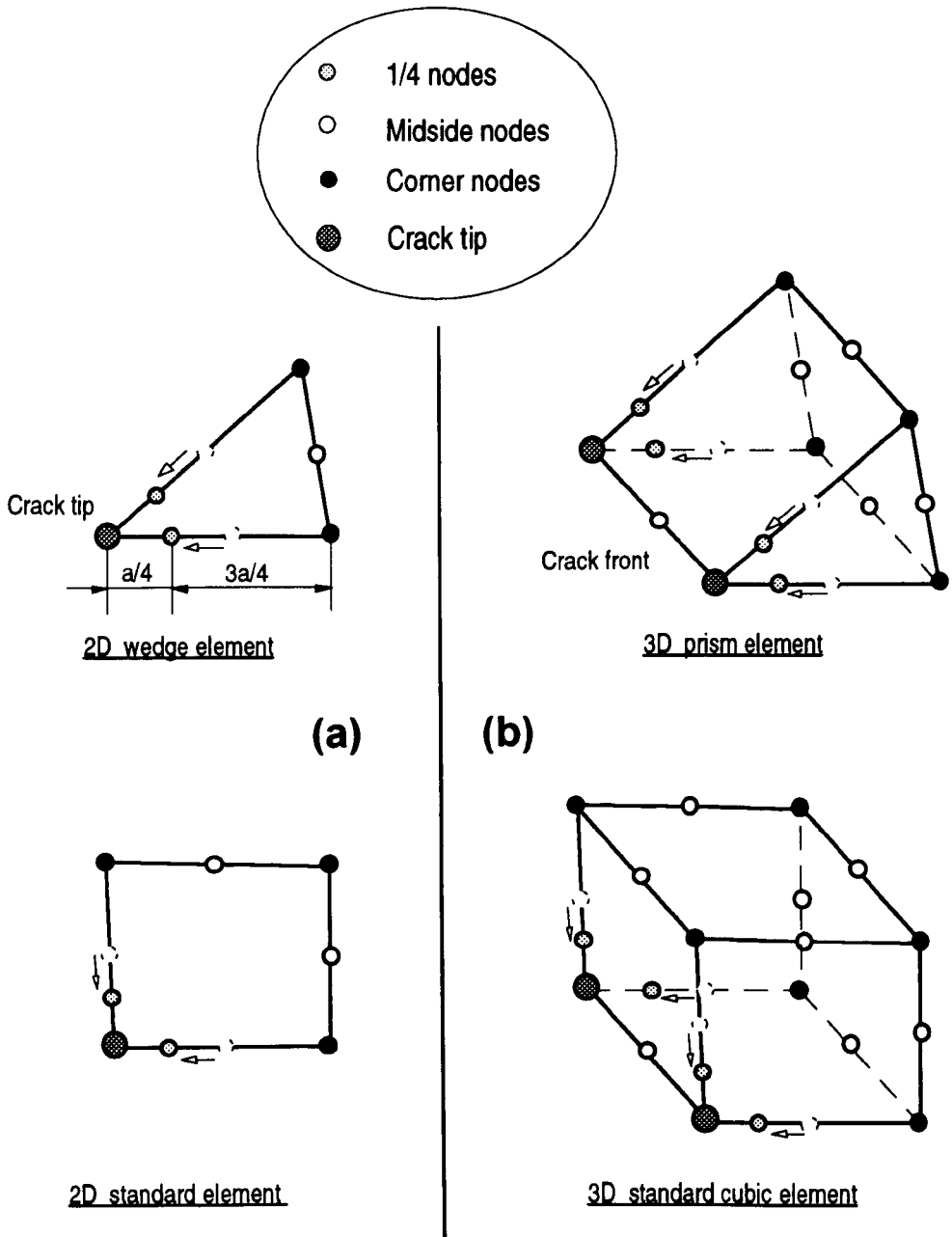
Figure 2.8   2D and 3D elements with midside nodes
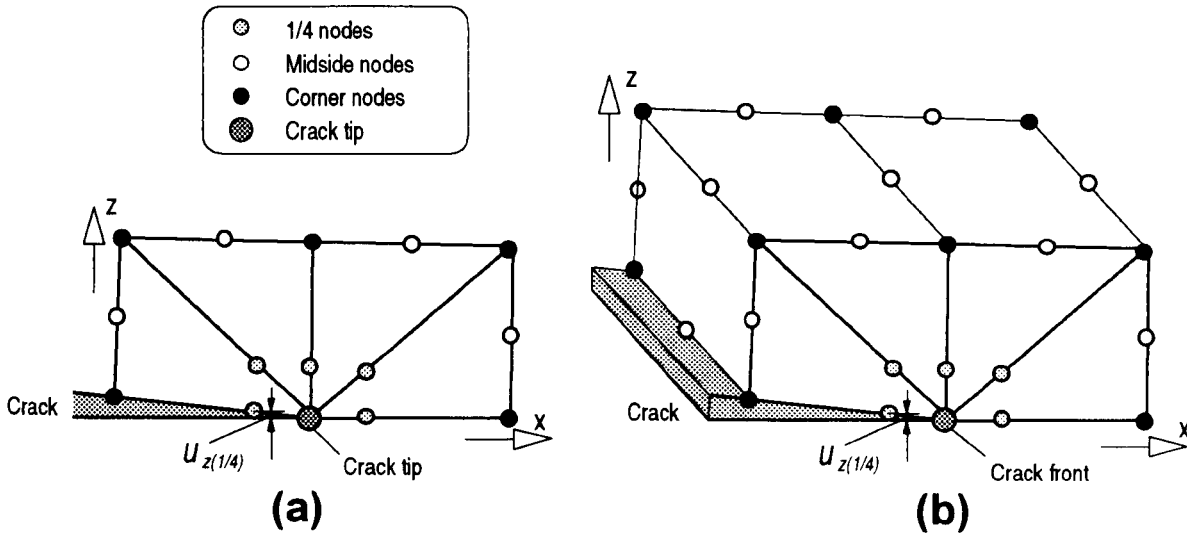moved to 1/4-points

Figure 2.9   Displacements at 1/4-points for 2D line crack
and 3D planar crack; (a) 2D, (b) 3D

$1/\sqrt{r}$ strain singularity. The numerical verification tests showed that the accuracy of the 1/4-point 3D prism (*wedge*) and 2D triangular shaped elements was better than of the 1/4-point 3D cubic (*brick*) and 2D quadrilateral elements.

Arranging these elements with the $1/\sqrt{r}$ strain singularity around a crack tip (or a crack front), the 1/4-point displacement method uses the crack opening displacements at the 1/4-points behind the crack tip, $u_{z(1/4)}$, to calculate K. Eq. (2.21) for K reduces to:

$$K = \mu \sqrt{\frac{2\pi}{r_{(1/4)}}} \frac{u_{z(1/4)}}{2(1-\nu)} \qquad (2.22)$$

where $r_{(1/4)}$ is the distance of the 1/4-point away from the crack tip, as shown in Fig. 2.9.

It is convenient to use this method to estimate SIFs for both 2D and 3D crack configurations through FE analyses. But, care should be taken on the generation of the mesh, especially for a 3D planar crack. The mesh abutting the crack front should be orthogonal, which will be demonstrated in a special section of this chapter.

J-integral (VCE energy release rate) method

The energy release rate (*or the J-integral, both are identical for planar fracture with the crack extending in the plane of the crack*), in addition to emerging as one of the leading parameters for characterising crack initiation and subsequent crack growth when the material

around the crack front undergoes a substantial amount of plastic flow, is also related to the calculation of stress intensity factor through Eq. (2.7). Once the *J*-integral has been calculated the stress intensity factor can be readily obtained.

There are two different techniques presently widely used for calculating the *J*-integral. The first is the contour integral method, which is based on a path independent surface (3D) or line (2D) integral surrounding the crack tip; the second is the virtual crack extension (VCE) method, which models a crack extension by a shift of node points in a finite element model. The virtual crack extension method was introduced independently by Parks (1974) and Hellen (1975). The earlier formulations were developed by them solely through a finite element approach. On the basis of the virtual crack extension principle, an analytical expression for the energy release rate in a general 3D crack configuration was derived by deLorenzi (1982) from a continuum mechanics concept. That is

$$
\begin{aligned}
G = & \frac{1}{A_c} \int_V \left\{ \left(\sigma_{ij} \frac{\partial u_j}{\partial x_k} - W\delta_{ik} \right) \frac{\partial \Delta x_k}{\partial x_i} - f_i \frac{\partial u_i}{\partial x_j} \Delta x_j \right\} dv \\
& - \frac{1}{A_c} \int_S t_i \frac{\partial u_i}{\partial x_j} \Delta x_j ds \qquad (i,j,k=1,2,3)
\end{aligned}
\tag{2.23}
$$

In this equation, the traction is included, and

A_c — the increase in cracked area generated by the virtual crack extension,

V — the volume,

S — the surface of the cracked body,

σ_{ij} and u_i — the stress and displacement tensors, respectively

W — the strain energy density, $\int \sigma_{ij} d\varepsilon_{ij}$

f_i — the body force vector

t_i — the surface traction vector

δ_{ij} — Kronecker's delta

Δx_i — a mapping function which maps the body containing the crack into a body with a slightly increased crack length

deLorenzi (1985) also established a finite element framework of this method for 2D plane strain/stress, axisymmetric and general 3D crack configurations. The FE formulation corresponding to Eq. (2.23) for general 3D crack geometries is

$$G = \frac{1}{A_c} \sum_{n=1}^{N} \sum_{i=1}^{I} \sum_{j=1}^{J} \sum_{k=1}^{K} \left(\text{trace} \left[\left(\{\sigma\} \left\{ \frac{\partial U}{\partial X} \right\} - W\{I\} \right) \left\{ \frac{\partial \Delta X}{\partial X} \right\} \right] \right.$$

$$\left. - \{f\}^T \left\{ \frac{\partial U}{\partial X} \right\} \{\Delta X\} \right)_{\xi_i \eta_j \zeta_k} \alpha(\xi_i)\alpha(\eta_j)\alpha(\zeta_k) \det(J) \qquad (2.24)$$

$$- \frac{1}{A_c} \sum_{n=1}^{N'} \sum_{i=1}^{I} \sum_{j=1}^{J} \left(\{t\}^T \left\{ \frac{\partial U}{\partial X} \right\} \{\Delta X\} \right)_{\xi_i \eta_j} \alpha(\xi_i)\alpha(\eta_j) \det(J')$$

where N and N' are the number of elements and surfaces which have been affected by the node shifts, I, J, K are the integration orders, α is the weight function, and J and J' are the volume and surface Jacobians for the mappings of the global coordinates into the local coordinates. The subscripts ξ, η, ζ denote that the expressions in the parenthesis have to be evaluated at the respective Gauss points. The mapping function, ΔX, was generated for both 8-noded and 20-noded 3D elements in the work of deLorenzi (1985). For more details about the virtual crack extension method the reader can consult the work of deLorenzi (1982, 1985), Hellen (1975) and Parks (1974).

Nikishkov and Atluri (1987) presented a so-called equivalent domain integral (EDI) which was considered by them to be a new interpretation of the VCE technique and to be able to avoid the necessity of shifting the near-front nodes. The validity of the EDI formulation was demonstrated by solving some 3D mixed mode crack geometries. Actually, it can be proved that both the VCE formulation of deLorenzi (1982, 1985) and the equivalent domain integral can come to an identical result.

The commercial FE package ABAQUS (*version 4-7 and above*) has incorporated such an evaluation of the *J*-integral based on the virtual crack extension method. The user only needs to specify the node set forming each crack tip (*or the node sets forming the crack front in 3D solid meshes*), and the required number of "contours". Each "contour" must be a ring of elements completely surrounding the crack from one crack face to the opposite crack face, and can produce a *J*-integral value. These *J*-integral values obtained from different rings of

elements should be theoretically path independent for the elastic case, which may be taken as an indicator of the solution accuracy.

2.3 Numerical Simulation Technique

2.3.1 Brief description of the original software

The finite element technique for simulating the shape development of fatigue defects was originally developed by Smith and Cooper (1989) for their purpose of examining the effect of local brittle zones on the Mode I fatigue growth of planar defects. The modelling is principally based on finite element analyses together with the step-by-step Paris law described previously (*see Eq. (2.17)*). The variation of stress intensity factors was estimated using the 1/4-point crack opening displacement method. The shape change of the defect was predicted by determining local increments of crack length, due to different stress intensity factor values, at a set of arranged discrete points that form the crack front. A kind of automatic remeshing technique was designed in their software which enables the time spent creating 3D finite element meshes of the propagating crack front to be reduced.

The technique was subsequently applied by Kishimoto *et al.* (1989) and Soboyejo *et al.* (1989) to investigate the interaction of two coplanar surface defects. Chipalo (1990) used the same technique to examine the tension fatigue growth of a single embedded defect in a finite thickness plate and semi-elliptical surface defects in both round bars and finite thickness plates. Gilchrist (1991) made some efforts to improve such aspects of this technique as applying different fatigue loads with components of tension and bending to finite thickness plates and introducing a layer of elements into the cracked block in order to increase the calculation accuracy.

The original software was based on the MARC finite element analysis solver and its interactive mesh generator (*pre-processor*), MENTAT, for the special purpose of their project, not for a general use. The framework of the software, which had been retained by the subsequent users, had some inconvenience in dealing with different crack profiles, boundary and loading conditions. It was frequently required to add extra program code to the original

source code, and then to reorganise it for different crack problems. The crack front was defined by a polyline (*an open polygonal*), which may cause a large error in evaluations of stress intensity factors in many cases (*to be discussed later*). Gilchrist (1991) attributed the larger error to the mesh mismatch between the cracked and uncracked blocks, and added an extra layer of elements into the cracked block to attempt to reduce its influence. In fact, the polyline approximation to a crack profile is a major cause. The software also did not allow to run the calculation loop continuously, especially overnight, since the input of an increment of fatigue cycles, ΔN, was interactive for obtaining a reasonable small crack growth and the frequent modification of the position of some nodes within a 2D cracked mesh was required for maintaining the orthogonal mesh requirement.

2.3.2 Preview of the new software

In order to pursue a good accuracy and efficiency as well as a convenient application of this modelling technique to a wide range of practical cracked structures, the present author has re-developed a suite of software, which consists of DUCKPRE (*pre-processor*), DUCKPOST (*post-processor*) and DUCKCONN (*command stream*). This new software currently provides interfaces to ABAQUS-FEMGV and MARC-MENTAT finite element analysis suites, but only runs in connection with ABAQUS and FEMGV during the practical modelling computations in this thesis.

In the pre-processor DUCKPRE, a new cubic spline is introduced to define the crack front, which will be shown to be effective in reducing a large SIF error possibly occurring due to the use of the polyline approximation. Two kinds of 3D crack tip elements which are more ideal for planar crack problems are designed. A good flexibility is provided for establishing the desired 3D mesh configurations of the cracked block through combinations of these crack tip and cubic elements. An improvement on applying various fatigue loads and displacement constraints to specified planes has been achieved. Particularly, the constraints on the cracked plane with multiple cracks can be readily dealt with.

The post-processor, DUCKPOST, of the new software first calculates the SIF variation along the crack front from the results of both the displacement and *J*-integral results obtained by ABAQUS. In addition to the 1/4-point displacement method which the old software has used, DUCKPOST also incorporates the 3D *J*-integral method described previously to
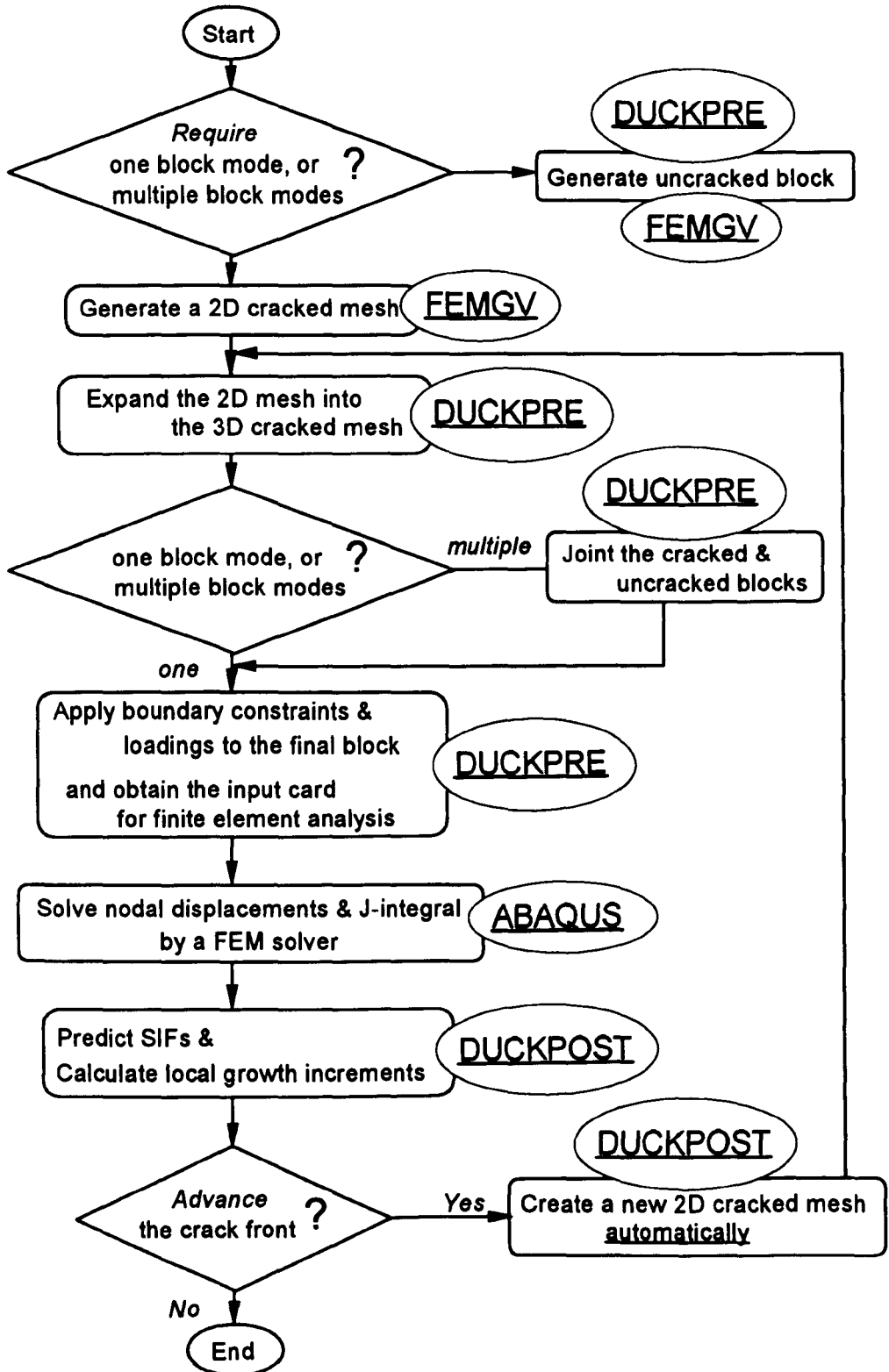
Figure 2.10   Analysis procedure of the present numerical simulation technique

estimate the stress intensity factor and then to allow a verification of the SIF accuracy of each other. A Paris law is subsequently applied to evaluate the local normal outward increments of crack growth in terms of Eq. (2.19), in which the technique of specifying a maximum increment of crack growth, Δa_{max}, along the crack front, as detailed previously, is employed instead of interactively feeding an increment of fatigue cycles, ΔN. A new crack front is formed according to these new locations of this set of nodes on the original crack front by using either a cubic spline curve or a polyline, and the nodal positions can be automatically re-arranged along the new crack front with a reasonable interval between them (*only for the cubic spline definition*). DUCKPOST then can automatically generate a new 2D cracked block mesh that corresponds to the new advanced crack front. The new 2D cracked block mesh, as an output of the post-processor of the present technique, can be completely transferred, in most cases, to the next step computation as an input of the pre-processor, and enables the fatigue crack growth computation to be entirely followed.

Fig. 2.10 is the schematic flowchart which details the actual stages of the new technique. What software, DUCKPRE, DUCKPOST, ABAQUS or FEMGV is used at each stage is clearly shown in this figure. A bridge between the present software and the commercial packages has been constructed by the present author through DUCKCONN, a UNIX *C*-shell program that permits the ceaseless execution of the flowchart in Fig. 2.10 on a UNIX-based workstation. This significantly raises the calculation efficiency of the present simulation technique. Some more details about this technique are now given in the following section.

2.3.3 Some details of DUCKPRE and DUCKPOST

Creation of finite element models

The idea, proposed by Smith and Cooper (1989), that a cracked 3D structure is divided into two blocks: cracked and uncracked (loading) blocks as shown in Fig. 2.11, facilitates conveniently the automatic technique of remeshing the FE model of successive crack front positions, and is also used in the new software. The uncracked block, meshed relatively coarsely, defines the bulk of the structure and usually remains unchanged during the whole analysis procedure. The cracked block, meshed finely, represents the small volume of material surrounding the crack and is automatically reconstructed and subsequently reconnected to the uncracked block after each successive increment of crack growth.

The design of an uncracked block configuration requires a careful consideration of the geometry and loading conditions of an actual cracked structure as well as its deformation characteristic. The boundaries of the uncracked block that abut on the cracked block, as shown in Fig. 2.11, must be planes due to the necessity of dealing with the constraint equations. The uncracked block consists of isoparametric quadrilateral 20-noded brick elements with 3×3×3 integration points.

The 3D cracked block mesh is created by initially defining a 2D cracked mesh on its base plane (*crack plane*) and then expanding it into a 3D mesh. The 2D cracked mesh is composed of 8-noded quadrilateral isoparametric elements. The elements abutting the crack front within the 2D cracked mesh are oriented so that their edges intersect the crack front orthogonally, as shown in Fig. 2.12(a), which is required by the 1/4-point displacement method. When the crack front approaches a free edge or sharply changes its direction which often occurs when two co-planar cracks meet, it is obvious that the orthogonal condition cannot be satisfied. Special arrangements are made for these situations, as shown in Fig. 2.12(b) and (c).

Figure 2.11   Creation of 3D finite element model from separate blocks

An 8-noded element within the 2D crack mesh can be expanded into three kinds of 3D elements shown in Fig. 2.13:

(a) one 20-noded cube element.

(b) two 20-noded wedge elements (degenerated from 20-noded elements) and four 20-noded brick elements.

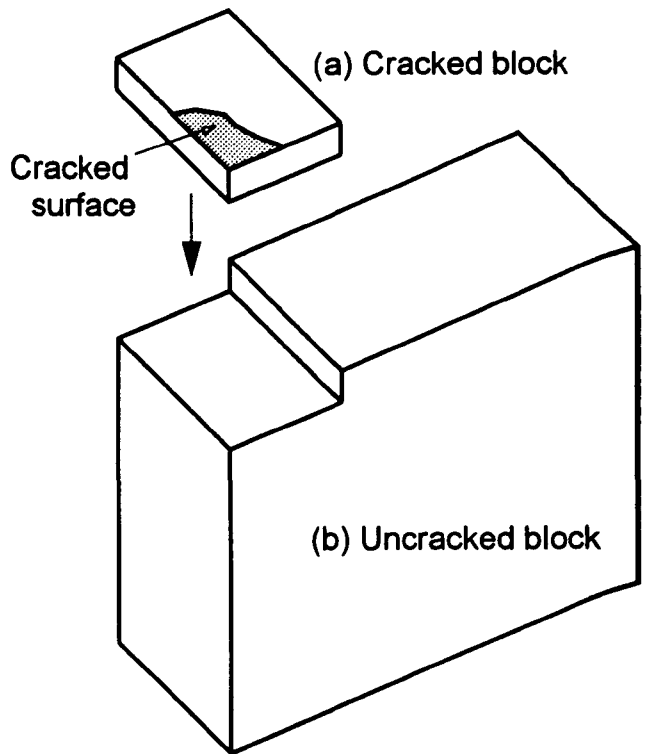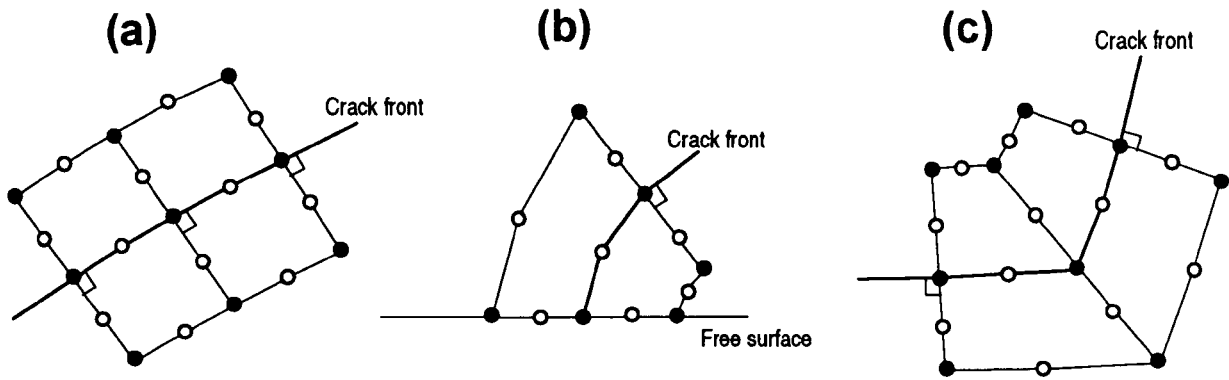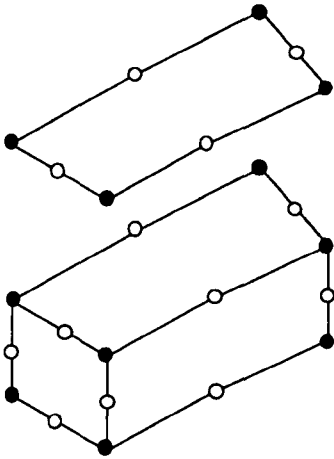(c) four 20-noded wedge elements and eight 20-noded brick elements.

Figure 2.12   Mesh arrangement along a crack front;
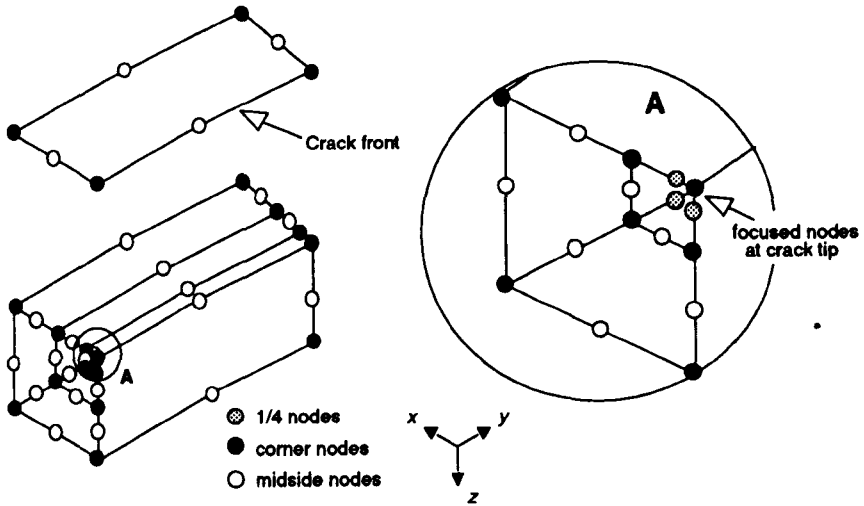(a) orthogonal, (b) and (c) non-orthogonal

The wedge elements surrounded by the 20-noded bricks in both (b) and (c) are designed as the 3D crack-tip elements that are proper for the FE analysis of a 3D crack. The midside nodes adjacent to the crack front are located at the 1/4-points, as suggested by Henshell and Shaw (1975) and Barsoum (1976). Those 2D elements abutting the crack front are usually expanded into the 3D crack-tip elements, (b) or (c), the latter having much more degrees of freedom and generally giving more accurate results than (b). A desired 3D cracked block can be assembled by combining these 3D elements. It is very straightforward to choose the number of layers and to vary the thickness of each layer. Any kind of 3D cracked block mesh can be created by feeding some control parameters as well as important data such as the identification number of the nodes along the crack front and the identification number of the elements within the cracked surface to DUCKPRE. These data necessary for creating a 3D cracked block mesh are contained in a file. Fig. 2.14 shows a 3D cracked block mesh generated automatically by DUCKPRE from its 2D cracked mesh.

Obviously, the technique of expanding a simple 2D mesh into a complicated 3D mesh is also able to create efficiently a whole 3D mesh with complete nodal compatibility in the situation where the uncracked block is unnecessary for some simple cracked geometries. Compared with Smith and Cooper's (1989) original software, the present software provides a good flexibility for assembling a desired cracked block by a proper arrangement of either (b) or (c) of 3D crack-tip elements and different layers of brick elements (a).

(a)

(b)

Crack front

1/4 nodes
corner nodes
midside nodes

focused nodes
at crack tip

x   y

z

(c)

Crack front

1/4 nodes
corner nodes
midside nodes
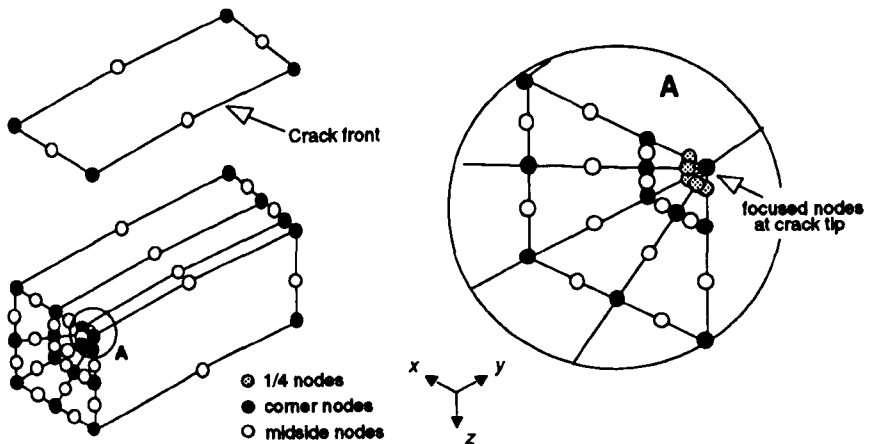
focused nodes
at crack tip

x   y

z

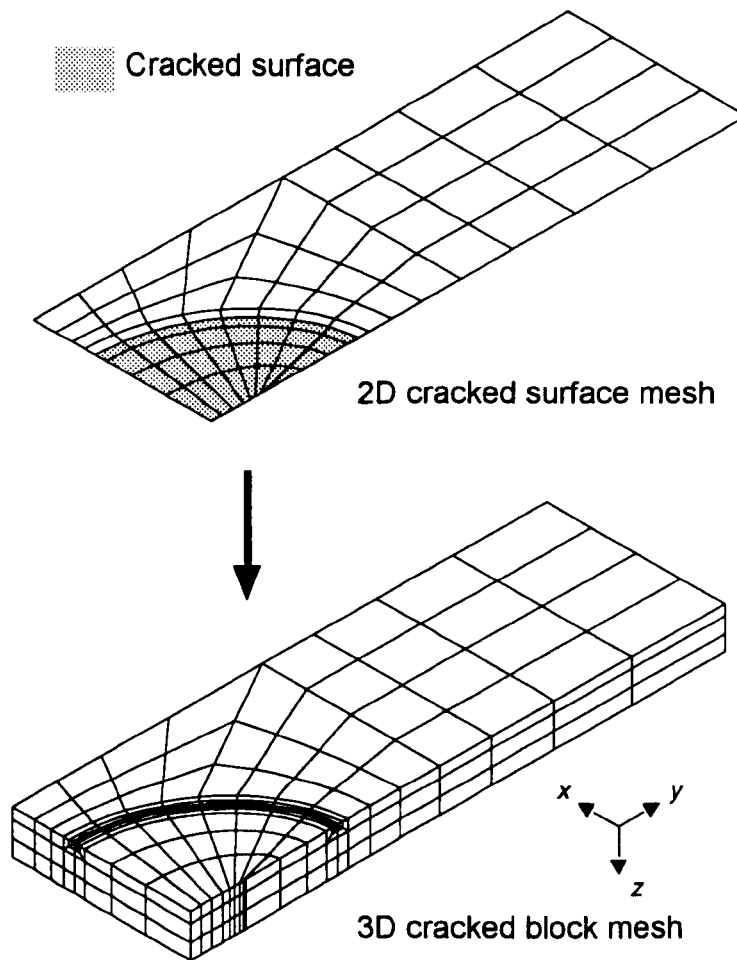Figure 2.13   Formations of 3D elements from 2D elements

Figure 2.14 A typical 3D cracked block mesh expanded
from its 2D cracked mesh

When the cracked block is assembled to the uncracked block with relatively coarse mesh, there are always many nodes which are not able to be merged between the cracked and uncracked blocks. The mesh mismatch will lead to noncontinuity of such quantities as displacements, stresses and strains across the mismatch plane and decrease the accuracy of FE analyses. A commonly used method to reduce the effect of this mesh mismatch is "multi-point constraints" in the FE method. Its principle is that nodes on the top surface of the cracked block which are not merged are constrained to the bottom surface of the uncracked block using constraint equations. For example, in Fig. 2.15 the displacements of nodes 7, 8, 13, 15 and 16 are constrained by interpolation to the displacements of nodes 1, 2, 3, 10, 11, 17, 18, and 19 whilst nodes 6, 9 and 14 are linked to 3, 4, 5, 11, 12, 19, 20 and 21. As the crack front moves the constraint equations will change and are required to reconstruct due to the remeshing of the cracked block. DUCKPRE can automatically formulate these constraint

equations after each successive reassembling of the cracked block to the uncracked block for the FE solver ABAQUS. In order to ensure a successful output of all constraint equations, it is important to be aware that the edges of out-of-plane elements on the abutting plane must be straight lines, but not necessarily intersect normally each other as required by the original software.

After the complete mesh, comprising both the cracked and uncracked blocks if the uncracked block appears, is assembled, the loads and boundary constraints are applied. Some subroutines included in the present simulation technique make it easy to apply various loads, such as point, line and uniformly or nonuniformly distributed surface loads, to specified positions of the mesh. The constraint conditions are also dealt with in a similar way.
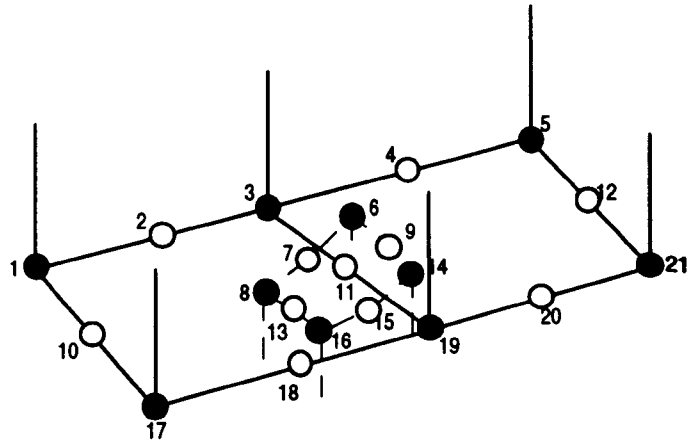

Figure 2.15 Nodal mismatch across boundary of mesh refinement

Particularly, a quite effective technique of specifying displacement constraints of the non-cracked area on the crack plane has been developed, which significantly enhances the ability to deal with a variety of irregular or multiple cracks.

Finally, the pre-processor of the present software, involved in what mentioned above, automatically provides a complete input file for the FE solver, ABAQUS.

Automatic crack advance and remeshing

Once the FE calculation is successfully completed, the post-processor of the present software, DUCKPOST, begins to work. Firstly, DUCKPOST extracts the displacement values at the 1/4-points behind the crack tip and the *J*-integral values at each crack tip position *(usually three J-integral values are available, each corresponding to three different rings of elements)* from the output file of ABAQUS. These FE results are used to calculate the SIF variation along the crack front by using both the 1/4-point displacement and *J*-integral methods. The three *J*-integral values at each position are averaged and then converted to the stress intensity factors through either the plane strain or the plane stress assumption, the latter

will be used at the free surface point in a so-called free boundary correction technique described later. Similarly, the calculation of stress intensity factors from the displacements also needs to employ either the plane strain or the plane stress condition.

Secondly, choosing proper material constants, C and n, in the Paris law, and using Eq. (2.19), DUCKPOST calculates the local normal outward increments of crack growth at these corner nodes on the crack front. The maximum increment of crack growth, Δa_{max}, along the crack front, as detailed previously, is usually chosen to be a small constant throughout most of analysis steps. This avoids a larger error which easily occurs when the stress intensity factor is large.

Thirdly, DUCKPOST automatically advances the corner nodes on the crack front to their new positions, and reconstructs a new crack front by using either a cubic spline curve or a polyline (*to be demonstrated later*). For the cubic spline curve definition, the new nodes, corner and midside nodes, are rearranged along the crack front in order to have them distanced reasonably (*by specifying a bias factor desired intervals can be obtained*). This can effectively maintain the crack front well-approximated and also greatly assist in recreating the new mesh. After these nodes that constitute the new front have been set, the software then generates a new 2D cracked mesh corresponding to the new crack front. Unlike the original software in which only the position of the nodes of these elements abutting the crack front is modified, the present software relocates almost all nodes within the 2D mesh to keep the mesh always in a good state (*having as few distorted elements as possible*). The new 2D cracked block mesh can be completely prepared, in most cases, for the next step computation, even a minor adjustment of some nodal positions having to be done in the original software is unnecessary. This allows the fatigue growth computation to be completely and automatically followed, and significantly increases the computation efficiency of this modelling technique.

Crack front definitions

The shape of a curved crack front must be established by a set of discrete nodes in a finite element model. Fig. 2.16 shows two definitions of the crack front within 8-noded quadrilateral isoparametric elements.

In Fig. 2.16(a), the thick polyline that connects the corner and midside nodes constitutes the crack front. When the FE mesh for an initial crack configuration is created, the positions of the corner nodes usually are exactly determined from the known crack front shape and the
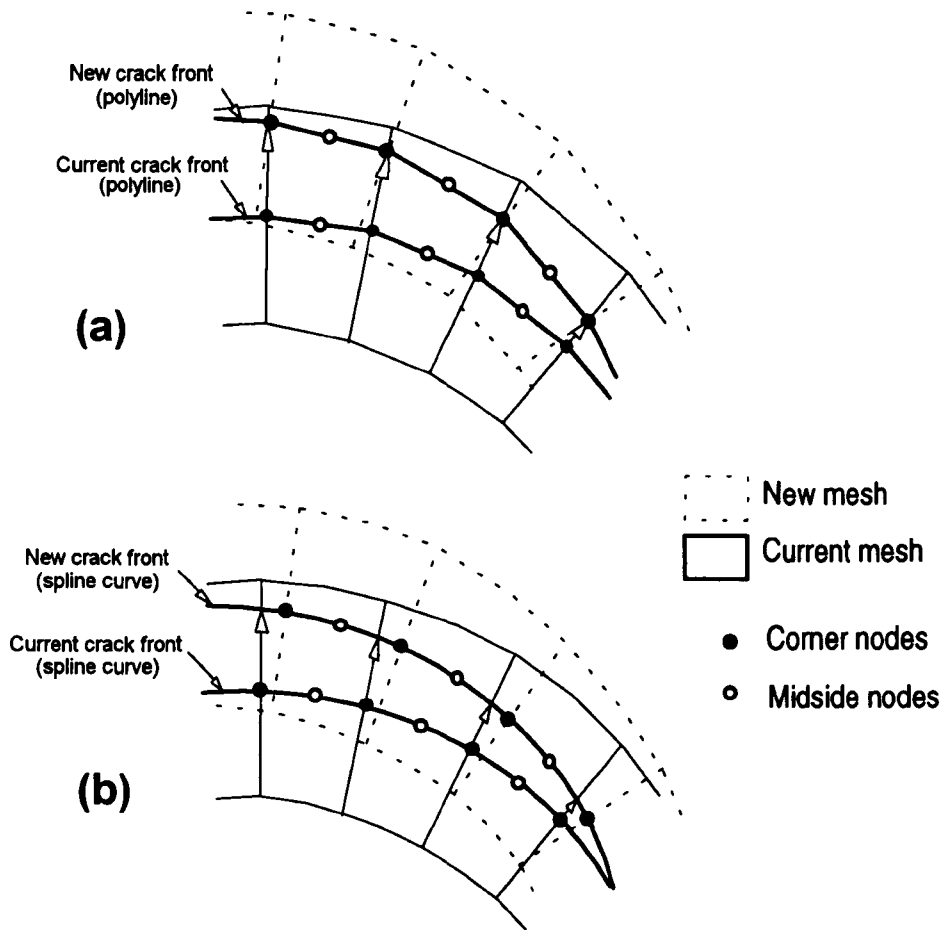
Figure 2.16   Crack front shape definitions in finite element models;
(a) Polyline, (b) Cubic spline curve

positions of the midside nodes are then obtained as the mid-points of both neighbouring corner nodes. The so-called polyline definition was first suggested in the original software (Smith and Cooper, 1989). Once the stress intensity factors at these corner nodes (*no SIFs are available at midside nodes by the 1/4-point displacement method*) are obtained, the local increments of fatigue crack growth along these edges of elements that are nearly normal to the crack front as shown in Fig. 2.16(a) can be determined by applying an appropriate Paris law to these nodes, and a set of new points are obtained. The set of new points are still taken as the corner nodes for the new crack profile, and then employed to calculate the new midside nodes by the linear interpolation method. These new corner and midside nodes redefine the new crack front, as shown in Fig. 2.16(a). Obviously, such a polyline definition for the crack front will lead to a possible requirement for certain nodes to be moved or inserted when the

distances between these corner nodes become unreasonable. It is frequently necessary to modify manually such nodal positions in the original software for large crack shape changes. This considerably reduces the automation degree of the modelling technique. Also the definition will cause a relatively larger error in estimates of stress intensity factors along the crack front, which had not been realised by Smith and Cooper (1989), Chipalo (1990) and Gilchrist (1991), and will be clearly revealed later. The polyline definition still remains in the new software and has been employed by Lin and Smith (1994a, b) in the investigations of the fatigue growth starting from initially long and shallow cracks and multiple small cracks in finite thickness plates.

Fig. 2.16(b) shows the cubic spline definition proposed by the present author. The crack front is approximated by a cubic spline curve (*black curve*) that passes through both the corner and midside nodes. The main difference between the polyline and cubic spline definitions is the position of these midside nodes. The initial crack front is constructed by the prearranged corner and midside nodes which both are precisely located on the specified crack front curve. Compared with the polyline, the smooth spline curve is able to give more accurate estimates of stress intensity factors along the crack front, as demonstrated later. Similarly, the local increments of crack growth are calculated only at the corner nodes, in spite of being available at the midside nodes by the *J*-integral method. After the locations of these advanced corner nodes are determined, the new crack front that is a cubic spline curve is established according to these advanced corner nodal positions. The advanced corner nodes, however, are not chosen as the new corner nodes, as shown in Fig. 2.16(b). The positions of the new corner and midside nodes are rearranged by a criterion that these nodes are well distanced on the spline curve. This can avoid modifying frequently nodal positions when a large crack shape change occurs, and achieve a high automation for the remeshing of FE models. Once these new corner and midside nodes are set, the 2D 8-noded elements abutting the crack front, as shown in Fig. 2.16(b), are automatically recreated with the help of the software FEMGV.

Free boundary layer correction technique

It can be easily observed in experiments that an initially straight fronted crack in specimens such as a compact tension specimen usually grows to a slightly curved shape (*see Fig. 2.17(a)*) under a fatigue load, or a surface crack shows a slower propagation along the crack free surface direction than at interior crack front positions (Newman and Raju, 1981), even leading

to a retardation of crack growth along the surface direction (*see Fig. 2.17(b)*) where the crack front actually makes an acute or negative angle of intersection with the surface (Putra and Schijve, 1992). This is the so-called free surface layer effect.
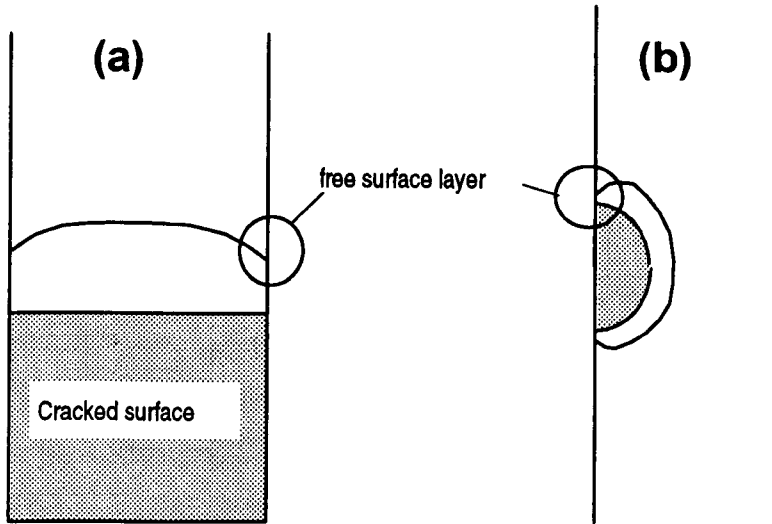

Figure 2.17   Effect of free surface on fatigue crack growth

The presence of a free surface layer mainly is a result of the effect of the stress state ahead of the crack tip. The three dimensionality of the stress state, more nearly plane strain, away from a free surface is degenerated to the two dimensionality, approximately plane stress state, close to the surface. The region of more plane stress near the surface (*i.e. the surface layer*) is more resistant to fatigue crack growth than the region away from the surface. However, the Paris law, which describes the relationship between the fatigue crack growth rate and the stress intensity factor, is generally obtained under as near plane strain condition as recommended in the ASTM E647-88 (1988). Applying these same material constants all around the crack front certainly introduces an error, though it is probably conservative. On the other hand, it is also difficult to obtain an accurate stress state adjacent to the crack tip in the region close to the free surface, especially for cracks not being normal to the surface. Some attempts (Benthem, 1977; Bazant, 1974; Bazant and Estenssoro, 1979) have been made to investigate the asymptotic field for 3D surface cracks. Benthem (1977) showed that at the actual point of intersection of a crack front with a free surface there are no stresses that vary with $1/\sqrt{r}$, where r is the distance from the crack tip, so the usual concept of a SIF at this point is not valid. He suggested that at this point the crack tip singularity can be expressed by

a weaker exponent, $\sigma \propto r^{\lambda}$, ($\lambda < 0.5$). Many investigators such as Hartranft and Sih (1970), Sih (1978) and Raju and Newman (1979) have indicated that SIF falls off to zero at the free surface.

In order to consider the effect of the free boundary layer during the fatigue crack growth, the present author proposed the following correction technique which is an option in the present numerical simulation technique, i.e. when the stress intensity factor is converted from either the 1/4-point displacement or the *J*-integral value, the free surface point is considered to be in the plane stress state while the other positions along the crack front to be in the plane strain state. Obviously, the free surface layer correction has considered the local two dimensionality of the stress state at the free surface, in spite of being too rough to describe precisely the stress state change from the interior to the surface. It should also be noted that this correction is not related to the material resistance to fatigue propagation which actually varies with the stress state as mentioned above.

2.4 Three Important Aspects in SIF Estimates

2.4.1 SIF sensitivity to crack front shape

The above section has described the two methods of approximating a crack front shape within a FE model, i.e. the polyline and cubic spline methods. Cooper and Smith (1987), Chipalo (1990) and Gilchrist (1991) found that the SIF estimates along certain crack fronts from the FE analyses were not in good agreement with their existing solutions, sometimes, the discrepancy even may reach approximately 20%. Gilchrist (1991) attributed it to the smaller thickness of the cracked block chosen by Cooper and Smith (1987) and Chipalo (1990) when they expanded into the block from the 2D mesh, and thought this might lead to an increase of the model stiffness around the defect due to the constraint equations applied on the interface between the cracked and uncracked (loading) blocks. He subsequently added an extra element layer to the cracked block. The SIF results he obtained for a particular surface crack in a finite thickness plate subjected to tension appeared to be improved, closer to the Newman and Raju prediction than those of Cooper and Smith (1987). However, the difference between the

Gilchrist and Newman and Raju results was still not so small, nearly 6 ~ 8%. The other possible reasons were not mentioned further by him.

Actually, the presence of large errors in estimates of SIFs by using the original software is mainly due to the crack front approximation made by the software, i.e. the polyline method, as shown in Fig. 2.16(a). In order to clarify the difference between the polyline and cubic spline definitions, an internal penny-shaped defect (radius: a = 10mm) in an infinite body under remote uniform tension and a semi-elliptical surface crack (a/c = 0.5, a/t = 0.2) in a finite thickness plate subjected to remote tension were examined.

Figs. 2.18 and 2.19 show two FE models created by the present software DUCKPRE, respectively corresponding to the internal and surface cracks. The 3D mesh (*Fig. 2.18(*a*))* for the internal crack was entirely generated from its 2D cracked mesh, while that (*Fig. 2.19(a)*) for the surface crack was formed by combining both the cracked and pre-defined uncracked blocks. The crack front was approximated within the 2D mesh by both the polyline and cubic spline methods for each crack, as shown in Figs. 2.18(b, c) and 2.19(b, c). It can be seen in both figures that there were seventeen nodes arranged along the crack front. The cubic spline method arranged for all nodes to pass exactly through the circle or the semi-ellipse, but the polyline definition only had the corner nodes situated exactly on the crack profile and the midside nodes positioned to the mid-points of the straight lines connecting two adjacent corner nodes. The number of degrees of freedom was 14265 for the internal crack and 6981 for the surface crack. The Poisson's ratio ν is assumed to be 0.3.

The stress intensity factor results along the circular crack front are displayed in Fig. 2.20 for the two different approximations of crack front. For each approximation the SIF values are converted from both the 1/4-point displacements behind the crack tip and the *J*-integral values with plane strain assumed. It can be seen that along the crack front defined by the cubic spline curve the SIF variation calculated by the 1/4-point displacement is a straight line (*noting that no SIF values are available at corner nodes*), whilst the SIF by the *J*-integral method shows a slightly waved line, where the values at the midside nodes are a little bit lower (*about 0.3%*) than those at the corner nodes. Sneddon's (1946) exact solution, $K/(\sigma\sqrt{\pi a})$, is 0.6366, very close to both the present author's average SIF values, 0.6337 (*from the displacement method*) and 0.6354 (*from the J-integral method*). For the crack front approximated by the polyline, the dimensionless SIF values obtained by the displacement

Edge length: 400mm

Crack radius: 10mm

Numer of nodes: 4755

Number of elements: 976

(a)

(b)

Straight line

(c)
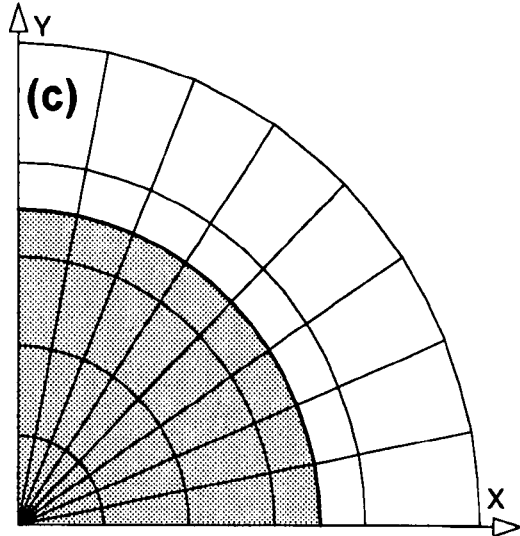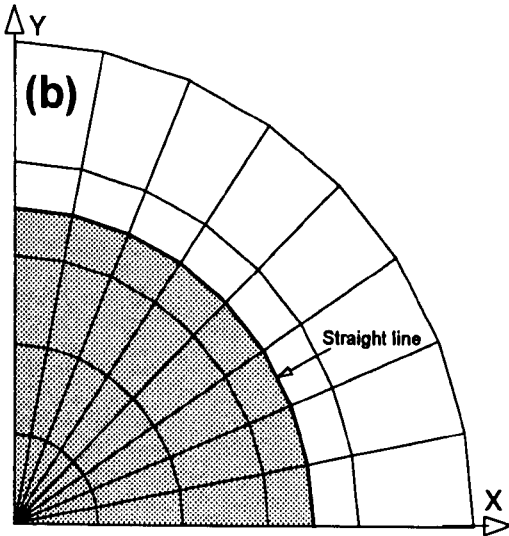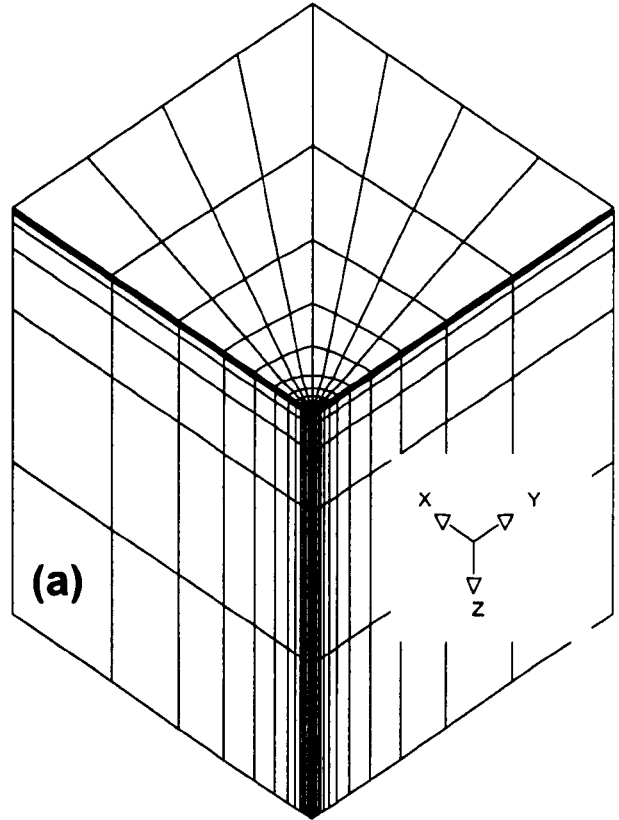
Figure 2.18   A circular internal crack in an infinite solid under tension; (a) 3D finite element mesh; (b) Polyline approximation to crack front; (c) Cubic spline approximation to crack front, (▨ cracked surface)

(a)
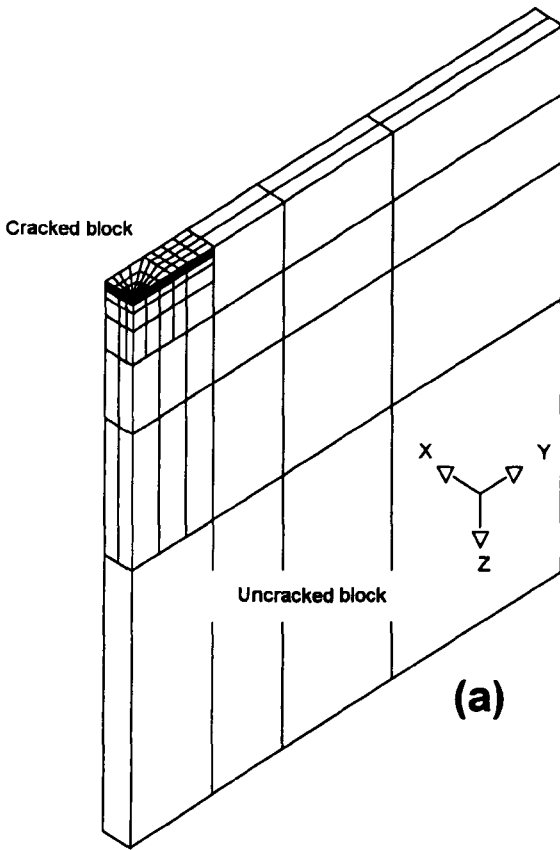
Height and width of plate mesh: 400mm

Crack surface half length: 8.33mm

crack depth: 5mm

Number of nodes: 2327

Number of elements: 396

(b)

Straight line

(c)
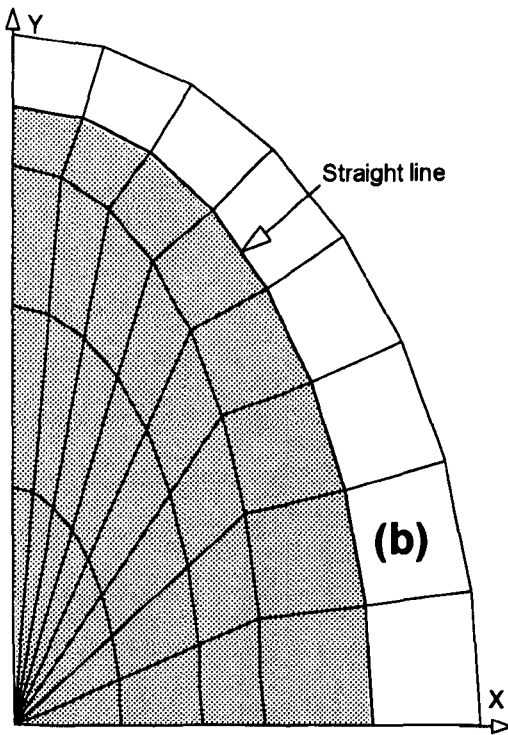
Figure 2.19   A semi-elliptical surface crack in a finite thickness plate subjected to tension; (a) 3D finite element configuration; (b) Polyline approximation to crack front; (c) Cubic spline approximation to crack front (cracked surface)
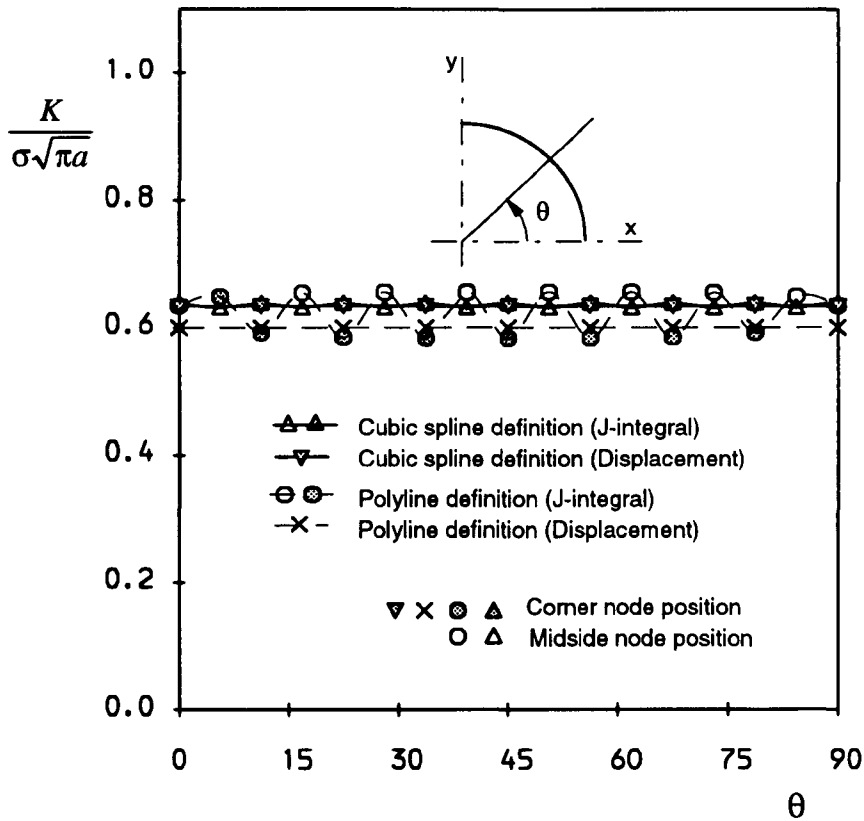
Figure 2.20   Stress intensity factor variations estimated from *J*-
integral and 1/4-point displacement along the internal circular
crack front approximated by two methods

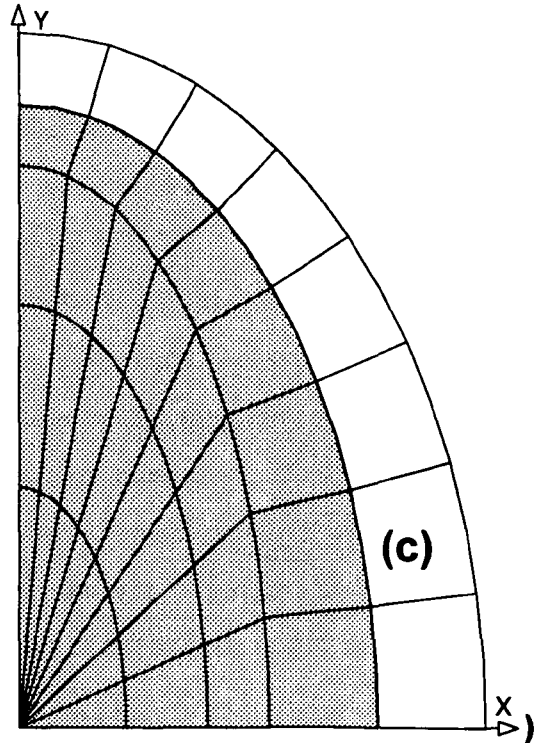method along the crack front are also identical but nearly 5% lower $(K/(\sigma\sqrt{\pi a}) = 0.5995)$ than those along the spline crack front, whilst the SIF variation estimated by the *J*-integral method is an obvious wave line, along which the values at the midside nodes are about 11% higher than those at the corner nodes. Such a waved SIF variation, apparently, is due to the midside nodes that are not exactly located on the circle. The large difference of SIF values between the corner and midside nodes demonstrates that the SIF variation along the crack front is very sensitive to the crack shape, even a very small difference in crack front shapes as shown in both Figs 2.18 and 2.19 will cause a great discrepancy in estimates of SIF values. The waved SIF distribution in Fig. 2.20 actually can explain the general experimental fact that under the fatigue loading a non-smooth crack front will rapidly grow to a smooth profile, since this trend of crack growth requires higher SIFs at those concave points, like the midside nodes, of the crack front.
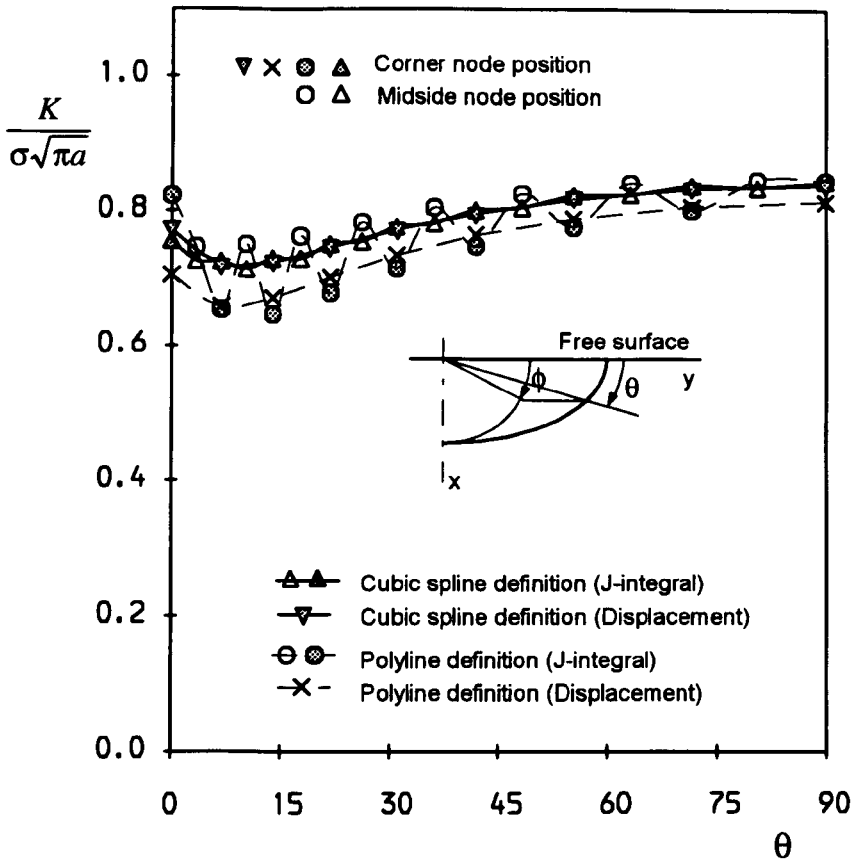
Figure 2.21   Stress intensity factor variations estimated
from *J*-integral and 1/4-point displacement along
the semi-elliptical surface crack (*a/c* = 0.6, *a/t* =
0.2) front approximated by two methods

Fig. 2.21 shows the normalised SIF variations along the semi-elliptical surface crack. Both solid lines represent, respectively, the SIF results calculated from the 1/4-point displacement and *J*-integral methods by defining the crack front as a cubic spline curve. It is shown that they agree well with each other. The SIF values at the corner nodes of the polyline front obtained by both the 1/4-point displacement and *J*-integral methods also agree well but lower than those at the corner nodes of the cubic spline front. The SIFs at the midside nodes, similar to those displayed in Fig. 2.20, are greater than those at the corner nodes, and even greater than the results of the cubic spline front. Clearly, in Fig. 2.21 the larger SIF error indicated by Gilchrist (1991) does exist (*Chapter 4 is going to compare the present results with Newman and Raju's (1981) solutions*). The lower SIF results obtained by Chipalo (1990) or Gilchrist (1991) by the 1/4-point displacement method, actually, is mainly caused by the polyline definition they used, not just what Gilchrist (1991) thought.

From the above SIF comparisons it can be concluded that the cubic spline definition for a crack front proposed by the present author is superior to the polyline definition, and is able to obtain more accurate SIF estimates and further better predictions of fatigue crack growth. In the following chapters involved in examining different cracked geometries, the cubic spline approximation will be used except in Chapter 4.

2.4.2 Effect of non-orthogonal mesh on SIF estimates

As has been indicated previously, it is very important that the mesh abutting the crack front should be orthogonal when the 1/4-point displacement method proposed by Henshell and Shaw (1975) and Barsoum (1976) is used to evaluate the stress intensity factors along a curved crack front. However, the orthogonal mesh seems unnecessary for the *J*-integral method based on the virtual crack extension principle. This section aims to numerically investigate the effect of the mesh non-orthogonality on the SIF accuracy achieved by both the 1/4-point displacement and *J*-integral methods.

The investigation focused on the particular defect embedded in an infinite body under remote tension shown in Fig. 2.18. Five different 2D crack plane meshes were designed for this defect, as shown in Fig. 2.18(c) (*mesh (a)*) and Fig. 2.22 (*mesh (b-e)*). Obviously, the degree of mesh non-orthogonality is different for each, and gradually varies from the precisely orthogonal mesh (*Fig. 2.18 (c)*) to the most distorted one (*Fig. 2.22(e)*). The 3D meshes, like that shown in Fig. 2.18(a), were directly established from those 2D meshes by the present software DUCKPRE, and the cubic spline definition was used for the crack front.

Fig. 2.23 shows the SIF variations, obtained respectively by using the 1/4-point displacement method (*Fig. 2.23(a)*) and the *J*-integral method (*Fig. 2.23(b)*), along the crack front for all five different meshes. The 1/4-point displacement method converted the displacement value at the 1/4-point to the SIF through Eq. (2.22), where the $r_{(1/4)}$ was taken as the distance, $\overline{QA}$ (*see Fig. 2.22*), between the corner node and the 1/4-point as usual. The results in Fig. 2.23(a) show that the obtained SIFs are not identical along the crack front for these non-orthogonal meshes, and the difference increases with an increase of the degree of mesh non-orthogonality. But the results in Fig. 2.23(b) are quite different from those in Fig. 2.23(a), all SIF values along the crack front are nearly the same as Sneddon's analytical solution, no matter which mesh is referred to. These results demonstrate that the non-

orthogonal mesh abutting the crack front will bring a error when such a 1/4-point displacement method as described above is used to calculate the SIFs, but hardly affects the *J*-integral values even when the mesh is severely non-orthogonal.
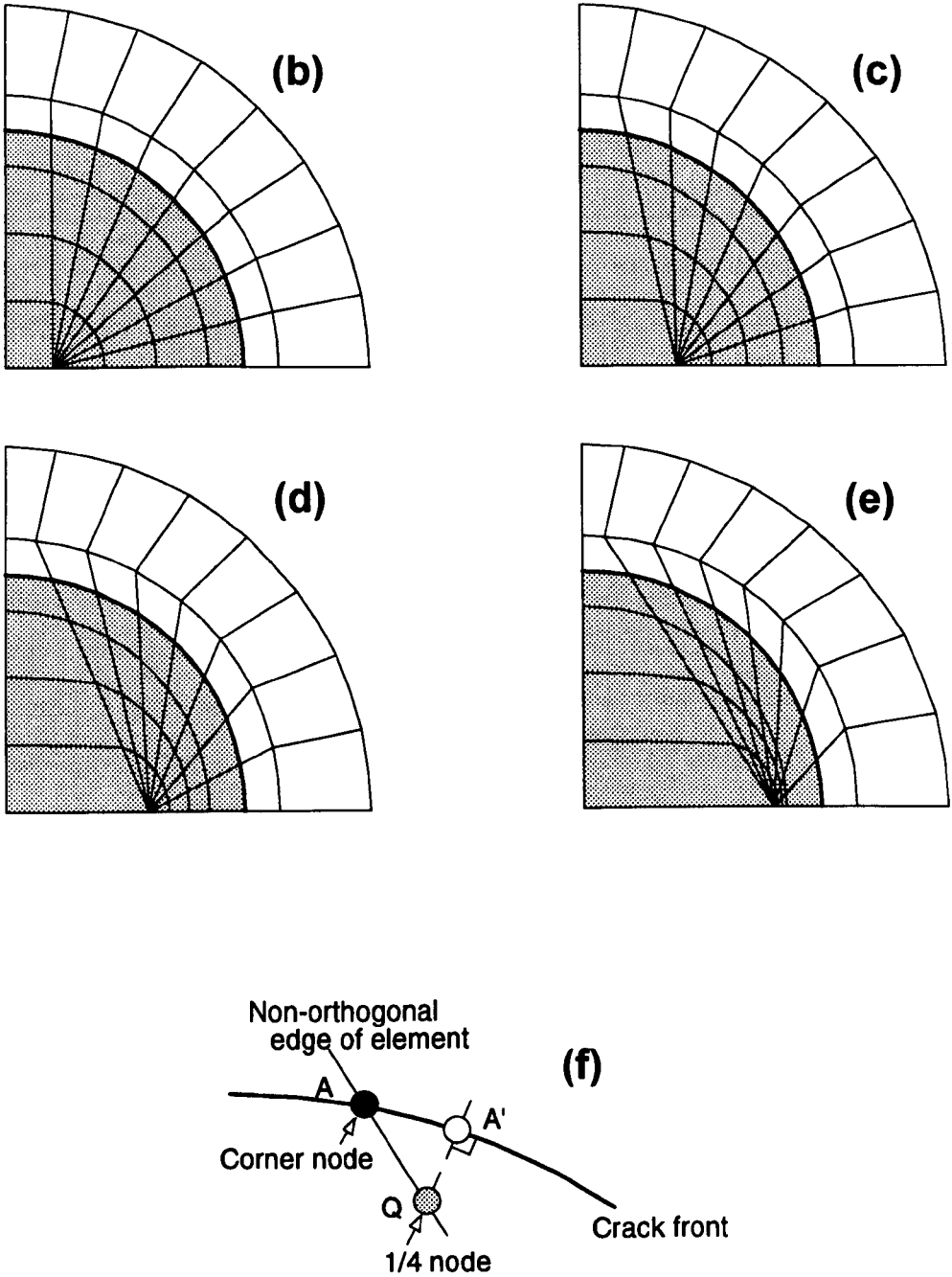
Figure 2.22   Different 2D crack plane meshes for an embedded defect with different degree of mesh orthogonality; (b-e) non-orthogonal mesh, (f) detail of non-orthogonal crack front mesh
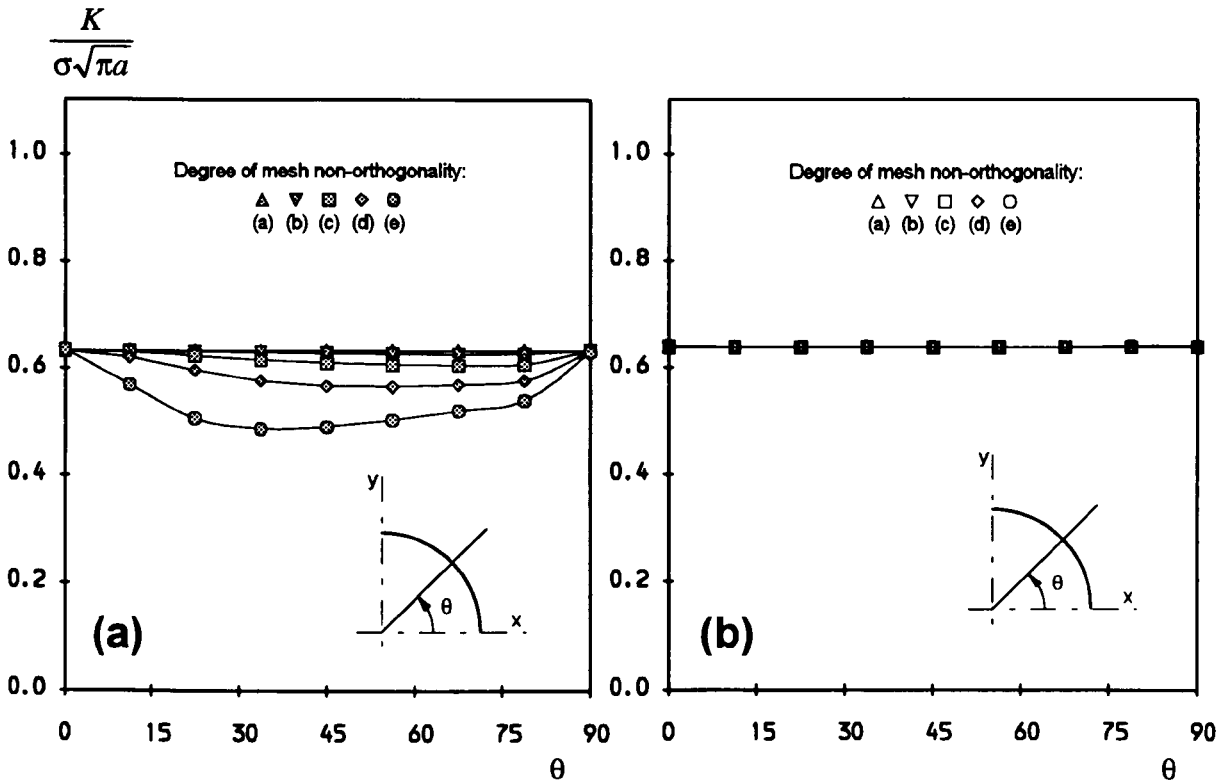
Figure 2.23   Study of effect of mesh non-orthogonality on stress intensity factor
estimates along an internal circular crack; (a) usual 1/4-point
displacement method, (b) J-integral method

Fig. 2.24 also shows the SIF variations obtained by using the displacement method that takes the distance between the 1/4-point and point A', $\overline{QA'}$ as the $r_{(1/4)}$ in Eq. (2.22), where the line $\overline{QA'}$ is normal to the circular crack front.   It actually means that the 1/4-point displacement within a non-orthogonal mesh is considered as the displacement behind the point A' instead of the point A, which is reasonable in theory.   As a result, the stress intensity factor at the point A' is calculated.   It can be seen in Fig. 2.24 that for all five different meshes the SIF distributions along the crack front become horizontal lines and very close to each other. Their average SIF values are also very close to Sneddon's exact solution.   Such results demonstrate that if the 1/4-point displacement is taken as that behind the point A' instead of the point A during the practical calculation of SIFs, the non-orthogonal mesh might still be able to achieve a good SIF estimate.   However, the non-orthogonal mesh should be avoided as possible since it may lead to an extra difficulty in finding the right position of the point A', which usually is not coincident with the corner node, A.

According to the above numerical analyses, it can be concluded that the non-orthogonal mesh abutting the crack front hardly affects the SIF results for the *J*-integral method, but does cause a large error for the usual 1/4-point displacement method. Such an error may be eliminated if the position at which the SIF is currently calculated is adjusted to its correct position as done above. It is also important to be aware that the fatigue crack growth increment at a certain point should still be calculated along the direction normal to the crack front when a non-orthogonal mesh is employed.
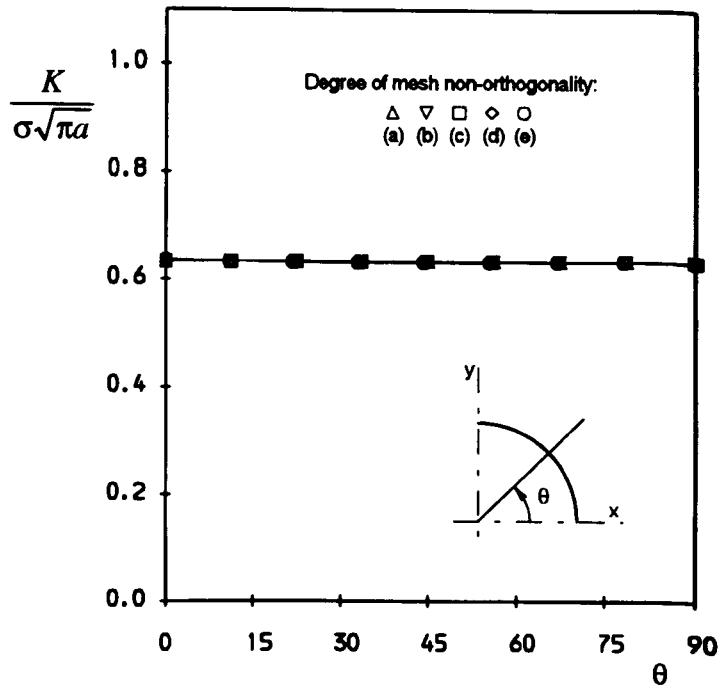
Figure 2.24 Effect of mesh non-orthogonality on stress intensity factor estimates for the 1/4-point displacement method that adjusts the calculated points

2.4.3 *J*-integral path independence

The *J*-integral is a path independent parameter for the elastic case, as mentioned above. This characteristic can usually be used to verify the calculation accuracy of a finite element analysis. The present numerical simulation technique has arranged for three "contours" (*or domains for the VCE method*) to be calculated. Each "contour" actually is a ring of elements surrounding the crack tip, as shown in Fig. 2.13. So, three *J*-integral values can be obtained from the three different "contours".

Generally, the agreement among the three *J*-integral values is excellent at each calculated crack-tip position. Table 2.1 shows the *J*-integral results, normalised by $\sigma^2 \pi a / E$, as functions of angular position, ϕ, along the crack front (*only these values at the corner nodes are given*) for the semi-elliptical surface crack in a plate under remote tension shown in Fig. 2.19. The crack front was approximated by the cubic spline, i.e. corresponding to Fig. 2.19(c). It can be

Table 2.1 *J*-integral path independence for the surface crack
(a/c = 0.6, a/t = 0.2) using the cubic spline approximation

Crack front location, $\phi°$ (see Fig. 2.21)	$J/(\sigma^2\pi a/E)$			Average value	Error (%)
	Contour I	II	III		
0.00	0.526	0.514	0.520	0.520	2.4
11.25	0.486	0.472	0.477	0.478	2.8
22.50	0.494	0.478	0.480	0.484	3.1
33.75	0.523	0.507	0.508	0.512	3.2
45.00	0.560	0.542	0.543	0.548	3.2
56.25	0.597	0.578	0.578	0.584	3.3
67.50	0.630	0.609	0.610	0.616	3.3
78.75	0.654	0.632	0.633	0.640	3.3
90.00	0.663	0.641	0.642	0.649	3.3

seen in Table 2.1 that the values provided by the three contours are very close at each crack-tip position, all relative errors, $(J_{max} - J_{min})/J_{max}$, being below 3.3%. This means that good path independence has been achieved. Similar path independence can also be seen for the embedded defect in Fig. 2.18, whose crack front is defined by the cubic spline method. It is particularly worth indicating that good *J*-integral path independence still exists even when these non-orthogonal meshes shown in Fig. 2.22 are used for the internal defect.

Nevertheless, the path independence might be lost as the crack approaches the free surface

Table 2.2 *J*-integral path independence for the surface crack
(a/c = 0.6, a/t = 0.2) using the polyline approximation

Crack front location, $\phi°$ (see Fig. 2.21)	$J/(\sigma^2\pi a/E)$			Average value	Error (%)
	Contour I	II	III		
0.00	0.444	0.558	0.846	0.616	47.5
11.25	0.373	0.376	0.421	0.390	11.2
22.50	0.390	0.373	0.377	0.380	4.3
33.75	0.433	0.412	0.410	0.418	5.2
45.00	0.481	0.459	0.456	0.465	4.6
56.25	0.526	0.502	0.500	0.509	4.9
67.50	0.546	0.541	0.541	0.549	4.1
78.75	0.594	0.574	0.585	0.584	1.4
90.00	0.616	0.630	0.707	0.651	12.8

that the crack front does not intersect orthogonally. A simple case is given in Table 2.2, in which the normalised J-integral results for the surface crack approximated by the polyline definition, i.e. corresponding to Fig. 2.19(c), are shown. It is clear in Fig. 2.19(c) that the intersecting angle between the free surface and the crack front is slightly less than 90°. It is the slightly non-orthogonal intersection that causes a great loss of path independence near the free surface. The maximum difference even reaches 47.5%, occurring at the free surface. The loss of path independence makes it very difficult to decide which J-integral value is reasonable for calculating the stress intensity factor. As mentioned previously, their average value is used in the present technique, but sometimes it seems to lead to a strangely higher SIF estimate. Hence, during the following modelling computations the 1/4-point displacement method is actually employed.

Up to now the present author has not found any publications reporting such a great and sensitive loss of J-integral path independence. In fact, a large J-integral error often appears near the free surface even though the cubic spline definition is used during the fatigue growth calculations. This is because the non-orthogonal intersection between the free surface and the crack front, as shown in Fig. 2.12(b), usually cannot be avoided during the fatigue crack growth. Clearly, the reason that the path independence is lost near the boundary should be the non-orthogonal intersection, which leads to a complex stress and strain state near the free surface and a loss of the $1/\sqrt{r}$ singularity adjacent to the crack tip. Further investigations on this matter will not be performed, and it is beyond the scope of the present thesis.

2.5 Accuracy and Efficiency of Simulation Technique

2.5.1 Accuracy

The accuracy of the present simulation technique depends not only on how accurate stress intensity factor estimates can be achieved by FE analyses, but also on how small crack growth increments can be chosen during the fatigue growth process. The former has been verified by

Smith and Cooper (1989), Chipalo (1990) and Gilchrist (1991) against many other numerical SIF solutions available. Nevertheless, due to the use of the polyline approximation to the crack front shape, their SIF estimates sometimes were not within a reasonable region of error with other existing solutions. As for the latter, the effect of the step-length of crack growth on crack shape changes and fatigue growth curves has not been referred to.

A SIF verification for an internal defect in an infinite solid has been made in this chapter comparing two different crack front definitions. The agreement, which is due to the improved crack front definition, with Sneddon's exact solution is encouraging. A wide range of SIF comparisons will appear in the future chapters in which the present numerical technique is applied to different practical cracked geometries. It will be seen that the stress intensity factor estimates obtained by the present author always agree quite well with other well-recognised solutions.

The investigation of the effect of different crack growth increments on crack shape developments and fatigue growth curves will also be carried out in some of the following chapters. It will be shown that it is possible to satisfy a required fatigue growth accuracy by selecting a sufficiently small maximum crack growth increment during the fatigue growth computations.

2.5.2 Efficiency

The efficiency is another important aspect for a successful simulation technique, and mainly related to the achieved ability to automatically follow the crack advance. The present technique can easily achieve fully automatic remeshing during the whole fatigue growth process, currently with the help of the commercial mesh generator FEMGV. This will be further demonstrated in each following chapter. Mostly, the step-by-step fatigue crack growth simulations performed in this thesis can be automatically and continuously completed from beginning to end. Compared with the original software which frequently requires manual operations as indicated previously, there is no doubt that the present numerical simulation technique has made significant progress.

2.6 Conclusions

A new significantly improved finite element technique which can automatically model a broad spectrum of defects of practical engineering significance has been established by the present author. The theoretical background related to the present technique has been given, covering the basic linear elastic fracture mechanics principles, the Paris fatigue crack growth law and its extension to planar crack problems, and the methods of evaluating stress intensity factors by the FE method. A description of the present software has also presented most of technical details, from which the potential versatility and adaptability of this technique can be impressed. Three important problems in numerical estimates of stress intensity factors by 3D finite element analyses, i.e. the SIFs sensitivity to crack front shape, the mesh orthogonality and the *J*-integral path independence, were investigated and clarified, which allows the errors during SIF calculations due to an inappropriate crack front definition or an non-orthogonal mesh to be avoided as much as possible, and more trust to be given to the use of the present simulation technique.

The SIF accuracy of the present technique has essentially been verified in this chapter to be quite good if the cubic spline curve introduced by the present author is used to define the crack front. This basically ensures the accuracy of the fatigue growth simulation. It will be seen in the following chapters that the present technique is able to reach an excellent theoretical accuracy for a variety of cracked structures. Similarly, the automatic ability of the present technique to follow the fatigue crack growth is also outstanding, which will be demonstrated in the following practical computations. It is concluded that the present FE simulation technique has progressed significantly in predicting numerically the fatigue growth of defects of practical engineering significance.

The major restriction of the present technique currently is that it can only simulate the fatigue growth of planar defects. For initially nonplanar defects or planar defects under mixed mode loads the present technique has not equipped the automatic 3D remeshing capabilities for them yet, since these defects would change their crack orientations during the crack growth, leading to a nonplanar crack growth. Moreover, the fatigue growth law currently contained in the present software is the linear Paris law, but other different laws such as described previously are readily incorporated.

2.7 References

ASTM E647-88 (1988) *Standard test method for measurements of fatigue crack growth rates.* <u>American society for testing and materials standards</u> Vol. **03.01**, 636-654.

Barsoum, R. S. (1976) *On the use of isoparametric finite elements in linear fracture mechanics.* **Int. J. num. Meth. Engng 10**, 25-37.

Bazant, Z. P. (1974) *Three-dimensional harmonic functions.* **Int. J. Engng Sci. 12**, 221-243.

Bazant, Z. P. and Estenssoro, L. F. (1979) **Int. J. Solids Struct. 15**, 405-426.

Benthem, J. P. (1977) *State of stress at the vertex of a quarter-infinite crack in a half space.* **Int. J. Solids Struct. 13**, 479-492.

Brown, M. W. (1988) *Aspects of fatigue crack growth.* **Proc. Instn Mech. Engrs 202**, (C1), 19-29.

Carpinteri, A. (1993) *Shape change of surface cracks in round bars under cyclic axial loading.* **Int. J. Fatigue 15**(1), 21-26.

Cooper, J. F. and Smith, R. A. (1987) *Significance of low-toughness zones in defect assessments.* <u>Final Report for the Defect Assessment in Offshore Structures</u> 1985-87 Programme, Marine Technology Directorate.

Chipalo, M. I. (1990) *Aspects of defect assessment in fatigue and fracture.* <u>PhD thesis</u>, Cambridge University.

deLorenzi, H. G. (1982) *On the energy release rate and the J-integral for 3-D crack configuration.* **Int. J. Fracture 19**, 183-193.

deLorenzi, H. G. (1985) *Energy release rate calculations by the finite element method.* **Engng Fract. Mech. 21**(1), 129-143.

Forman, R. G., Kearney, V. E. and Engle R. M. (1967) *Numerical analysis of crack propagation in cyclic-loaded structure.* Trans. ASME, Ser. D, **J. Basic Engng 89**, 459-464.

Gilchrist, M. D. (1991) *Crack shape development in plates and bonded joints.* <u>PhD thesis</u>, Sheffield University.

Griffith, A. A. (1921) *The phenomena of rupture and flow in solids.* **Phil. Trans. R. Soc. London A221**, 163-197.

Hartranft, R. J. and Sih, G. C. (1970) *An approximate three dimensional theory of plates with application to crack problem.* **Int. J. Engng Sci. 8**(8), 711-729.

Hellen, T. K. (1975) *On the method of virtual crack extension.* **Int. J. num. Meth. Engng 9**, 187-207.

Henshell, R. D. and Shaw, K. G. (1975) *Crack tip finite elements are unnecessary.* **Int. J. num. Meth. Engng 9**, 495-507.

Hoeppner, D. W. and Krupp, W. E. (1974) *Prediction of component life by application of fatigue crack growth knowledge.* **Engng Fract. Mech. 6**, 47-70.

Irwin, G. R. (1962) *Crack-extension force for part-through crack in a plate.* Trans. ASME, Ser. E, **J. Appl. Mech. 29**, 651-654.

Kassir, M. K. and Sih, G. C. (1966) *Three-dimensional stress distribution around an elliptical crack under arbitrary loadings.* Trans. ASME, Ser. E, **J. Appl. Mech. 33**, 601-611.

Kishimoto, K., Soboyejo, W. O., Smith, R. A. and Knott, J. F. (1989) A numerical investigation of the interaction and coalescence of two coplanar semi-elliptical fatigue cracks. **Int. J. Fatigue 11**(2), 91-96.

Lin, X. B. and Smith, R. A. (1994) *Numerical prediction of fatigue crack growth of a surface defect.* (submitted to **Fatigue Fract. Engng Mater. Struct.**).

Lin, X. B. and Smith, R. A. (1994) *A numerical simulation of fatigue growth of multiple surface initially semi-circular defects under tension.* **Int. J. Pres. Ves. Piping** (in press).

McEvily, A. J. (1977) *Current aspects of fatigue,* **Metals Science 11**(8), 274.

Murakami, Y. (Ed.) (1987) Stress intensity factors handbook. Vol.1-3, Pergamon Press.

Newman, J. C., Jr. and Raju, I. S. (1981) *An empirical stress intensity factor equation for the surface crack.* **Engng Fract. Mech. 15**, 185-192.

Nikishkov, G. P. and Atluri, S. N. (1987) *Calculation of fracture mechanics parameters for an arbitrary three-dimensional crack, by the 'equivalent domain integral' method.* **Int. J. num. Meth. Engng 24**, 1801-1821.

Parks, D. M. (1974) *A stiffness derivative finite element technique for determination of elastic crack tip stress intensity factors.* **Int. J. Fracture 10**, 487-502.

Paris, P. C. and Erdogan, F. (1963) *Critical analysis of crack propagation laws.* Trans. ASME, Ser. D, **J. Basic Engng 85**(4), 528-534

Pook, L. P. (1975) *Analysis and application of fatigue crack growth data.* **J. Strain Analysis** 10(4), 242-250.

Putra, I. S. and Schijve, J. (1992) *Crack opening stress measurements of surface cracks in 7075-T6 Aluminium alloy plate specimen through electron fractography.* **Fatigue Fract. Engng Mater. Struct.** 15, 323-338.

Raju, I. S. and Newman, J. C., Jr. (1977) *Three-dimensional finite-element analysis of finite-thickness fracture specimens.* NASA TN D-8414.

Raju, I. S. and Newman, J. C., Jr. (1979) *Stress intensity factors for a wide range of semi-elliptical surface cracks in finite thickness plates.* **Engng Fract. Mech.** 11(4), 817-829.

Remzi, E. M., Blackburn, W. S. and Hellen, T. K.(1990) *Automatic growth of planar cracks in three dimensional geometries.* Proceedings of 5th International Conference on Numerical Methods in Fracture Mechanics, Numerical Methods in Fracture Mechanics (Ed. A. R. Luxmoore and D. R. J. Owen), 1989, 129-140.

Rice, J. R. (1968) *A path independent integral and the approximate analysis of strain concentrations by notches and cracks.* Trans. ASME, Ser. E, **J. Appl. Mech.** 35, 379-386.

Rolfe, S. T. and Barsom, J. M. (1977) Fracture and Fatigue Control in Structures. Prentice Hall, New Jersey, USA.

Rooke, D. P. and Cartwright, D. J. (1976) Compendium of Stress Intensity Factors, Procurement Executive, Ministry of Defence, HMSO.

Sih, G. C. (1970) *Three dimensional stress state in a cracked plate.* **Int. J. Fracture** 7, 39-61.

Smith, F. W., Emery, A. F. and Kobayashi, A. S. (1967) *Stress intensity factors for cracks, Part I: Infinite solid.* Trans. ASME, Ser. E, **J. Appl. Mech.** 34, 946-952.

Smith, R. A. (1984) *Thirty years of fatigue crack growth - an historical review.* Proceedings of a Conference on Fatigue Crack Growth, Fatigue Crack Growth, 20 September, 1984, Cambridge, UK, 1-16.

Smith, R. A. and Cooper, J. F. (1989) *A finite element model for the shape development of irregular planar cracks.* **Int. J. Pres. Ves. Piping** 36(4), 315-326.

Soboyejo, W. O., Kishimoto, K., Smith, R. A. and Knott, J. F. (1989) *A study of the interaction and coalescence of two coplanar fatigue cracks in bending.* **Fatigue Engng Mater. Struct.** 12(3), 167-174.

Thompson, K. D. and Sheppard, S. D. (1992) *Stress intensity factors in shafts subjected to torsion and axial loading.* **Engng Fract. Mech.** 42(6), 1019-1034.

Walker, K. (1970) *The effect of stress ratio during crack propagation and fatigue for 2024T3 and 7075T6 aluminium.* ASTM STP 462, Effect of environment and complex loading history on fatigue life, 1-15

Westergaard, H. M. (1939) *Bearing pressures and cracks.* Trans. ASME, Ser. E, **J. Appl. Mech. 61**, A49-53.

Chapter 3

SHAPE DEVELOPMENT CHARACTERISTICS OF INITIALLY IRREGULAR EMBEDDED CRACKS UNDER TENSION

In this chapter the fatigue growth characteristics of several initially different shape embedded defects in an infinite solid under remote tension are investigated using the finite element numerical technique. It is predicted that these initially irregular defects always grow to a circle (*iso-K configuration*) and subsequently maintain such a circular profile. The accuracy of this numerical technique is examined by comparing with either analytical or numerical results available, particularly with the exact prediction for an initially penny-shaped defect. The comparisons show that quite good calculation accuracy can be achieved by the technique. The numerical modelling is also extended to two more practical internal cracks under Mode I fatigue loading. The method of dealing with practical small irregular defects is also proposed.

3.1 Introduction

The Embedded crack problem is of practical importance as internal defects are often introduced during material and structure manufacturing. Subjected to cyclic loads, these internal defects may propagate to their critical sizes at which failure occurs, or to becoming surface cracks if free boundaries have been reached before the failure comes.

Many attempts have been made to estimate the stress intensity factor around the front of various embedded defects of either regular or irregular shape, in infinite or semi-infinite solids, in finite thickness plates, or within some practical components. Sneddon (1946) obtained an exact SIF solution for a penny-shaped embedded defect in an infinite solid under remote tension, and, sixteen years later, Irwin (1962) published his exact SIF equation for an elliptical crack in an infinite body in tension. The SIF for an rectangular defect embedded in an infinite solid, a semi-infinite solid and a finite thickness plate subjected to tension has been studied by Isida *et al.* (1991), using the body force method (Nisitani and Murakami, 1974; Isida *et al.*, 1983). Shah and Kobayashi (1973) and Isida and Noguchi (1984) obtained, respectively, the SIF for an elliptical crack adjacent to the free surface of a semi-infinite solid, and recently Chen *et al.* (1991) reported their SIF solution for an elliptical crack in a shaft under tension and bending, which is also fitted from the results obtained by the body force method. In addition to these SIF solutions relevant to the present study, there are many other SIF results published for different embedded crack geometries subjected to different loads. It is beyond the scope of this chapter to review these results.

However, the number of publications associated with the fatigue growth of internal cracks has been fewer than that for the SIF study in both numerical calculations and experiments. One of the earlier efforts was by Lotsberg and Bergan (1979) who used the energy release rate calculated by the FE method to model the shape development of an embedded fatigue crack. The formulation used by Lotsberg and Bergan assumed that the crack front geometry always was defined by three elliptical half axes, thus, it simply only required the calculation of the crack extension along the direction of the three elliptical axes. Chipalo (1990), using the original FE technique developed by Smith and Cooper (1989), also investigated numerically the fatigue growth behaviour of a particular embedded elliptical crack near a free surface under remote tension. The experimental examination of fatigue growth of internal cracks under controlled conditions has been also rare, due to the difficulty in introducing expected

cracks to specimens or practical structures. However, several experimental observations were still reported, for instance, the fatigue shape development starting from embedded welding flaws (Iida and Fujii, 1973) and internal inclusions (Forsyth, 1983; Wang, 1993). These results showed that the initially irregular internal flaws and inclusions became more smooth during the fatigue growth process, and the free surface had an effect on the crack shape change, especially when the fatigue crack approached it closely.

The objective of this chapter is to investigate the fatigue growth characteristics of various embedded cracks by using the FE simulation technique described in Chapter 2. Firstly, an initially penny-shaped embedded defect in an infinite solid subjected to remote tension cyclic load is to be numerically studied, and the results are mainly compared with the analytical solutions derived from Sneddon's exact SIF equation for the penny-shaped crack. The focus is on discussing the computational accuracy of the present numerical technique. Secondly, several initially irregular internal cracks in infinite solids under tension are examined, in order to reveal their fatigue growth behaviours, such as crack shape changes, iso-*K* (*a term introduced by Smith and Cooper (1989)*) crack profile studies, SIF comparisons with existing solutions and crack growth curve predictions. Thirdly, the fatigue growth of two more practical embedded defects, one in a round bar and the other within an internally pressurised cylinder, is numerically modelled and compared with an experimental observation. Finally, a method of dealing with small internal defects under tension fatigue is also proposed.

3.2 Crack Geometry and Computational Details

An internal planar crack in an infinite solid subjected to a remote uniform load perpendicular to the plane of the crack is shown in Fig. 3.1. The modelled four different initially irregular cracks are, respectively, circular, elliptical, square and key-hole shaped, as shown in Fig. 3.1. In the analysis, the infinite body was approximated by taking very large edge lengths *(H = L = W = 400mm, the unit of the length is mm if it is absent in the following figures)* of the cube relative to the defect size. Only one eighth of the volume was considered because of the symmetry.
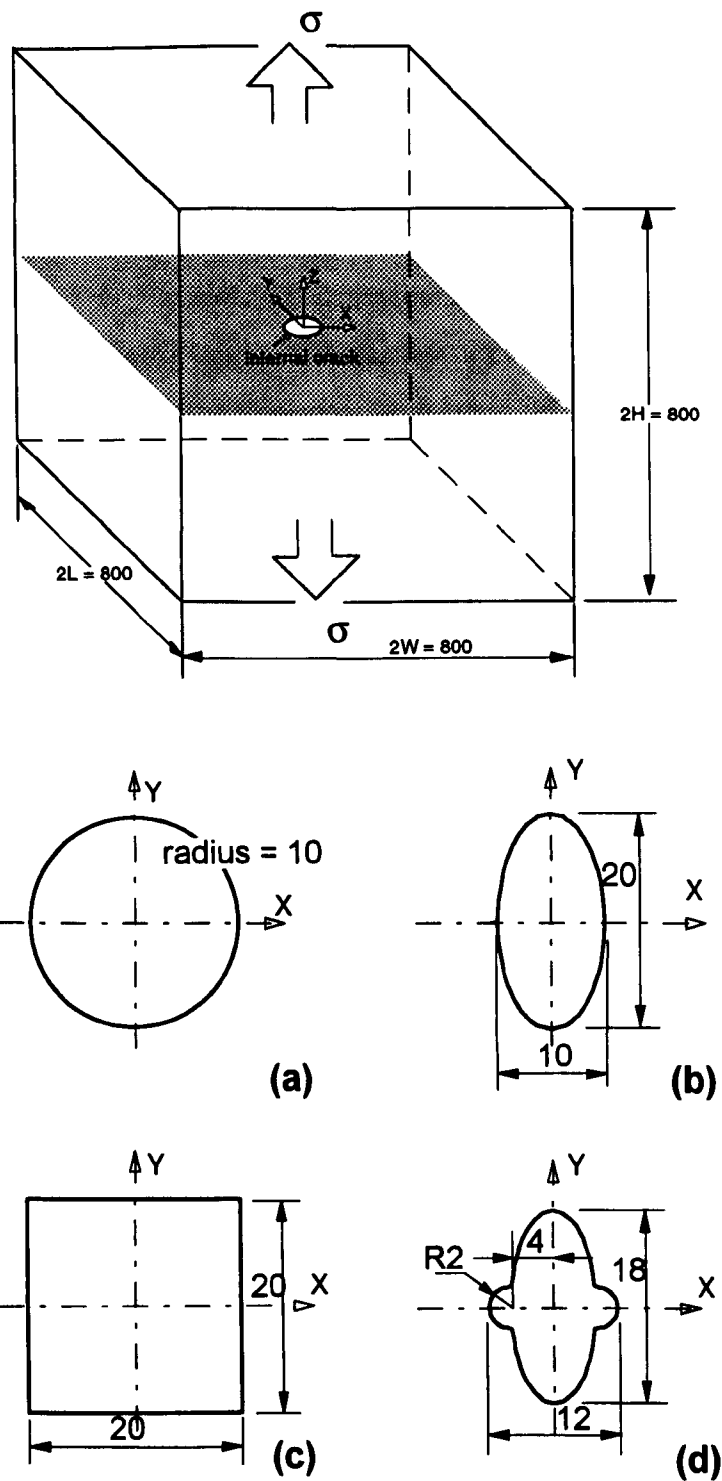
Figure. 3.1 Four different cracks embedded in infinite solids under remote tension; (a) circular, (b) elliptical, (c) square, (d) key-hole shaped
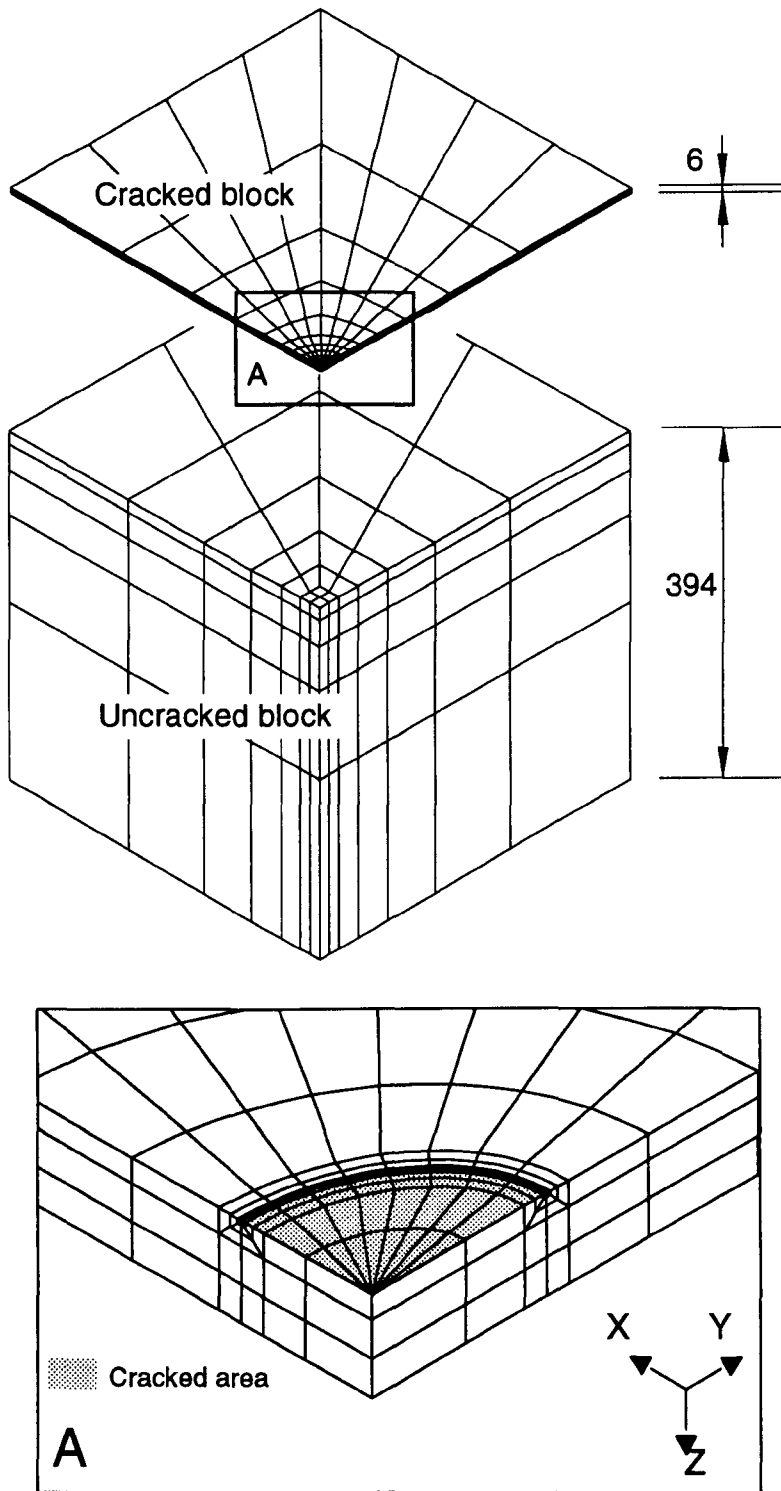
Figure 3.2   A typical two-block finite element model for
an embedded crack in an infinite solid

Mesh

Geometry
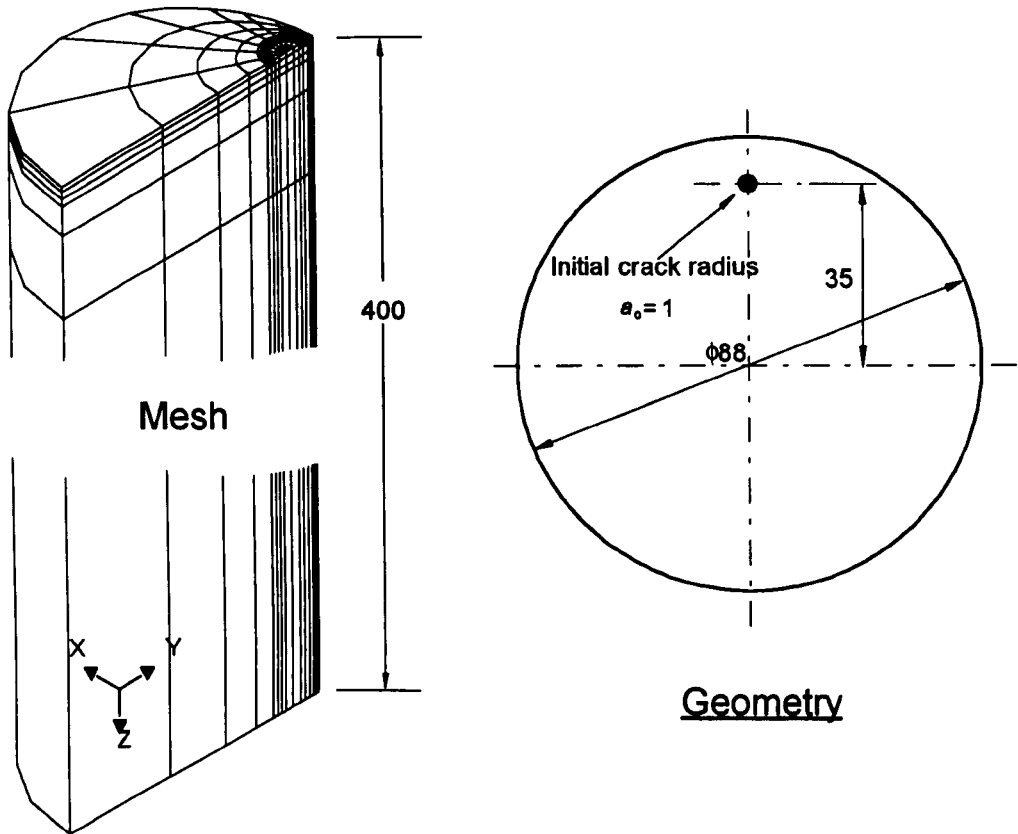
Initial crack radius
$a_0 = 1$

400

35

$\phi88$

Figure 3.3   Geometry and mesh of an internal crack situated
in a round bar under tension

The two-block FE model, as mentioned in Chapter 2, was used in the practical calculation, except the model for the key-hole shaped crack that possessed only one block in which the mesh was completely compatible. Fig. 3.2 shows a typical two-block mesh, within which the contact plane between the cracked and uncracked blocks was 6mm away from the crack plane, which will be demonstrated to be able to obtain a good calculation accuracy. For the initially circular, elliptical and square cracks, the crack front was defined by a cubic spline curve that was through seventeen nodes (*nine corner nodes and eight midside nodes*), while for the initially key-hole shaped crack through twenty-one nodes (*eleven corner nodes and ten midside nodes*). Around the crack front, three rings comprising four elements for each (*see Fig. 2.13(b)*) were arranged. The number of degrees of freedom ranged from 6807 to 8874 for these two-block models, whilst it was 18141 for one-block models, much more than the former due to the increased number of nodes along the crack front. Automatic remeshing of the two- or one-block FE models and then applying the loading and displacement constraints to the meshes were carried out by both the DUCKPRE and DUCKPOST software, so that the crack advance can be automatically followed.
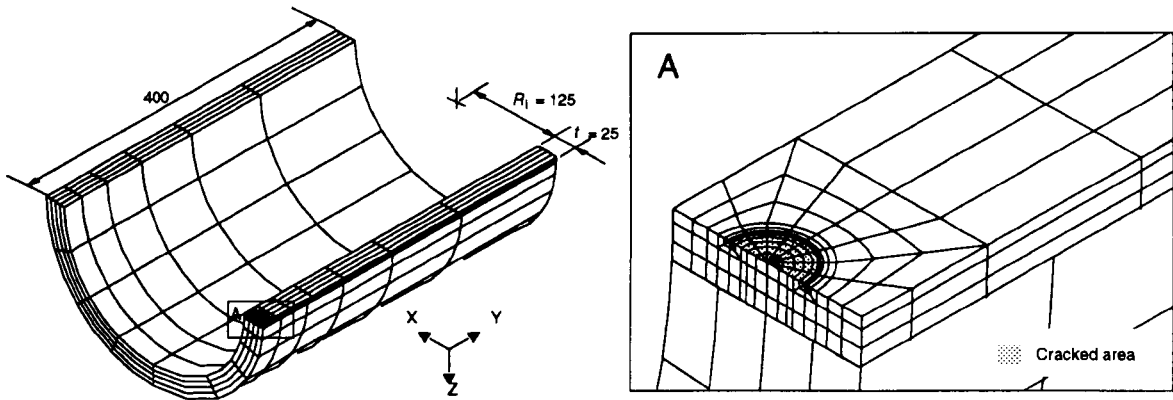
Figure 3.4   Mesh of an internally pressurised cylinder
with a circular embedded crack

In addition to the above four different embedded cracks, two more practical crack configurations, an internal circular crack situated in a round bar subjected to tension, as shown in Fig. 3.3, and an circular internal defect within an internally pressurised cylinder, as shown in Fig. 3.4, were also modelled. Due to the symmetry, a quarter of the geometry was only analysed for both. As shown in Fig. 3.3 and Fig. 3.4, the one-block FE model was used for the bar, and the two-block model for the cylinder, the contact plane was also 6mm far from the crack plane. Similarly, the cubic spline definition of crack front was employed, and there were seventeen nodes through the front of both cracks. The automatic computation procedure of following the crack growth was also achieved by the present software for these two defects.

During the simulation of fatigue crack growth, the material Poisson's ratio v was assumed to be 0.3, the coefficient C and the exponent n of the Paris law Eq. (2.8) were, respectively, 1.83×10^{-13} and 3, where the units of the SIF range and crack size are MPa$\sqrt{\text{mm}}$ and mm. The SIF was calculated by the 1/4-point displacement method with plane strain conditions assumed if not particularly indicated. The maximum crack growth increment, Δa_{max}, along the crack front was limited to a reasonable small value, 0.2mm for the initially circular, elliptical and rectangular cracks in infinite solids and the crack in the cylinder, while 0.25mm for the initially key-hole shaped crack and the defect in the bar. The Δa_{max} value was usually maintained during the whole crack growth process. In the following calculations, the constant amplitude stress range, $\Delta \sigma = 1$ MPa ($\sigma_{max} = 1$ and $\sigma_{min} = 0$) was taken.

3.3 Fatigue Growth Prediction of Circular Defect and Its Accuracy Verification

Sneddon (1946), using the stress function method, obtained an exact stress intensity factor analytical solution for an embedded penny-shaped crack in an infinite solid subjected to remote uniform tension, which can be expressed as follows:

$$K = 2\sigma\sqrt{a/\pi} \qquad (3.1)$$

where σ (MPa) is the tensile load normal to the crack plane, and a (mm) is the radius of the crack. Obviously, along the whole crack front, SIF values are identical, which permits the fatigue crack problem to be treated as a one-dimensional problem.

The fatigue crack growth for such an embedded circular defect can be theoretically predicted by substituting Eq. (3.1) to the Paris fatigue crack growth law Eq. (2.8),

$$da/dN = C \cdot \left(2\sigma\sqrt{a/\pi}\right)^n \qquad (3.2)$$

where N is the number of fatigue loading cycles and the range of SIF has been assumed to be K (i.e. $K_{max} = K$ and $K_{min} = 0$). Integrating Eq. (3.2), the following analytical fatigue growth curve, the relationship between the crack size, a, and the fatigue cycle, N, can be derived,

$$a = a_o\left(1 + \frac{(1-n/2)C\left(2\sigma/\sqrt{\pi}\right)^n}{a_o^{(1-n/2)}}(N-N_o)\right)^{1/(1-n/2)} \qquad n \neq 2 \qquad (3.3)$$

$$a = a_o \exp\left(C\left(2\sigma/\sqrt{\pi}\right)^n(N-N_o)\right) \qquad n = 2 \qquad (3.4)$$

When $n = 3$ and $C = 1.83\times10^{-13}$, Eq. (3.3) becomes :

$$a = a_o\left(1 - 7.32\times10^{-13}\left(\sigma/\sqrt{\pi}\right)^3\sqrt{a_o}(N-N_o)\right)^{-2} \qquad n = 3 \qquad (3.5)$$

where a_o (mm) is the initial radius of the circular defect and N_o is the initial number of fatigue cycles, usually taken as zero. It is obvious that the crack is always a circle during the fatigue propagation.

The Euler numerical integration method, which has been described in Chapter 2, can also be used to solve Eq. (3.2). The Euler iterative expression for an embedded circular crack can be obtained by substituting Eq. (3.2) into Eq. (2.14). Taking the same values of n and C as used above leads to:

$$N_{m+1} = N_m + \frac{1.83 \times 10^{-13} \Delta a}{\left(2\sigma\sqrt{a_m/\pi}\right)^3} \qquad (m = 0,1,...) \qquad (3.6)$$

where, as indicated in Chapter 2, Δa is the specified crack advance increment during the step-by-step calculation and has a major effect on the accuracy of the Euler method.

The fatigue growth of an embedded circular crack, whose initial crack radius is 10mm, as shown in Fig. 3.1, under tension has been modelled in this chapter by the FE simulation technique. Fig. 3.5 exhibits the fatigue shape development of the circular crack predicted by the present technique. Obviously, the circular profile, as expected, is always maintained during the fatigue growth process (*the degree of its deviation from a circle will be discussed later*).
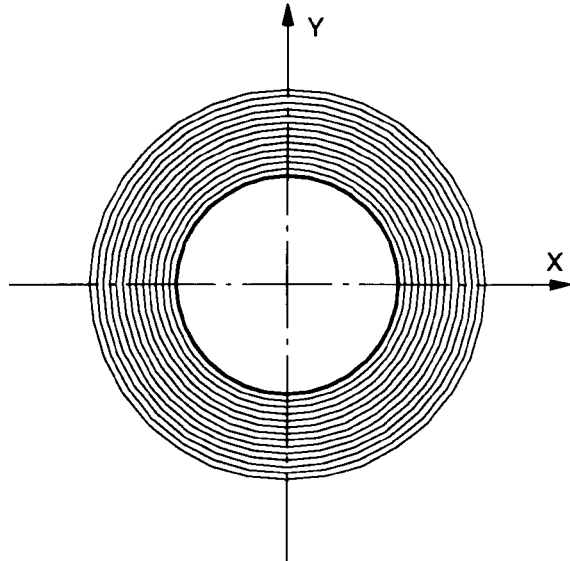
Figure 3.5   Shape development of an initially penny-shaped defect in an infinite solid under tension

Fig. 3.6 shows the SIF variations along the front of several crack profiles grown from the initially penny-shaped crack. The notations appearing in Fig. 3.6 are: a_o — initial crack radius (10mm); a_0 — current crack length along $\theta = 0°$ axis; a_{90} — current crack length along $\theta = 90°$ axis; and $\bar{a}$ — current average crack radius. The crack size for these profiles along which the SIF variation was plotted is also included in the table in Fig. 3.6. It can be seen that the normalised SIF

$$\frac{K}{\sigma\sqrt{\pi\bar{a}}}$$

Sneddon's (1946) exact solution: 0.6366

Symbol	Crack size		
	$\dfrac{a_0}{a_o}$	$\dfrac{a_{90}}{a_o}$	$\dfrac{\bar{a}}{a_o}$
—⊖—	1.000	1.000	1.000
—△—	1.179	1.176	1.178
—▽—	1.377	1.371	1.376
—⊟—	1.577	1.569	1.574
—◇—	1.775	1.764	1.772

θ
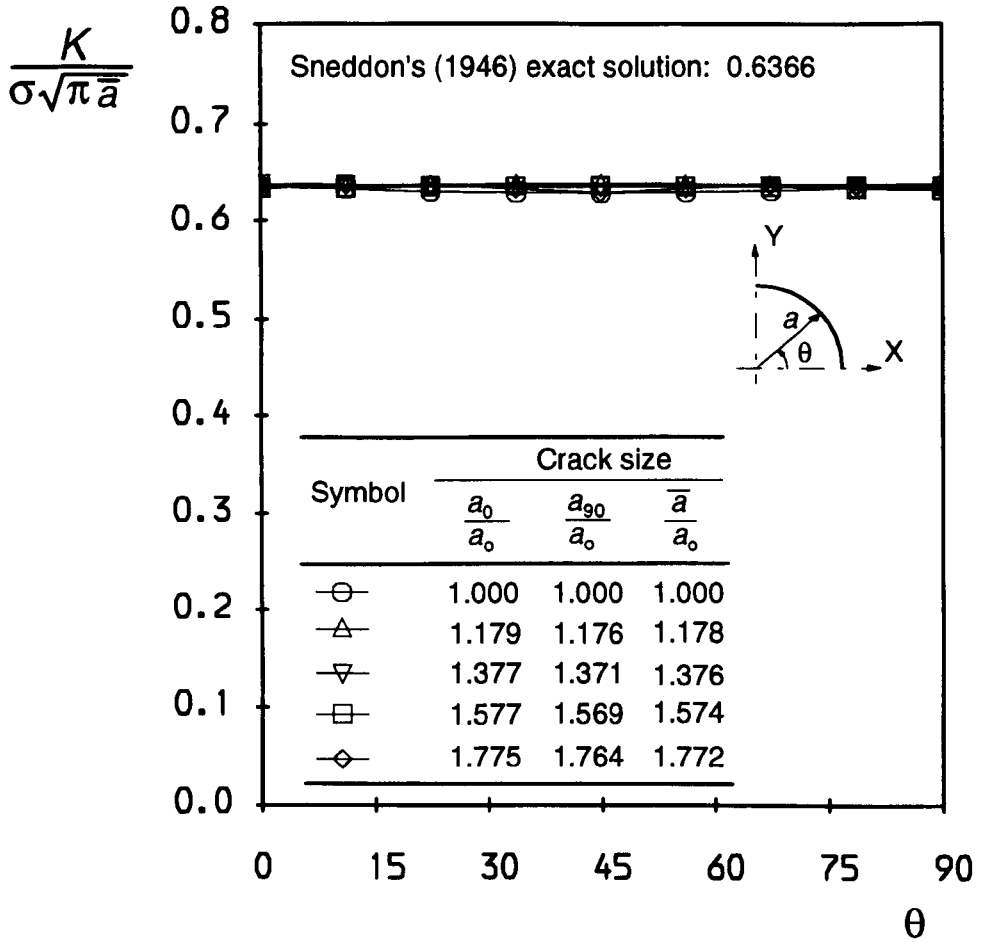
Figure 3.6   Variation of stress intensity factors along crack front
for initially circular crack.

Exact solution

0.2

0.8

$\Delta a_{max} = 1.6$

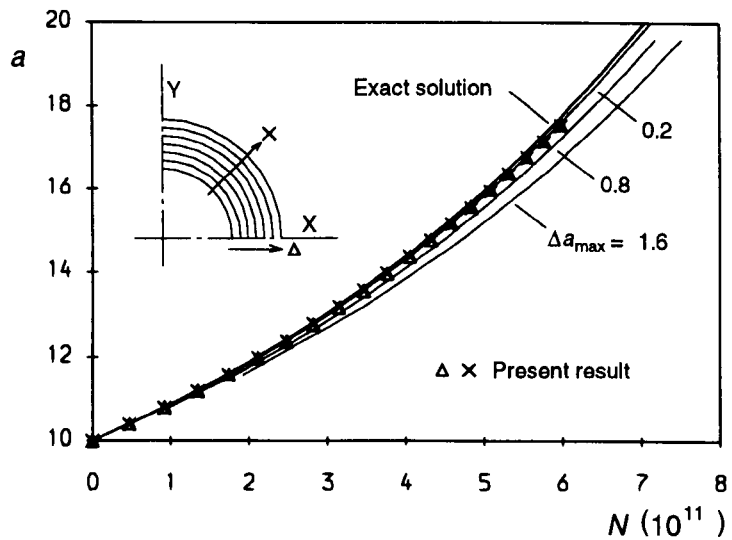△ X Present result

$N\ (10^{11})$

Figure 3.7   Fatigue growth predictions for the initially
circular defect made by different methods

distributions along the crack front are always approximately equal during the fatigue process and in quite good agreement (*error being below 2%*) with Sneddon's (1946) exact solution.

The present fatigue growth predictions are displayed in Fig. 3.7 together with those by the Euler numerical integration (3.6), which employed several different crack increments, Δa = 0.2, 0.8 and 1.6mm, and that by Sneddon's exact relation (3.5). For all these calculations, the constant amplitude stress range, $\Delta \sigma$ = 1 MPa was taken, as indicated previously. It can be seen that the curve obtained by the Euler method varies with the crack increment used, the smaller the value is, the larger the crack size for the same number of fatigue cycles. Generally, when the crack increment approaches zero, the predicted curve converges. This can be easily found in Fig. 3.7, where the curves by the Euler method converge to the exact solution based on the Sneddon's SIF equation, as the crack increment is gradually reduced. The predictions by the FE simulation technique are in excellent agreement with the exact and the Euler Δa = 0.2mm solutions in either $\theta = 0°$ or $\theta = 45°$ direction, and appear to be slightly closer to the Euler Δa = 0.2mm solution than to the exact one. This even demonstrates that the present FE technique can really obtain a quite good accuracy since the present calculation used the same crack growth increment, Δa_{max} = 0.2mm, and also can achieve a quite good convergence, as indicated in Chapter 2.

3.4 Fatigue Growth Characteristics of Initially Irregular Defects

The fatigue shape development of several embedded cracks of initially non-circular shape in infinite solids under tension is displayed in Fig. 3.8. It is seen that no matter what initial profile the crack is, elliptical, square or more irregular key-hole shaped crack, it grows in such a manner that a circle is always approached and subsequently maintained. The more irregular the current crack front is, the greater the shape change that occurs. Such a trend of crack shape change is what can be anticipated in theory, since the circle is an equilibrium profile around which the crack driving force is equalised for the crack in an infinite solid subjected to remote tension.

In order to examine the degree of crack shape approaching to a circle, the relative residual, E_i, and the relative standard deviation, S_r, are introduced in this thesis. The relative residual defined by

$$E_i = \frac{\overline{OP} - \overline{OP'}}{\overline{OP'}} = \frac{\sqrt{x_i^2 + y_i^2} - a}{a} \tag{3.7}$$

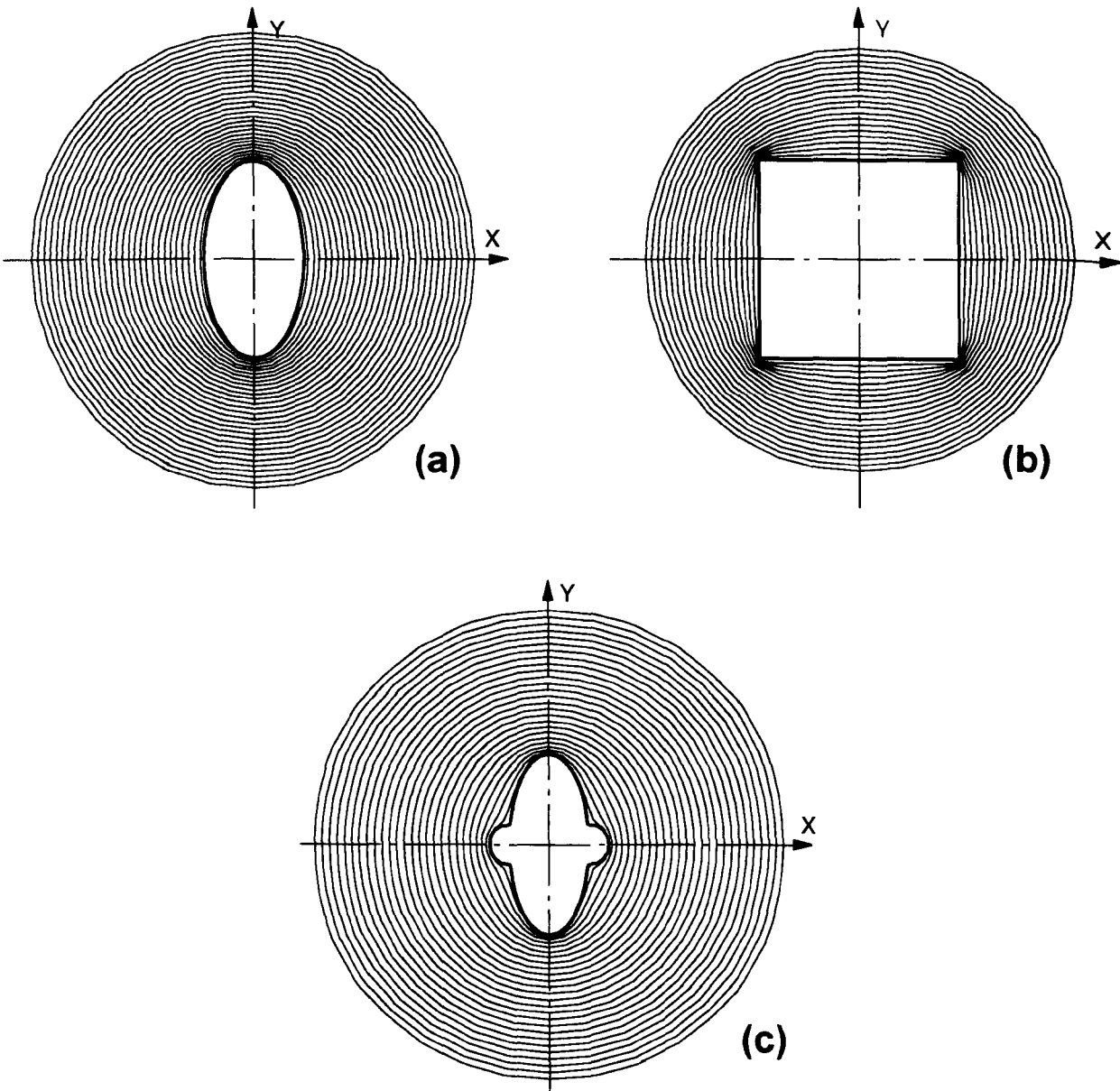represents the relative degree of deviation of the point P from the circle, as shown in Fig. 3.9,

Figure 3.8   Shape development of initially different shape embedded cracks within infinite solids under tension; (a) Elliptical; (b) Square (c) Key-hole shaped

where the $\overline{OA}$ is taken to be the radius of the circle, a, which means that the predicted crack front is compared with a particular circle (*actually, the size of the compared circle is not important for the shape deviation study*). The total relative standard deviation is defined as follows:

$$S_r = \sqrt{\frac{1}{n}\sum_{i=1}^{n}(E_i)^2} \qquad (3.8)$$

Figure 3.9   Comparison of a numerically predicted crack shape with a circle

where n is the number of the corner nodes (*solid points in Fig. 3.9*) along the crack front in FE models. Obviously, the smaller S_r value means that the crack is closer to the particular circle. The above two definitions, to some extent, can quantitatively describe the degree of shape deviation of an arbitrary profile from a circular despite not being perfect.

Fig. 3.10 shows the distribution of the relative residual, E_i, along the front of several cracks from the initially square (a) and key-hole shaped (b) profiles. The corresponding crack shape and size as well as the number of elapsed fatigue cycles are also displayed in Fig. 3.10. It can be found that as the crack advances the E_i distribution tends toward an equal distribution, i.e. $E_i = 0$, as marked by the arrow. The maximum E_i value for the largest crack in Fig. 3.10(a) beginning from the initially square crack is less than 1%, and that for the largest crack in Fig. 3.10(b) from the initially key-hole shaped crack is below 2%. This actually means that the crack profile has become a very approximate circle if $E_i = 0$. The same trend would be seen if the distributions of the relative residual for the initially circular and elliptical defects were drawn. Fig. 3.11, showing the variation tendency of the total relative standard residual with the crack growth for the above four initial defects, provides a further clear illustration, i.e. the initially circular crack propagates with its original shape maintained during the fatigue growth (*always $S_r \approx 0$*), and other three originally non-circular defects grow towards a circle ($S_r \to 0$). Therefore, the numerical results in Fig. 3.10 and Fig. 3.11 further numerically verified that any initially irregular embedded planar cracks in an infinite solid
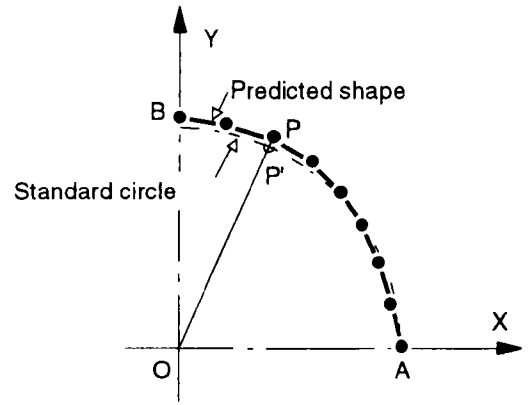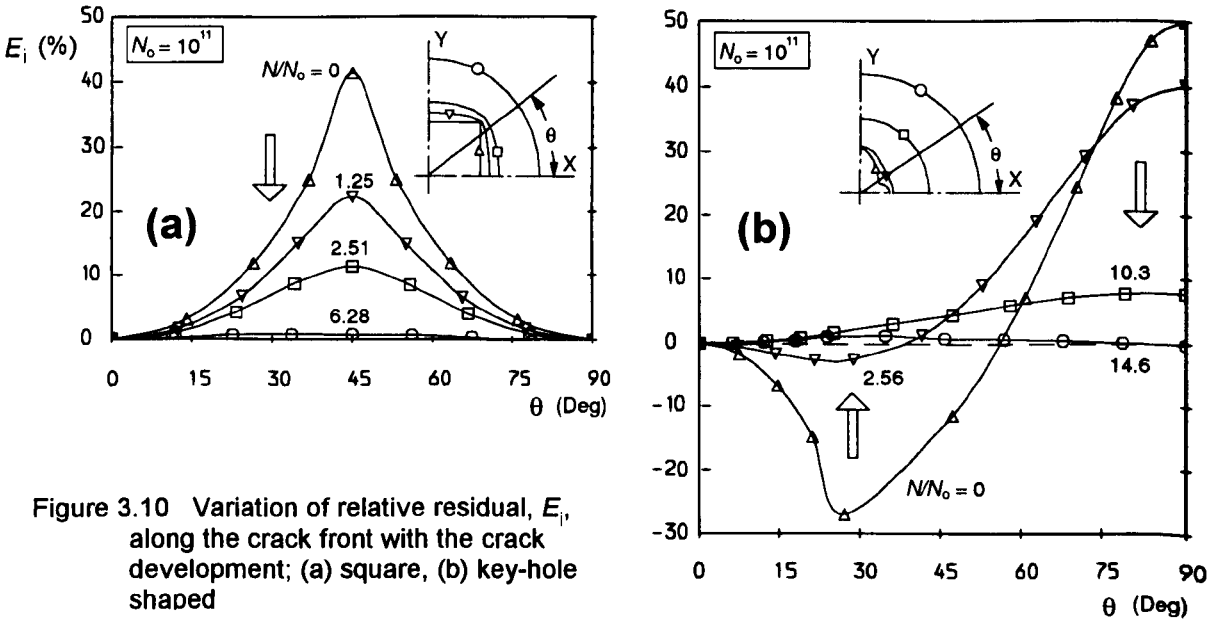
71

Figure 3.10   Variation of relative residual, E_i, along the crack front with the crack development; (a) square, (b) key-hole shaped

subjected to remote tension fatigue will evolve into a circular crack and subsequently the circular shape will be retained.

The calculation accuracy of stress intensity factor has a strong influence on the prediction of fatigue crack shape changes, and further of crack growth curves, as mentioned in Chapter 2. Fig. 3.6 has shown that an excellent agreement between the FE result and Sneddon's exact solution has been achieved, despite using the two-block FE model in the present computations. The SIF variations along the crack front for the three initial cracks, i.e. the elliptical, rectangular and key-hole shaped cracks, are exhibited in Fig. 3.12. It can be seen that the more intensely non-uniform SIF variations occur, particularly for the more irregular initial crack configurations, the square (b) and the key-hole crack (c), the former has a sharp drop at its protruding point, whilst the latter shows a sudden rise at the concave position. Such SIF variations make cracks propagate towards a more and more smooth shape and finally reach a circular profile around which the SIF values are
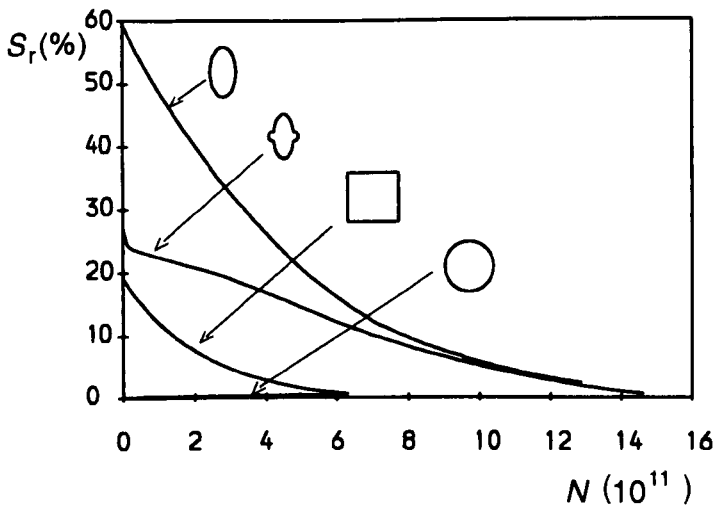

Figure 3.11   Variation trend of the total relative residual, S_r, with crack growth for different initial defects

72
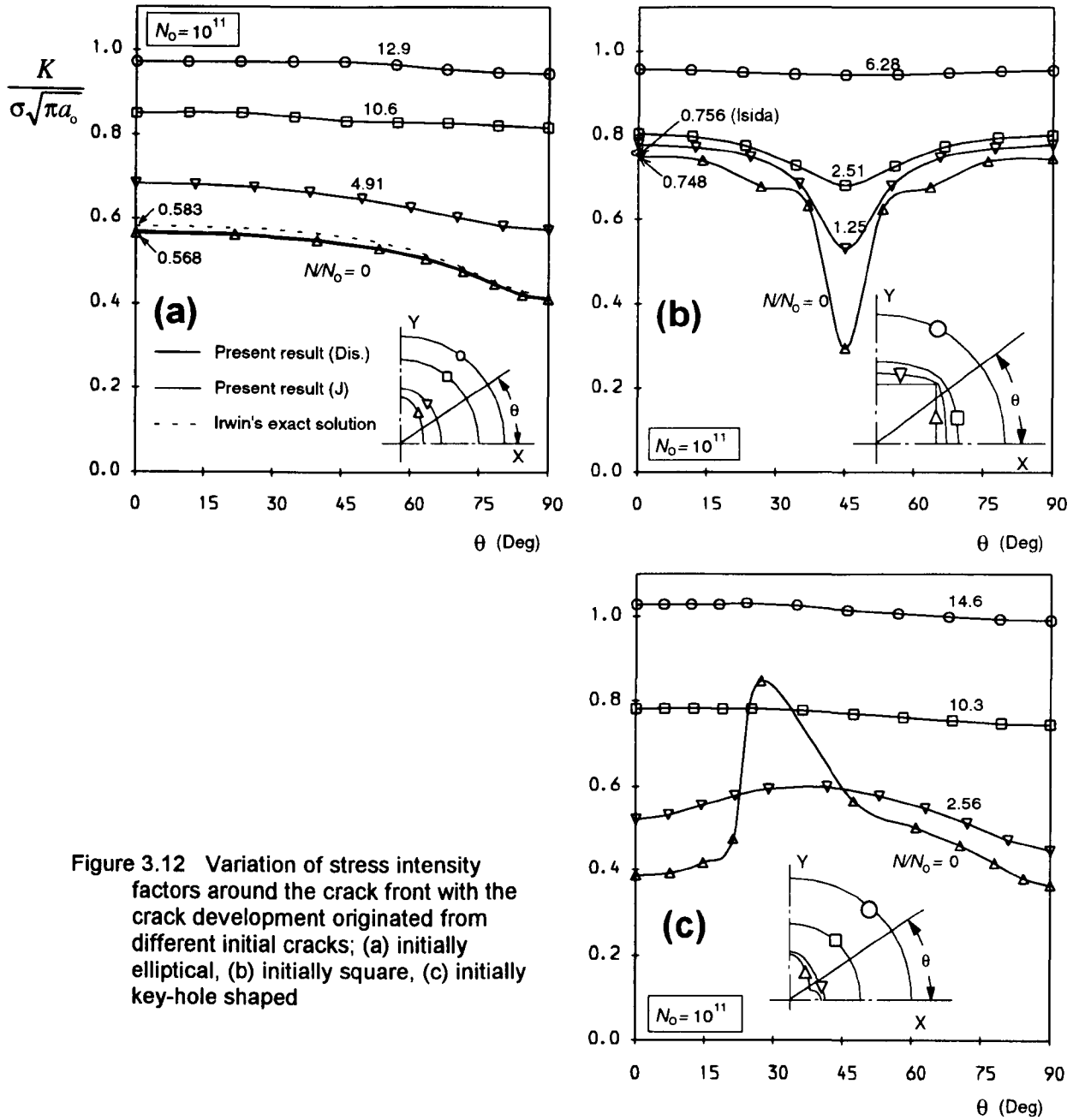
Figure 3.12 Variation of stress intensity factors around the crack front with the crack development originated from different initial cracks; (a) initially elliptical, (b) initially square, (c) initially key-hole shaped

identical. It is apparent in Fig. 3.12(a, b and c) that the SIF variation along the front of each ending crack front finally almost reaches a constant. Fig. 3.12(a) includes Irwin's (1962) exact solution (*dashed line*) for the initial ellipse, which agrees very well with the present result, the maximum error being below 2%. The SIF result calculated by the *J*-integral using the plane strain assumption is also compared in Fig. 3.12(a) with that by the 1/4-point displacement method. Their discrepancy is extremely small and basically always so during the crack growth process. In Fig. 3.12(b) the maximum SIF value for the initially square crack occurs at the

73

mid-edge of the square. Isida *et al.*'s (1991) result from the body force method is also indicated in the figure, whose error relative to the present result, is 1.07%. The minimum SIF occurring at the protruding point, i.e. at $\theta = 45°$, is much less than the maximum for the initial square, but as the crack grows the SIF along $\theta = 45°$ increases more rapidly than along the mid-edge direction, leading to the disappearance of the protruding point and also an equal SIF distribution along the crack front. Fig. 3.12(c) shows that the maximum SIF occurs at the concave position of the initially key-hole shaped crack, and tends to be close to the SIFs elsewhere as the crack propagates. All the above SIF comparisons with the analytical or numerical results available in the literature demonstrate that the 3D finite element analyses can achieve a quite good accuracy for the SIF computation, which can further ensure the fatigue crack growth prediction.

Fig. 3.13 shows the ratio of the minimum to the maximum stress intensity factor (K_{min}/K_{max}) along each crack profile. The ratio characterises the variation of the degree of the SIF non-uniformity along a crack front with crack development. It can be seen that for the initially circular crack the ratio has been maintained close to unity, and for the other three initial cracks the ratio gradually increases from the lowest point towards one, i.e. the crack tends towards an iso-K configuration, which also means that the crack tends to grow to a circular profile, as indicated above.

Figure 3.13   Change of K_{min}/K_{max} along the crack front during crack development for different initial crack configurations

Fig. 3.14 shows the relations of the crack length along either the minor or major axe of the initially elliptical defect with the number of fatigue cycles predicted by the present technique. Also shown in Fig. 3.14 is the prediction based on Irwin's (1962) exact SIF equation, by assuming that the elliptical shape is maintained during the fatigue propagation and just calculating the crack size change along both minor and major axes. The Euler numerical calculation similar to that for the initially circular crack was also used, and the maximum crack increment was taken as 0.2mm, the same value as employed in the FE modelling computation

Figure 3.14 Comparison of crack growth curves for the initially elliptical crack, predicted by the present simulating technique with those from Irwin's SIF exact solution
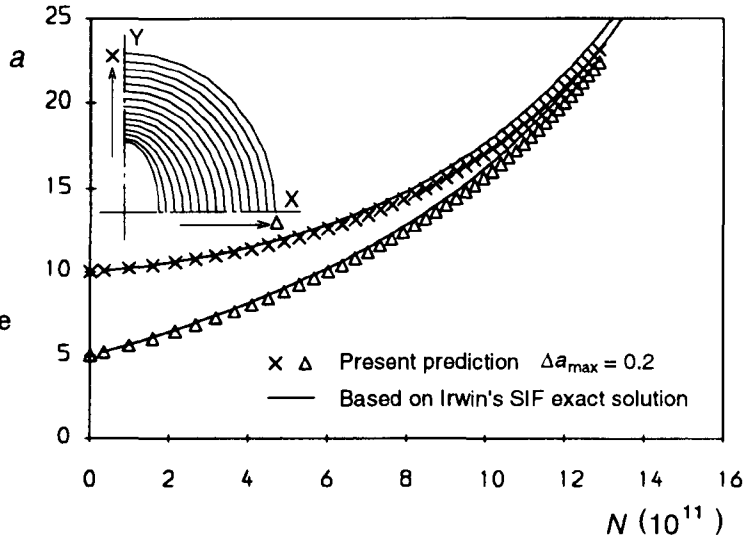
Figure 3.15 Crack growth curves for the initially square crack, predicted by the present simulation technique
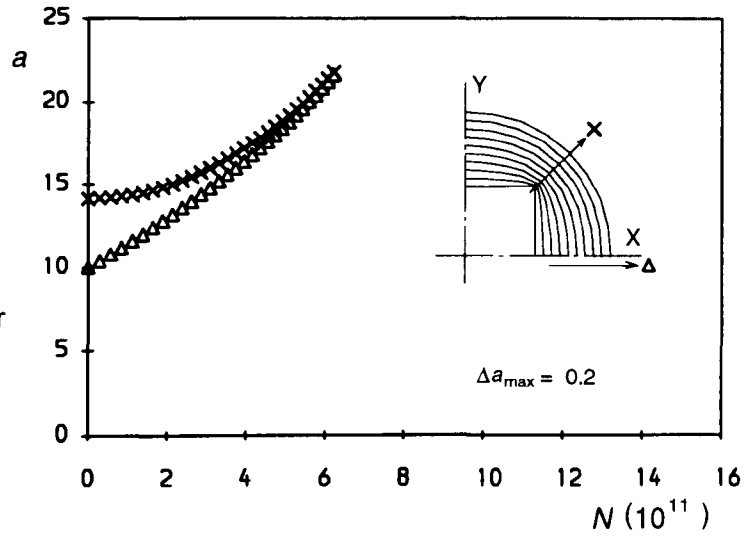
Figure 3.16 Crack growth curves for the initially key-hole shaped crack, predicted by the present simulation technique
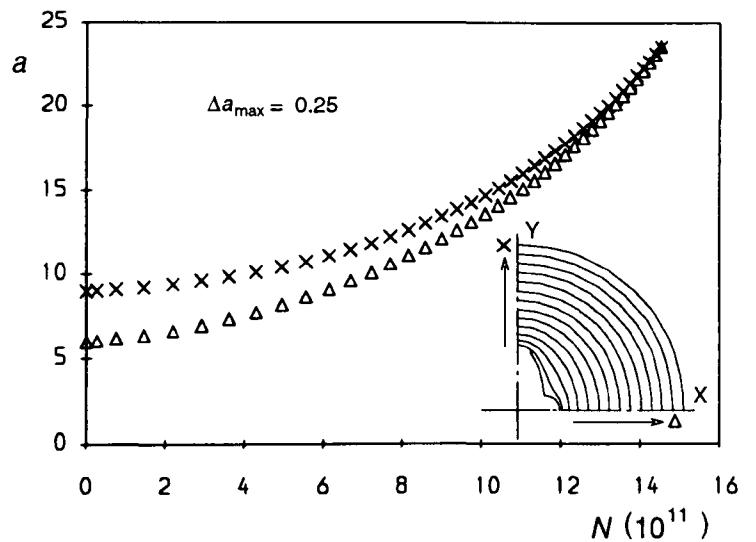
for the initially elliptical crack. The comparison shows that the present results are slightly lower than that from the Irwin's equation with the crack development.

The crack growth predictions for the initially square and key-hole shaped cracks made by the present numerical technique are, respectively, presented in Fig. 3.15 and Fig. 3.16. The

corresponding maximum crack growth increment, Δa_{max}, is indicated in both figures. Due to the unavailability of other either analytical or numerical results, no comparison was given.

3.5 Two Practical Circular Internal Defects

The fatigue growth characteristics of four embedded cracks with different initial shape have been numerically examined, but these cracks are within an ideal infinite solid subjected to remote uniform tension. Embedded defects in practical structures, usually, might behave in a different way due to the limited bounds of structures and the non-uniform Mode I loads applied, which makes it sometimes impossible for an initial defect to reach and subsequently maintain a circular shape.

3.5.1 An circular internal crack in a round bar

Fig. 3.17 shows the numerical results for the fatigue shape development of an initially circular internal crack located near the free surface of a round bar under remote tension, as shown in Fig. 3.3. It is quite clear that the propagating crack almost retains its original shape at the early stage of crack growth, but as the crack approaches very closely the free surface, the part of the crack front adjacent to the boundary grows more rapidly than elsewhere, which results in a distortion of the circular crack profile. Such a crack shape can be readily understood if considering the effect of the free surface on the SIF distribution along the crack front.

The SIF variations along the crack front with the crack development are shown in Fig. 3.18. When the internal crack is a little far from the free boundary, its influence is so weak that the SIF values are almost identical along the crack front, but as the crack approaches nearly the boundary, the free surface has a considerable influence on the SIF variation and the maximum value occurs at the nearest point to the free surface. Sneddon's (1946) exact SIF solution for the initial crack is also included in Fig. 3.18 for comparison, the error being below 2%. This also demonstrates that quite good accuracy of estimating SIFs has been achieved by the present FE technique.
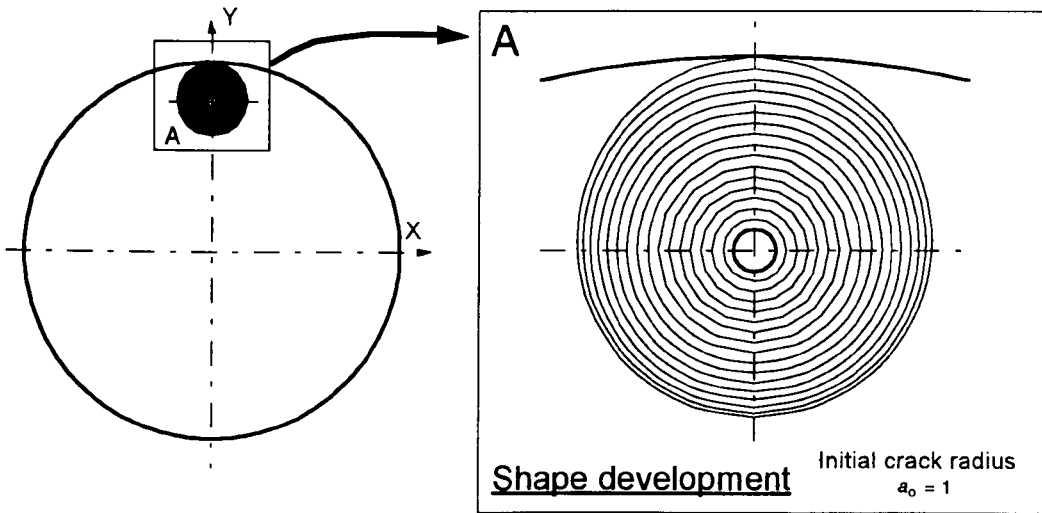
Figure 3.17   Shape development of an initially circular small crack in a round bar under tension
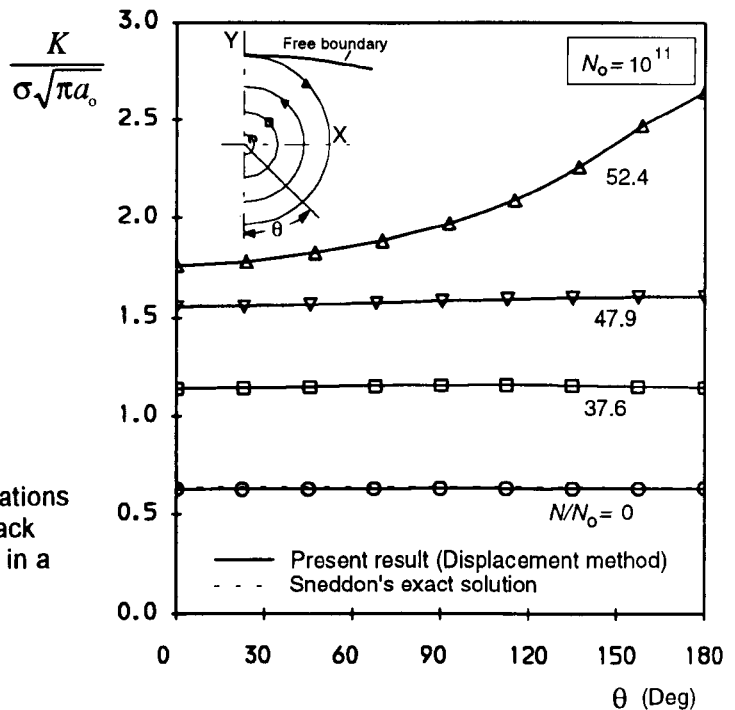
Figure 3.18   Stress intensity factor variations around the crack front with the crack growth for the initially small crack in a round bar under tension

An experimental observation has also been obtained by Wang (1993) for a similar crack nucleated from an internal inclusion with a diameter about 60 μm (*likely to be an aluminium oxide according to the X-ray analysis*) within a round bar, made of a high strength spring steel *251A58*. Fig. 3.19 shows an optical stereo macroscopical image of the fracture surface. The crack origin can be seen at the centre of the shiny area caused by the fretting of the two crack surfaces due to the repeated tension and compression loading. The shiny area, according to the change in the brightness, has generally outlined a circle before it breaks out the free
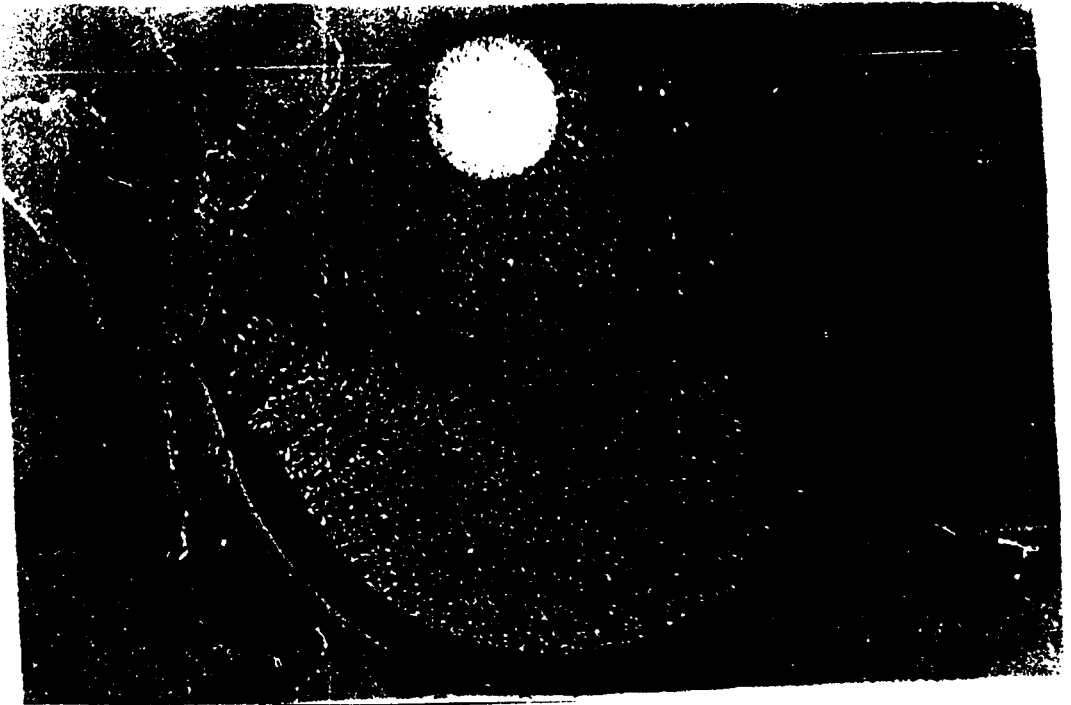
Figure 3. 19 Optical stereo image of the
fracture surface of a fatigue failure
specimen (R = -1)

surface. However, a slightly distorted circle can be observed when the crack approaches the free surface, which agrees well with the numerically predicted crack shape in Fig. 3.17.

The above analyses of both the numerical and experimental results, together with the fatigue growth characteristics of irregular defects in infinite bodies, indicate that if an initially arbitrary irregular defect under uniform fatigue tension is small compared with the size of the component in which the crack is contained, it will first develop into a circle and then maintain a circular front until it approaches the free surface very closely. Thus, it might be adequate and reliable to consider such a crack to be a circle in the calculation of fatigue growth until it breaks out the free surface. However, it should be noted that an initially large irregular internal crack, usually, is unable to come to a circle, due to the presence of the free boundary, so a larger error will possibly appear if it is also dealt with as a circle.

3.5.2 An external surface crack in a pressure vessel

Fig. 3.20 presents the shape development of an initially penny-shaped embedded crack situated at the centre of the wall thickness of an internally pressurised cylinder, whose geometry and mesh have been shown in Fig. 3.4. Due to the non-uniform stress distribution, normal to the crack plane, along the wall thickness direction, the initially circular crack is gradually distorted as the crack develops, and first reaches the inner wall of the cylinder because of the relatively larger normal stress at the inner surface than that at the outer surface. The further crack shape developments are also displayed in Fig. 3.20.
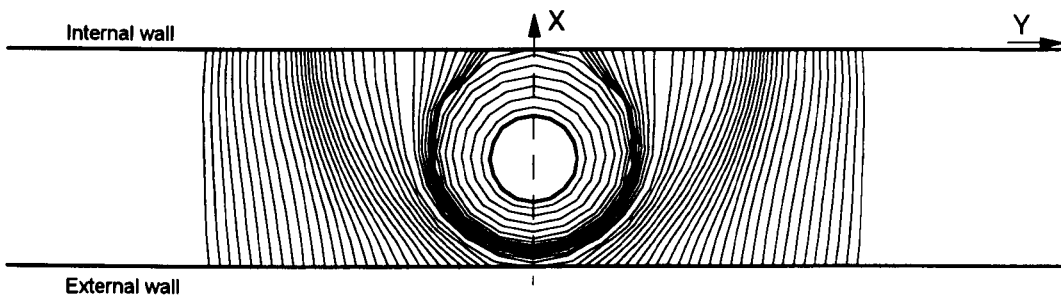
Figure 3.20   Shape development of an initially circular embedded crack
within an internally pressurised cylinder

The shape development demonstrates that the non-uniform stress will always modify the crack shape as the crack advances, therefore, a more precise method, like the present FE simulation technique, should be used in the prediction of fatigue growth of practical internal cracks, in order to obtain more accurate results.

3.6 Conclusions

This chapter has numerically investigated the fatigue growth characteristics, such as the crack shape development, the crack shape deviation, the stress intensity factor variation and the fatigue life prediction, for initially different shape embedded defects in infinite solids by using the FE simulation technique. The numerical accuracy of this technique was examined, particularly by comparing with the exact solution for an initially penny-shaped crack. The

numerical modelling has also been extended to two more practical internal defects under Mode I fatigue loading. The following principal conclusions are drawn:

1) The FE simulation technique possesses good numerical accuracy. The fatigue growth prediction can converge to a required accuracy if a sufficiently small maximum crack growth increment is chosen during the crack growth calculation.

2) The study of fatigue shape changes for several embedded cracks has numerically demonstrated that an initially irregular embedded crack in an infinite solid subjected to remote uniform tension will grow to a circle (*iso-K configuration*) and subsequently maintain a circular front, which agrees with the expectation of theory.

3) The SIF comparison with the existing either analytical or numerical solutions shows that the FE analyses performed by the present author have achieved good calculation accuracy, which further ensures the calculation of fatigue lives.

4) For a practical irregular small internal defect under remote uniform tension, it might be adequate and reliable to assume the crack to be a circle in the calculation of fatigue growth until the crack reaches the free surface. However, care must be taken when an initially larger irregular internal crack is dealt with. Usually, it is unable to come to a circle due to the effect of the free surface. When a small crack is subjected to a non-uniform Mode I fatigue load, a more precise method, like the present numerical technique, should be employed, since the crack shape might be always changing.

3.7 References

Chen, D., Nisitani, H. and Mori, K. (1991) *Stress intensity factors for a fish-eye in a shaft.* **Trans. Japan Soc. Mech. Engrs. 57**(540), 1768-1774.

Forsyth, P. J. E. (1983) *A unified description of micro and macroscopic fatigue crack behaviour.* **Int. J. Fatigue 5**(1), 3-14.

Iida, K. and Fujii, E. (1973) *Fatigue crack propagation from weld defect in 100 mm thick joint.* Proceedings of 2nd International Conference on Pressure Vessel and Piping Technology, San Antonio, Texas, 209-228.

Irwin, G. R. (1962) *Crack-extension force for a part-through crack in a plate.* Trans. ASME, Ser. E, **J. Appl. Mech. 29**, 651-654.

Isida, M., Tsuru, H. and Noguchi, H. (1983) *New method of analysis of three dimensional crack problem.* Memoris of Faculty of Engineering, Kyushu University, **43**(4), 317-334.

Isida, M. and Noguchi, H. (1984) *Tension of a plate containing an embedded elliptical crack.* **Engng Fract. Mech. 20**(3), 387-408.

Isida, M., Yoshida, T. and Noguchi, H. (1991) *A Rectangular crack in an infinite solid, a semi-infinite solid and a finite-thickness plate subjected to tension.* **Int. J. Fracture 52**(2), 79-90.

Lotsberg, I. and Bergan, P. G. (1979) *Calculation on fatigue growth of internal cracks by the finite element method.* **Engng Fract. Mech. 12**, 33-47.

Nisitani, H. and Murakami, Y. (1974) *Stress intensity factors of an elliptical crack or a semi-elliptical crack subjected to tension.* **Int. J. Fracture 10**(3), 353-368.

Shah, R. G. and Kobayashi, A. S. (1973) *Stress intensity factors for an elliptical crack approaching the surface of a semi-infinite solid,* **Int. J. Fracture 9**(2), 133-146.

Smith, R. A. and Cooper, J. F. (1989) *A finite element method for the shape development of irregular planar cracks.* **Int. J. Pres. Ves. Piping 36**(4), 315-326.

Sneddon, I. N. (1946) *The distribution of stress in the neighbourhood of a crack in an elastic solid.* **Proc. R. Soc. Lond.**, Ser. A, **187**, 229-260.

Wang, Y. Z. (1993) Private Communication.

BLANK PAGE
IN
ORIGINAL

Chapter 4

FATIGUE GROWTH MODELLING OF INITIALLY SEMI-ELLIPTICAL SURFACE CRACKS IN PLATES

This chapter, using the 3D step-by-step finite element technique, analysed the fatigue growth behaviours of initially semi-elliptical surface cracks in finite thickness plates subjected to different combinations of tension and bending loads. A wide range of significant results, such as aspect ratio changes, deviations of predicted crack profiles from semi-ellipses, stress intensity factor variations during crack growth and fatigue growth curves, were obtained and discussed. A great effort was made to make the fatigue crack modelling calculations as accurate as possible, which includes the examination of the validity of two-block finite element models and the convergence of both aspect ratios and fatigue lives by varying the maximum crack growth increment. The free surface correction was also employed to investigate the possible difference caused. Most of the present results were compared with those by Newman and Raju's 'two-point plus semi-ellipse' method.

The analyses of propagating crack fronts show that the semi-elliptical profile, basically, can be approximately maintained during crack growth for both pure tension and DOB = 0.5 loads; but, for pure bending, a great deviation from the semi-ellipse commences to appear when the crack grows to nearly 75% of the plate thickness and subsequently the deviation increases rapidly. Generally, the trend of aspect ratio changes predicted agrees with that from the Newman and Raju's method for all three loading cases, DOB = 0, 0.5 and 1. However, for pure tension, as the crack approaches the plate back surface very closely, a slight rise of aspect ratio was observed within the present results, but was absent in the Newman and Raju's predictions. Most of the defects can come to but cannot subsequently maintain the iso-K profile due to the presence of both the front and back surfaces of the plate, or the bending component of the load. The free boundary correction produces a slight effect on aspect ratio variations but seems to have extremely little influence on fatigue growth curves. Agreement between the fatigue growth curves estimated from the present technique and the Newman and Raju's $C_c = 0.9^n C_a$ method is excellent for pure tension, while it becomes slightly worse for pure bending.

4.1 Introduction

Surface cracks, which are most likely to be found in many structures in service, such as pressure vessels, pipeline systems, off-shore structures and aircraft components, have been recognised as a major origin of potential failure for such components. The study of fatigue crack propagation from such a type of crack has been an important subject during recent decades. The surface crack in a finite thickness plate subjected to remote tension, bending or combined loading, as shown in Fig. 4.1, is a well-studied configuration, to which most effort for surface crack problems have been devoted so far, and is commonly considered to be representative of the surface crack family.

4.1.1 Stress intensity factor calculations

The early studies of surface cracks were mainly focused on the estimation of stress intensity factors along a semi-elliptical crack front, as shown in Fig. 4.1. Irwin (1962), on the basis of the exact SIF solution of an embedded elliptical defect, presented the first engineering estimation of SIF for such a surface crack under remote uniform tension. Due to the complexity of the problem, an exact solution for the semi-elliptical surface crack has not been obtained since Irwin's (1962) estimation was published. From 1965 to 1979, with the availability of powerful computers, considerable efforts were made to use various numerical techniques, such as the finite element method, the alternating method and the line-spring model, in order to obtain more accurate solutions for the SIF of semi-elliptical surface cracks. Newman (1979) reviewed the approximate SIF solutions published before 1979 for surface cracks in finite thickness plates subjected to uniform tension. These solutions are, in chronological order, due to: Irwin (1962), Paris and Sih (1965), Smith *et al.* (1967), Kobayashi and Moss (1969), Masters *et al.* (1969), Smith and Alavi (1969), Rice and Levy (1970), Anderson *et al.* (1970), Newman (1972), Shah and Kobayashi (1972), Smith and Sorenson (1974), Kobayashi (1976), Raju and Newman (1977;1979) and Newman and Raju (1978). Most solutions give the SIF at the deepest point and have limitations on the aspect and depth ratios.

Fig. 4.2 shows the comparison, made by Newman (1979), of these proposed solutions. Obviously, the differences are quite large, particularly for larger values of *a/t*. The various SIF solutions were ranked by Newman (1979) on a statistical basis of comparing them with

Crack plane geometry

Loads

Surface crack under Mode I loading
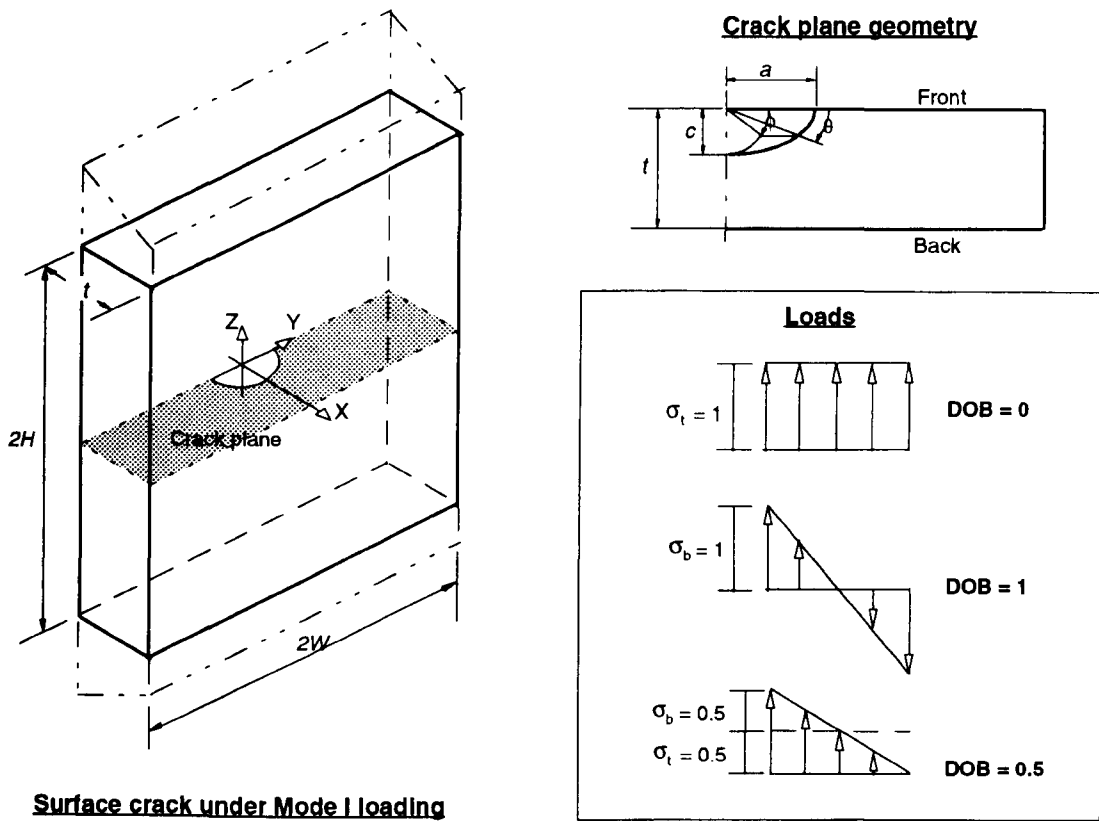
Figure 4.1   A surface crack in a finite thickness plate subjected to remote tension, bending, or both combined fatigue load

experimental fracture data obtained in brittle epoxy material. The first three are: Newman and Raju (1979), Smith *et al.* (1967) and Newman and Raju (1977). On the basis of 3D finite element analyses (Newman and Raju, 1979; Raju and Newman, 1979) of the SIFs along the front of some semi-elliptical surface cracks in finite thickness plates subjected to remote uniform tension or bending, Newman and Raju (1981) constructed a SIF equation which is capable of analysing a wide range of crack configurations and convenient to use. The equation, outlined in Appendix B, has the following format:

$$K = \left(\sigma_t + H\sigma_b\right)\sqrt{\frac{\pi a}{Q}}F\left(\frac{a}{t},\frac{a}{c},\frac{c}{W},\phi\right) \tag{4.1}$$

where H is a function of crack depth ratio a/t, aspect ratio a/c and parameteric angle ϕ; σ_t is tensile stress and σ_b is bending stress at surface, as shown in Fig. 4.1.

85
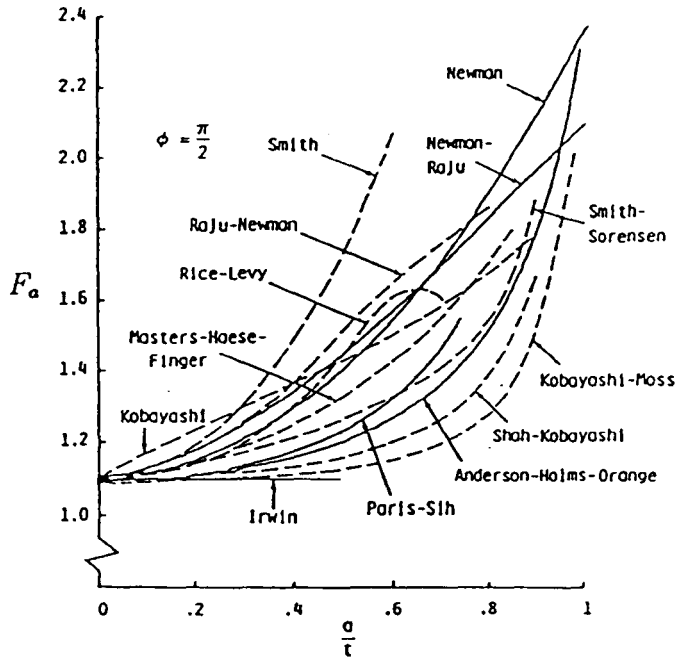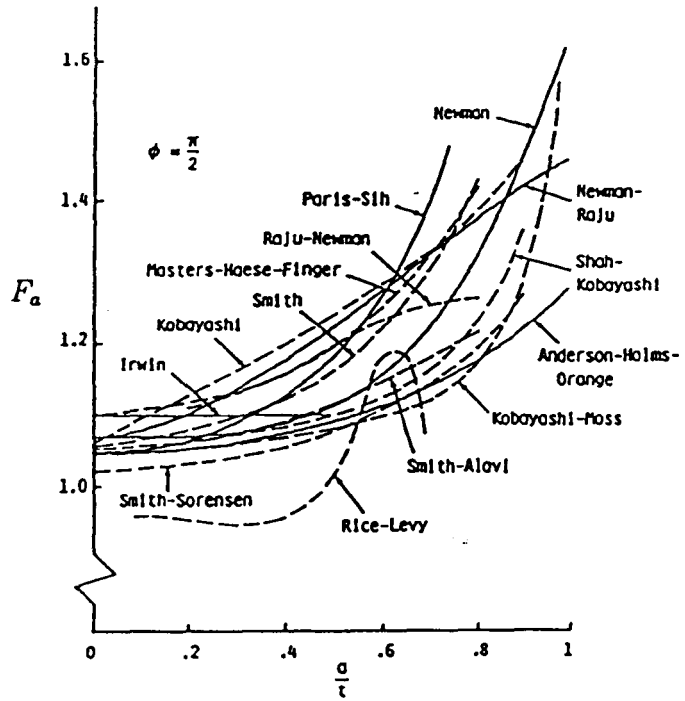
(a) $a/c = 0.2$

Figure 4.2   Stress intensity factors at the maximum depth point of a semi-elliptical surface crack, Newman (1979); (a) $a/c = 0.2$, (b) $a/c = 0.6$

The validation of Newman and Raju's SIF equation was subsequently confirmed by the Society for Experimental Stress Analysis (SESA) (1985), Hosseini and Mahmoud (1985) and Mahmoud and Hosseini (1986), the latter two indicating that the SIF values from Newman and Raju's (1981) equation were well within the natural error bounds of the photoelastical studies of surface cracks under tension or bending. The accuracy of this equation was also demonstrated by Newman and Raju (1981) and many other investigators through comparisons of the crack shape change between experimental data and those predicted from the Newman and Raju's equation, which will be detailed later.

Holdbrook and Dover (1979), Scott and Thorpe (1981), and Isida *et al.* (1984) also proposed, respectively, different SIF equations for semi-elliptical surface cracks under tension or bending. Holdbrook and Dover's equation was based on a simple analysis considering the effects of free front surface, finite area and finite second moment of area. Scott and Thorpe's equation appeared to be a combination of curves fitted to results and modified equations from the 'best' available solutions judged by them. Isida *et al.* achieved the SIF equation by fitting polynomials in a/c and a/t to their results, obtained by the body force method. The equation of Isida *et al.* was reported to have a good agreement with Newman and Raju's (1981) empirical equation over the range of $0.125 \leq a/c \leq 1.0$, $0 \leq a/t \leq 0.8$. Unlike Newman and Raju's (1981) equation that is able to estimate all SIF values along the crack front, the above three equations only give the SIF calculation at one point (*depth point*) or two points (*both depth and surface points*).

4.1.2 Crack shape change predictions

The fact that a surface crack under fatigue loading always changes its crack front as it grows has involved many investigators in predicting crack shape changes. A considerable amount of experimental results (Yen and Pendleberry, 1962; Hoeppner *et al.*, 1968; Corn, 1971; Grandt and Sinclair, 1972; Hall *et al.*, 1974; Iida and Kawahara, 1975; Kawahara and Kurihara, 1975; Nagai *et al.*, 1975; Kobayashi *et al.*, 1977; Kawahara and Kurihara, 1977; Cruse *et al.*, 1977; Pierce and Shannon, 1978; Hodulak *et al.*, 1979; Holdbrook and Dover, 1979; Newman and Raju, 1979; Portch, 1979; Lloyd and Walls, 1980; Truchon and Lieurade, 1981; Vosikovsky and Rivard, 1981; Lee *et al.*, 1982; Jolles and Tortoriello, 1983; Carter *et al.*, 1987; Chen and Cui, 1988; McFadyen *et al.*, 1990; and Putra and Schijve, 1992) have
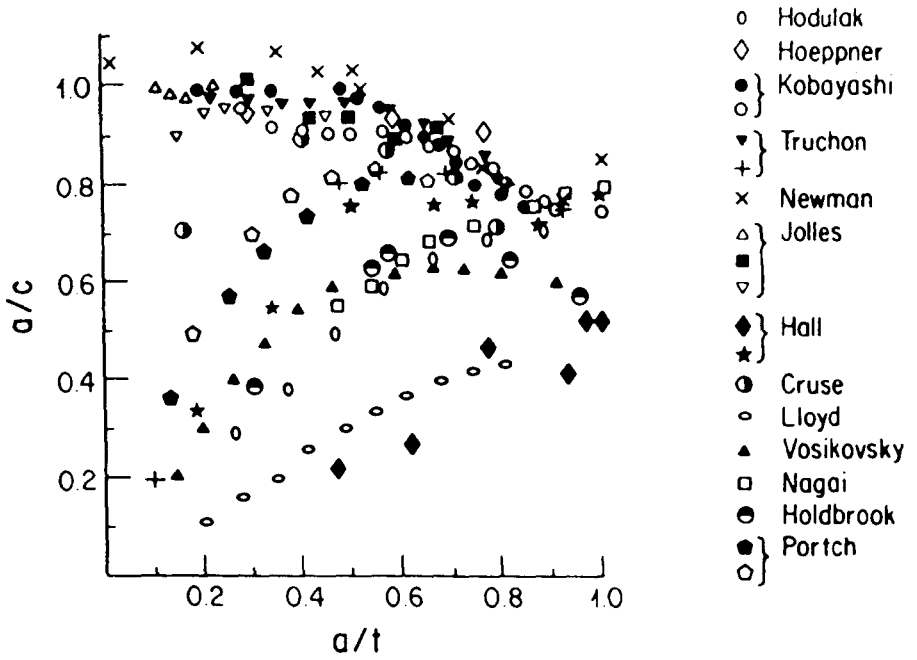
(a) Tension, Hosseini & Mahmoud (1985)
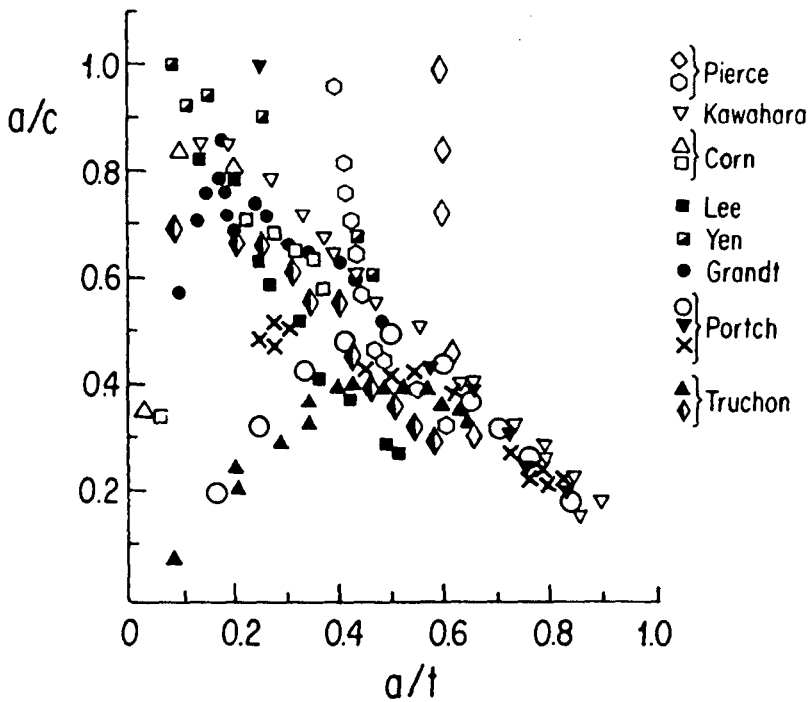
(b) Bending, Mahmoud & Hosseini (1986)

Figure 4.3   Aspect ratio changes due to surface fatigue crack growth in plates
under cyclic Mode I loading; (a) Tension, Hosseini and Mahmoud (1985),
(b) Bending, Mahmoud and Hosseini (1986)

been published for shape development of surface cracks, of various initial sizes, in plates made of various materials and subjected to tension or bending fatigue loads. Fig. 4.3 shows some of these data in tension and bending plates. Most of the measurements of crack shape development were performed using the electrical potential or the beachmark method with their own experimental standards. These experimental results show that the profile of surface cracks growing under tension or bending fatigue can be usually approximated as a semi-ellipse if the retardation of crack growth along the free surface, where the crack front makes an acute or negative angle of intersection with the free surface, is neglected. The changes in defect aspect ratio, a/c, depend principally upon initial configuration, relative crack depth and loading condition, but also depend weakly upon stress ratio (Scott and Thorpe, 1981; Mahmoud, 1985, 1988a, 1988b), loading frequency, growth rate exponent n (Wu, 1985; Mahmoud, 1985, 1988a, 1988b), mean stress (Iida and Kawahara, 1975; Scott and Thorpe, 1981; Mahmoud, 1988a, 1988b; Cater *et al.*, 1987) and the crack tip stress conditions (Putra and Schijve, 1992) which alter with changes in crack shape. A surface cracks will grow towards a so-called preferred propagation path (PPP) that is related to the loading mode, whatever the shape of its initial defect. The rate of such a tendency towards the PPP is greater for a larger deviation between the current crack shape and the PPP.

The aspect ratio equation, which describes the propagation path of a crack, is useful in calculations of fatigue lives of surface cracks. Portch (1979) and Iida (1983), the latter being the culmination of several previous studies of Iida and Kawahara (1975), Kawahara and Kurihara (1977), Iida and Kawahara (1980) and Iida *et al.* (1982), have formulated their own aspect ratio equations, by fitting curves to experimental data. These equations are applicable to surface cracks in plates under tension, bending or combined tension and bending. Obviously, they are empirical and not relevant to these slight influences mentioned above on the shape change of surface cracks. Contrary to the direct experimental fitting method, Newman and Raju (1979) suggested that the aspect ratio change of surface cracks should be calculated by assuming that an semi-elliptical profile is always maintained and only using the two coupled Paris fatigue growth laws (*in this thesis this method is called Newman and Raju 'two-point plus semi-ellipse'*):

$$\frac{da}{dN} = C_a \left(\Delta K_a \right)^n; \qquad \frac{dc}{dN} = C_c \left(\Delta K_c \right)^n$$

where ΔK_a and ΔK_c are the ranges of stress intensity factors at the depth and surface points of a surface crack and calculated from their SIF equation (Newman and Raju, 1981). C_a should be obtained from standard specimens under near plane strain conditions as possibly, and C_c was proposed to take the coefficient correlation, $C_c = 0.9^n C_a$, in order to consider the effect of the surface layer where the retardation of the crack growth was often observed by many investigators. Such a correction appears to lead to a better agreement between predicted and experimental aspect ratio change curves than the $C_c = C_a$ relation.

According to the Newman and Raju 'two-point plus semi-ellipse' method, Wu (1985) derived an analytical aspect ratio equation for pure tension using the Newman and Raju's (1981) closed SIF equation. The analytical equation makes it unnecessary to use the initially required cycle-by-cycle calculation. Following the same procedure, Wu (1985) also obtained an approximate analytical solution of considerable length for pure bending, due to the complexity of the solved differential equations. In order to rank the accuracy of aspect ratio equations in practical applications, Mahmoud (1988a, 1988b) compared a wide range of experimental data published in the literature with those by different methods of predicting the aspect ratio change of surface cracks under tension or bending. The comparison was based on a quantitative criterion as well as a statistical examination of the level of agreement with the data. Mahmoud's conclusion was that the best shape change predictions are those obtained by the Newman and Raju 'two-point plus semi-ellipse' method using their own SIF solutions with suitable constants in the Paris law, rather than the aspect ratio equations that are only based on experimental observations. This should be anticipated since a SIF/Paris law analysis has a convincing theoretical basis compared with an experimental fitting method. Mahmoud (1988a, 1988b) also thought that Kawahara and Kurihara's (1977) equation, which was one of those involved in the eventual formulation of the improved Iida's (1983) aspect ratio equations, can provide an acceptable approximation of the general shape change of a surface crack under tension or bending. Before the work of Mahmoud (1988a, 1988b), Wu (1985) also compared the Newman and Raju's prediction of the shape change, using the correlation $C_c = 0.9^n C_a$, with more than 680 pairs of experimental data for 22 different metallic materials published before, and concluded that the agreement is excellent between predicted and experimental results.

However, it should be further indicated that the 'two-point plus semi-ellipse' method for the prediction of aspect ratio changes has used two assumptions. Although Mahmoud (1988a,

1988b) and Wu (1985) have obtained a similar positive conclusion for its applicability, from a theoretical point of view, it might be unavoidable for the two assumptions embedded in this method to cause an error.

4.1.3 Objectives

The objective of this chapter is to use the numerical simulation technique, which has been described in Chapter 2, to directly predict the fatigue growth of initially semi-elliptical surface cracks in plates subject to tension, bending and a combination of both. It is obvious that such a numerical simulation is more sophisticated and superior to the 'two-point plus semi-ellipse' method since it has explicitly considered the SIF variation along a crack front and avoided using the semi-ellipse assumption. In order to ensure the reliability of the results obtained by the present simulation technique, some numerical examinations are to be performed in this chapter, such as the verification of stress intensity factor accuracy for initially semi-elliptical defects, and the convergence study of both aspect ratios and fatigue lives by varying the crack growth increment for a tension crack. The technique of free boundary layer correction detailed in Chapter 2 is also applied to the tension surface crack problem to investigate the difference between using and not using this correction. The effect of the Paris exponent n on the aspect ratio is also examined. The degree of deviation of the predicted crack shapes from the corresponding semi-ellipses during the fatigue growth process will be quantitated through the proposed relative residual and the relative standard deviation in order to clarify the shape change characteristics for surface cracks subjected to different combinations of tension and bending. A wide range of numerical results, including aspect ratio changes, distributions of stress intensity factors along the front of several cracks, variations of the stress intensity factors at both the surface and depth points and predictions of fatigue cycles will be presented for all three different fatigue loads, and mostly compared with those made using the Newman and Raju 'two-point plus semi-ellipse' method, which enables the errors caused by the semi-elliptical shape assumption to be numerically revealed.

4.2 Numerical Simulation Details

Fig. 4.1 has defined the nomenclature used in this chapter to describe a surface crack in a plate. Two non-dimensional ratios, i.e. crack depth to surface half-length (*aspect ratio*), a/c, and crack depth to plate thickness (*depth ratio*), a/t, are commonly used to describe the geometry of a surface crack. The remote load applied to a plate is identified by defining the degree of bending (DOB), DOB $= \sigma_b/(\sigma_b + \sigma_t)$, as shown in Fig. 4.1. DOB $= 0$ and 1 represent pure tension and pure bending, respectively.

Six different initially semi-elliptical crack configurations were analysed in this chapter. The initial aspect ratios were, respectively, $a_o/c_o = 0.2, 0.4, 0.5, 0.6, 0.8$ and 1.0, and the initial depth of all cracks was taken to be 20% of the plate thickness, i.e. $a_o/t = 0.2$ (5mm/25mm). The selected height ($2H = 800$mm) and width ($2W = 800$mm) of the plate were larger for them to have negligible effect on the crack growth. Three different remote fatigue loads, DOB $= 0, 0.5$ and 1, were applied to each initial crack configuration.

During the simulation of fatigue crack growth, the assumed material properties were: the Poisson's ratio $\nu = 0.3$, the Paris coefficient $C = 1.83 \times 10^{-13}$ (*the units are*: $\Delta K \sim \text{MPa}\sqrt{\text{mm}}$; $da/dN \sim \text{mm} / \text{cycle}$) and the exponent $n = 3$. $n = 2$ and 4 were also employed for the semi-elliptical crack of $a_o/c_o = 1$, in order to investigate the effect of the power n on the crack shape change. The numerical approximation to the crack front employed in this chapter was the cubic spline curve, which is an improvement achieved recently and was detailed in Chapter 2. The boundary layer correction technique, which uses the plane stress assumption at the surface point and the plane stain assumption elsewhere, instead of using plane strain assumption along a whole crack front, was also applied to the tension fatigued cracks. The maximum crack growth increment, Δa_{max}, along the crack front was confined to a reasonable small value, $t/100$ (0.25mm), and such a value was always maintained during the whole crack growth process except at the late stage of crack growth for DOB $= 0.5$ and 1, when relatively larger crack growth increments were chosen in order to speed up the crack advance along the crack depth direction and to reduce the CPU consumption. Three different values of the maximum crack growth increment, $\Delta a_{max} = t/167, t/100$ and $t/50$, were also taken for the tension crack of $a_o/c_o = 0.6$ in the investigation of its effect on aspect ratio changes and fatigue lives. The fatigue growth computation was not terminated until the crack approached (for DOB $= 0.5$ and 1) or reached (for DOB $= 0$) the back surface of the plate. The 1/4-point displacement method was

Table 4.1   Crack geometry, loading conditions and details associated with the performed numerical computations

Name	a_o/c_o $(a_o/t=0.2)$	Fatigue loads DOB	Paris exponent, n	Crack growth increment Δa_{max} (mm)	Boundary layer correction (YES/NO)
T2	0.2	0 (tension)	3	0.25	NO
T4	0.4	0	3	0.25	NO
T5	0.5	0	3	0.25	NO
T6	0.6	0	3	0.25	NO
T6-Δ15	0.6	0	3	0.15	NO
T6-Δ50	0.6	0	3	0.50	NO
T8	0.8	0	3	0.25	NO
T10	1.0	0	3	0.25	NO
T10-n2	1.0	0	2	0.25	NO
T10-n4	1.0	0	4	0.25	NO
T2-C	0.2	0	3	0.25	YES
T4-C	0.4	0	3	0.25	YES
T5-C	0.5	0	3	0.25	YES
T6-C	0.6	0	3	0.25	YES
T8-C	0.8	0	3	0.25	YES
T10-C	1.0	0	3	0.25	YES
H2	0.2	0.5	3	0.25~2.0	NO
H4	0.4	0.5	3	0.25~2.0	NO
H5	0.5	0.5	3	0.25~2.0	NO
H6	0.6	0.5	3	0.25~2.0	NO
H8	0.8	0.5	3	0.25~2.0	NO
H10	1.0	0.5	3	0.25~2.0	NO
B2	0.2	1 (bending)	3	0.25~2.0	NO
B4	0.4	1	3	0.25~2.0	NO
B5	0.5	1	3	0.25~2.0	NO
B6	0.6	1	3	0.25~2.0	NO
B8	0.8	1	3	0.25~2.0	NO
B10	1.0	1	3	0.25~2.0	NO

used in this chapter for practical modelling computations (if not mentioned, all SIF results are calculated from this method).

Due to the variety of considered problems in the simulation of fatigue crack growth, each modelling process was given a name. Table 4.1 shows all analyses performed in this chapter, in which the initial crack size, the loading condition, the employed Paris exponent and the maximum crack growth increment as well as whether using the free boundary layer correction are clearly differentiated.

The finite element calculation was performed of only a quarter of the problem, due to there being two planes of symmetry. All FE models created in practical analyses consisted of two blocks, as mentioned in Chapter 2, i.e. cracked block and uncracked block, except the models used to check the effect of mesh mismatch which usually exists for the two-block model on the SIF accuracy. Such exceptional models possessed complete mesh compatibility. The 3D cracked block, as described in Chapter 2, was automatically generated from the 2D cracked plane mesh and subsequently assembled to the pre-designed uncracked block by the DUCKPRE software. Fig. 4.4 shows two typical FE models, the uncracked block in Fig. 4.4(a) being designed for the tension fatigue while that in Fig. 4.4(b) for DOB = 0.5 and 1. The number of degrees of freedom for these two-block models ranged from 7000 to 8500. The planes on which the multi-point constraint method was applied to reduce the effect of mesh mismatch on the calculation accuracy are also marked in Fig. 4.4. The contact plane between both uncracked and cracked blocks was 6mm away from the cracked plane, which will be verified later to be far enough to reduce its mesh mismatch effectively. During the whole modelling process, the uncracked block of either (a) or (b) in Fig. 4.4 was maintained unchanged.

The 2D cracked plane mesh was always recreated after the crack had propagated to a new position, which was done automatically by the DUCKPOST software. Fig. 4.5 shows some typical finite element configurations of 2D cracked planes. The crack front was defined by seventeen nodes (*nine corner nodes and eight midside nodes*) and there were eight 8-noded iso-parameteric elements abutting it each side. Similar FE meshes were used by Newman and Raju (1979) in the evaluation of stress intensity factors for semi-elliptical surface cracks in finite thickness plates under tension, and it was found by them through a convergence study that the models with eight edges along the crack front are sufficient. Although it is not a problem for the present simulation technique to create FE configurations with any desired number of the elements along the crack front, a larger number of elements means a larger number of degrees of freedom for the created models, and further means more consumption of computer resource. From Fig. 4.5 it can be seen that the edges of the elements abutting the crack front intersect the crack front nearly orthogonally, which is very important for the 1/4-point displacement method to achieve a good SIF estimate, as indicated in Chapter 2. The elements within the 2D cracked plane meshes can always be in a quite good state, i.e. less distorted.
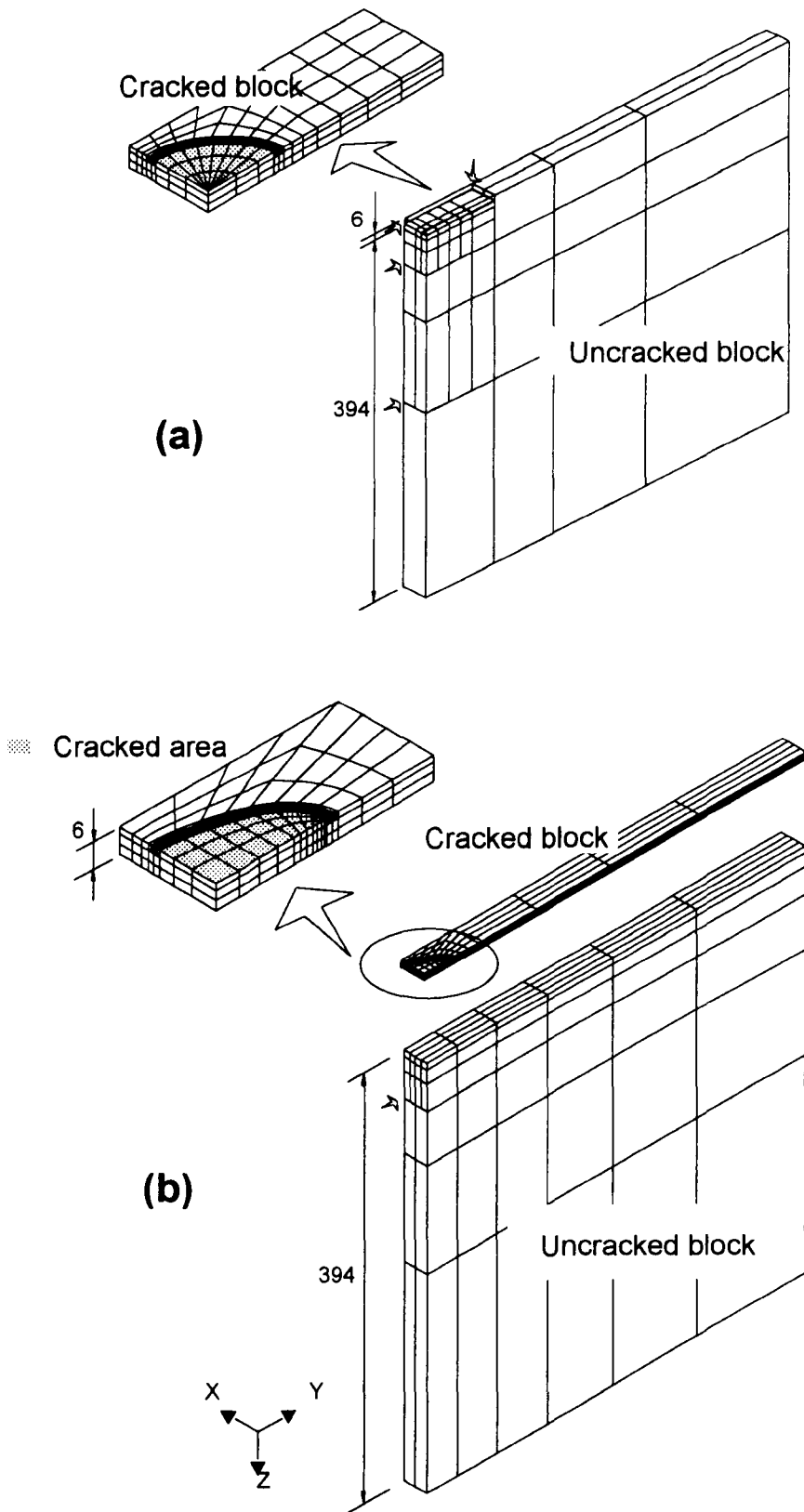
Figure 4.4   Typical finite element meshes comprising two blocks, cracked and uncracked blocks, used during the fatigue growth modelling; (a) for tension (DOB = 0), (b) for DOB = 0.5 and 1
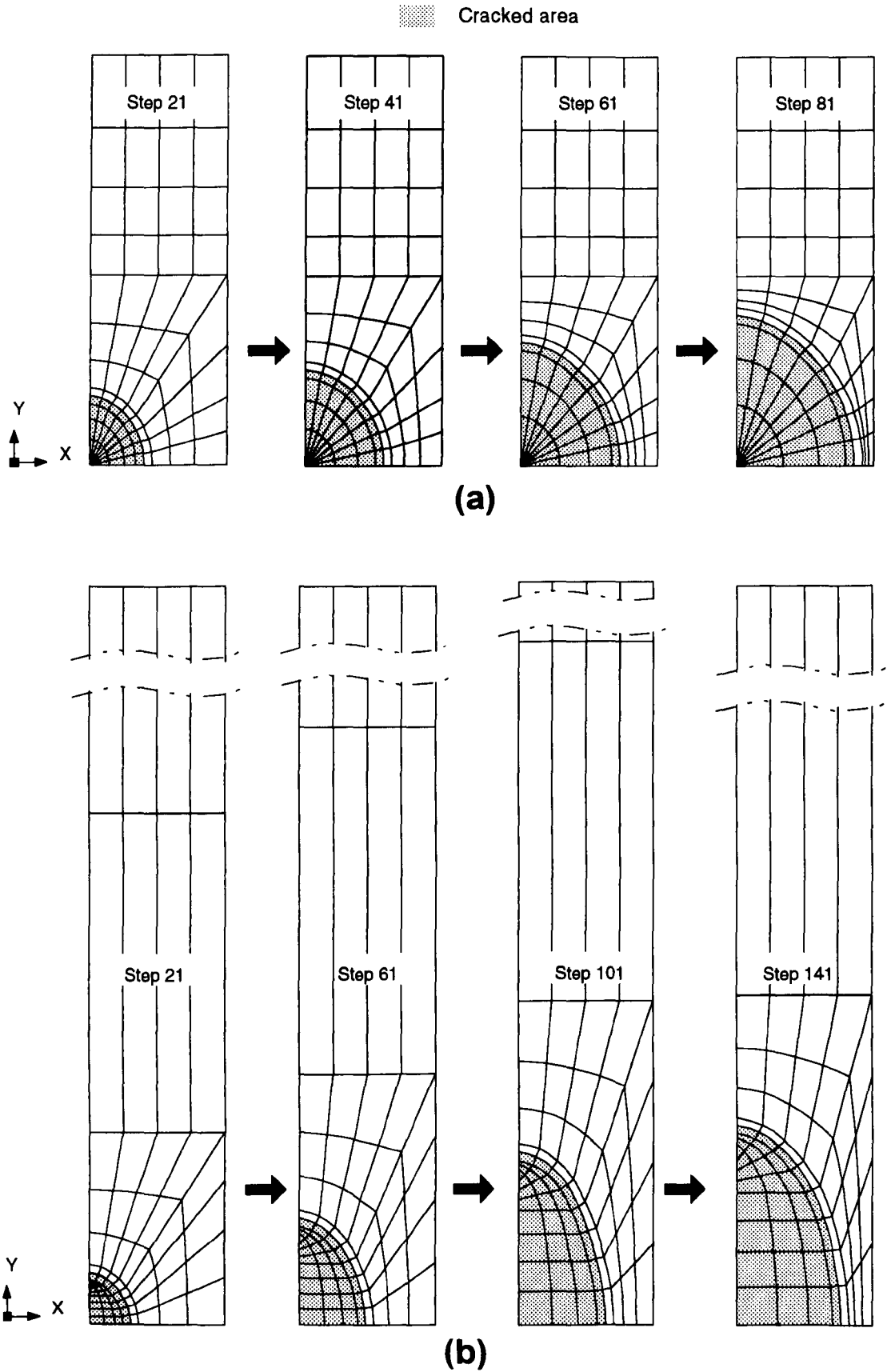
Figure 4.5   Some typical 2D finite element meshes of cracked planes
for both DOB = 0 and 0.5; (a) T6, (b) H10

During most of the modelling processes, no intervention had been required for modifying the automatically formed meshes or something else since the modelling computation was launched, which owes to the highly automated software developed by the present author. All computations in this chapter were completed on a Silicon Graphic Workstation.

4.3 Crack Shape Development and Deviation

The study of crack shape changes, as indicated in the above review, has been one of the important subjects for surface fatigue cracks since the prediction of crack shape development is necessary for a more accurate estimate of fatigue lives. This section aims at presenting the fatigue shape development of initially semi-elliptical cracks predicted by the present numerical technique and examining the degree of deviation of the predicted crack profiles from semi-elliptical shapes through proposed quantitative criteria.

4.3.1 Defect shape development

Fig. 4.6 shows the fatigue shape development of the initially semi-elliptical surface cracks subjected to pure tension, whose names listed in Table 4.1 are T2, T4, T5, T6, T8 and T10. Crack growth due to tension fatigue has been modelled until the crack advances to the back surface of the plate. The crack profiles displayed in Fig. 4.6 are those condensed from a range of 84 ~ 121 analyses for each defect, in order for them to be identified clearly. It is obvious that the normal outward increments of crack growth are not equal around a crack perimeter as the crack advances due to the variation of stress intensity factors around the crack front. At the early stage the shape change of each crack is different and strongly dependent on its initial aspect ratio. As these cracks propagate, however, they tend asymptotically towards a preferred aspect ratio, reaching a very similar final defect shape except the initially long and shallow crack, a_o/c_o = 0.2 (T2), which reaches an obviously longer surface length when it propagates to the back surface of the plate. In general, the final profile (*the shape when the crack reaches the plate back surface*) which a crack will adopt depends on its initial aspect ratio, but if the initial aspect ratio, a_o/c_o, of the crack is not so small and the
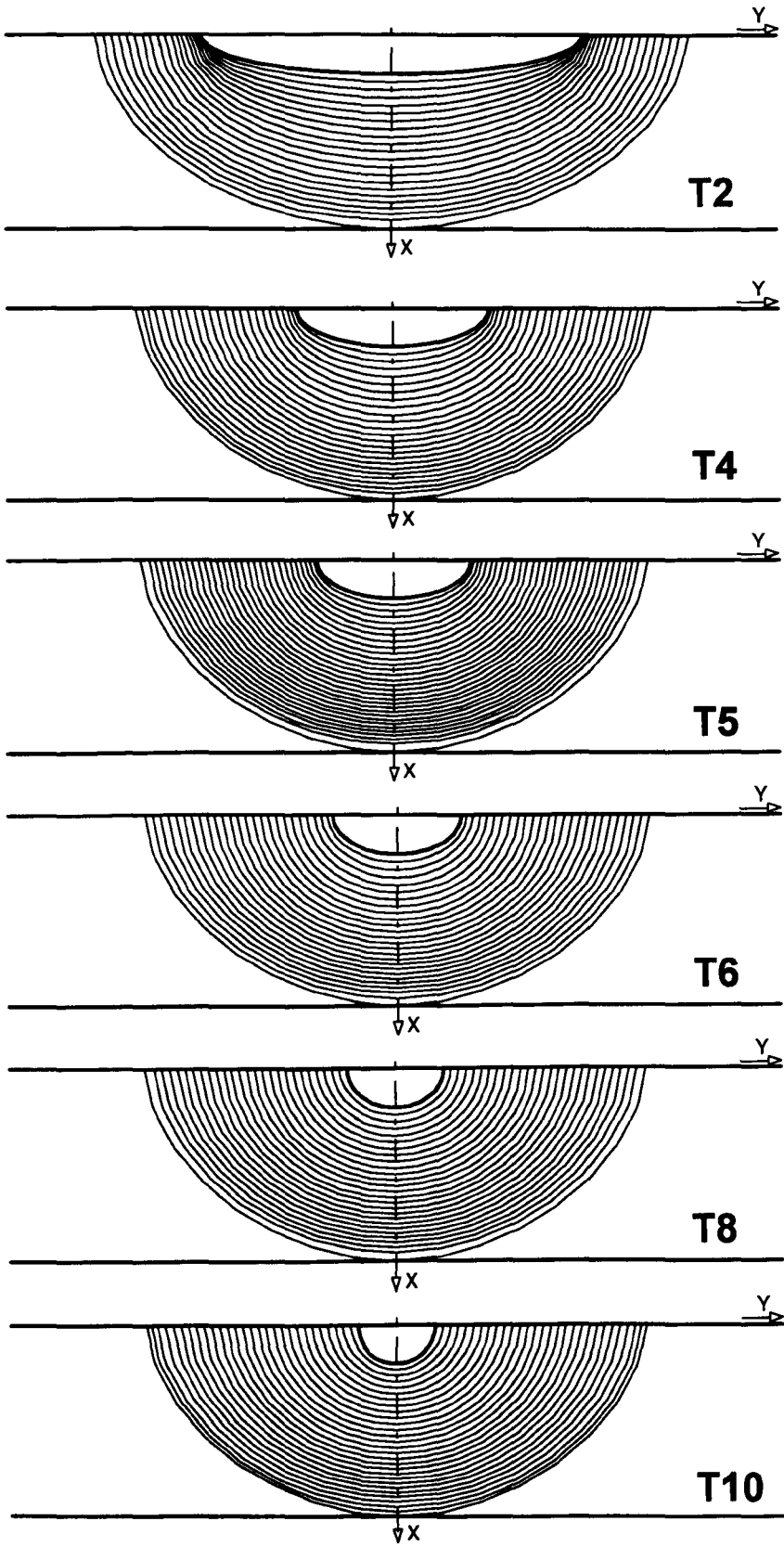
Figure 4.6   Shape development of initially semi-elliptical surface cracks
subjected to tension fatigue

initial depth ratio, a_o/t, is not too large, an approximately stable final shape does exist. This can be seen from the crack shape development in Fig. 4.6. The clearer aspect ratio changes will further be presented later.

The fatigue crack profiles adopted by the plates subject to pure bending are detailed in Fig. 4.7. An obvious feature is that the crack grows more and and quickly along the free surface than in its depth, especially when it gradually becomes larger, the crack is extremely difficult to advance along the plate thickness direction whilst only increases its surface length, leading to a nearly straight front. This can be explained by examining the variation of stress intensity factors around the crack front due to pure bending, which will be demonstrated in the following analysis of stress intensity factors. Totally, 180 crack advance steps were calculated in the modelling analyses for all bending cracked plates. The maximum crack growth increment, Δa_{max}, was between $t/100$ and $t/12.5$, the larger Δa_{max} was employed for larger cracks. Due to the extreme difficulty in crack advancing along the plate thickness when it approaches the back surface of the plate, the crack growth computation was terminated at about 80% of the plate thickness. For a good view, a part of the fatigue crack fronts that are very flat and long was cropped and just nearly a quarter of the obtained crack growth profiles are displayed in Fig. 4.7. Similar to the tension fatigue propagation, the fatigued bending cracks also show a trend towards a certain aspect ratio as they grow, but the tendency is much more intense.

Fig. 4.8 represents the shape prediction of initially semi-elliptical surface cracks fatigued by a combination of tension and bending, DOB = 0.5. Evidently, different fatigue loads lead to different preferred propagation patterns for the same initial crack. Due to the half bending component, these cracks in Fig. 4.8 are not so difficult to advance throughout the plate thickness, although much more rapid crack growth at the surface point than that at the depth point, similar to pure bending growth, can still be seen as they approach the back surface of the plate. A trend towards a stable shape can also be observed for all exhibited defects in Fig. 4.8. The asymptotic shape growth trend is intermediate.

4.3.2 Deviation of crack profiles from semi-ellipses

The semi-elliptical configuration has been used in estimates of stress intensity factors or in analyses of surface crack fatigue problems. This is based on experimental observations which
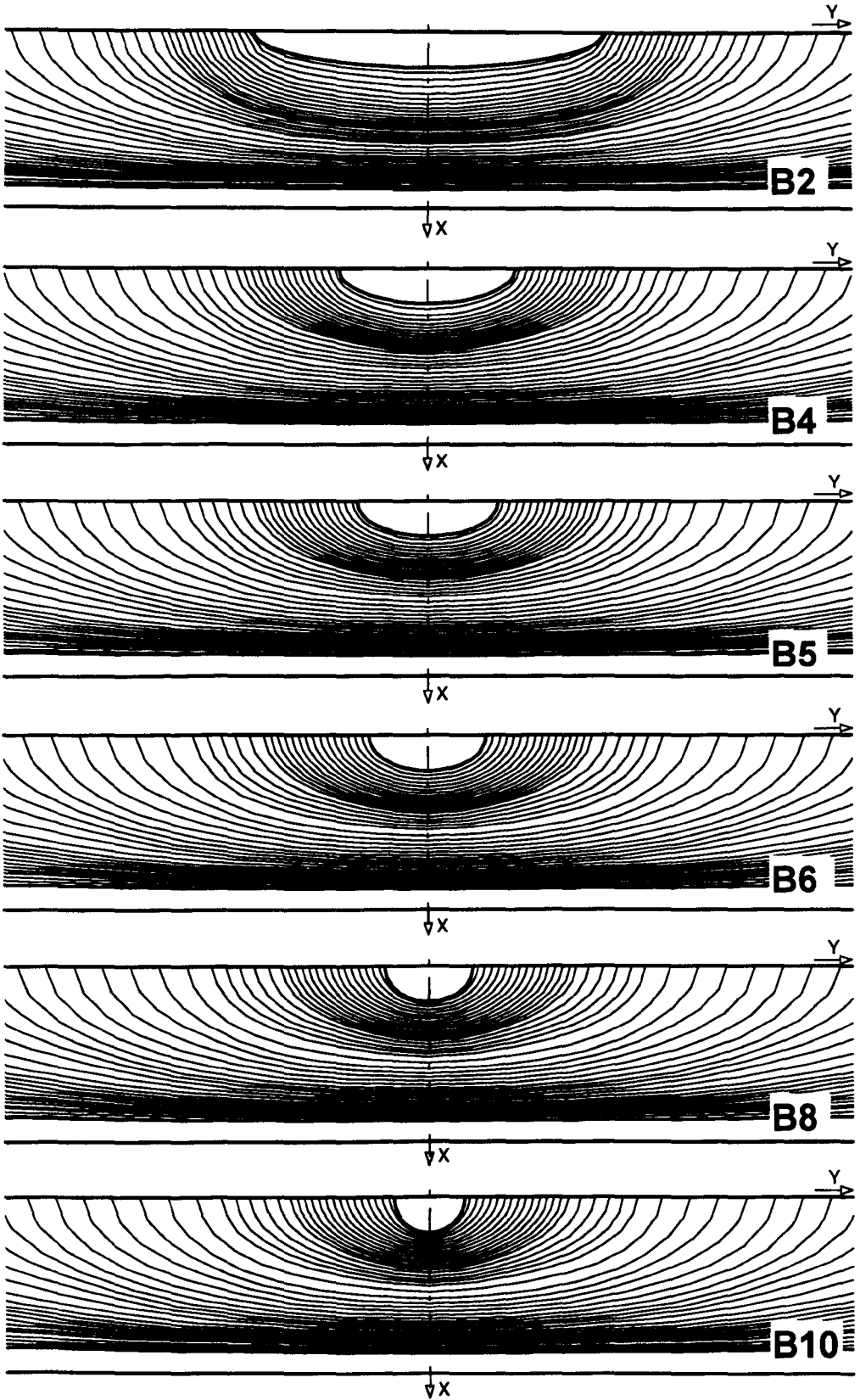
Figure 4.7   Shape development of initially semi-elliptical surface cracks
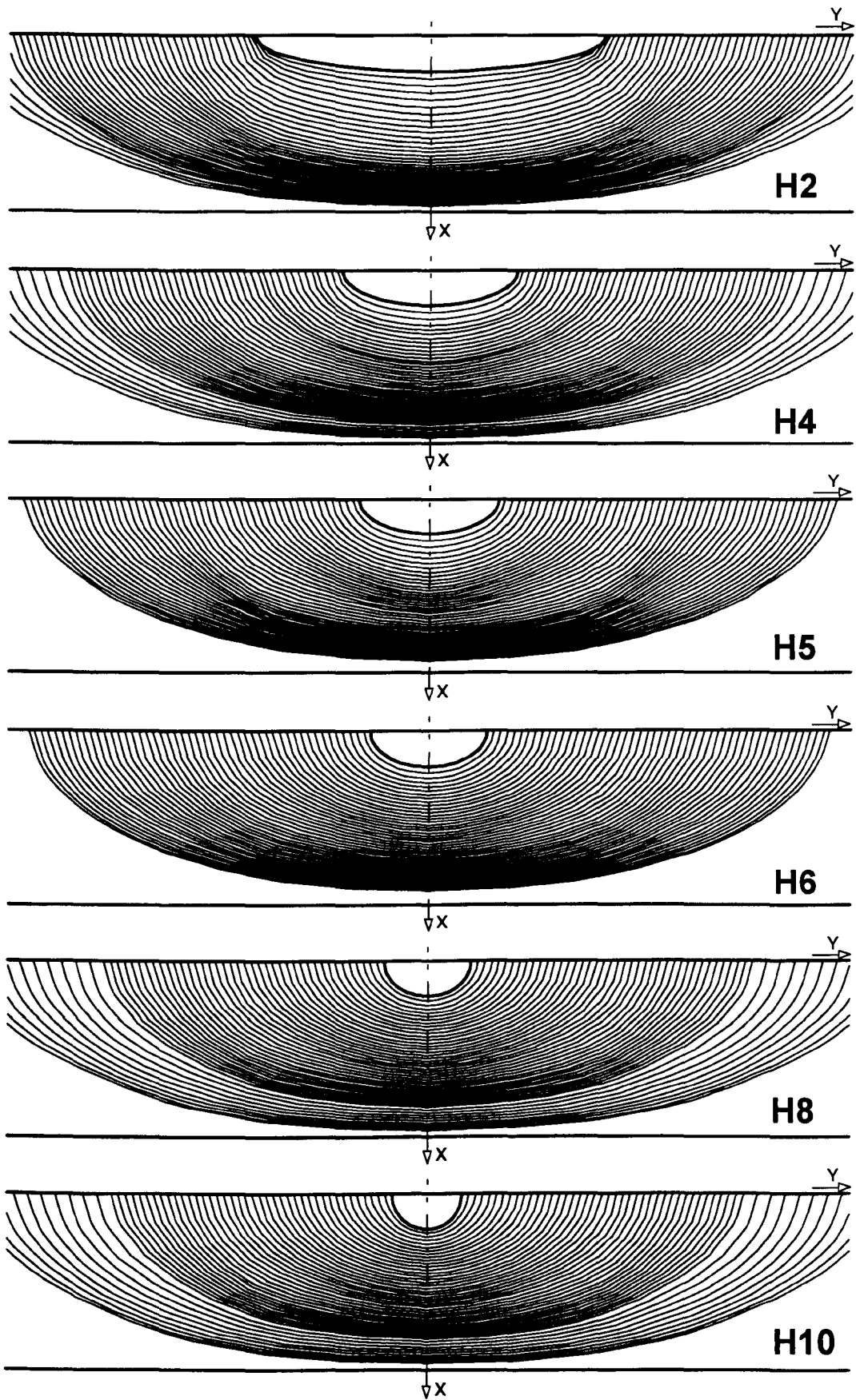subjected to bending fatigue

Figure 4.8   Shape development of initially semi-elliptical surface cracks under a combination of tension and bending, DOB = 0.5

indicate that an irregular surface crack growing by fatigue in a linear stress field very quickly adopts and then maintains a semi-elliptical shape. The investigators have been unable to avoid employing the SIF solutions of semi-elliptical surface cracks to correlate their experimental results to the Paris fatigue crack growth law. The widely recognised method of predicting the fatigue growth of surface cracks, presented by Newman and Raju (1981), was also based on the semi-elliptical shape, as stated above. There is no doubt, in the strict sense, that the surface crack, no matter what initial configuration, may change its shape (*not the aspect ratio of a semi-ellipse*) during the fatigue growth process and cannot possibly be an exact semi-ellipse. One should be aware that what a large number of experimental observations have shown is that the semi-elliptical shape is a very good approximation to the fatigue propagating front of surface cracks.

What fatigue crack fronts will be adopted? How far are they from the semi-ellipses? It has become possible to answer the two important questions by carefully examining a series of the fatigue growth profiles obtained by the present simulation technique. For this purpose, a realistic and quantitative criterion, similar to that used in Chapter 3 for examining the deviation of predicted embedded crack fronts with the circles, is defined for examination of the degree of agreement between the predicted surface crack profile and the semi-elliptical shape.

As shown in Fig. 4.9, a predicted crack front (*solid line*) is compared with a standard semi-ellipse (*dashed line, actually only a quarter of the ellipse is considered due to the symmetry*), whose major and minor axes are, respectively, taken as the surface half-length, c, and the depth, a, of the predicted crack shape.

The ellipse can be analytically described as follows in the polar co-ordinate system.

$$r^2\left(a^2 \sin^2 \theta + c^2 \cos^2 \theta\right) = a^2 c^2 \tag{4.2}$$

where,

$$r = \sqrt{x^2 + y^2}, \qquad \theta = \tan^{-1}(x/y)$$

The relative residual, E_i, at the ith corner node of the predicted crack front is defined as

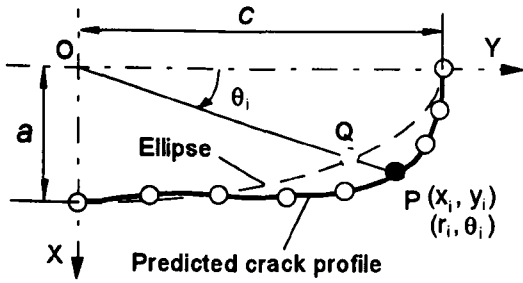$$E_i = \frac{\overline{OP} - \overline{OQ}}{\overline{OQ}} \tag{4.3}$$

Figure 4.9   Comparison of a numerically predicted crack shape with a semi-ellipse

Using Eq. (4.2), the following expression can be obtained

$$E_i = \frac{r_i\sqrt{c^2 \sin^2 \theta_i + a^2 \cos^2 \theta_i}}{a \cdot c} - 1 \qquad (4.4)$$

where r_i and θ_i are the polar co-ordinates of the ith point P along the crack front. The definition of E_i represents a relative deviation of the point P from the semi-ellipse.

In order to estimate the total relative error of the predicted crack front from the semi-ellipse, the relative standard deviation is defined to be:

$$S_r = \sqrt{\frac{1}{n}\sum_{i=1}^{n}(E_i)^2} \qquad (4.5)$$

Substituting Eq. (4.4) into the above definition leads to

$$S_r = \sqrt{\frac{1}{n}\sum_{i=1}^{n}\left(\frac{r_i\sqrt{c^2 \sin^2 \theta_i + a^2 \cos^2 \theta_i}}{a \cdot c} - 1\right)^2} \qquad (4.6)$$

where n is the number of the corner nodes used to constitute the crack front in FE models, as shown in Fig. 4.9. Obviously, the smaller S_r value means the better approximation to the semi-ellipse. In the following practical calculations of E_i and S_r, taking the surface half-length and depth of the predicted crack shape as the c and a of the ellipse means that the comparison is always performed between the predicted crack shape and the semi-ellipse with the same surface and depth points as the predicted crack shape.

Fig. 4.10 shows the distributions of the relative residual, E_i, around several representative fatigue crack fronts displayed on the same plot for the particular initial crack, $a_o/c_o = 0.6$ (T6), under all three fatigue loads, DOB = 0, 0.5 and 1. It can be seen that for pure tension fatigue, the E_i value is always negative and the maximum magnitude of its values increases as the crack propagates, which demonstrates that the predicted profiles are always on the inside of the semi-ellipses, as shown in Fig. 4.10(a), and such a relative deviation to the inside gradually increases. The crack under pure bending fatigue at the early stage of crack growth is on the
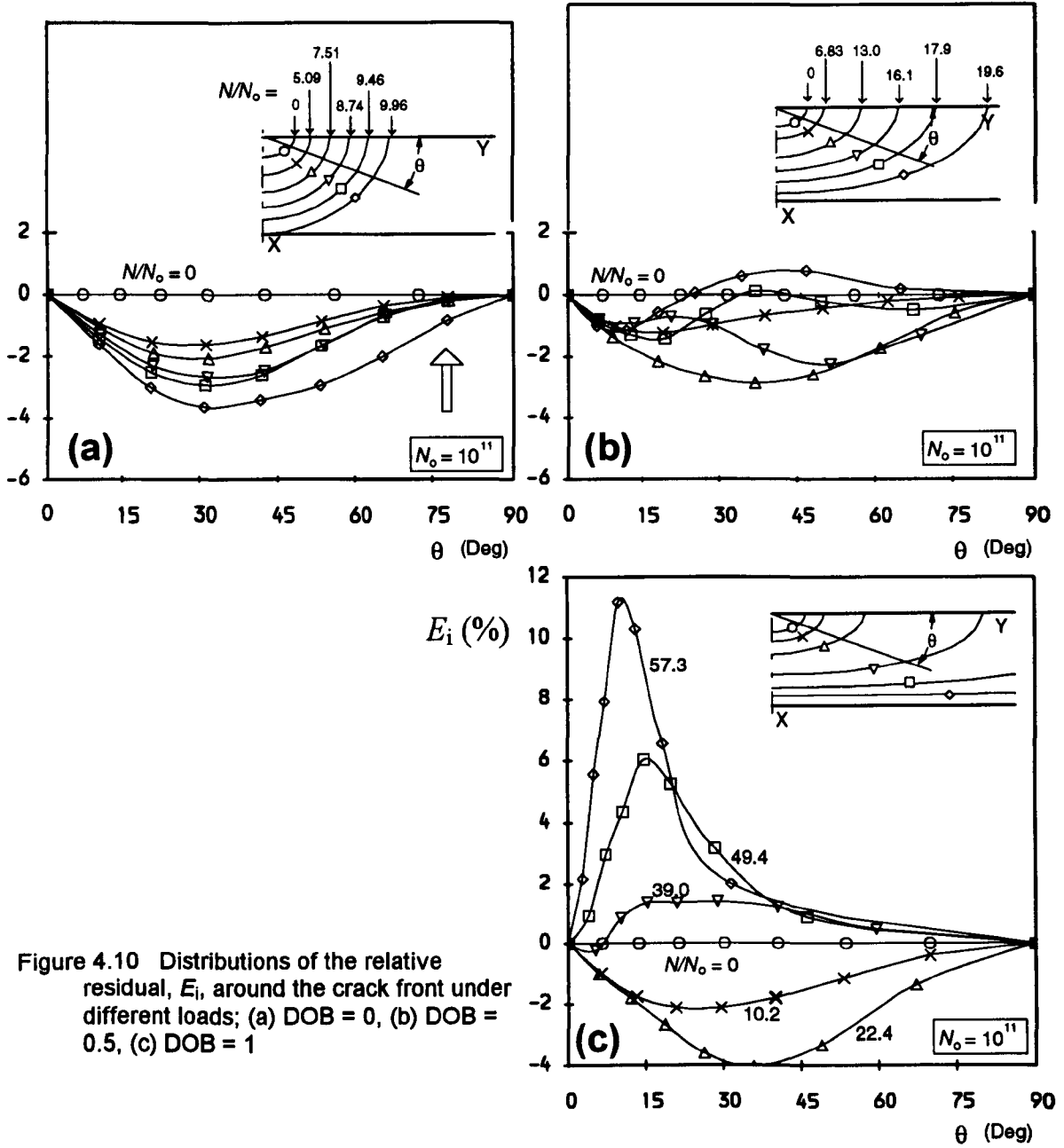
Figure 4.10 Distributions of the relative residual, E_i, around the crack front under different loads; (a) DOB = 0, (b) DOB = 0.5, (c) DOB = 1

inside of the semi-ellipse, but as the crack grows it gradually transfers from the inside to the outside of the semi-ellipse, as shown in Fig. 4.10(c). The subsequent outward relative deviation becomes larger and larger as the crack propagates to a nearly straight front, the maximum E_i even reaches 12%, which occurs at $\theta \approx 15°$. Fig. 4.10(b) shows several variations of the relative residual due to the combined fatigue loading, DOB = 0.5, where the final shape (*the largest crack shown in Fig. 4.10(b)*), a part of which is on the inside and the other outside

of the semi-ellipse, seems to be the closest to the semi-ellipse, because the relative residual curve is between about -1% and 1%.

Fig. 4.11 shows the distributions of the relative residual, E_i, around the six different crack fronts that correspond to six different initial defects marked in the plot. These six crack profiles are selected from those at the later stage of crack growth for each crack, and have approximately equal surface half-length, c, and depth, a. It can be found that the E_i distributions along these crack fronts are very similar for the same type of loading. Particularly, for the pure bending case, an excellent agreement is reached between all analysed cracks, although their shapes are evolved into from different initial cracks. Such similar distributions of the relative residual, E_i, attained at the later growth stage of these analysed cracks makes it believed that the crack growth does follow a preferred

Figure 4.11 Distributions of the relative residual, E_i, around six different crack fronts, each of which is grown from six initial cracks of different aspect ratio; (a) DOB = 0, (b) DOB = 0.5, (c) DOB = 1

propagation pattern whose shape, despite not being an exact semi-ellipse, seems to have relatively stable deviation from the semi-ellipse for a given crack size. The degree of deviation basically varies with the crack development. What relatively stable profile can be adopted depends mainly upon the applied fatigue load, which has been reflected by quite different distributions of the relative residual for three loads.

The variations of the relative standard deviation, S_r, with crack growth for all three fatigue loads are shown in Fig. 4.12. Similarly, six different initial defects are analysed for each load.
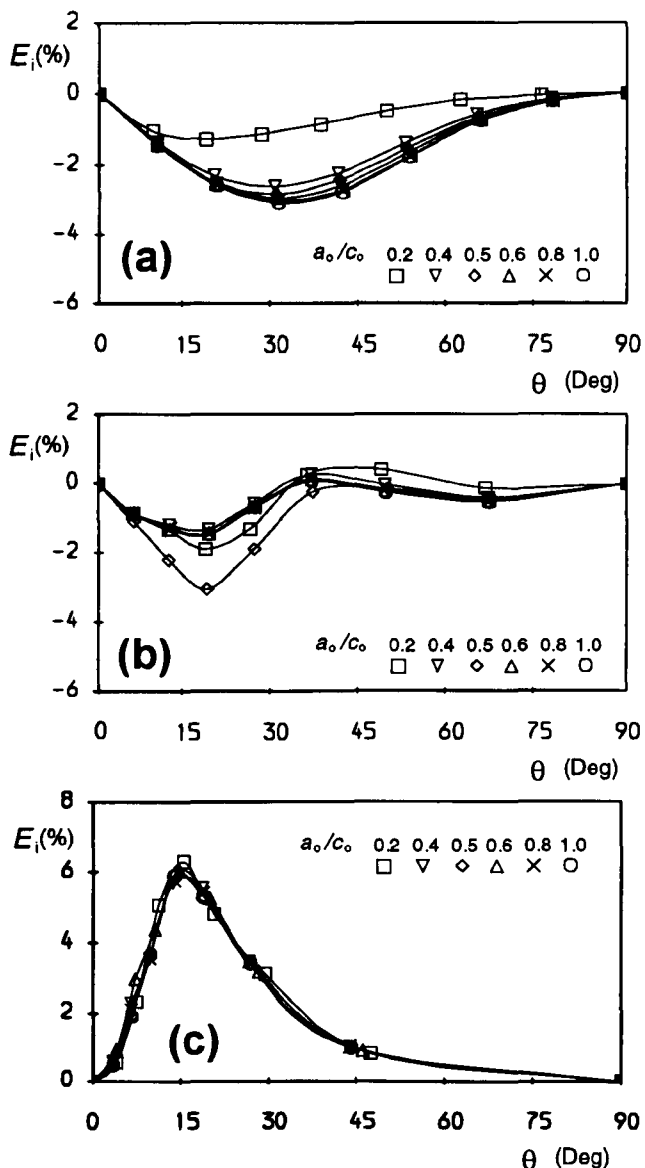
Figure 4.12 Variations of the relative standard deviation, S_r, with crack growth for different fatigue loads; (a) DOB = 0, (b) DOB = 0.5, (c) DOB = 1

It is surprised that for each fatigue loading there is a good convergence of the relative standard deviation. Particularly, the much more intense convergence for the pure bending than for the other two loads can be seen in Fig. 4.12. The convergence of the relative standard deviation strongly implies again that the crack growth always attempts to follow a preferred propagation pattern. Another important finding in Fig. 4.12 is that all values of the relative standard deviation, S_r, during the whole crack growth process for both DOB = 0 and 0.5 cases are very small, below 3%. This greatly enhances the confidence in the use of the semi-elliptical crack shape approximation for the prediction of fatigue crack growth under the two loads. However, this semi-ellipse assumption must be used carefully for pure bending crack, because of the result that the relative standard deviation increases continuously and rapidly after the depth ratio of the crack, a/t, attains about 0.75 ($S_r > 3\%$). Such a tendency of increasing crack shape deviation from the semi-ellipse probably is an intrinsic characteristic for crack fatigue growth, not just the error caused by the present numerical analysis, although the numerical error usually is unavoidable. Further investigations are needed to clarify this point.

The above analyses show that the initially semi-elliptical surface crack, basically, can maintain an approximate semi-ellipse during the whole crack growth process for both pure tension and DOB = 0.5 loads, but for pure bending, the crack shape deviates greatly from the semi-ellipse when the crack becomes larger.

4.4 Aspect Ratio Changes

That the aspect ratio, *a/c*, variation against the depth ratio, *a/t*, has been used to describe the shape change of surface cracks in plates during the fatigue process is because of its validity, if the propagating cracks are assumed to be semi-elliptical. In this section the variation of the aspect ratio is still used to reflect the crack shape change, in spite of the existence of crack shape deviations from exact semi-ellipses, as mentioned above.

4.4.1 Effect of the maximum crack growth increment

As indicated in Chapter 2, it is necessary to select a proper crack growth increment for the fatigue growth problem being modelled, in order to achieve good calculation accuracy. Fig. 4.13 shows a comparison of aspect ratio variations predicted using three different maximum crack growth increments, $\Delta a_{max} = t/50$, $t/100$, and $t/167$, for a particular initial surface crack configuration ($a_o/c_o = 0.6$, $a_o/t = 0.2$) under pure tension. The difference among the three predictions is extremely difficult to be identified in the plot, which demonstrates the values of the maximum crack growth increment employed in this chapter, as shown in Table 4.1, are basically small enough to ensure an accurate numerical prediction of aspect ratio changes for all analysed cracks.

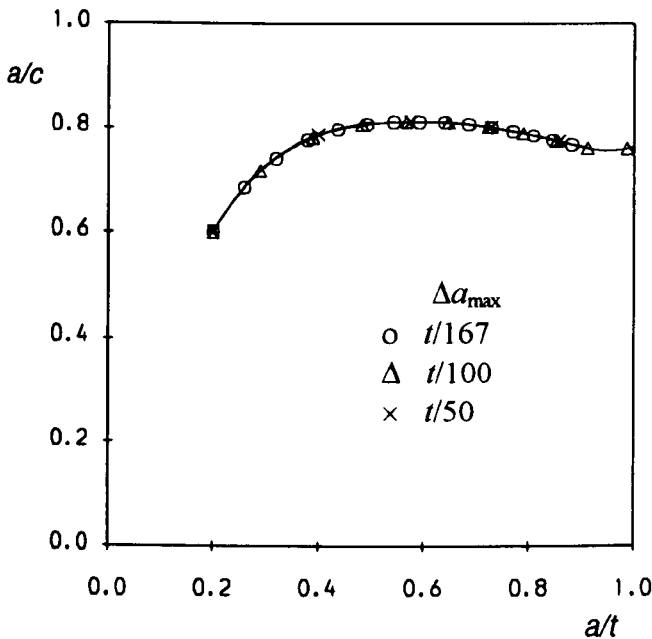

Figure 4.13   Convergence of aspect ratio changes for an initially semi-elliptical surface crack under tension (three cracks are: T6-Δ15, T6, and T6- Δ50)

4.4.2 Aspect ratio variations and comparisons with Newman and Raju's ($C_c = C_a$)

Fig. 4.14 presents the aspect ratio variation of pure tension fatigued surface defects. Clearly, all defects are seen to propagate towards an asymptotic leakage aspect ratio (*the ratio when the crack reaches the back surface of the plate*), but their actual leakage aspect ratios depend on both their initial aspect ratios and initial relative crack depths. Usually, the slender crack, like the initial crack, $a_o/c_o = 0.2$, reaches a less leakage aspect ratio due to the limited plate thickness. A slight increase of the aspect ratio can be seen in Fig. 4.14 as the crack approaches very closely the back surface of the plate, which is mainly caused by the larger stress intensity factor at the depth point than that at the surface point due to the effect of the plate back surface. In order to compare the present predictions with those made by the Newman and Raju 'two-point plus semi-ellipse' method, the following analytical solution has also been derived by the present author, following the same procedure as Wu's (1985) and using the coefficient relation $C_c = C_a$ and the Paris exponent $n = 3$:
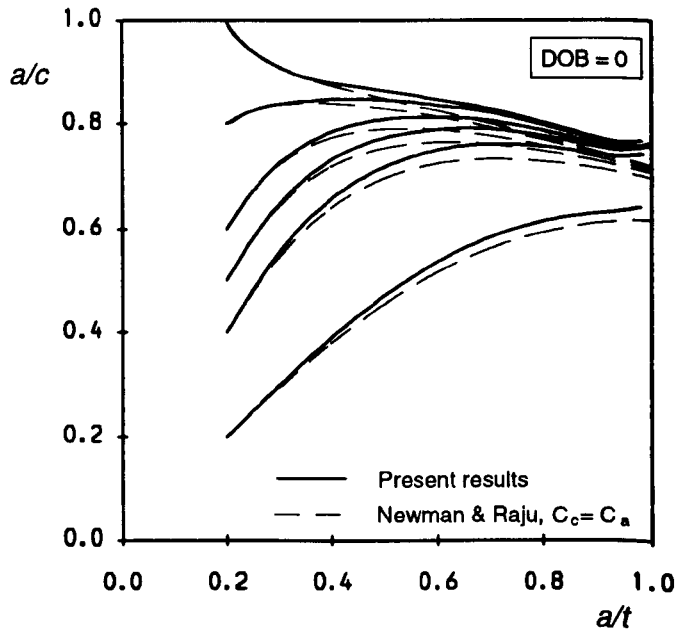

Figure 4.14   Variation of defect aspect ratios with depth growth for DOB = 0 (tension)
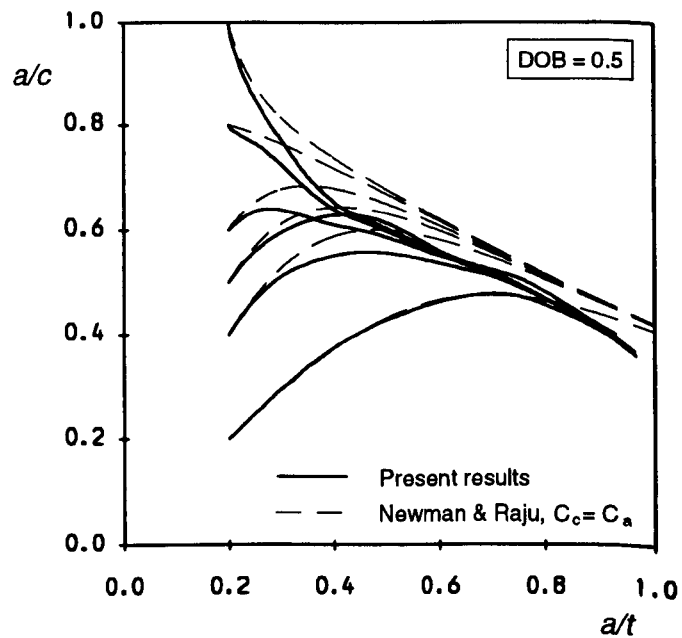
Figure 4.15   Variation of defect aspect ratios with depth growth for DOB = 0.5

$$\frac{a}{c} = \left\{ g\left(\frac{a}{t}\right) - \left(\frac{a_o}{a}\right)^{2.5} \left[g\left(\frac{a_o}{t}\right) - \left(\frac{a_o}{c_o}\right)^{-2.5} \right] \right\}^{-0.4}$$

(4.7)

where: $\quad g(u) = 1.331 + 0.706u^2 + 0.155u^4 + 0.013u^6$

The predictions from the above equations are also included in Fig. 4.14. Apparently, the difference is not large between the present predictions and those from Newman and Raju's method using the relation of $C_c = C_a$, and the present predictions are slightly larger than the 'two-point plus semi-ellipse' results for a given depth ratio, a/t. The slightly rising trend when the a/t approaches unity cannot be found among the aspect ratio curves predicted by the 'two-point plus semi-ellipse' method, which is probably because there is a larger error of stress intensity factors estimated by Newman and Raju's (1981) SIF equation for the approximate through-thickness cracks, $a/t \approx 1$. A further SIF comparison during the crack propagation process will be presented later.

Figure 4.16 Variation of defect aspect ratios with depth growth for DOB = 1 (bending)

The aspect ratio variations for DOB = 0.5 and DOB = 1 are shown in Fig. 4.15 and Fig. 4.16, respectively. It can be seen that the larger the DOB value, the more intense the asymptotic tendency is towards their own preferred propagation pattern. The aspect ratio curves for different initial defects almost converge to one curve at about a/t = 0.65 for pure bending fatigue. Fig. 4.15 and Fig. 4.16 also include Newman and Raju's $C_c = C_a$ predictions obtained by the Euler numerical integration method due to the unavailability of their analytical expressions. The relatively larger discrepancy than that for DOB = 0 between the present predictions and the Newman and Raju's results can be observed for both DOB = 0.5 and 1.0, the largest almost reaches around 20% for a given depth ratio. The degree and trend of the

discrepancy vary with the crack development, but, a common characteristic for both DOB = 0.5 and 1 is that the present predictions are generally lower than those obtained by the Newman and Raju's $C_c = C_a$ method. Such a difference is believed to be mainly caused by removing the semi-elliptical shape assumption during the whole fatigue growth process in the present simulation technique.

4.4.3 Effect of the Paris exponent *n*

As can be seen from the aspect ratio expressions derived by Wu (1985) on the basis of the Newman and Raju's SIF equation, the Paris exponent *n* affects aspect ratio variations. An investigation of such effects has also been performed in this chapter by selecting three different exponents, *n* = 2, 3 and 4, in modelling a particular initially semi-circular surface defect (T10-*n*2, T10 and T10-*n*4; where a_o/c_o = 1, a_o/t = 0.2) subjected to both tension and bending. The results are shown in Fig. 4.17, which indicate that the effect of the Paris exponent *n* on aspect ratio changes is apparent and a larger *n* always makes the aspect ratio change more intense. This can be easily explained by the exponential nature of the *n*. The degree of the effect also varies with different initial cracks under different fatigue loads. However, it must also be indicated that the investigation of effect of the exponent *n* is theoretical, due to its idealised basis of modelling crack fatigue growth, i.e. assuming the same Paris law along the crack front. Generally, during the actual crack growth, the resistance to fatigue crack growth might be influenced by many factors, such as the material non-homogeneity and the stress state adjacent to the crack tip. The different resistance along the crack depth and surface directions was usually reported by many experimental investigators in two different Paris laws. However,
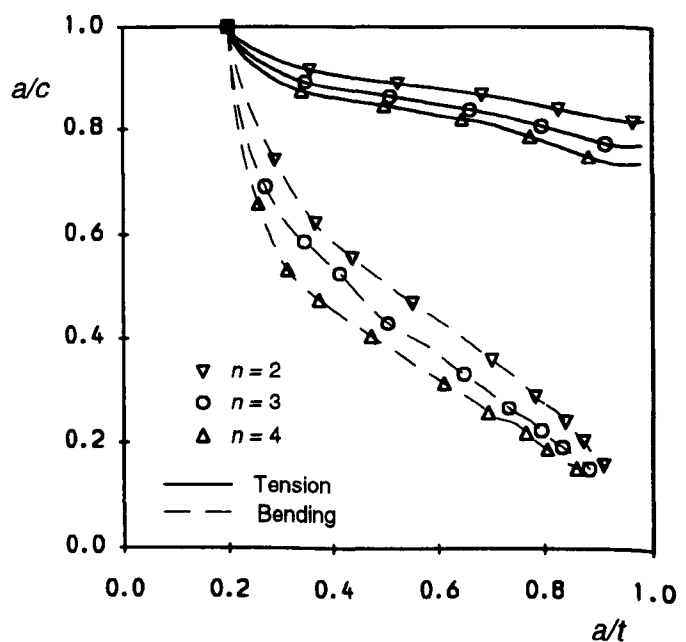
Figure 4.17 Effect of Paris exponent, *n*, on aspect ratio change for both tension and bending

almost all these reported different Paris laws along the crack depth and surface directions were obtained by using Newman Raju's SIF equation to correlate their experimental results to stress intensity factors.   This naturally introduces the semi-elliptical shape assumption and consequently might lead to a suspicion against the reported Paris laws, but the fact that the practical resistance variation around the crack front does exist should be admitted. Compared with the aspect ratio equations proposed by Portch (1979) or Iida (1983), which were directly obtained from experimental observations for many different materials and obviously was unable to consider the effect of the exponent *n* on aspect ratio changes, the present simulation technique and Newman and Raju's method can provide a more accurate and further theoretical consideration for different materials.

4.4.4 Consideration of the free surface layer

The free surface correction, as described in Chapter 2, which considers the surface point to be in the plane stress state while the other positions along the crack front still to be in the plane strain state, was applied to the fatigue growth simulation of the initially semi-elliptical surface cracks subjected to pure tension (T2-C, T4-C, T5-C, T6-C, T8-C and T10-C).   Fig. 4.18 shows the aspect ratio changes obtained by the present simulation technique with the free surface correction. The results obtained by the present simulation technique without the free surface correction (T2, T4, T5, T6, T8 and T10) are also shown in Fig. 4.18 for comparison. Obviously, the present technique that takes the free surface correction into account predicts a slightly higher value of the aspect ratio for a given depth ratio than does the present technique without considering the free surface

Figure 4.18   Aspect ratio variations predicted by the present simulation technique, both with and without the free surface correction

correction. The difference is less than 3 ~ 5% for all analysed initial crack profiles. Newman and Raju's prediction of aspect ratios was also made using the relation, $C_c = 0.9^n C_a$, which is shown in Fig. 4.19 together with the present prediction with the free surface correction. The disagreement is generally greater than that shown in Fig. 4.14, where the prediction from the present FE technique without using the free surface correction is compared with the Newman and Raju's $C_c = C_a$ result. This might be caused by both different deviations of the predicted crack

Figure 4.19 Comparison of aspect ration variations predicted by the present simulation technique with the free surface correction to those from the Newman & Raju's method, $C_c = 0.9^n C_a$

profiles during the fatigue process from the semi-ellipses, since, from a theoretical point of view, it appears to be simplistic to use the same semi-ellipse assumption for the two different relations, $C_c = C_a$ and $C_c = 0.9^n C_a$. If Fig. 4.14 and Fig. 4.19 are put together, it can also be seen that the difference betwe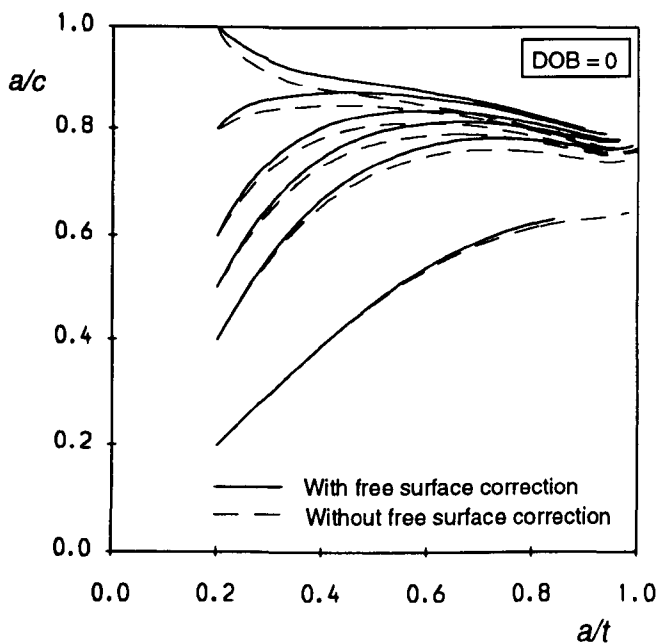en aspect ratio variations predicted by the present simulation techniques both with and without the free surface correction is not so as great as that of the predictions obtained by the Newman and Raju's method using both $C_c = C_a$ and $C_c = 0.9^n C_a$. The free surface correction was not used for the cracks under both DOB = 0.5 and 1.

4.4.5 Comparison with experimental data

A variety of experimental data associated with aspect ratio changes have been obtained for surface cracks subjected to tension or bending load, as shown in Fig. 4.3. Summarising these experimental results can lead to that although there is a certain scattered observation of aspect ratio changes caused by some differences in experiments, such as stress ratio, loading frequency, mean stress and growth rate exponent, n, etc., the trend of crack shape changes
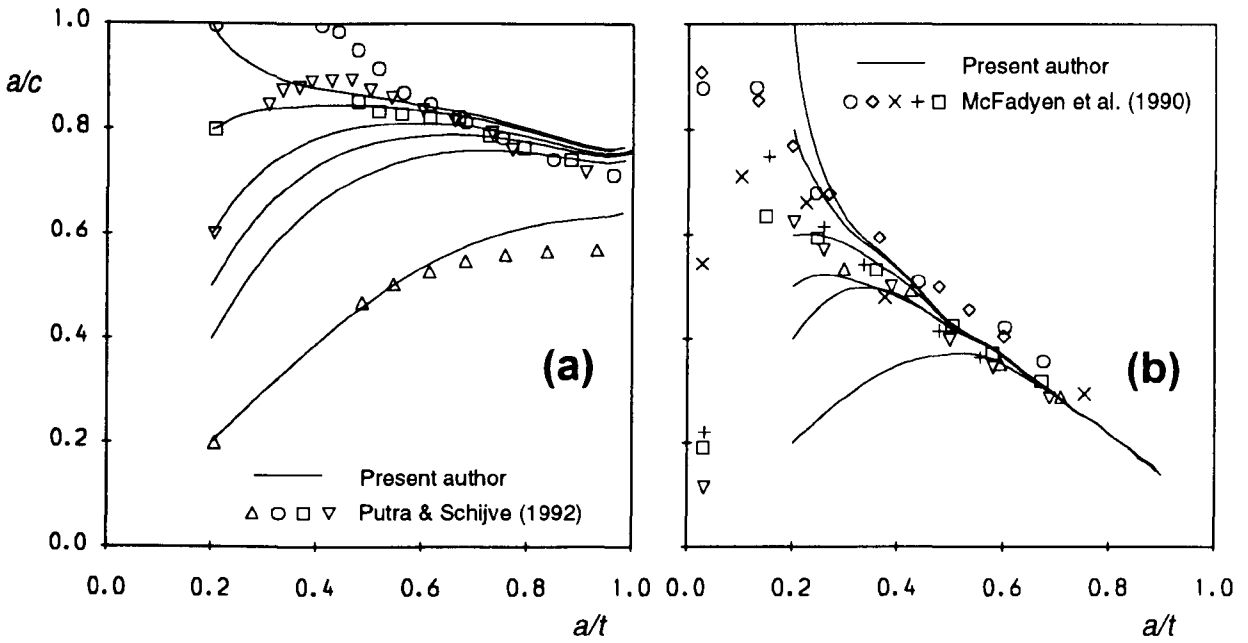
Figure 4.20   Comparison of aspect ratio changes predicted by the present
technique with experimental data; (a) tension, (b) bending

towards a preferred propagation path is obvious and depends principally on initial crack aspect
and depth ratios, and loading conditions.

Due to the unavailability of the experimental results corresponding to the present
modelling computations, Fig. 4.20(a) only compares the present predictions (T2, T4, T5, T6,
T8 and T10) of aspect ratio changes for pure tension with recently published results of Putra
and Schijve (1992). Putra and Schijve tested a 7075-T6 aluminium alloy plate containing
initially semi-elliptical notches introduced by electro-spark erosion machining for the
investigation of fatigue crack growth until 'breakthrough'. It was found that the crack shape
marked on the fracture surface by the beachmark method was very close to a semi-ellipse
except near the front surface, where there was a clear retardation of crack growth. The aspect
ratio variations against the depth ratio were presented by Putra and Schijve using the least
square method to fit semi-ellipses to the measured crack fronts. The Paris exponent, n, for the
material, obtained from the crack growth rate of through cracks, was 2.88, so close to the
value of $n = 3$ used in the present computations. It can be seen that there is a quite large
difference between the present results and Putra and Schijve's experimental data at the early
stage of crack growth, particularly for the initial cracks of $a_o/c_o = 0.6$ and 1.0. One possible
reason is that the initial crack profile formed by the electro-spark erosion machine hardly is a

precise semi-ellipse. Actually, a great deviation of the initial front of $a_0/c_0 = 0.6$ from an ellipse can be seen in the presented shape figure of actual crack profiles. As the crack grows, the agreement between the present predictions and the experimental results obviously becomes good, and the aspect ratio, a/c, of both the numerical and experimental results gradually converges to the preferred propagation path, finally reaches $0.7 \sim 0.8$.

Fig. 4.20(b) shows a comparison of aspect ratio variations (B2, B4, B5, B6, B8 and B10) under pure bending fatigue predicted by the present simulation technique with the experimental observations by McFadyen *et al.* (1990). In McFadyen *et al.*'s experimental tests, the initial cracks of different aspect ratio were introduced using a slitting saw or a spark discharge machine, and four-point bending was applied to the specimens. The shape and depth of the growing fatigue cracks were monitored by the AC potential drop technique and beach marking (*five to six beach marks were produced on each specimen*). Fig. 4.20(b) shows that due to the different initial crack sizes used in the present calculations and in the experiments of McFadyen *et al.*, the disagreement of aspect ratio changes is definite at the early stage of crack growth. But as these cracks grow, their aspect ratio variations against depth ratio for both the numerical and experimental results quickly (*after $a/t > 0.3$*) converge and are in good agreement, although the experimental data are a little bit scattered.

Moreover, it should be indicated that it usually is difficult to achieve an excellent agreement between theoretical or numerical predictions and experimental results, due to the intrinsic scatter of fatigue crack growth, as shown in Fig. 4.3 .

4.5 Estimates of Stress Intensity Factors

As indicated in Chapter 2, accurate predictions of crack shape changes and fatigue lives require accurate estimates of stress intensity factors around the crack front because of the exponential nature of the Paris crack growth law. In many cases large errors of stress intensity factors will lead to somewhat strange or unstable crack growth shape, and, in all cases, to large errors in estimates of crack propagation lives. In order to obtain more accurate SIF estimates, every FE meshes during the fatigue growth process that were automatically created by the DUCKPOST software have been assured of being less distorted.

4.5.1 Effect of multi-point constraint plane on SIF

During practical modelling analyses, the created FE models consist of two blocks, cracked and uncracked blocks, as shown in Fig. 4.4. It is obvious that a mesh mismatch exists between the contact plane of the two blocks. Although the 'multi-point constraint' method, as described previously, has been used to reduce the effect of the mesh mismatch, it is still unavoidable to suspect the effectiveness of this method. To eliminate such a possible suspicion a verification has been made in Fig. 4.21, in which two SIF variations along the front
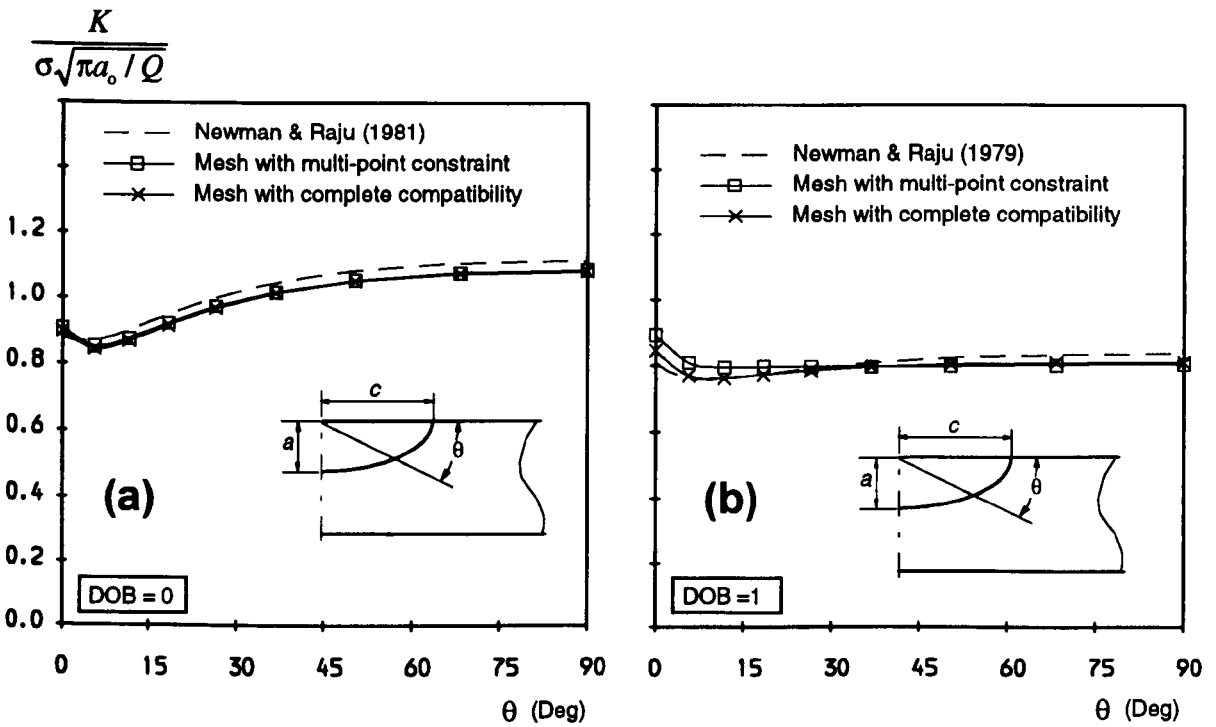
Figure 4.21   Comparison of stress intensity factors estimated from the present FE models with those from the Newman & Raju (1981) equation
$(a_o/t = 0.2, \; a_o/c_o = 0.5, \; Q = 1.466)$

of the crack $(a_o/t = 0.2, \; a_o/c_o = 0.5)$ are compared. One is the estimate from the FE model with a mesh mismatch, and the other from that with a completely compatible mesh which is particularly created from the same 2D crack plane mesh for the comparison. The SIF prediction from Newman and Raju's (1981) equation is also plotted in Fig. 4.21. Obviously, for the tension loading, as shown in Fig. 4.21(a), the SIF variations predicted from both kinds of FE models are coincident along the whole front. But, for the bending loading, as shown in Fig. 4.21(b), the agreement becomes slightly worse near the free surface, where the prediction from the compatible mesh is 4 ~ 5% lower than that from the mesh of mismatch. A good

agreement between both predictions and Newman and Raju's results can also be seen in **Fig.** 4.21(a) and (b). The above comparisons demonstrate that the two-block FE models employed in the present modelling analyses of surface crack problems can produce a quite good **SIF** accuracy. Generally, the 'multi-point constraint' method is quite acceptable as long as **the** contact plane is far enough from the crack plane.

4.5.2 SIF for initially semi-elliptical cracks

In order to further demonstrate the SIF accuracy achieved by the present technique (*using two-block FE models if not mentioned in this chapter*), an overall comparison with **the** estimates from Newman and Raju's (1981) equation for the initially semi-elliptical surface defects is listed in Table 4.2, in which both tension and bending cases are included, and **the** position around the crack front is represented by both parameteric angles, ϕ and θ, as shown **in** Fig. 4.1. It can be seen that all errors of the dimensionless stress intensity factor, calculated by $(F_P - F_{NR})/F_P$, along the front of all cracks are below 5.1% for tension, but relatively larger **for** bending, the maximum value being 12.6% which occurs at the symbolised position ($\blacklozenge$). **The** comparison indicates that the accuracy of the present FE analyses at least stands at the same order as that of the Newman Raju's equation, since Newman and Raju quoted their equation **as** being within 90% of accuracy. It is also worth indicating that there is an excellent agreement between the SIF estimates obtained by both the *J*–integral (*energy release rate*) and 1/4-point displacement methods for all initially semi-elliptical surface defects, which also verifies **their** accuracy.

4.5.3 SIF distributions along propagating crack fronts

As is known, during the fatigue growth process the stress intensity factors along the crack front usually change, which directly leads to the crack shape change if the fatigue growth resistance along all directions is assumed to be identical. Fig. 4.22 shows the SIF distributions along the initial, two intermediate and final (*near the back surface of the plate*) crack configurations under tension. The number of fatigue cycles, N/N_o, corresponding to each configuration, is also denoted in the plots. It is clear that the SIF distribution always changes, but appears to tend towards a similar distribution for all six different initial cracks

Table 4.2 Comparison of SIF along the initial crack fronts under both tension and bending

a_o/c_o (a_o/t=0.2)	ϕ (θ) (°)	$F = K/\left(\sigma\sqrt{\pi a_o}\right)$ Tension Present author (P)	Newman & Raju (1981)	Error %	Bending Present author (P)	Newman & Raju (1981)	Error %
0.2	0.00 (0.00)	0.560	0.559	0.2	0.591	0.519	12.2
	11.25 (2.28)	0.607	0.634	-4.4	0.621	0.543	12.6♦
	22.50 (4.74)	0.728	0.764	-4.9	0.710	0.632	11.0
	33.75 (7.61)	0.839	0.874	-4.2	0.769	0.705	8.3
	45.00 (11.31)	0.929	0.963	-3.7	0.799	0.760	4.9
	56.25 (16.66)	1.005	1.032	-2.7	0.819	0.802	2.1
	67.50 (25.77)	1.060	1.082	-2.1	0.840	0.832	1.0
	78.75 (45.16)	1.090	1.112	-2.0	0.866	0.850	1.8
	90.00 (90.00)	1.103	1.123	-1.8	0.886	0.856	1.2
0.4	0.00 (0.00)	0.715	0.693	3.1	0.688	0.640	7.0
	11.25 (4.55)	0.678	0.699	-3.1	0.629	0.609	3.2
	22.50 (9.41)	0.720	0.749	-4.0	0.638	0.627	1.7
	33.75 (14.96)	0.780	0.809	-3.7	0.656	0.656	0.0
	45.00 (21.80)	0.838	0.867	-3.5	0.667	0.684	-2.5
	56.25 (30.91)	0.887	0.915	-3.2	0.674	0.708	-5.0
	67.50 (44.00)	0.920	0.952	-3.5	0.683	0.725	-6.1
	78.75 (63.56)	0.950	0.976	-2.7	0.695	0.736	-5.9
	90.00 (90.00)	0.958	0.984	-2.7	0.701	0.740	-5.6
0.5	0.00 (0.00)	0.749	0.725	3.2	0.737	0.667	9.5
	11.25 (5.68)	0.703	0.718	-2.1	0.667	0.628	5.8
	22.50 (11.70)	0.722	0.743	-2.9	0.656	0.626	4.6
	33.75 (18.47)	0.762	0.783	-2.8	0.657	0.638	2.9
	45.00 (26.56)	0.804	0.826	-2.7	0.658	0.653	0.8
	56.25 (36.81)	0.842	0.864	-2.6	0.658	0.667	-1.4
	67.50 (50.36)	0.871	0.894	-2.8	0.658	0.678	-3.0
	78.75 (68.31)	0.890	0.913	-2.6	0.660	0.685	-3.8
	90.00 (90.00)	0.896	0.920	-2.7	0.662	0.688	-3.9
0.6	0.00 (0.00)	0.771	0.742	3.8	0.716	0.682	4.7
	11.25 (6.81)	0.721	0.728	-1.0	0.651	0.640	1.7
	22.50 (13.96)	0.725	0.737	-1.7	0.630	0.624	1.0
	33.75 (21.85)	0.746	0.760	-1.9	0.619	0.620	-0.2
	45.00 (30.96)	0.772	0.789	-2.2	0.611	0.624	-2.1
	56.25 (41.92)	0.797	0.817	-2.5	0.604	0.630	-4.3
	67.50 (55.38)	0.818	0.840	-2.7	0.600	0.635	-5.8
	78.75 (71.66)	0.833	0.855	-2.6	0.598	0.639	-6.9
	90.00 (90.00)	0.839	0.860	-2.5	0.598	0.640	-7.0
0.8	0.00 (0.00)	0.767	0.753	1.8	0.714	0.688	3.6
	11.25 (9.04)	0.717	0.730	-1.8	0.643	0.646	-0.5
	22.50 (18.33)	0.700	0.719	-2.7	0.601	0.613	-2.0
	33.75 (28.13)	0.698	0.719	-3.0	0.572	0.591	-3.3
	45.00 (38.66)	0.704	0.726	-3.1	0.549	0.576	-4.9
	56.25 (50.13)	0.713	0.736	-3.2	0.532	0.567	-6.6
	67.50 (62.63)	0.724	0.746	-3.0	0.520	0.561	-7.9
	78.75 (76.03)	0.732	0.753	-2.9	0.513	0.558	-8.8
	90.00 (90.00)	0.736	0.755	-2.6	0.511	0.557	-9.0
1.0	0.00 (0.00)	0.709	0.744	-4.9	0.727	0.677	6.9
	11.25 (11.25)	0.682	0.717	-5.1	0.651	0.638	2.0
	22.50 (22.50)	0.668	0.697	-4.3	0.599	0.599	0.0
	33.75 (33.75)	0.660	0.683	-3.5	0.560	0.565	-0.9
	45.00 (45.00)	0.656	0.674	-2.7	0.527	0.537	-1.9
	56.25 (56.25)	0.655	0.670	-2.3	0.501	0.515	-2.8
	67.50 (67.50)	0.655	0.668	-2.0	0.482	0.500	-3.7
	78.75 (78.75)	0.655	0.668	-2.0	0.470	0.491	-4.5
	90.00 (90.00)	0.655	0.668	-2.0	0.466	0.488	-4.7

when they approach the back surface of the plate, which provides an understanding of why these different initial defects asymptotically converge to a similar shape, as displayed in Fig. 4.6. It is particularly worth indicating that when the crack is very close to the free back surface of plate, the SIF value at the depth point ($\theta = 90°$) rises more quickly than that elsewhere, leading to a more non-uniform SIF distribution along the crack front, due to the presence of the effect of the free surface. The SIF distributions for pure bending are shown in Fig. 4.23, from which quite different SIF distributions from those of pure tension can be observed. The SIF value at the surface point keeps increasing with crack development whilst the value at the depth point is nearly frozen and even drops, which results in a more and more non-uniform SIF distribution.

Fig. 4.24 represents, respectively, the variations of the ratio of the minimum to maximum stress intensity factor (K_{min}/K_{max}) along each crack front with the normalised crack depth a/t for different fatigue loads, DOB = 0, 0.5 and 1. These curves characterise effectively the change of SIF distributions during the fatigue growth process, as mentioned in Chapter 3. Absolutely speaking, unlike the embedded defects in infinite solids under remote uniform tension, for which, as mentioned before, the K_{min}/K_{max} variation tends towards unity (iso-K), it is impossible for a surface crack to reach and then maintain such an iso-K shape due to the effect of both front and back surfaces of the plate, or due to the bending component of the load if it appears. This can be found from Fig. 4.24, in which some of the curves almost reach unity (iso-K) and subsequently drop as the crack continues to advance. However, it can also be seen that some of the initial cracks, such as the initially semi-circular crack ($a_o/c_o = 1$, $a_o/t = 0.2$) under all three loads, are unable to reach their iso-K profiles. Therefore, whether to be able to come to an iso-K shape generally depends on not only the initial shape and size of the surface crack, but also the applied fatigue load. In Fig. 4.24 the non-uniformity of SIF along the crack front is clearly displayed. In addition to the effect of the free surface, the larger bending component of a fatigue load is the other contribution to the more severe non-uniformity (K_{min}/K_{max} *deviates significantly from unity*). The convergence of the ratio of the minimum to maximum stress intensity factor is also apparent for all the analysed initial defects except the more shallow defect ($a_o/c_o = 0.2$) under tension. This means the preferred propagation pattern does exist and the crack always tries to grow to the preferred profile.
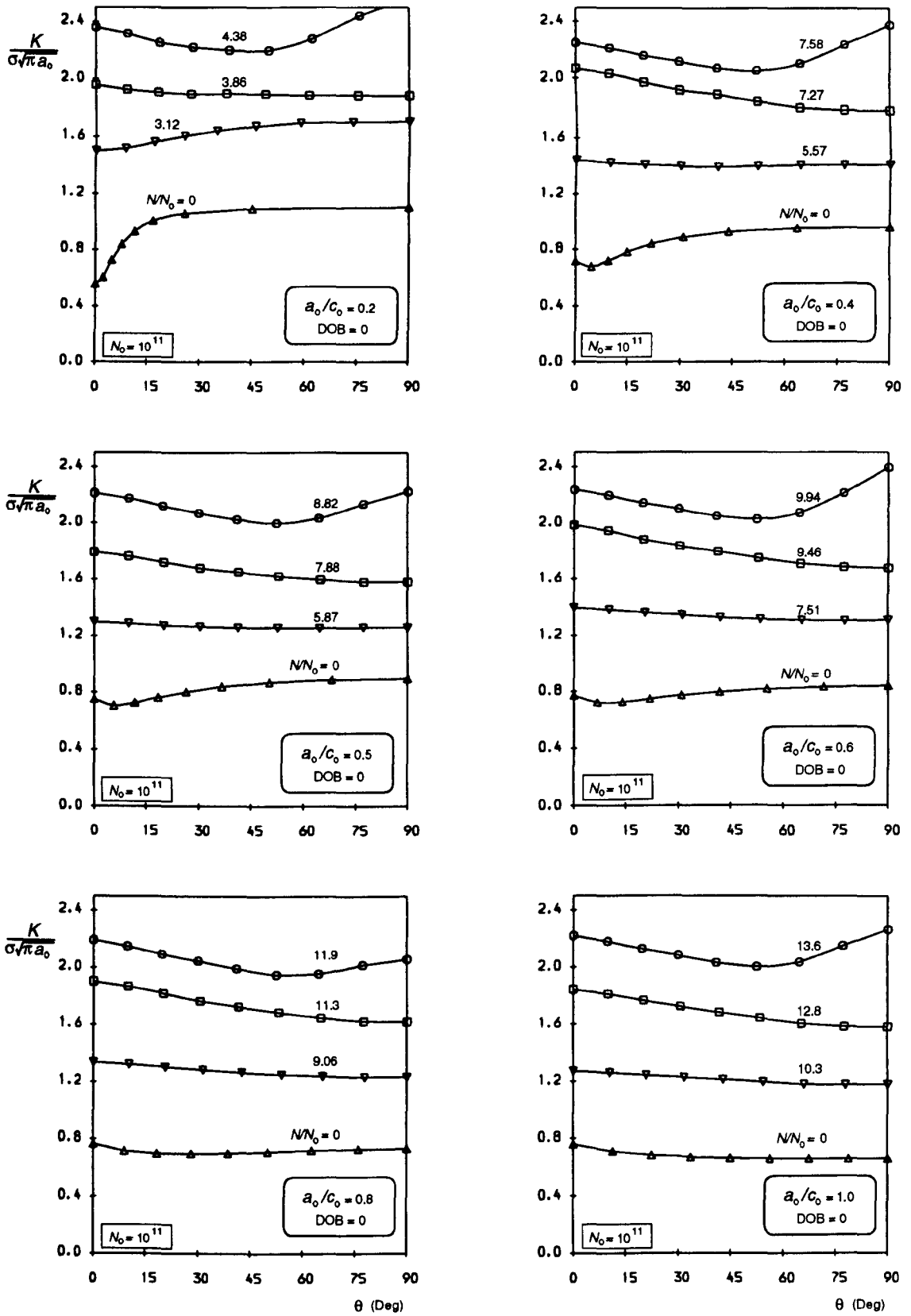
Figure 4.22   Distributions of stress intensity factors along the crack front for tension loading
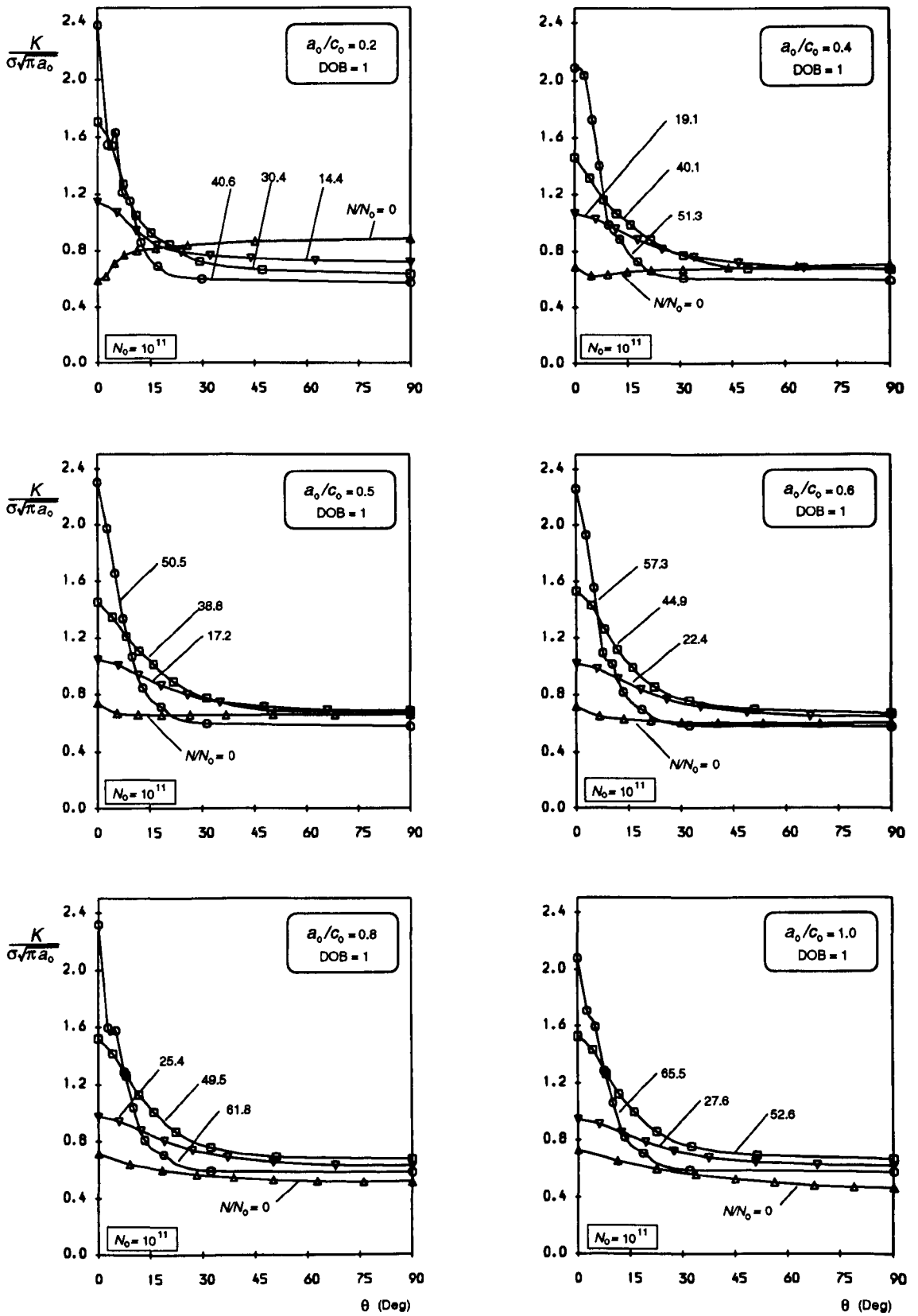
119

Figure 4.23   Distributions of stress intensity factors along the crack front for bending
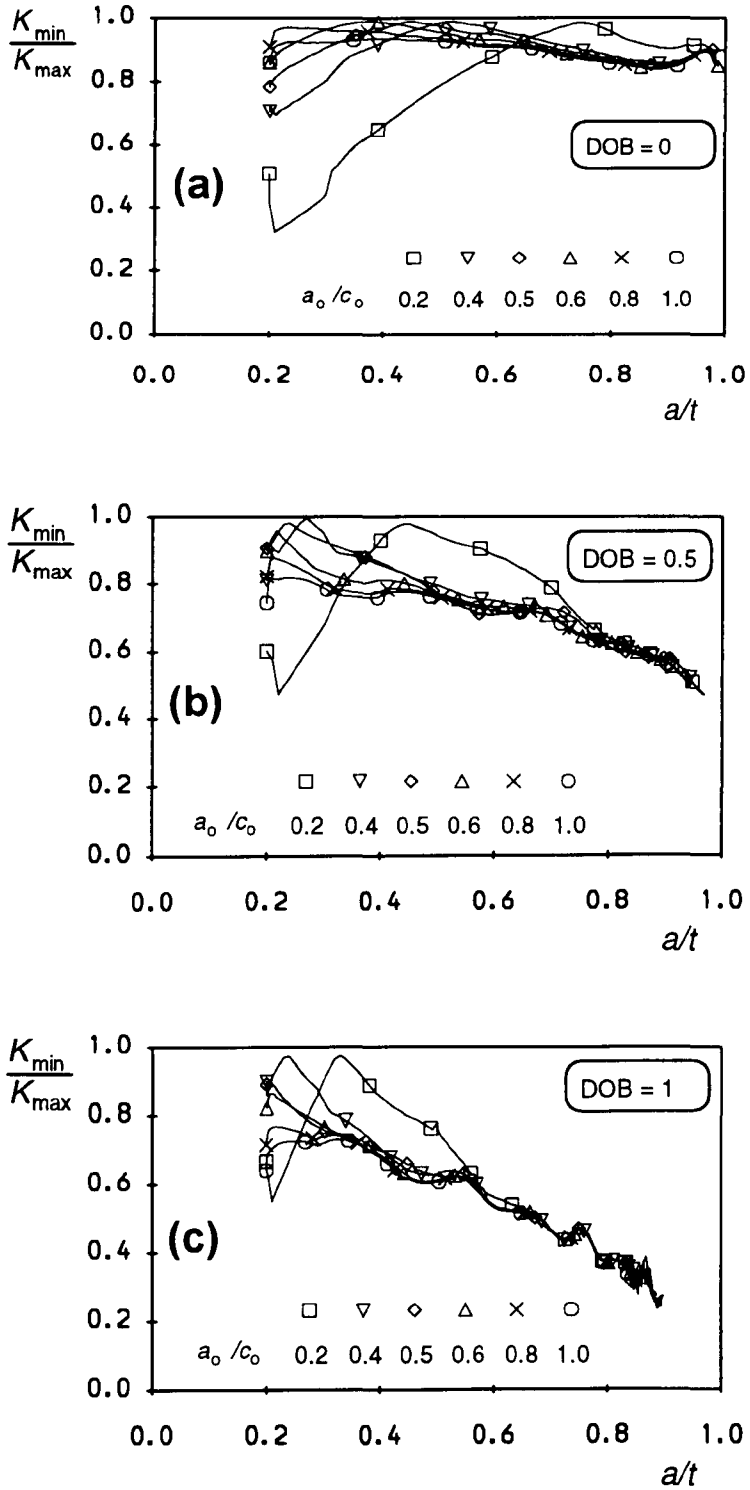
Figure 4.24 Change of K_{min}/K_{max} along the crack front
during crack development

4.5.4 SIF variations at crack surface and depth points during fatigue growth

Figs. 4.25, 4.26 and 4.27 display, respectively, the variation of stress intensity factors at both the crack surface and depth points during the fatigue growth process for all three loading cases, together with the predictions *(dashed lines)* made using Newman and Raju's 'two-point plus semi-ellipse' method with the relation $C_c = C_a$ for comparison. All six different initial defects are included for each loading. From Fig. 4.25 an important finding is that after the crack grows to about 90% of the plate thickness, the rise of the SIF value at the deepest point suddenly accelerates. As a result, its absolute SIF value approaches or even exceeds that at the surface point when the crack nearly reaches the back surface of the plate. Obviously, this is due to the influence of the plate back surface. However, such a phenomenon cannot be seen from the prediction by the Newman and Raju's method. If considering the crack profile to be nearly semi-elliptical (*S*ᵣ < 2%, *having been analysed previously*), a reasonable explanation is that Newman and Raju's SIF equation may have a relatively worse accuracy for the crack of $a/t > 0.9$. Overall, Newman and Raju's predictions are higher than the present results, which is particularly obvious when the crack becomes larger. Figs. 4.26 and 4.27 show that for both DOB = 0.5 and 1.0 there is a good agreement between the present and Newman and Raju's results at the early stage of crack growth, but the deviation from each other occurs as the crack grows close to the plate back surface. It is clearer than those displayed in Fig. 4.23 that the SIF value at the deepest point for bending almost keeps unchanged and even drops a little whilst the SIF value at the surface point increases significantly due to the bending load. This makes the crack propagate almost along the free surface whilst stopping in the direction of the plate thickness, leading to a nearly straight crack front, as shown in Fig. 4.7. It should also be indicated that some oscillations of the SIF variation can be particularly observed in Fig. 4.27, which is usually unavoidable for large changes in crack profile and size. The good convergence of the SIF variations for different initial defects can also be seen if these curves for each loading are put together. Moreover, one must be aware that the SIF variation with the fatigue growth presented above depends on the Paris exponent *n*. Different *n* values in the modelling process will lead to different variation curves.

By summarising the above SIF analyses and comparisons, it can be concluded that a quite good calculation accuracy has been achieved for the surface crack problem by the present FE simulation technique; and although the present results are widely in good agreement with

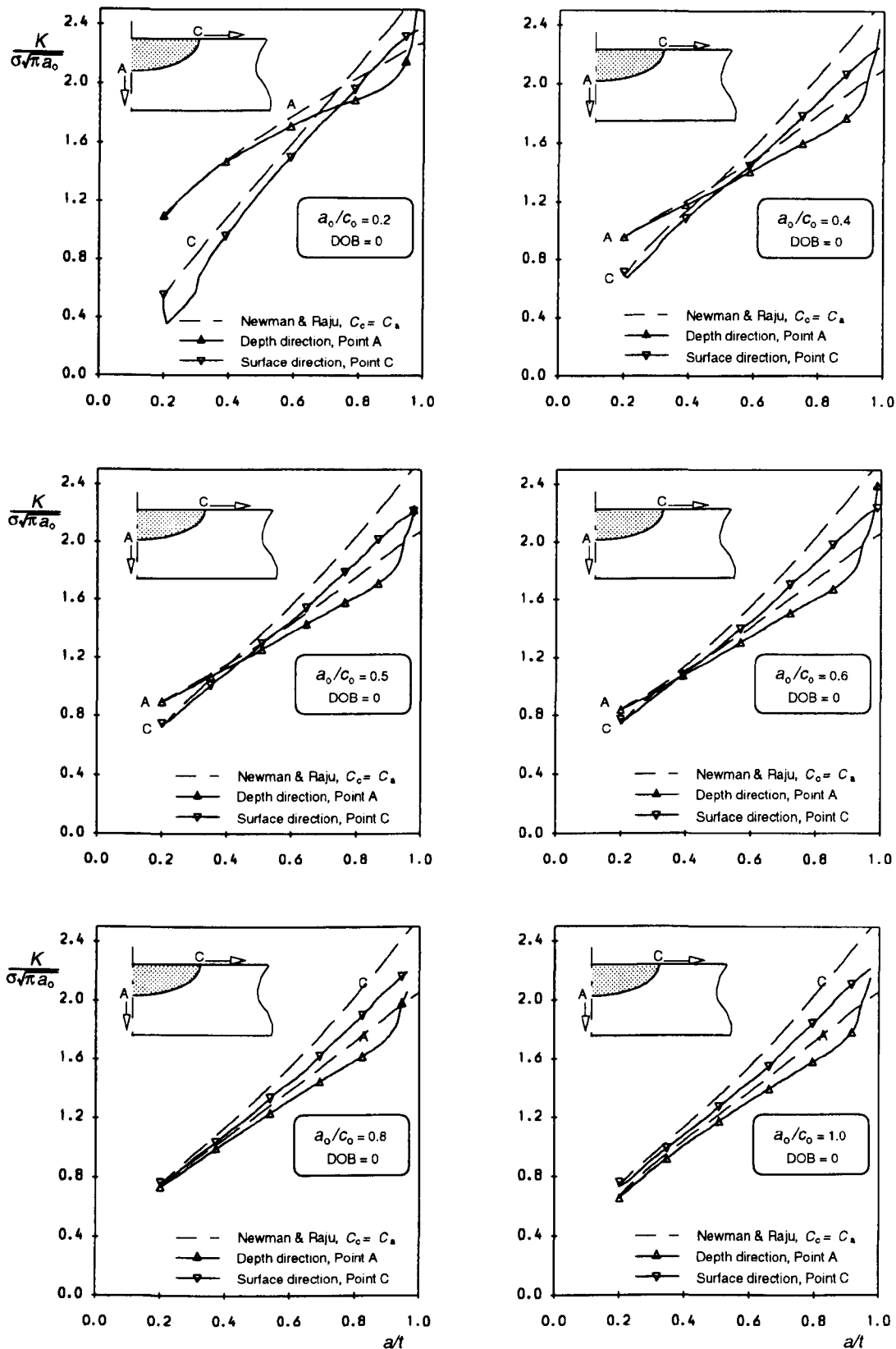Figure 4.25   Variations of stress intensity factors along both depth and surface directions during crack growth for DOB = 0 (tension)
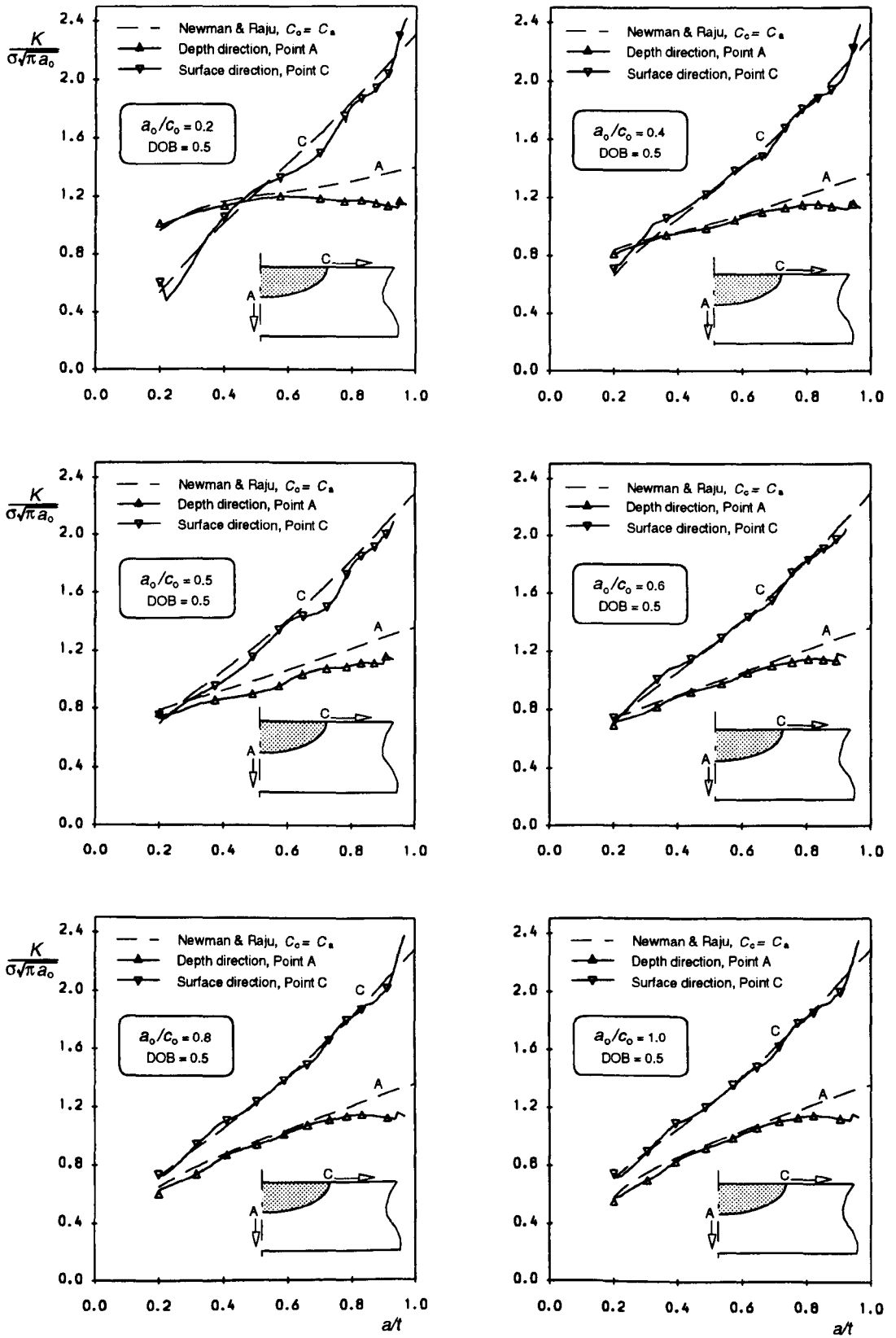
Figure 4.26   Variations of stress intensity factors along both depth and
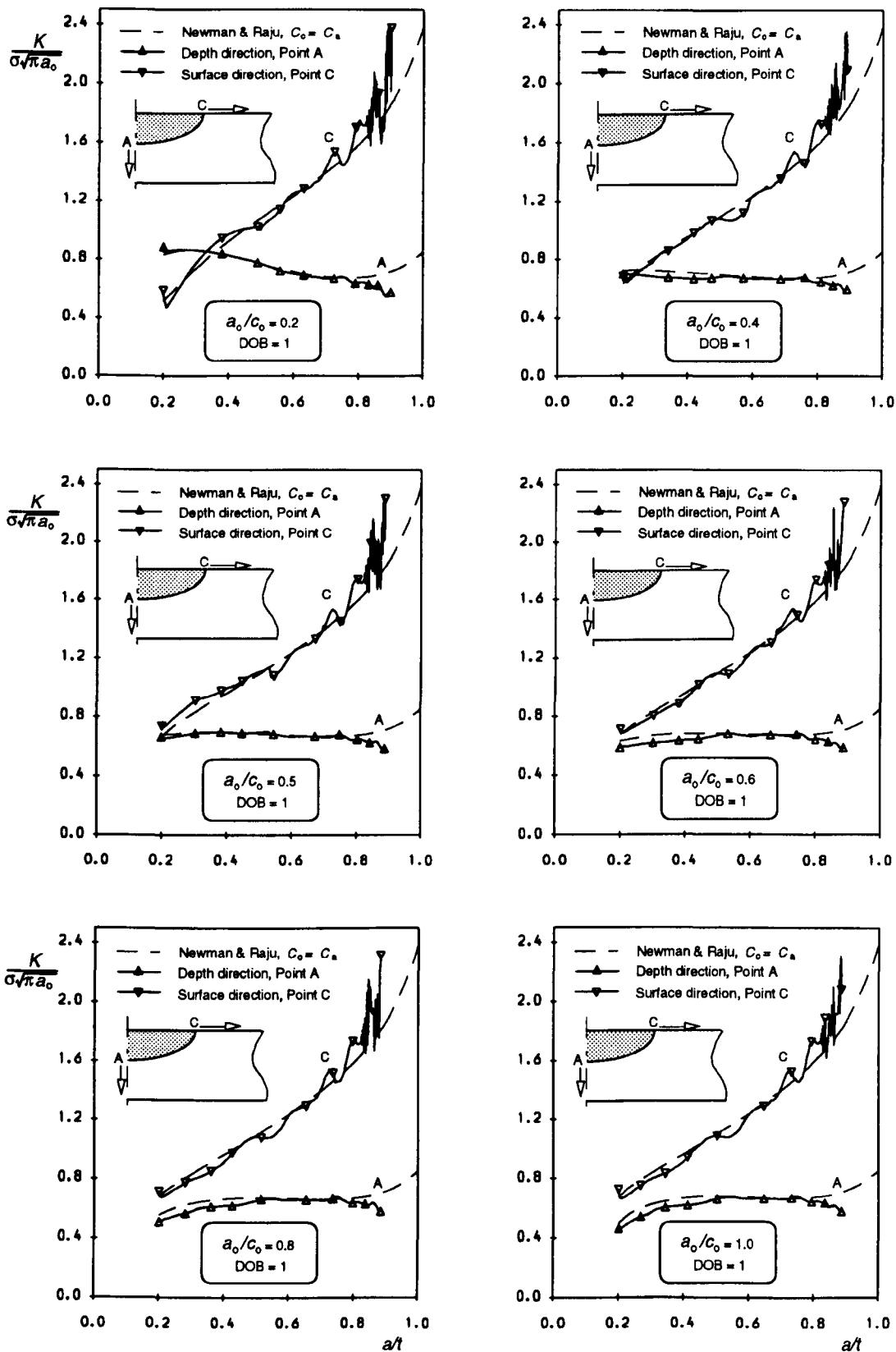surface directions during crack growth for DOB = 0.5

Figure 4.27   Variations of stress intensity factors along both depth and surface directions during crack growth for DOB = 1 (bending)

Newman and Raju's predictions, their difference is also apparent especially as the crack approaches the back surface of the plate. In addition to the discrepancy caused possibly by the deviation of the crack profile from the semi-elliptical shape, a relatively worse accuracy of Newman and Raju's (1981) SIF equation is believed by the present author to probably exist and is another source to such greater differences displayed at the late stage of crack growth in Figs. 4.25, 4.26 and 4.27.

4.6 Predictions of Fatigue Growth Curves

Conservative approximations are often made of the fatigue lives of cracked practical engineering structures, such as in the two widely used reference documents, ASME XI code (1977) and BSIPD 6493 (1980), which deal with surface cracks. The ASME XI code assumes that the crack grows to a geometrically similar larger flaw, i.e. constant aspect ratio, a/c, whilst the BSIPD 6493 suggests that the crack surface length, $2c$, should be kept constant until the crack depth a equals half the surface length c, i.e. $a = c$, after that this semi-circular shape should be maintained until the crack reaches the back surface. More accurate predictions can be made by Newman and Raju's 'two-point plus semi-ellipse' method, which has considered the crack shape change during the fatigue growth process, but made a semi-elliptical profile assumption. It is still not clear whether such a crack shape assumption leads to a conservative prediction of fatigue growth cycles for initially semi-elliptical surface defects. From a numerical analysis point of view, the present simulation technique obviously can provide even more accurate predictions of fatigue growth cycles than Newman and Raju's method since no crack shape assumption is employed.

The effect of the crack growth increment on the aspect ratio change discussed in Section 4.4.1 has shown that an excellent agreement has been achieved for the three different crack increments, $\Delta a_{max} = t/50$, $t/100$ and $t/167$, but it is still necessary to see what effect of the crack growth increment happens on the prediction of fatigue growth cycles. Fig. 4.28 shows the relations of the crack depth ratio with the number of fatigue growth cycles for the three different crack increments. A slight difference exists among the three curves, the larger crack increment predicts the greater number of fatigue cycles for a given crack depth.
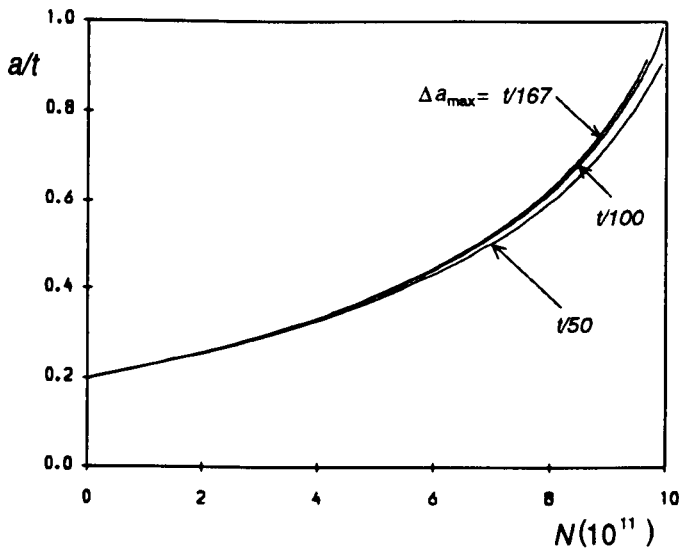
Figure 4.28 Effect of crack growth increment, Δa_{max}, on the fatigue growth curve predicted by the present simulating technique

Importantly, as the crack increment decreases, the convergence of the relation between the crack size and fatigue cycles does exist, which further demonstrates that a required accuracy of fatigue growth cycles can be achieved as long as the chosen crack increment is small enough during the calculation process. From Fig. 4.28 it can be said that quite good accuracy for the prediction of fatigue growth cycles (*the relative accumulative error possibly being less than 2% between* Δa_{max} = $t/100$ *and* $t/167$, *when the crack reaches the plate back surface*) has been achieved. Therefore, the crack increment value, Δa_{max} = $t/100$, is really small enough for these surface cracks analysed in this chapter.

Fig. 4.29 shows the fatigue growth curves, the dimensionless crack depth against the number of fatigue cycles, for the surface cracks subjected to pure tension. Four different predictions are compared in Fig. 4.29. Both solid lines represent the results obtained by the FE simulation technique without and with the free surface correction, and both dashed lines correspond to the results from the 'two-point plus semi-ellipse' method using the Paris growth rate coefficient relations, $C_c = C_a$ and $C_c = 0.9^n C_a$. The results show that Newman and Raju's $C_c = C_a$ method predicts the smallest number of fatigue cycles for a given crack depth, and the present results, no matter whether the free surface correction is considered, are always in an excellent agreement with those from Newman and Raju's $C_c = 0.9^n C_a$ method for all analysed initial crack configurations. If Newman and Raju's $C_c = 0.9^n C_a$ method is considered to be better in correlating the experimental results than the $C_c = C_a$ method, which seems to be confirmed by many investigators, it is implied that the present simulation technique can also provide a more accurate prediction of fatigue crack growth. In Fig. 4.29 it is obvious that there is a quite large difference for the fatigue growth prediction between the relations
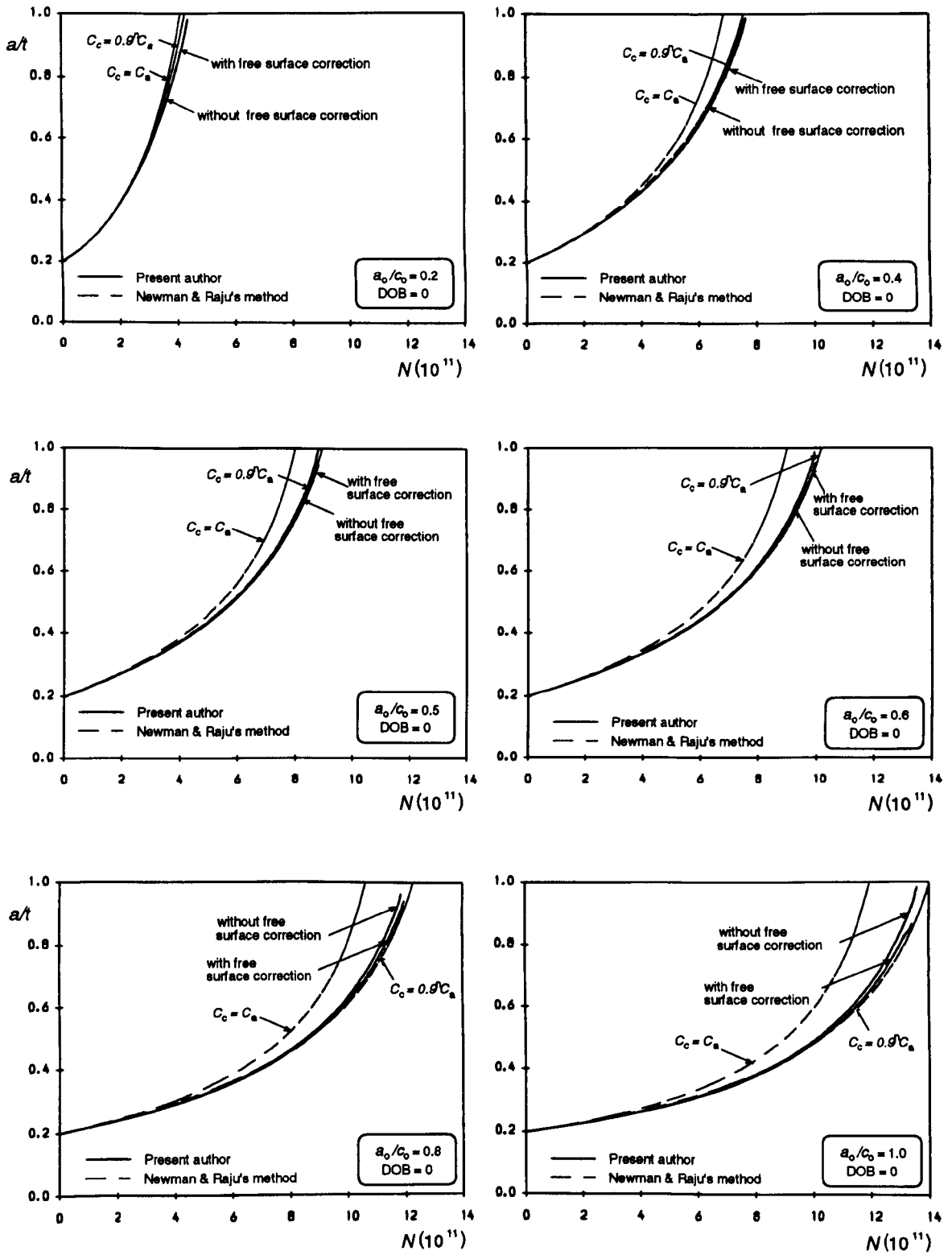
Figure 4.29   Variations of crack growth depth against the number of
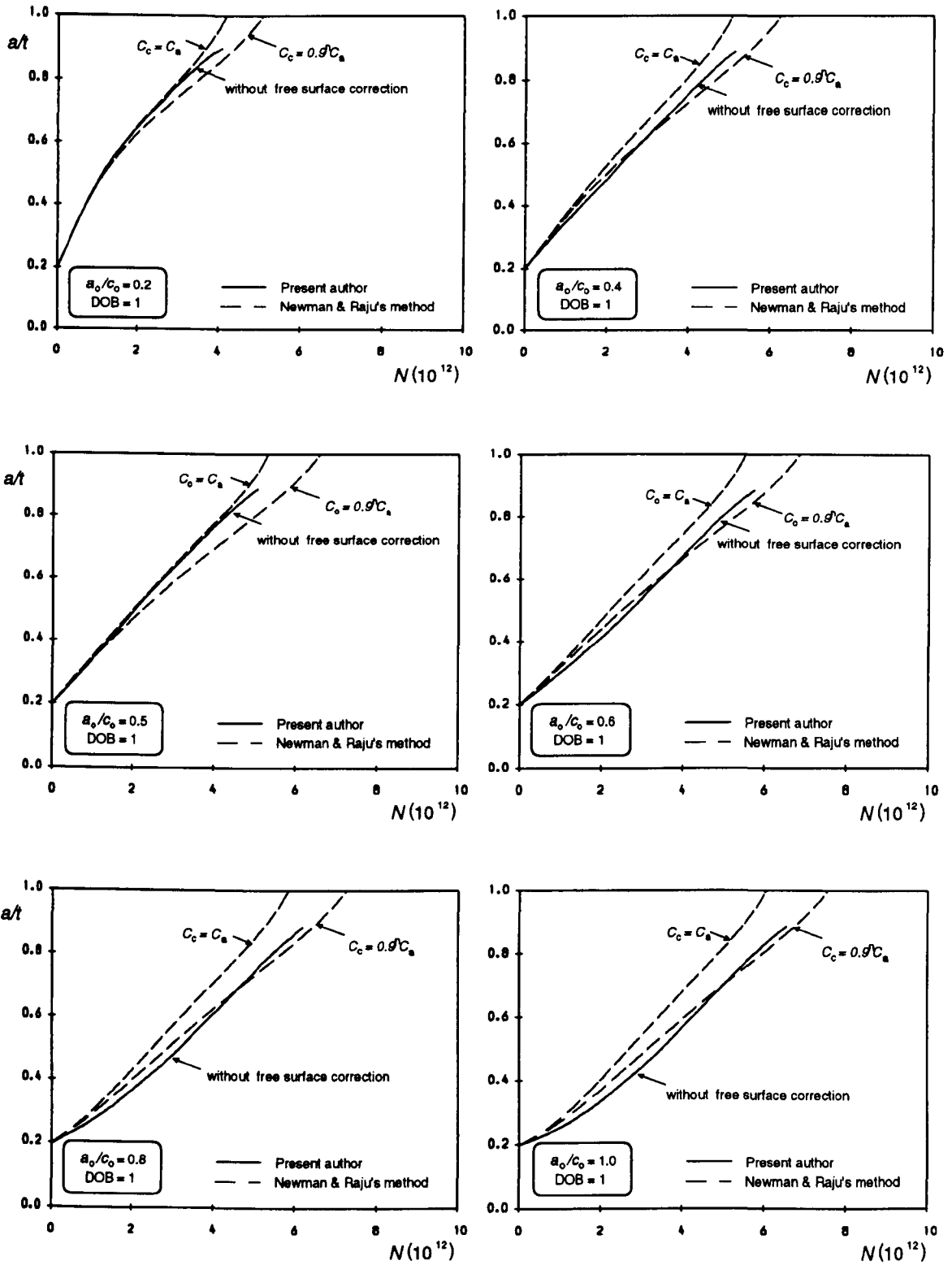fatigue growth cycles for DOB = 0

Figure 4.30   Variations of crack growth depth against the number of
fatigue growth cycles for DOB = 1

$C_c = C_a$ and $C_c = 0.9^n C_a$. However, the free surface correction considered in the present technique hardly affects the fatigue growth curve. This is easily understood if considering the cracked area corrected by the $C_c = 0.9^n C_a$ in the 'two-point plus semi-ellipse' method to be much larger than that by the free surface correction in the present technique.

The fatigue growth curves for pure bending cracks without the correction of free surface layer are displayed in Fig. 4.30, in which Newman and Raju's predictions are also included for comparison. Obviously, the difference between both Newman and Raju's results is also large, but, unlike pure tension cracks, it seems to be a little bit difficult to identify whether the present prediction agrees better with Newman and Raju's $C_c = 0.9^n C_a$ estimate than the $C_c = C_a$. However, the present results are generally between the $C_c = 0.9^n C_a$ and $C_c = C_a$ predictions.

4.7 Conclusions

This chapter has examined in detail the fatigue growth behaviours of initially semi-elliptical surface cracks in finite thickness plates subjected to different combinations of tension and bending loads. Crack propagation up to nearly the back surface of the plate was modelled by the 3D finite element step-by-step technique that has been significantly improved by the present author. Some numerical studies have been performed, such as the applicability of two-block FE models, the SIF accuracy for initially semi-elliptical defects, and the convergence of both aspect ratios and fatigue lives by varying the crack growth increment for a tension crack. The free surface layer correction has also been considered in investigations of the tension surface crack problem. The effect of the Paris exponent n on the aspect ratio was also examined. The shape change characteristics of surface cracks subjected to different combinations of tension and bending were quantitatively examined by both the proposed relative residual and the relative standard deviation. A wide range of numerical results, including aspect ratio changes, distributions of stress intensity factors along the front of several cracks, variations of the stress intensity factors at both the surface and depth points and predictions of fatigue growth cycles, have been obtained for all three different fatigue

loads, and mostly compared with those by Newman and Raju's 'two-point plus semi-ellipse' method.

The principal findings of this chapter are summarised as follows:

1) The comparison of SIFs for the initially semi-elliptical defects with Newman and Raju's equation shows that the two-block FE model employed in the present simulation computation can obtain good SIF accuracy, and, thus, is quite acceptable.

2) The effect of three different maximum crack growth increments, $\Delta a_{max} = t/167$, $t/100$ and $t/50$, employed in this chapter, is very small on the prediction of aspect ratio changes, and is also weak on the estimate of fatigue cycles, which demonstrates that the convergence is good and the Δa_{max} value is really small enough to be able to ensure the computation accuracy for these surface cracks analysed in this chapter.

3) The initially semi-elliptical surface crack, basically, can maintain an approximate semi-ellipse ($S_r < 3\%$), during the whole fatigue growth process (*from the initial defect up to the back surface of the plate*) for both pure tension and DOB = 0.5 loads. However, for pure bending, although the initially semi-elliptical crack shape can also be approximately maintained at the early stage of crack growth, a greater deviation ($S_r > 3\%$) from the semi-ellipse commences to appear when the crack grows to nearly $a/t = 0.75$, and subsequently the deviation increases continuously and very quickly. Such a tendency of increasing crack shape deviation from the semi-ellipse probably is an intrinsic characteristic for crack fatigue growth, not just the numerical error caused by the present modelling analysis though it is unavoidable. This conclusion is based on the quantitative analyses of the predicted crack profiles.

4) The aspect ratio changes have been obtained and compared with those predictions from Newman and Raju's $C_c = C_a$ method. For pure tension, it is shown that the difference between both predictions is not too large. A slight rise of the aspect ratio occurs as the crack approaches very close to the back surface of the plate, mainly due to the influence of the plate back surface. However, it is impossible for Newman and Raju's method to predict such a phenomenon. For DOB = 0.5 and pure bending cases, the discrepancy between the present predictions and Newman

and Raju's results is relatively larger than that for DOB = 0, the largest even reaches around 20%. The degree and the trend of the discrepancy vary with the crack development. During the fatigue growth process, the crack always propagates asymptotically towards the preferred propagation pattern, the larger the DOB value is, the more intense the asymptotic tendency is.

The free surface correction has also been considered for the surface cracks under pure tension. The obtained aspect ratio change usually is 3~5% higher than that predicted by the present technique without considering the free surface correction for a given depth ratio. The comparison of the present results with Newman and Raju's predictions of aspect ratio, using the relation, $C_c = 0.9^n C_a$, has shown that the disagreement is generally greater than that between both predictions made by the present simulation technique without considering the free surface correction and Newman and Raju's $C_c = C_a$ method.

An investigation of the effect of the Paris exponent n on aspect ratio changes for a particular crack subjected to different combinations of tension and bending indicates that the effect is evident and the larger n always makes the aspect ratio change more intense, because of its exponential nature.

5) The crack always attempts to advance in such a manner that the stress intensity factors along the crack front tend towards a constant, i.e. iso-K, which has been demonstrated in the examination of fatigue growth of initially irregular embedded defects in infinite solids under remote uniform in Chapter 2. However, the presence of both the front and back free surfaces of the plate, or the bending component of the load, makes it impossible, in a strict sense, for the surface crack to reach and subsequently to maintain such an iso-K shape, although it is true for most of the initial surface defects to pass through the iso-K shape.

The comparison of the SIF variations at both the crack surface and depth points against the crack depth ratio with Newman and Raju's $C_c = 0.9^n C_a$ results shows that, generally, there is a good agreement for all three different fatigue loads, but as the crack approaches the back surface of the plate very closely, the agreement becomes worse. This is believed to be due to the relatively worse accuracy of Newman and Raju's SIF equation for a large crack depth, $a/t > 0.9$, in

addition to the discrepancy caused possibly by the deviation of the crack profile from the semi-elliptical shape.

6) For pure tension, the relations of fatigue cycles with the dimensionless crack depth, a/t, predicted by the present simulation technique, no matter whether the free surface correction is considered, are always in an excellent agreement with those from Newman and Raju's $C_c = 0.9^n C_a$ method for all analysed initial crack configurations. The considered free surface correction hardly affects the fatigue growth curves. The fatigue growth curves for pure bending cracks obtained by the present technique are basically situated between Newman and Raju's $C_c = 0.9^n C_a$ and $C_c = C_a$ estimates, and it seems to be difficult to judge whether the present prediction agrees better with Newman and Raju's $C_c = 0.9^n C_a$ estimate than with the $C_c = C_a$ estimate.

4.8 References

Anderson, R. B., Holms, A. G. and Orange, T. W. (1970) Stress intensity magnification for deep surface cracks in sheets and plates. NASA TN D-6054.

A.S.M.E. Boiler and pressure vessel code, section XI (1977) *Rules for in-service inspection of nuclear power plant components.*

British Standards Institution (1980) *Guidance on some methods for the derivation of acceptance levels for defects in fusion welded joints,* Section 3, BSIPD 6493.

Carter, D. W., Canda, W. R. and Blind, J. A. (1987) *Surface flaw crack growth in plates of finite thickness.* Air Force Wright Aeronautical Laboratories, Material Laboratory, Wright-Patterson Air Force Base, Ohio, AFWAL-TR-86-4034.

Chen, S. and Cui, Z. (1988) *Surface crack growth behaviour under tensile cyclic loading.* **Int. J. Fatigue 10,** 43-47.

Corn, D. (1971) *A study of cracking techniques for obtaining partial thickness cracks of pre-selected depths and shapes.* **Engng Fract. Mech. 3,** 45-52.

Cruse, T., Meyers, G. and Wilson, R. (1977) *Fatigue growth of surface cracks.* Flaw Growth and Fracture, ASTM STP **631**, 174-189.

Grandt, A. and Sinclair, G. (1972) *Stress intensity factors for surface cracks in bending.* Stress Analysis and Growth of Cracks, ASTM STP **513**, 37-58.

Hall, L., Shah, R. and Emgstrom, W. (1974) *Fracture and fatigue crack growth behaviour of surface flaws and flaws originating at fastener holes.* Boeing Aerospace Co., AD/A-001 597.

Hodulak, L., Kordisch, H., Kunzelmann, S. and Sommer, E. (1979) *Growth of part through cracks.* Fracture Mechanics (Edited by C. W. Smith), 399-410.

Hoeppner, D., Pettit, D., Featherson, C. and Hyler, W. (1968) *Determination of flaw growth characteristics of Ti-6Al-4v sheet in the solution treated and aged condition.* NASA CR-65811.

Holdbrook, S. J. and Dove, W. D. (1979) *The stress intensity factor for a deep surface crack in a finite plate.* **Engng Fract. Mech. 12**, 347-364.

Hosseini, A. and Mahmoud, M. A. (1985) *Evaluation of stress intensity factor and fatigue growth of surface cracks in tension plates.* **Engng Fract. Mech. 22**(6), 957-974.

Iida, K. and Kawahara, M. (1975) *Change in fatigue crack shape during growth.* Dept. of Naval Architecture University of Tokyo, NAUT Report No. 9011.

Iida, K. and Kawahara, M. (1980) *Propagation and coalescence of fatigue cracks initiated from collinear or parallel adjacent surface flaws.* Proceedings of 4th International Conference on Pressure Vessel Technology, Vol. **1**, Materials, Fracture and Fatigue, 257-263.

Iida, K., Ando, K. and Hirata, T. (1981) *An evaluation procedure for multiple surface cracks during axial and bending fatigue loadings.* Proceedings of U.S. - Japan Cooperative Seminar, 'Fracture Tolerance Evaluation', Honolulu, USA, Available as document XIII-1044-82, International Institute of Welding, 1982.

Iida, K. (1983) *Shapes and coalescence of surface fatigue cracks.* Proceedings of ICF International Symposium on Fracture Mechanics, Beijing, China, 22-25 November, 679-693.

Irwin, G. R. (1962) *Crack extension force for a part through crack in a plate.* Trans. of ASME, Ser. E, **J. Appl. Mech. 29**, 651-654.

Isida, M., Noguchi, H. and Yoshida, T. (1984) *Tension and bending of finite thickness plates with a semi-elliptical surface crack.* **Int. J. Fracture 26**, 157-188.

Jolles, M. and Tortoriello, V. (1983) *Geometry variation during fatigue growth of surface flaws.* Fracture Mechanics, ASTM STP 791 (Edited by J. Lewis and G. Sines), Vol. 1, 297-307.

Kawahara, M. and Kurihara, M. (1975) *A preliminary study on surface crack growth in a combined tensile and bending fatigue process.* J.S.N.A. Japan, 137, 86-92.

Kawahara, M. and Kurihara, M. (1977) *Fatigue crack growth from a surface flaw.* Proceedings of 4th International Conference on Fracture (Edited by D. Taplin), Waterloo, Canada, Vol. 2, 1361-1373.

Kobayashi, A. S. and Moss, W. L. (1969) *Stress intensity magnification factors for surface flawed tension plate and notched round tension bar.* Proceedings of 2nd International Conference on Fracture, Brighton, England, 31-45.

Kobayashi, A. S. (1976) *Crack opening displacement in a surface flawed plate subjected to tension or plate bending.* Proceedings of 2nd International Conference on Mechanical Behaviour of Materials, ASME, 1073-1077.

Kobayashi, K., Narumoto, A. and Tanaka, M. (1977) *Prediction of crack propagation life in axial loading fatigue of structural steels.* Proceedings of 3rd International Conference on Pressure Vessel Technology, Tokyo, 807-813.

Lee, K. *et al.* (1982) *Experimental research on surface crack propagation laws for low alloy steel.* Engng Fract. Mech. 16, 105-113.

Lloyd, G. L. and Walls, J. D. (1980) *Propagation of fatigue cracks from surface flaws in austenitic type 316 butt welds.* Engng Fract. Mech. 13, 897-911.

Mahmoud, M. A. and Hosseini, A. (1986) *Assessment of stress intensity factor and aspect ratio variability of surface cracks in bending plates.* Engng Fract. Mech. 24(2), 207-221.

Mahmoud, M. A. (1988a) *Quantitative prediction of growth patterns of surface fatigue cracks in tension analysis.* Engng Fract. Mech. 30, 735-746.

Mahmoud, M. A. (1988b) *Growth patterns of surface fatigue cracks under cyclic bending - a quantitative analysis.* Engng Fract. Mech. 31, 357-369.

Masters, J. N., Haese, W. P. and Finger, R. W. (1969) *Investigation of deep flaws in thin walled tanks.* NASA CR-72606.

McFadyen, N. B., Bell, R. and Vosikovsky, O. (1990) *Fatigue crack growth of semi-elliptical surface cracks.* Int. J. Fatigue 12, 43-50.

McGowan, J. (1985) *A critical evaluation of numerical solutions to the benchmark surface flaw problem.* **Exper. Mech. 20(8)**, 253-264.

Nagai, A., Toyosada, M. and Okamoto, T. (1975) *A study on fatigue crack growth in 9% Ni steel plate.* **Engng Fract. Mech. 7**, 481-490.

Newman, J. C., Jr. (1973) *Fracture analysis of surface- and through-cracked sheets and plates.* **Engng Fract. Mech. 5**, 667-689).

Newman, J. C, Jr. and Raju, I. S. (1978) *Analyses of surface cracks in finite plates under tension or bending loads.* NASA Technical Paper 1578, USA.

Newman, J. C., Jr. (1979) *A review and assessment of the stress-intensity factors for surface cracks.* Part-through Crack Fatigue Life Prediction, ASTM STP 687, 16-42.

Newman, J. C., Jr. and Raju, I. S. (1979) *Analyses of surface cracks in finite plates under tension or bending loads.* NASA Technical Paper 1578.

Newman, J. C, Jr. and Raju, I. S. (1981) *An empirical stress intensity factor equation for the surface crack.* **Engng Fract. Mech. 15**, 185-192.

Nisitani, H. (1968) *The two-dimensional stress problem solved using an electric digital computer.* **Bull. Japan Soc. Mech. Engrs 11**, pt. 1, 14-23.

Nisitani, H. and Murakami, Y. (1974) *Stress intensity factors of an elliptical crack or a semi-elliptical crack subject to tension.* **Int. J. Fracture 10(3)**, 353-368.

Paris, P. C. and Sih, G. C. (1965) Fracture Toughness Testing and Its Application, ASTM STP **381**, 30-83.

Pierce, W. S. and Shannon, J. L. (1978) *Surface crack shape change in bending fatigue using an inexpensive resonant fatiguing apparatus.* **J. Test. Eval. 6**, 183-188.

Portch, D. J. (1979) *An investigation into the change of shape or fatigue cracks initiated at surface flaws.* Central Electricity Generating Board, Report RD/B/N-4645.

Putra, I. S. and Schijve, J. (1992) *Crack opening stress measurements of surface cracks in 7075-T6 Aluminium alloy plate specimen through electron fractography.* **Fatigue Fract. Engng Mater. Struct. 15**, 323-338.

Raju, I. S. and Newman, J. C. Jr. (1977) *Improved stress-intensity factors for semi-elliptical surface cracks in finite thickness plates.* NASA TMX-72825.

Raju, I. S. and Newman, J. C., Jr. (1979) *Stress intensity factors for a wide range of semi-elliptical surface cracks in finite thickness plates.* **Engng Fract. Mech.** 11(4), 817-829.

Rice, J. R. and Levy, N. (1970) *The part-through surface crack in an elastic plate.* Technical Report NASA NGL 40-002-080/3, Division of Engineering, Brown University, Trans. of ASME, Ser. E, **J. Appl. Mech.,** paper no. 71-APM-20.

Scott, P. M. and Thorpe, T. W. (1981) *A critical review of crack tip stress intensity factors for semi-elliptical cracks.* **Fatigue Fract. Engng Mater. Struct.** 4(4), 291-309.

Shah, R. C. and Kobayashi, A. S. (1972) *On the surface flaw problem, in the Surface Crack:* Physical Problems and Computational Solutions, (Edited by J. L. Swedlow), 79-124.

Smith, F. W., Emery, A. F. and Kobayashi, A. S. (1967) Trans. of ASME, Series E, **J. Appl. Mech.,** 34(4), 953-959.

Smith, F. W. and Alavi, M. J. (1969) Proceedings of 1st International Conference on Pressure Vessel Technology, Delft, The Netherlands, ASME, 783-800.

Smith, F. W. and Sorensen, D. R. (1974) *Mixed mode stress intensity factors for semi-elliptical surface cracks.* NASA CR-134684.

Truchon, M. and Lieurade, H. -P. (1981) *Experimental study of surface crack propagation.* Advances in Fracture Mechanics, Proceedings of 5th International Conference on Fracture, (Edited by D. Francois), Elmsford, 33-39.

Vosikovsky O. and Rivard, A. (1981) *Growth of surface fatigue cracks in a steel plate.* **Int. J. Fatigue 3,** 111-115.

Wu, S. X. (1985) *Shape change of surface during fatigue growth.* **Engng Fract. Mech.** 22, 897-913.

Yen, C. S. and Pendleberry, S. L. (1962) *Technique for making shallow cracks in sheet metals.* **Mater. Res. Stands 2,** 913-916.

BLANK PAGE
IN
ORIGINAL

Chapter 5

INTERACTION AND COALESCENCE OF MULTIPLE INITIALLY SEMI-CIRCULAR SURFACE FATIGUE DEFECTS

A brief review is made in this chapter on the investigations related to static or fatigue multiple crack geometries. The shape development, starting from a row of five small initially semi-circular surface defects, throughout the plate thickness subjected to different combinations of tension and bending fatigue loads is numerically predicted by the step-by-step finite element simulation technique developed by the present author. The fatigue growth of the initially multiple crack configuration during pre-coalescence, coalescence and post-coalescence periods is examined in detail. The fatigue growth modelling of a single surface crack with the same initial size is also performed and compared with that of the multiple crack configuration. The comparison shows that the fatigue growth of each individual defect is almost independent prior to coalescence and the interaction between them is very limited even as they approach each other very closely. The fatigue crack growth curves predicted by the present numerical technique are compared with those obtained by the ASME XI code and a "no interaction and immediate transition (NIIT)" simplified method. The results show that both the ASME XI code and the "NIIT" method estimate the crack growth more conservatively than the present simulation technique, however, the "NIIT" method is relatively less conservative than the ASME XI code which is too conservative for the crack configuration under examination.

5.1 Introduction

In practical engineering components irregularly shaped and/or adjacent defects are often found in inspections. These adjacent defects usually undergo significant shape change during the fatigue propagation process and finally become one single crack if the defects are close enough. Fig. 5.1 depicts three typical stages of fatigue growth of two adjacent cracks which have been observed from experiments, i.e. pre-coalescence, coalescence and post-coalescence. 'Pre-coalescence' represents the fatigue growth period during which the initial twin cracks have not contacted and usually behave as isolated cracks, however, interaction occurs when both cracks approach each other very closely. 'Coalescence' is the stage of the process during which the adjacent cracks join together to become one; which is defined from their first touch to ending when the single crack profile is no longer concave. The 'post-coalescence' stage is where the non-concave single crack continues its growth.

5.1.1 Interaction studies of static adjacent cracks

At the stage of pre-coalescence, the term 'interaction' usually means that the stress intensity factor around each crack is affected by the presence of other cracks, as shown in Fig. 5.1(a). Many numerical studies on the SIF of twin static adjacent cracks, such as the work of Murakami *et al.* (1981, 1982, 1983), Heath and Grandt (1984) and O'Donoghue *et al.* (1984, 1985) have indicated that interaction does exist. Usually, the interaction is quantified in terms of an interaction factor which is defined as the ratio of the dimensionless stress intensity factor in the presence of another crack to that of a single crack (*in absence of another crack*) subjected to the same load.

Murakami *et al.* (1981, 1982, 1983), using the body force method, analysed various configurations of two semi-elliptical coplanar surface cracks in a semi-infinite elastic body under overall tension and bending. The SIF results they obtained show that the interaction factor varies around the crack front and is the largest at the inner point (*the nearest point to the other crack*), and depends on the distance between the cracks and the shape of each crack. One of the conclusions they drew is that when the inner points of the two cracks are separated by a distance exceeding the smaller crack's largest axis, the interaction factor at the inner crack tip for the larger crack can be neglected.
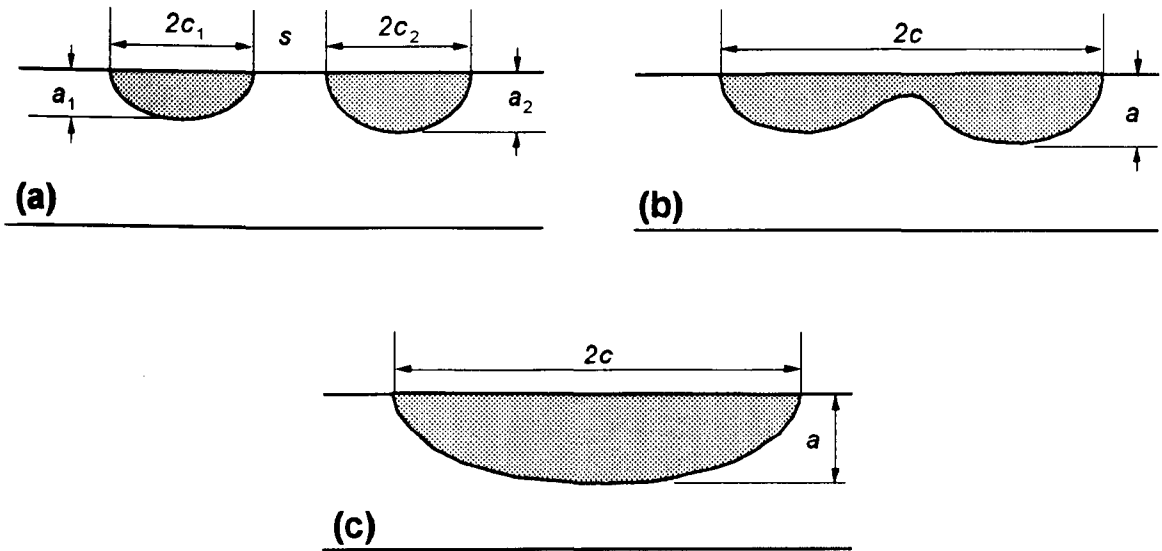
Figure 5.1 Schematic representation of the stages of growth of twin coplanar cracks;
(a) Pre-coalescence; (b) Coalescence; (c) Post-coalescence

Heath and Grandt (1984) used the finite element alternating method to investigate the effect of crack interaction on the stress intensity factor for two symmetric coplanar corner cracks located along a hole bore. They obtained a particular conclusion for their crack configurations that the crack interaction does not occur when the crack separation distance, s (*see Fig. 5.1(a)*), is equal to or greater than the crack surface half-length.

O'Donoghue *et al.* (1984) also used the same method as Heath and Grandt (1984) to calculate the stress intensity factor of two coplanar surface semi-elliptical interacting cracks in a cylindrical pressure vessel, and then compared the SIFs with those obtained by recharacterising the two cracks to an enveloping crack according to the recommendations of ASME XI (1977). They concluded that there are significant effects on the stress intensity factor due to the interaction of the two adjacent surface cracks particularly at their inner points, and the re-characterisation might tend to underestimate the stress intensity factor. Multiple coplanar embedded elliptical cracks in an infinite solid have also been investigated by O'Donoghue *et al.* (1985).

Estimating the stress intensity factors of two adjacent static cracks as mentioned above, obviously, is helpful in revealing the interaction of each other. However, as reported by the above researchers, who have investigated crack configurations of their interest, the interaction

of two adjacent cracks is quite complicated and varies with the separated distance between them, the shape and size of each crack, the geometry and the applied load. A widely recognised conclusion is that the SIF values will increase due to the interaction of adjacent cracks being in close proximity. The complexity leads to an actual difficulty in obtaining a general criterion for the assessment of practical adjacent static defects. Both ASME XI (1977) and BSIPD 6493 (1980) have suggested a number of rules for the analyses of crack interaction and coalescence problems by recharacterising adjacent cracks to one different enveloping crack, but their origins for these rules are unknown.

5.1.2 Fatigue growth studies of adjacent cracks

The assessment of adjacent cracks growing by fatigue is obviously more difficult than that of static interacting cracks since the shape and size of the cracks may change under fatigue loading even at the 'interaction' stage of crack growth, generally followed by significant shape change during coalescence. It is very difficult to apply the SIF solutions of static interacting cracks to fatigue interacting cracks.

Currently, there are several approaches to the fatigue assessment of interacting surface cracks. Two of them are the widely known ASME XI and BSIPD 6493 codes, which both suggest that adjacent cracks should be re-characterised to one single crack if certain conditions are satisfied. Some numerical analyses (O'Donoghue *et al.*, 1984), by comparing the SIF results between two adjacent cracks and a single enveloping crack assumed by ASME XI or BSIPD 6493 codes, have indicated that the maximum SIF around the assumed single crack will generally be greater than the actual maximum SIF around the two cracks, which means both the ASME XI and BSIPD 6493 codes will give conservative predictions of fatigue growth. Apparently, the assessment method explicitly excludes the stages of interaction and coalescence, which actually happen during the fatigue growth, and only accounts for them by introducing a simple assumption. Due to the exponential nature of the Paris fatigue crack growth law, the method might cause a large error, an unnecessarily over-conservative result, in estimates of fatigue lives of two adjacent surface cracks.

An alternating method (Iida, 1983; Grandt, 1986; McComb *et al.*, 1986; Morgan, 1986) of assessing the fatigue growth of adjacent cracks assumes no interaction before the inner tips of the cracks touch and immediate coalescence to a single thumbnail-shaped crack after they

touch. This actually means that the advance of each adjacent crack is individually computed until they come together, and the region of coalescence is neglected.

Iida (1983) modified the SIF solution of Kobayashi (1969, 1976) by formulating his own finite width correction factors as a basis of his investigation of interacting fatigue cracks. The specimens he examined were plates under different combinations of tension and bending, and pipes internally pressurised, both containing coplanar surface cracks. He compared the experimental results with the numerical predictions made by both the ASME method and the alternative just mentioned. In the alternating method, a different re-characterisation of the touched adjacent cracks to a single crack from that of the ASME XI and BSIPD 6493 was used. The conclusion he drew is that the assessment method he used predicts more agreeable fatigue lives and shape changes of coplanar surface cracks with the experiment results, and the ASME method usually gives poor estimates for crack shape and too conservative predictions for crack growth but also may give risky prediction especially in the case where coplanar cracks, of which initial aspect ratios are more than unity, are subjected to out-of-plane bending.

Morgan (1986), after completing a short experimental investigation into two coplanar surface defects, indicated that the analytical approach taken by Iida (1983) gave a reasonable approximation of crack growth.

McComb *et al.* (1986) performed an experimental study of interaction and coalescence of a pair of surface and/or corner cracks in a plate with a central hole under remote tension and in a beam subjected to cyclic bending, and also used the analytical procedure which assumes immediate transition to a new uniform crack when the pair of cracks merge. Their SIF calculations were based on Newman and Raju's (1981) SIF equations, but took the interaction effect of the adjacent crack into account by incorporating Heath and Grandt's (1984) results of interaction factor into their analytical algorithm. The comparison of the measured crack growth curves with the computed predictions showed that the predictions of crack lengths were generally quite accurate prior to coalescence, but somewhat conservative after coalescence, which was thought by them to be attributed to the assumption of immediate transition employed in their analysis.

It can be concluded from the work of Iida (1983), Grandt (1986), McComb *et al.* (1986) and Morgan (1986) that the assessment method that assumes immediate coalescence to a single uniform shaped crack, as described above, can provide a more accurate prediction of

fatigue growth for adjacent cracks than that proposed in the ASME XI and BSIPD 6493 codes, although it ignores the stage of coalescence.

Further consideration of the coalescence stage has recently been taken into the prediction of fatigue growth of two coplanar surface cracks under bending loading by Soboyejo *et al.* (1989), who used the step-by-step FE technique originally developed by Smith and Cooper (1989). The technique directly follows the fatigue growth of two adjacent cracks at all three stages shown in Fig. 5.1, and has apparently considered both the interaction and coalescence. They also performed a fatigue test of the two surface cracks, starting from being separate through the interacting and coalescence stages and on to form a single thumbnail-shaped crack, and compared the experimental results with their numerical modelling results. The comparison showed that there was a good agreement between the experimental and numerical results. They also concluded that the coplanar initially semi-elliptical cracks grew almost independently before contact, and the high stress intensity factor occurred in the region of coalescence, which resulted in a rapid transition to a single thumbnail shaped crack.

Kishimoto *et al.* (1989) also performed a FE simulation of two coplanar surface cracks growing under tension, and obtained similar results to those of two surface cracks under bending. In addition, Kishimoto *et al.* (1989) compared the numerical modelling results for the bending cracks with those obtained by using a simple assessment method, which assumes no interaction up to the contact of the inner tips of the cracks and immediate transition to a uniform enveloping crack, similar to that used by Grandt (1986) and McMomb *et al.* (1986), and employs Newman and Raju's (1981) SIF solutions. The comparison showed that the simple assessment method slightly overestimated the crack growth predicted by the FE simulation technique. This is a reasonable result since the stage of coalescence is neglected by the simple assessment method.

5.1.3 Objectives

This chapter aims to continue the effort of directly modelling the fatigue growth of adjacent cracks by using the step-by-step FE technique recently developed by the present author. The fatigue growth of a row of five small initially semi-circular surface defects in a finite thickness plate subjected to different combinations of tension and bending loads is simulated. The fatigue shape development of the multiple cracks at three different stages, i.e.

pre-coalescence, coalescence and post-coalescence, is more precisely predicted. The interaction prior to coalescence is studied by comparing the fatigue growth of the multiple cracks with that of a single crack of the same initial shape and size. The SIF variations along the crack front, calculated from the FE analyses, during different crack growth stages are presented and discussed. Comparison of the predicted crack growth curves is also made with those obtained by the recommendations for multiple surface cracks as laid down in ASME XI code and a simplified method similar to that of Grandt *et al.* (1986).

5.2 Modelling Computation Details

The geometry analysed here consists of a row of five small semi-circular (radius 0.15mm) defects situated with centres 10mm apart at the surface of a 25mm thick plate subject to different combinations of tension and bending cyclic loads. Fig. 5.2 shows the geometry of the cracked plate, and also defines the nomenclature used in this chapter. Both the height (2*H*) and width (2*W*) of the plate are assumed to be 800mm. Three different remote loads, DOB = 0 (pure tension), 0.5 and 1 (pure bending), applied on the plate are considered, as shown in Fig. 5.2.

The FE modelling calculation was only confined to a quarter of the plate since the crack geometry and loading are symmetrical. The FE model of the plate consisted of two blocks, i.e. cracked block and uncracked block, as mentioned in Chapter 2. Two different uncracked blocks that are the same as that employed in Chapter 4 (*see Fig. 4.4*), were used in this chapter. As described in Chapter 2, the uncracked block defining the bulk of the plate basically remained unchanged throughout the series of analyses, while the cracked block was automatically expanded by the present software DUCKPRE from its 2D cracked plane mesh and subsequently reconnected to the uncracked block after each successive increment of crack growth. Fig. 5.3 shows a typical 3D cracked block mesh.

The 2D cracked plane mesh mostly was automatically recreated by the software DUCKPOST after the crack front had advanced to a new position, however, manual operation was also performed during transitions from two cracks to one coalesced crack or when larger changes in crack shape occur. Fig. 5.4 shows several typical FE configurations of 2D cracked planes at different stages of crack growth. It can be seen that prior to coalescence each whole
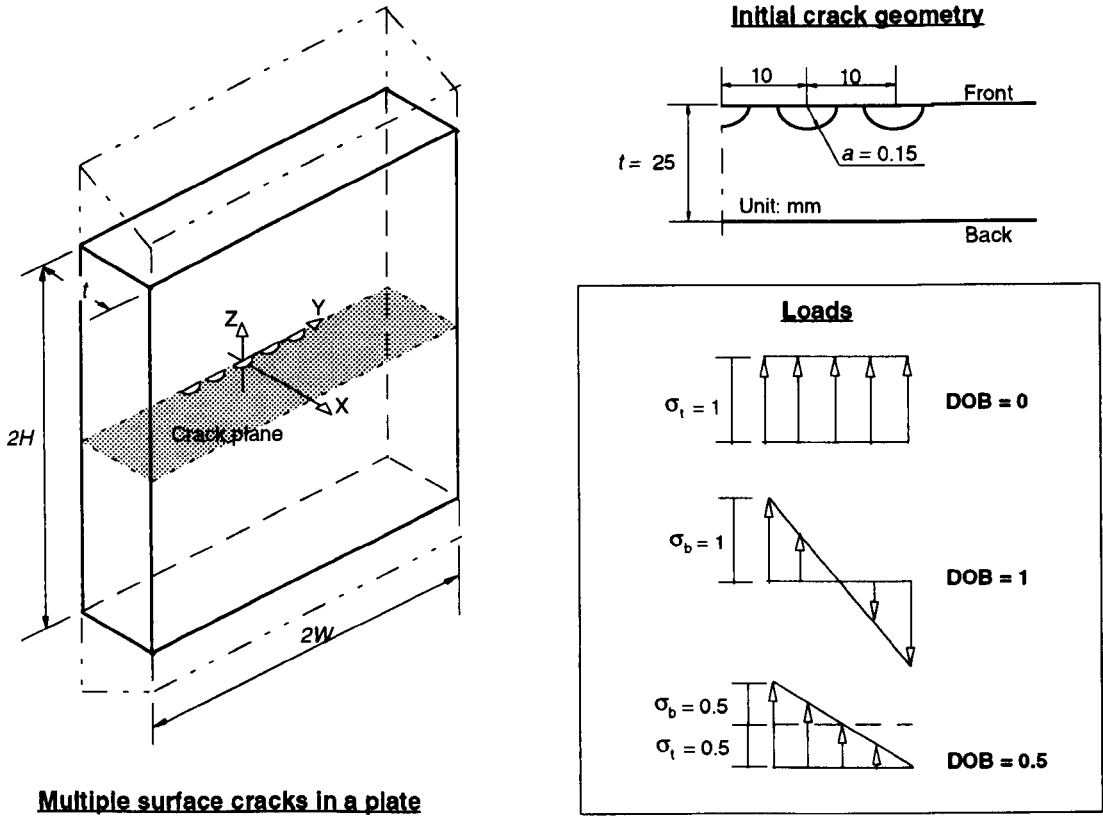
Figure 5.2 A surface crack in a finite thickness plate subjected to remote tension, bending, or both combined fatigue load

crack front was defined by seventeen nodes (*nine corner nodes and eight mid-side nodes*), and there were eight 8-noded isoparameteric elements abutting the crack front each side. Due to the limitation of computer resource, it was difficult to arrange more nodes along the crack front. The number of degrees of freedom for some FE models has reached 15198. The polyline, as described in Chapter 2, was used to approximate the crack front, and the free surface layer correction was not employed.

The Poisson's ratio, v, of the material was assumed to be 0.3, the Paris coefficients $C = 1.83 \times 10^{-13}$ and the exponent $n = 3$, where the unit of stress intensity factor employed during calculations was MPa$\sqrt{mm}$, and the unit of crack size was mm. The maximum crack growth increment, Δa_{max}, along the crack front was confined to the range of 0.05 ~ 0.8mm, which should be considered to be very small. The relatively larger values were chosen only at the

crack transition and when the crack under pure bending approached the back surface of the plate for the purpose of speeding up the crack advance along the crack depth direction and reducing the CPU consumption.
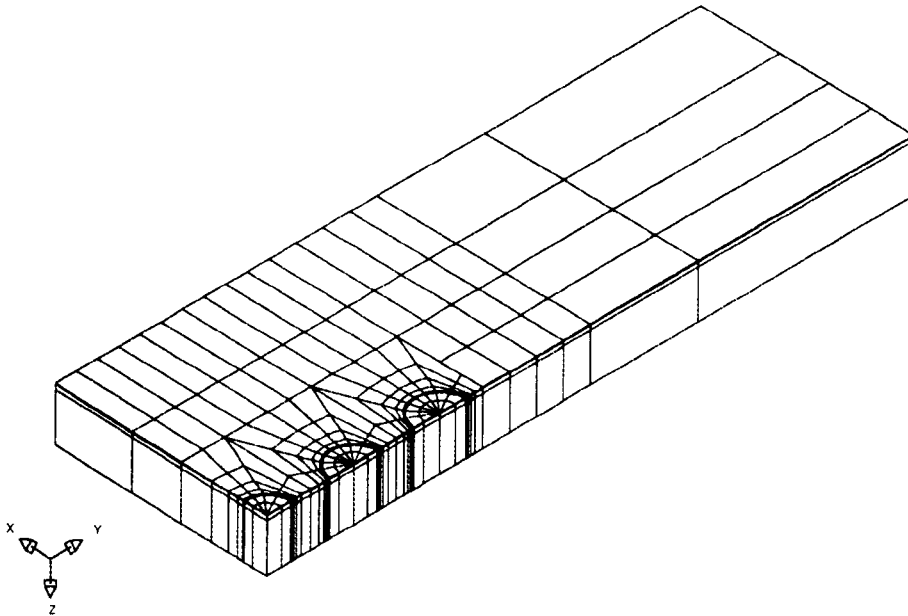

Figure 5.3   A typical cracked block

In order to examine the interaction effect between multiple cracks before coalescence, the fatigue growth of a single initially semi-circular small crack subjected to tension fatigue was also numerically modelled by the present technique.   The same type of FE models as that used for the multiple crack geometry was employed except constraining the loading direction displacements of the crack II and III surfaces.   The maximum crack growth increment, Δa_{max}, was taken to be 0.05mm, the same value as that chosen for all three loading cases prior to coalescence.

Manual intervention was reduced to a very small extent during the whole modelling computation, owing to the highly automatic software developed by the present author.   All computations were performed on a Sun Workstation.
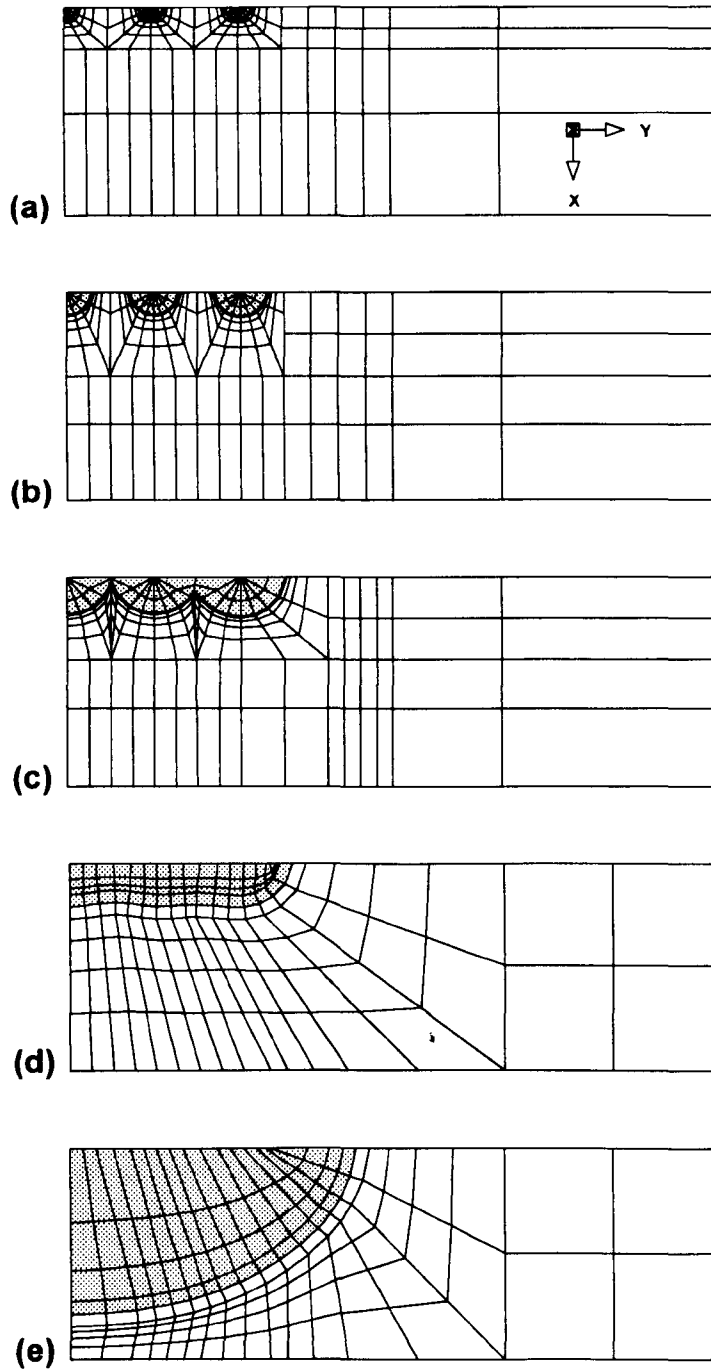
Figure 5.4   Typical finite element configuration at different crack growth stages for tension; (a, b) pre-coalescence; (c, d) coalescence; (e) post-coalescence

5.3 Crack Shape Development

Fig. 5.5 shows the shape development of a row of five initial small semi-circular defects under pure tension (DOB = 0). The plotted crack profiles are those selected from a total of 290 growth steps in order for them to be identified clearly. The shape development on the whole crack surface is presented by mirroring the results obtained on the half crack surface. It is found that at the early stage these small cracks grow almost independently in a nearly self-similar manner until they contact, immediately after which they coalesce rapidly to form a single smooth thumbnail shaped crack (*all concave points along the crack front disappear*). Finally this single crack continues its advancement and behaves as a single surface crack in a finite plate under tension. If Fig. 5.5 is observed more closely, it can be seen that crack III shows slightly more rapid growth than the other two. This is because the maximum stress intensity factor along the initially semi-circular crack III is about 0.43% larger than that of both cracks I and II. It is the 0.43% difference in the numerical calculation that leads to more and more rapid growth of the crack III, due to the exponential nature of the crack growth law and the growth independence of these cracks during the period of pre-coalescence.

Fig. 5.6 shows another shape development of this geometry which is the result of the first attempt made by the present author, where a different FE mesh was used for this problem. Obviously, compared with the crack III in Fig. 5.5, the crack III in Fig. 5.6 advances even more rapidly than cracks I and II. The reason is that, in this case, the initially semi-circular crack III has about 1.2% larger maximum stress intensity factor than both cracks I and II. A similar phenomenon can also be found in experiment or engineering practice. Soboyejo *et al.*'s (1989) experimental result for twin coplanar defects with almost, but not quite, identical initial size, as shown in Fig. 5.7, is an example.

Fig. 5.8 and Fig. 5.9 show, respectively, the fatigue shape development, starting from a row of five small cracks and ending at a single smooth surface crack, for DOB = 0.5 and 1 (pure bending) cases. Those profiles are extracted from a total of 340 (DOB = 0.5) and 380 (DOB = 1) crack growth steps. It can be seen that the crack shape change prior to coalescence for both cases is nearly similar to that for DOB = 0, and the outermost crack grows slightly faster than the others, which is also similar to the pure tension case. But the effect of different bending components of the fatigue load on the crack shape gradually becomes clear during the period of crack coalescence, and significant after coalescence.

Enlarged region

Figure 5.5   Fatigue shape development of
a row of five initially semi-circular
small surface cracks under tension
(DOB = 0)

Detailed
 pre-coalescing process
  process

Figure 5.6   Shape development of a row
of five initially semi-circular small
surface cracks under tension
(DOB = 0), which was obtained by
the first attempt

Figure 5.7   Soboyejo *et al*'s (1989) experimental observation for two initial small cracks;
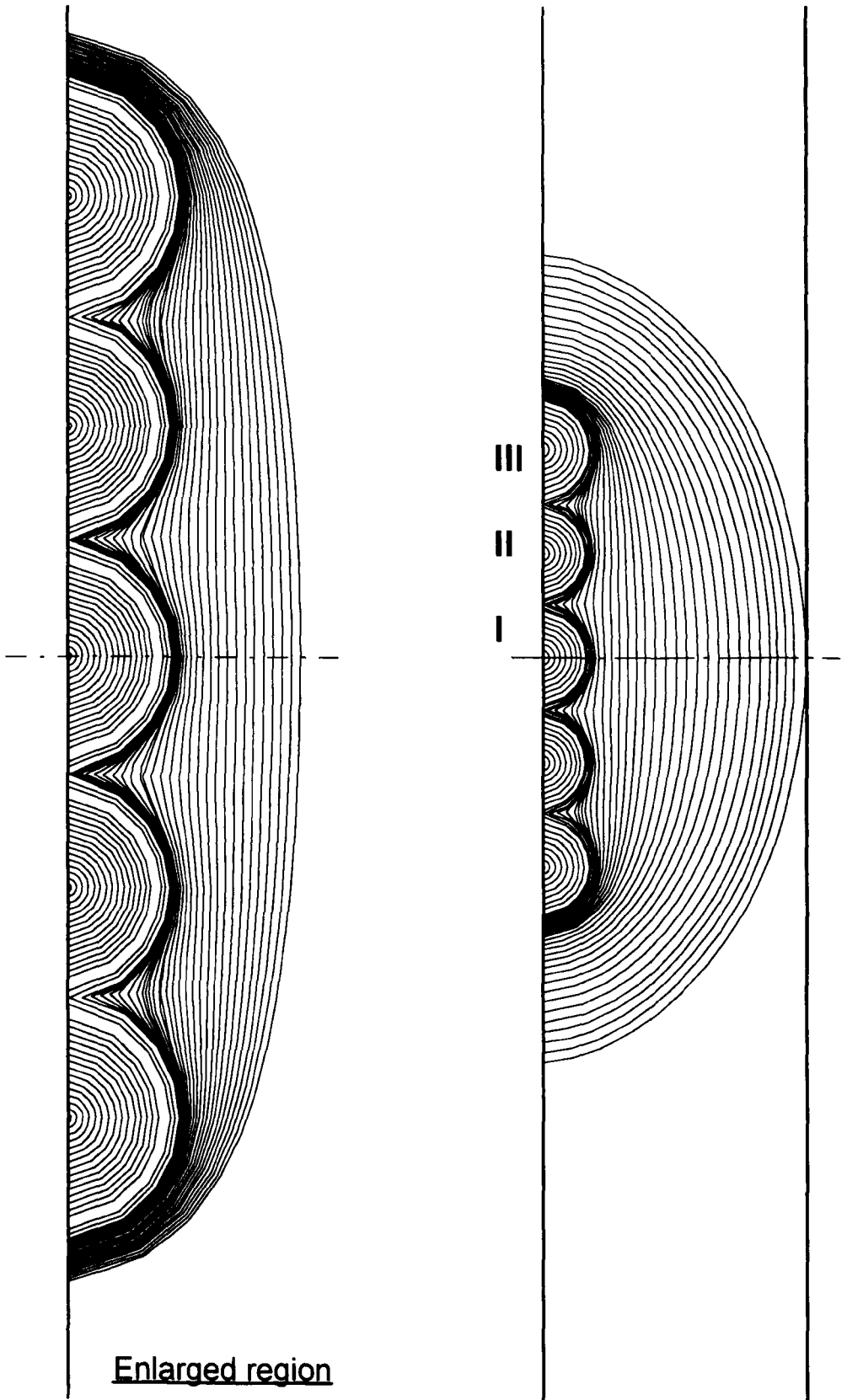(I) interaction, (II) coalescence, (III) post-coalescence

Figure 5.8   Shape development of
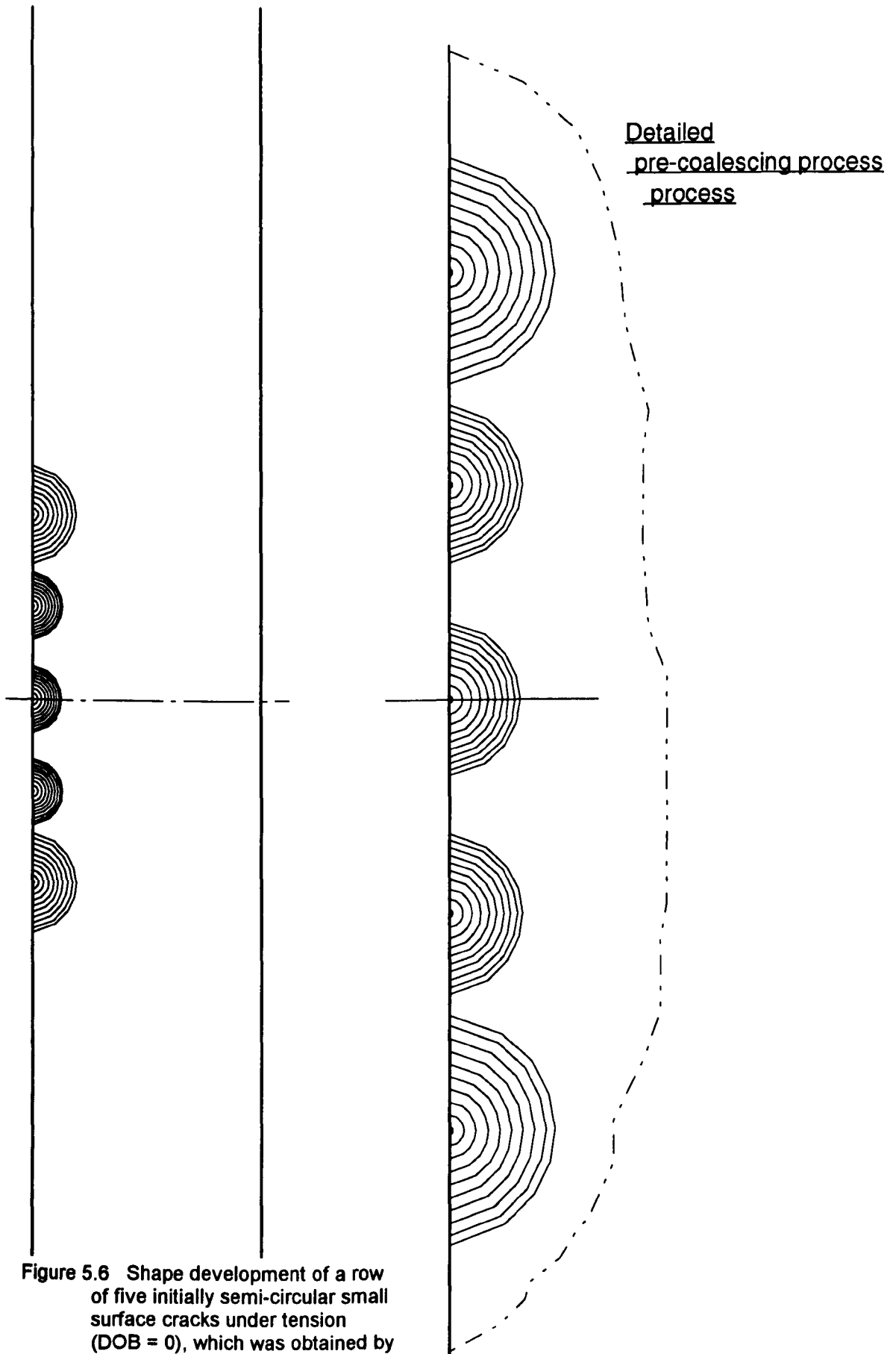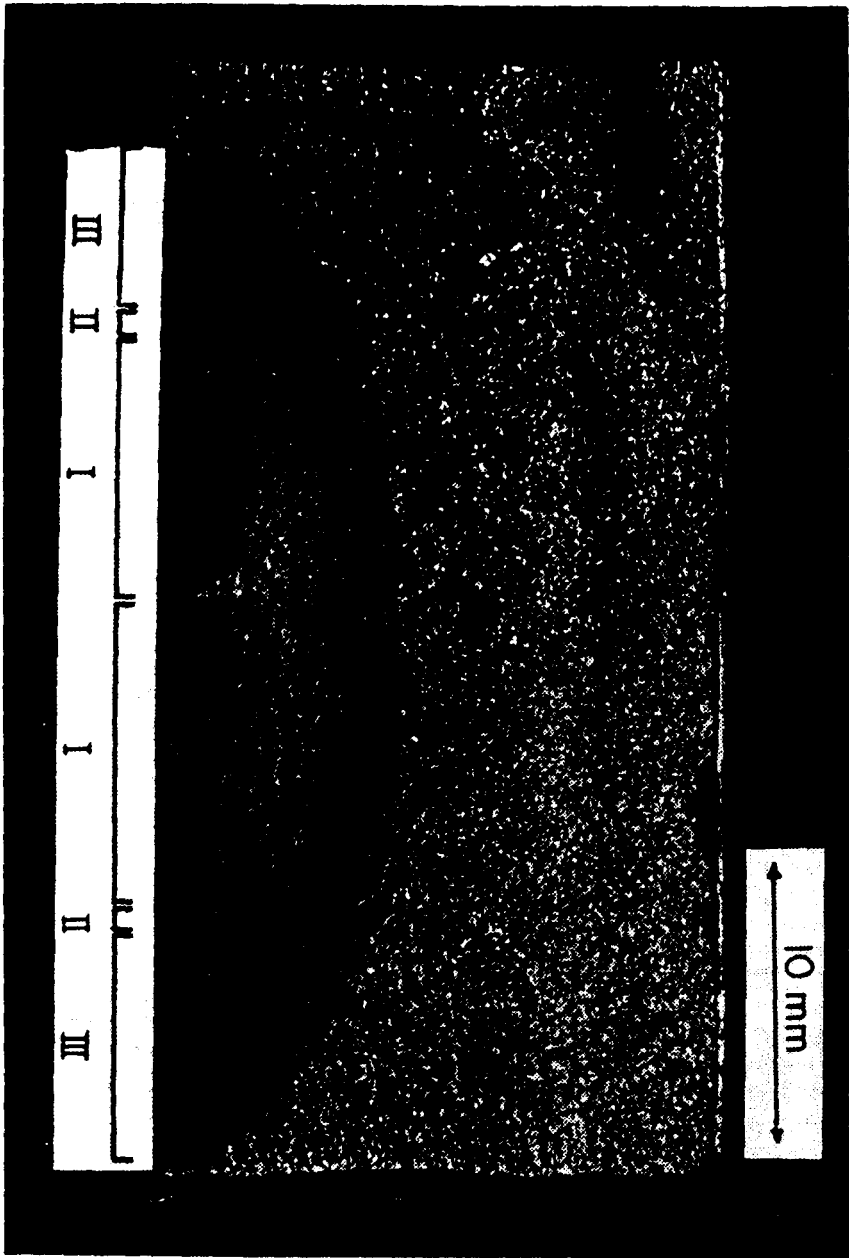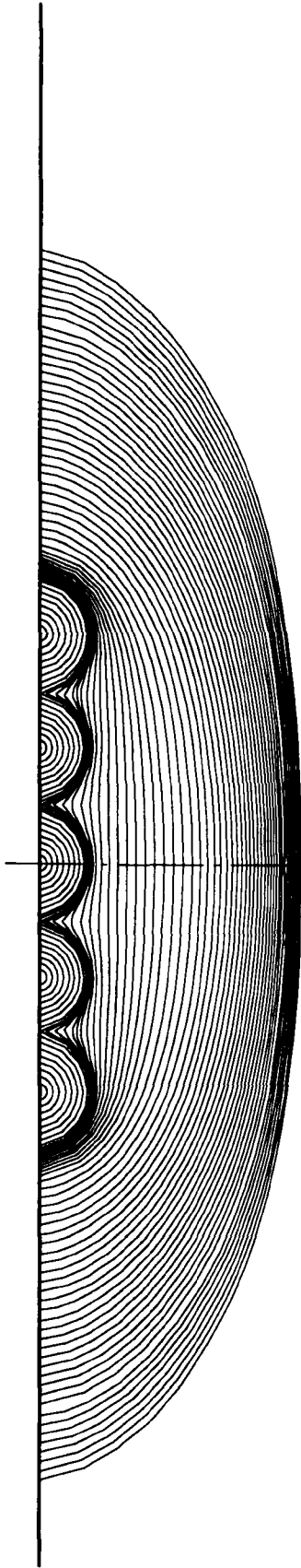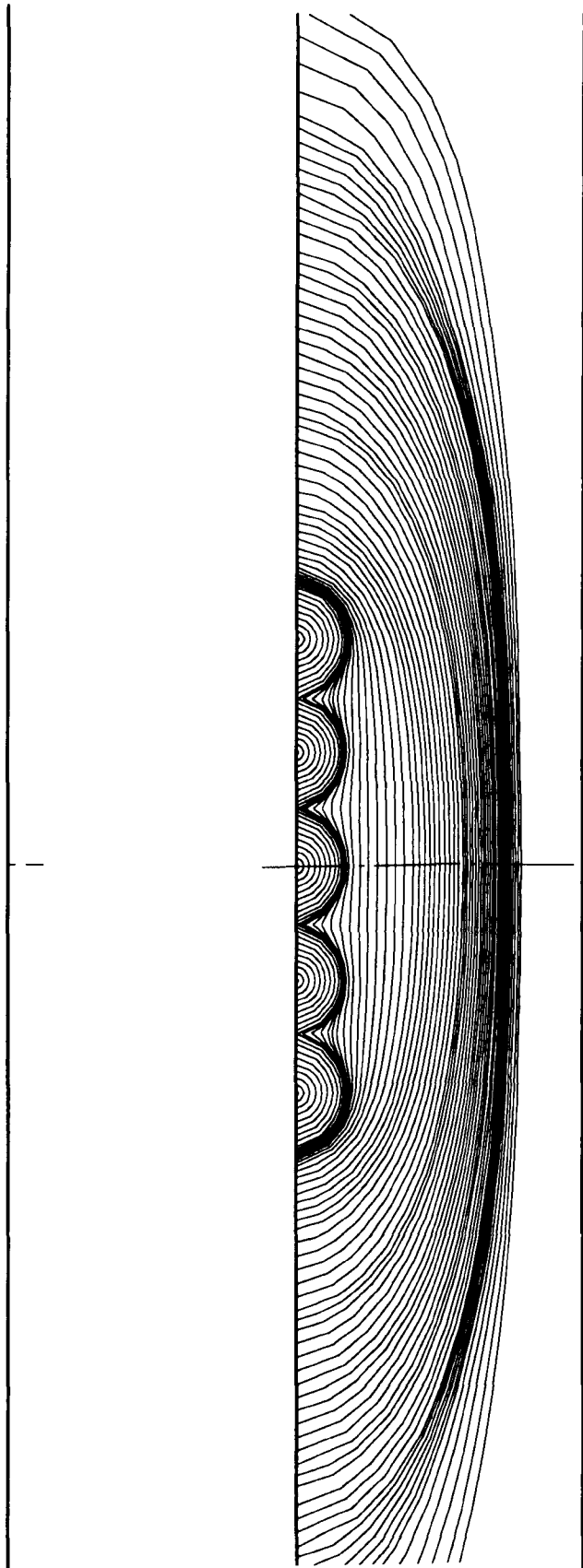a row of five initially semi-
circular small surface cracks
for DOB = 0.5

Figure 5.9   Shape development of
a row of five initially semi-
circular small surface
cracks under bending
(DOB = 1)

Actually, the bending component, as indicated in Chapter 4, makes it more difficult for a surface crack to advance along the plate thickness direction. As a result, the crack fatigued in pure bending grows to the flattest and longest profile, as shown in Fig. 5.9.

As seen in Figs. 5.5, 5.8 and 5.9, the crack shape change for each loading case is almost independent at the stage of pre-coalescence. Fig. 5.10 presents a more clear demonstration of this, in which the aspect ratio changes of cracks I, II and III within the plate under tension before coalescence are shown, where a and c represent the crack depth at the deepest point and the surface half-length of each crack, respectively. The aspect ratio variation for the single crack geometry is also plotted in Fig. 5.10 in dashed line for comparison. It can be found that the aspect ratio curves for all three cracks are difficult to identify separately and the a/c value is almost a constant, nearly 0.9. The difference between the single and multiple crack configurations is very small, which demonstrates that these initially semi-circular cracks grow almost independently and maintain a nearly unchanged shape until they coalesce. However, it can also be observed that interaction does appear when adjacent cracks nearly come into contact, leading to a weak decrease of the aspect ratio for the multiple crack configuration compared with the single crack geometry. A further demonstration will be given later.

Figure 5.10   Variation of aspect ratios with depth growth before coalescence

Fig. 5.11 shows the aspect ratio variation at all three stages for the crack under tension, in which a and c have different definitions for different stages as shown in the figure. The sudden decrease in aspect ratio, a/c, is due to the merging of the adjacent cracks and represents the beginning of the coalescing process. It is obvious that the aspect ratio variation

Figure 5.11 Variation of aspect ratios with depth growth throughout the plate thickness under pure tension (DOB = 0)

is unable to reflect the actually significant shape change during the coalescence period, which is shown in the enlarged region in Fig. 5.5, since only the crack sizes at depth and surface points are considered. But the crack shape change after coalescence is essentially able to be described by an aspect ratio curve if the crack profile is considered to be approximately semi-elliptical. It is also clear that at the post-coalescence stage the single smooth convex surface crack grows so that it follows a preferred propagation pattern which has been obtained and extensively discussed by the present author in Chapter 4. When the crack approaches very closely the back surface of the plate, a slightly accelerating rise in aspect ratios also occurs, as seen in Chapter 4. In Fig. 5.11 three different stages of crack growth are marked based on an approximate judgment of the obtained crack shape development.

The aspect ratio changes for DOB = 0.5 and 1 are, respectively, shown in Fig. 5.12 and 5.13. Compared with the aspect ratio change for DOB = 0 in Fig. 5.11, it can be seen that prior to coalescence the aspect ratio variations are similar for all three cases and the

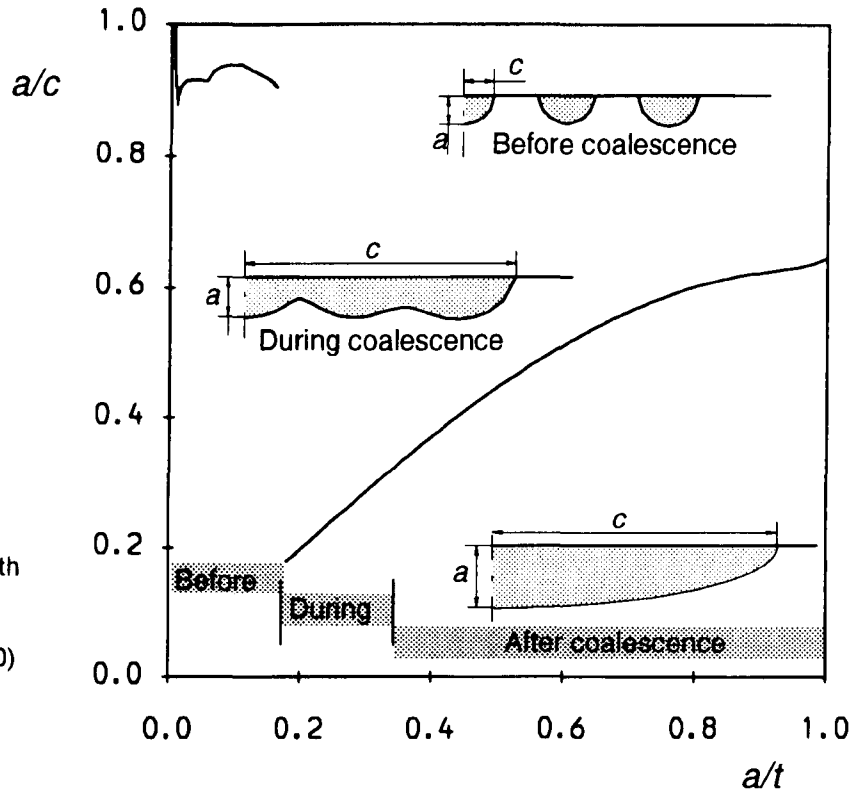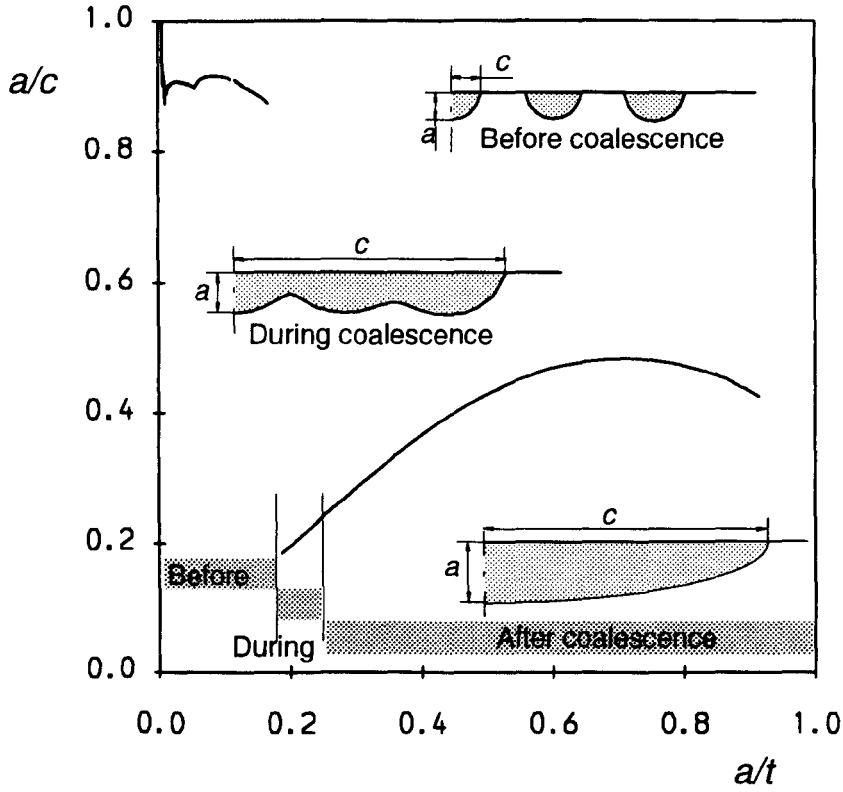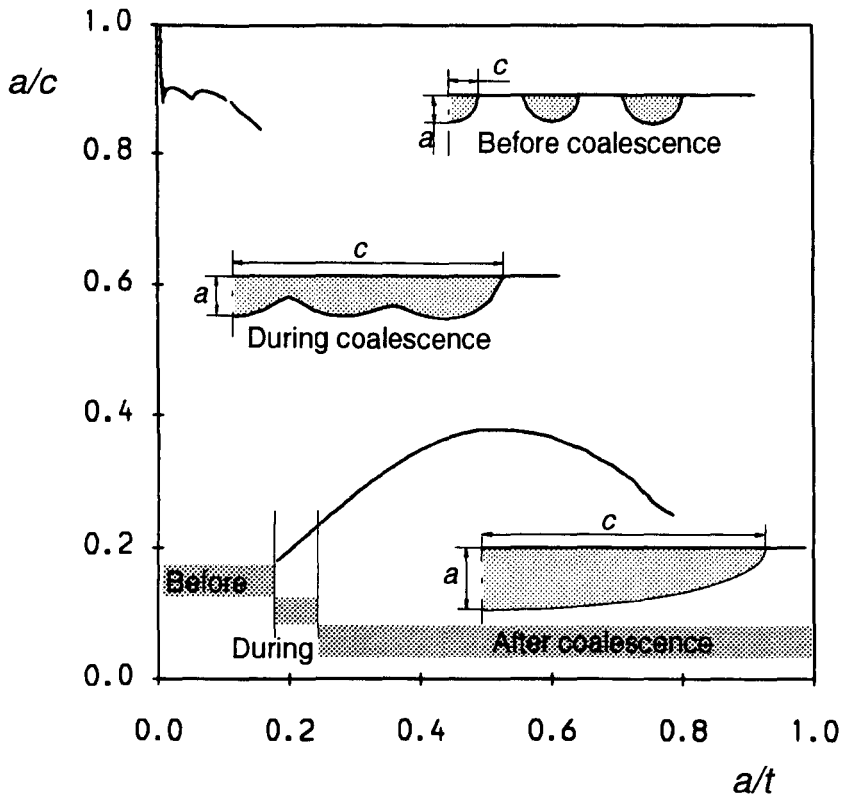Figure 5.12 Variation of aspect ratios with depth growth throughout the plate thickness for DOB = 0.5

Figure 5.13 Variation of aspect ratios with depth growth throughout the plate thickness under pure bending (DOB = 1)

coalescence occurs at nearly the same a/t, about 0.16. The difference between them is that the aspect ratio value slightly decreases with an increase of the DOB value when the coalescing process begins. This further demonstrates that the bending component has little influence on the crack shape change at the pre-coalescence stage. However, the influence gradually increases with the further growth of the coalesced crack. The aspect ratio variations, similar to the results obtained in Chapter 4, tend towards their preferred propagation patterns. The larger the DOB value is, the more quickly the crack grows along the surface direction and the harder the crack advances in the depth direction, finally leading to the decreasing a/c value as the crack approaches the back surface of the plate. The coalescing stage is also indicated in both Fig. 5.12 and Fig. 5.13.

5.4 SIF Variations during Different Crack Growth Stages

As indicated previously, the prediction of crack shape development is actually based on the estimate of SIF variations around the crack front through the Paris crack growth law. Revealing the SIF variation characteristics during the fatigue process enables one to understand the crack shape change at different growth stages.

Fig. 5.10 has compared the aspect ratio changes during the pre-coalescence period between the multiple and single crack configurations and concluded that the interaction between the adjacent cracks is very weak even as adjacent cracks approach very closely to each other. Fig. 5.14 further examines the interaction by comparing the SIF variations against the dimensionless crack depth, a/t, at the depth point A and surface point B of the multiple crack geometry with those of the single crack geometry. The vertical solid line in Fig. 5.14 represents the depth position of crack I at which cracks I and II come into contact. It is seen that for either the multiple or single crack cases the stress intensity factor at the point B is very close to but slightly larger than that at the point A as the a/t value increases. There is also an excellent agreement between both the multiple and single crack cases, except that from the value of about $a/t = 0.1$ the SIF values at both points for the multiple crack case gradually

become larger than those at the corresponding points of the single crack, but their maximum deviation values are less than 7% and 5% for the points A and B, respectively. The comparison in Fig. 5.14 also confirms that the interaction between the adjacent cracks does exist but seems to be very limited even when they approach each other very closely.
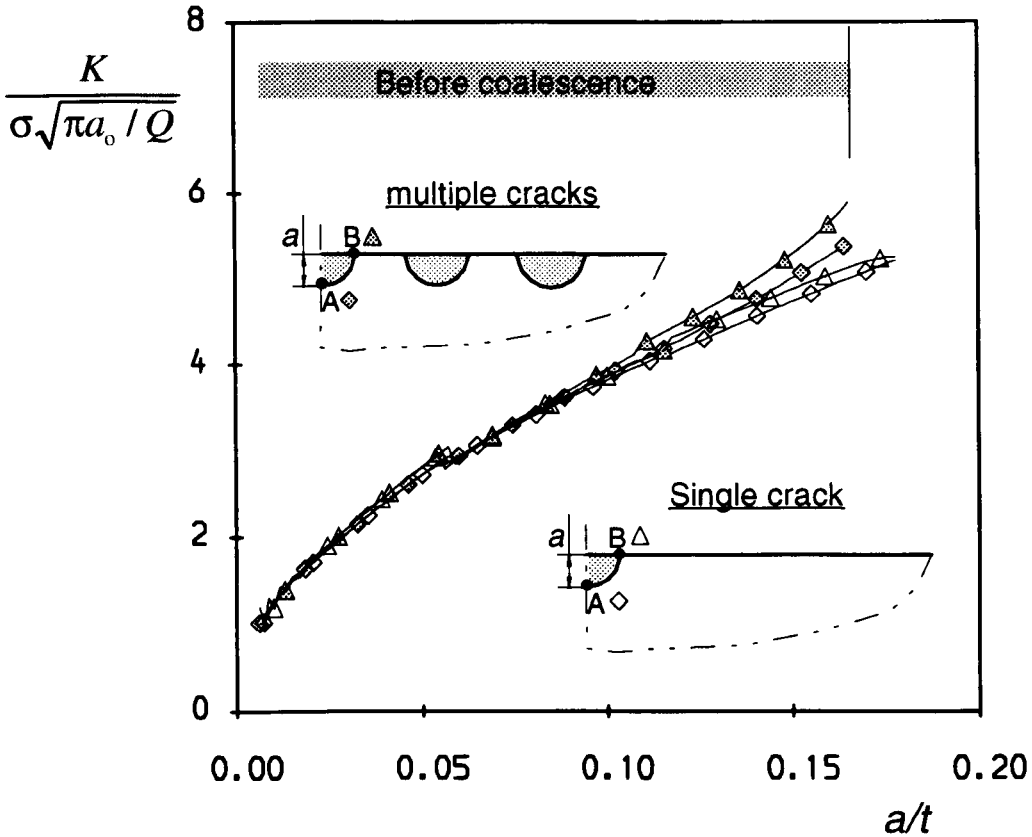
Figure 5.14 SIF Comparison of between multiple and single
crack configurations before coalescence for DOB = 0,
$(Q = 2.464, a_0 = 0.15mm)$

In Fig. 5.15, the SIF variations around the front of the tension crack at the four points of interest (A, B, E and H) during coalescence are plotted against the elapsed fatigue cycles, normalised by the number of cycles required for the tension crack to reach the back surface of the plate. The stress intensity factors at both concave locations show a sudden rise when the adjacent crack tips come into contact, and subsequently reach their maximum value which is about three times that at A and H at the same stage. The SIF value at the concave position then decreases as the crack evolves to become a smooth convex profile. It is also clear from Fig. 5.15 that the coalescence happens earlier between cracks II and III than does that

between cracks I and II. On the other hand, the SIF values at points A and H seem to increase with an increase of the crack area as usual, and do not appear to be influenced by the significant shape change of the crack. Similar results have also been reported by Kishimoto *et al.* (1989) after investigating the coalescence of twin surface cracks. However, it should be indicated that there is also a sudden drop in SIF at the same N/N_o position of the four curves during the period of coalescence. This is because the mesh type of FE models was changed there for the requirement of further numerical simulation. Sometimes, it is very difficult to avoid such a change of FE mesh type for convenience of the successive crack growth simulation.
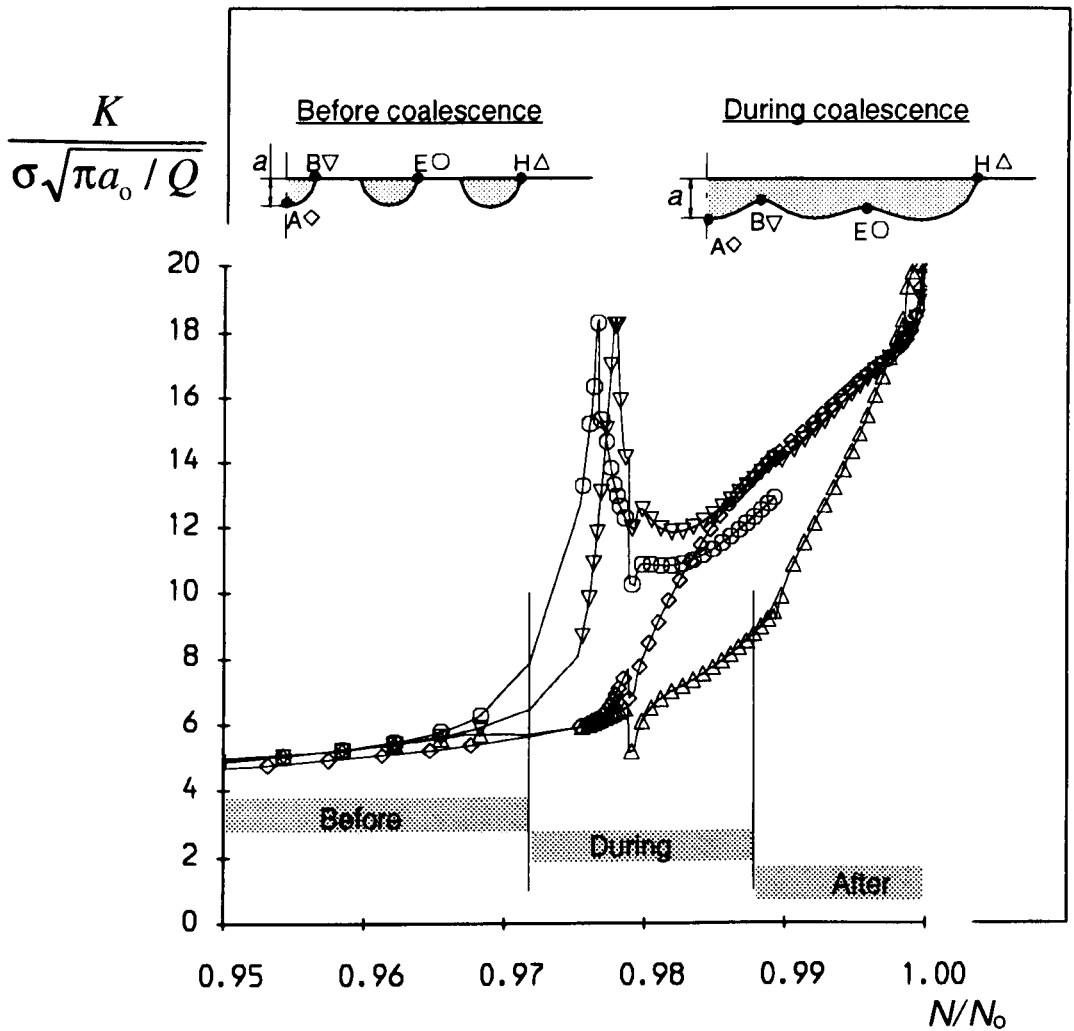
Figure 5.15   SIF variations at several points with crack development during coalescence for DOB = 0

The SIF variations at the four points of interest for both DOB = 0.5 and 1 are shown in Figs. 5.16 and 5.17, respectively. Compared with the results for the DOB = 0 loading case shown in Fig. 5.15, it can be found that the highest SIF which occurs during the coalescing process decreases with an increase of the DOB value. It is also clear that the coalescing process delays when the bending component of the fatigue load increases.
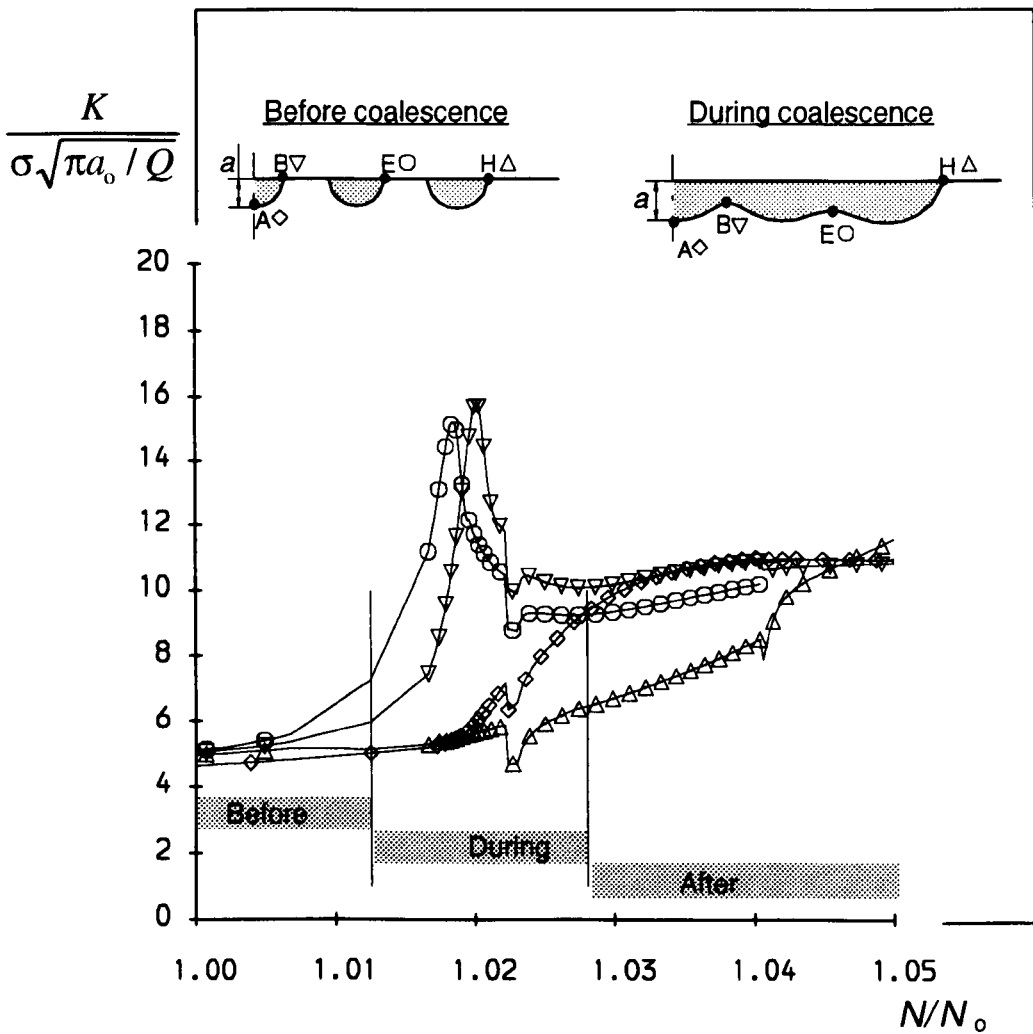
Figure 5.16 SIF variations at several points with crack development during coalescence for DOB = 0.5
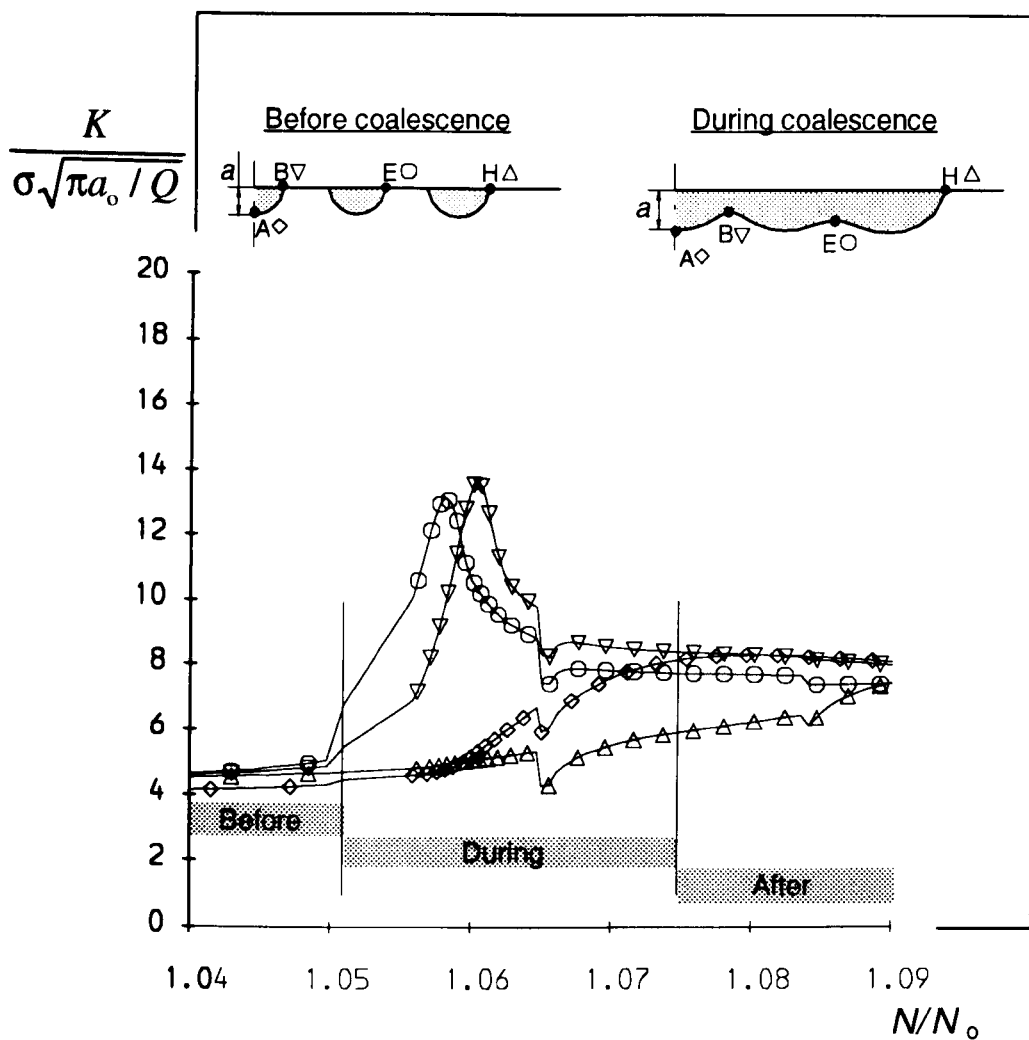
Figure 5.17   SIF variations at several points with crack
development during coalescence for DOB = 1

Fig. 5.18 shows the variations of the ratio of the minimum to maximum stress intensity factor (K_{min}/K_{max}) along each crack profile with the normalised crack depth a/t for all three different combinations of tension and bending loads. Only the ratio trend of crack I at the precoalescence stage is presented by considering its similarity to the other two. It can be seen that before coalescence the stress intensity factors along each crack front are nearly the same, the larger DOB value causes slightly greater deviation of the K_{min}/K_{max} value from unity. However, when the inner tips of the adjacent cracks touch, the difference of the stress intensity factors along the combined crack front suddenly becomes significant due to a sudden SIF increase at the concave position, as shown in Figs 5.15, 5.16 and 5.17. For all three loading cases, the ratios decrease very rapidly to their lowest values *(about 0.3 for DOB = 0,*

slightly greater for a larger DOB value) but subsequently increase during the coalescence period. As the crack continues to advance, the ratio for the pure tension crack tends toward one, which means the stress intensity factors along the crack front tend to be equal. For both DOB = 0.5 and 1, a similar trend can be seen in that the ratio curve reaches its highest point (*about 0.93 for DOB = 0.5 and 0.9 for DOB = 1*) earlier than that for DOB = 0. However, these nearly iso-*K* profiles cannot be maintained as the crack approaches the back surface of the plate, as has been discussed in Chapter 4 and Lin and Smith (1994). The ratio for the bending crack shows the most rapid drop. Except for the sharp changes of the ratio during coalescence, the other sudden or non-smooth variations of the ratios are mainly caused by the modification of the FE mesh type.
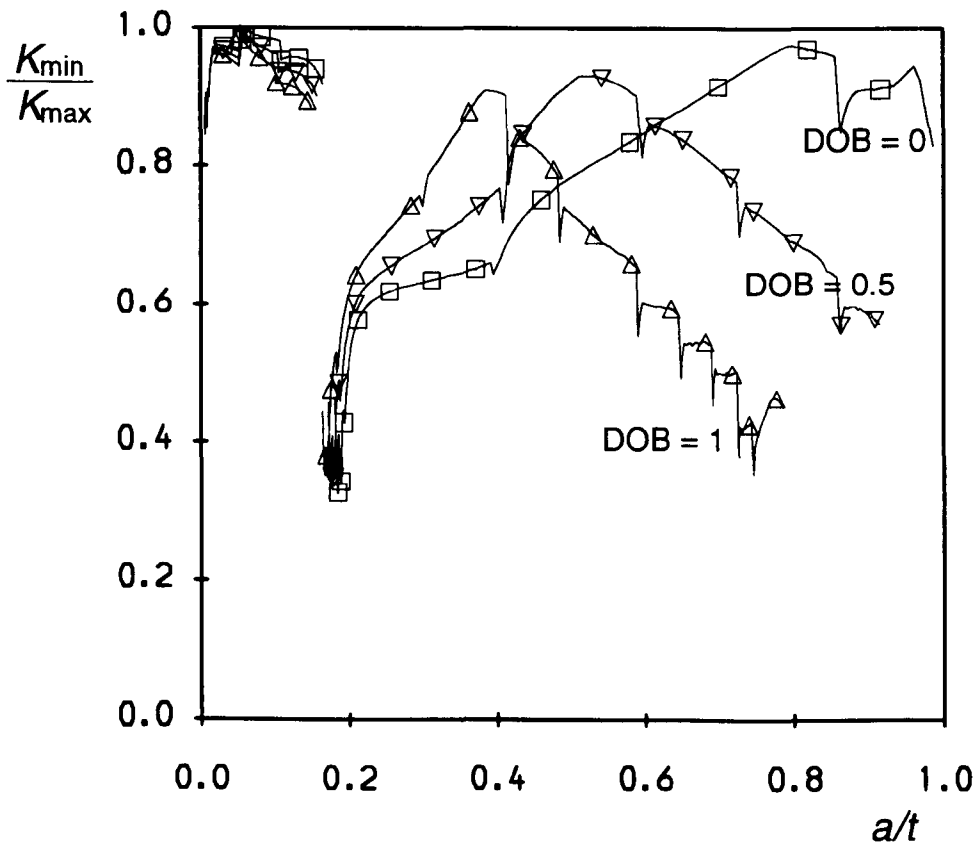
Figure 5.18   Variation of K_{min}/K_{max} along the crack front
with depth growth for different DOB values

5.5 Crack Growth Curves

The relations of fatigue cycles with the crack depth for DOB = 0.0, 0.5 and 1.0 are plotted in Fig. 5.19. The axis of the fatigue cycle is also normalised by the number of load cycles taken to propagate the initial small cracks to the back surface of the plate under pure tension. At the pre-coalescence stage, the crack depth a in Fig. 5.19 is represented by that of crack I. The relation of fatigue cycles against the crack surface length is not presented here, which can be readily obtained from the aspect ratio variations shown in Figs 5.5, 5.8 and 5.9. In Fig. 5.19 the starting and ending positions of each coalescing process are marked. It is found that for the tension cracks most of the fatigue cycles, approximately 97% of the total cycles, is spent in growing the initial cracks to touch, and so a small number of fatigue cycles is needed for both the coalescence and post-coalescence stages. Similar fatigue growth curves are also predicted for both DOB = 0.5 and 1. This is, of course, due to the initially small size of the semi-circular cracks and the exponential nature of the fatigue crack growth law. It is also obvious in Fig. 5.19 that for a larger DOB value the coalescence begins slightly later, and the crack advance in the direction of crack depth becomes more difficult, which can be easily understood by
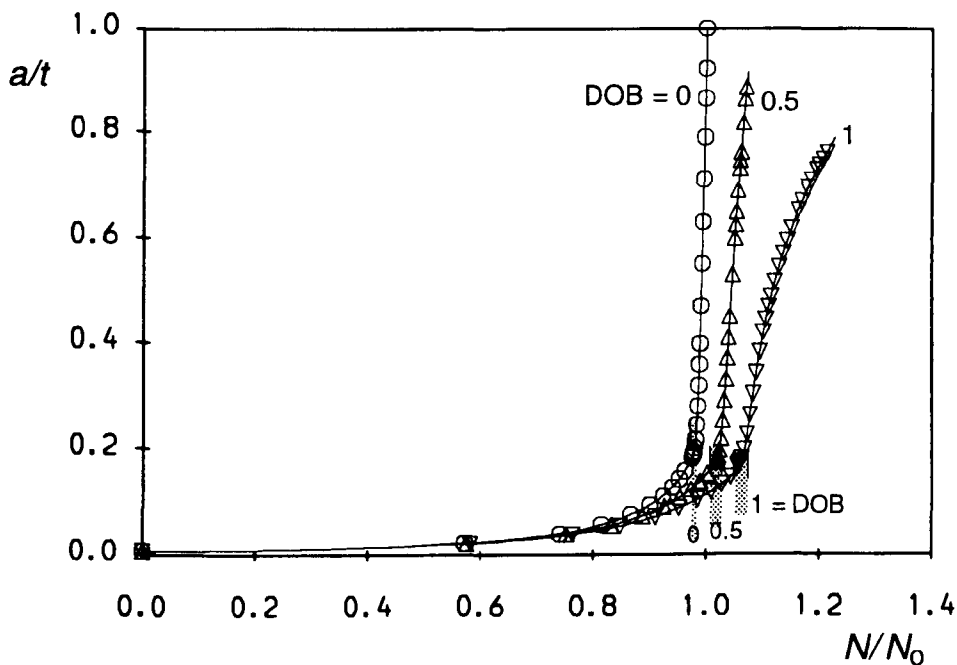
Figure 5.19   Crack growth curves predicted by the present simulation technique for all three different fatigue loads

Figure 5.20   Comparison of crack growth curves predicted by the present technique
and by the simplified methods for DOB = 0

considering the effect of the DOB value on the stress intensity factor at the crack depth position.

Fig. 5.20 shows a comparison of the fatigue growth curves for pure tension cracks predicted by the present numerical simulation technique and by two simplified methods. The comparison is focused on the crack growth stage excluding the non-interaction region of pre-coalescence. For this purpose, a particular multiple crack profile, as shown in Fig. 5.20, for which the interaction is considered to have occurred according to the ASME XI or BSIPD 6493 codes, is selected as the initial calculation profile for the fatigue cycle prediction (*i.e. the fatigue cycle is specified as zero for the particular crack configuration*), instead of the five initially semi-circular small cracks. The simplified computations include the ASME XI code recommendation that when $s \le 2a_{max}$ the adjacent two cracks should be re-characterised by a single elliptical crack that covers them, and fatigue crack growth in the depth direction should
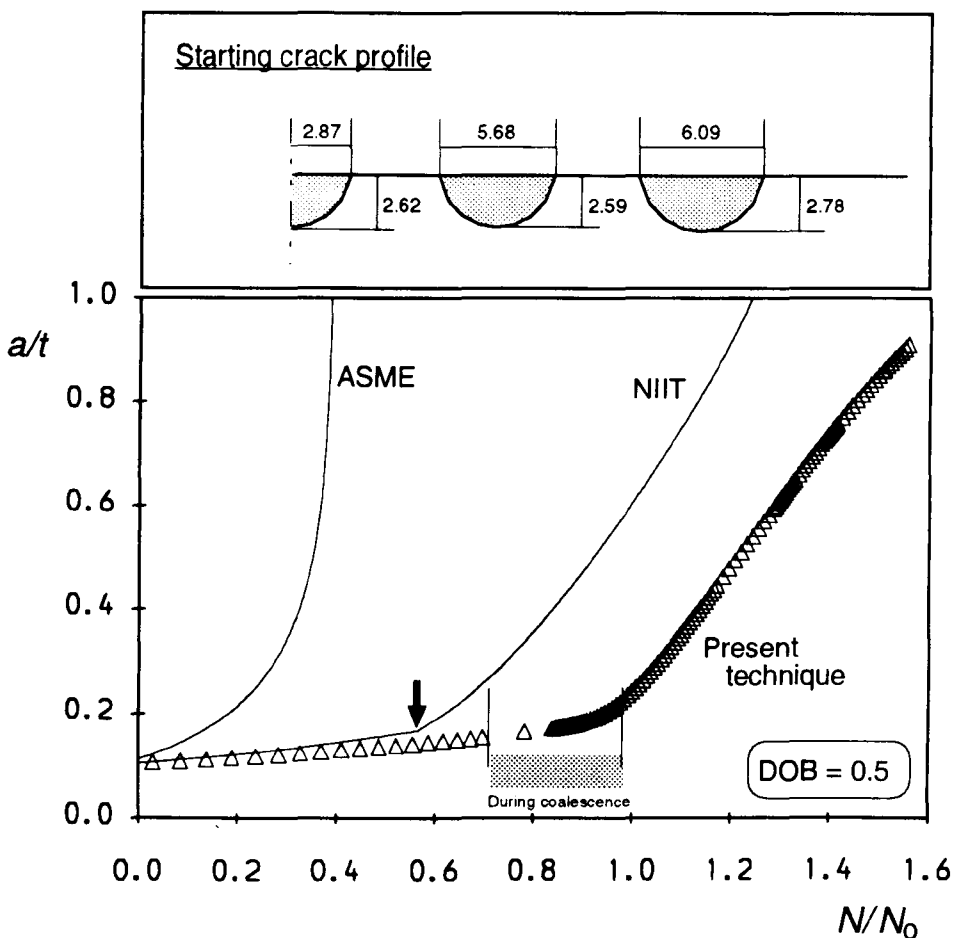
Figure 5.21   Comparison of crack growth curves predicted by the present technique and by the simplified methods for DOB = 0.5

be calculated using the Paris law and the surface length of the crack is obtained by assuming the crack grows to a geometrically similar larger flaw, i.e. constant aspect ratio, a/c. The other simplified method is similar to that suggested by Grandt (1986) and McComb et al. (1986), which assumed that no interaction before coalescence occurred, the transition from two cracks to one crack began instantaneously when the crack tips touched and neglected the region of coalescence. This method is herein called 'no interaction and immediate transition (NIIT)'. Newman and Raju's (1981) SIF equation was employed in both simplified methods. The comparison in Fig. 5.20 shows that both simplified methods overestimate the crack depth compared with the present simulation method due to the omission of the coalescence. The earlier re-characterisation of multiple cracks to a single crack, and the unreasonable constant aspect ratio assumption suggested by the ASME XI leads to the most conservative prediction.
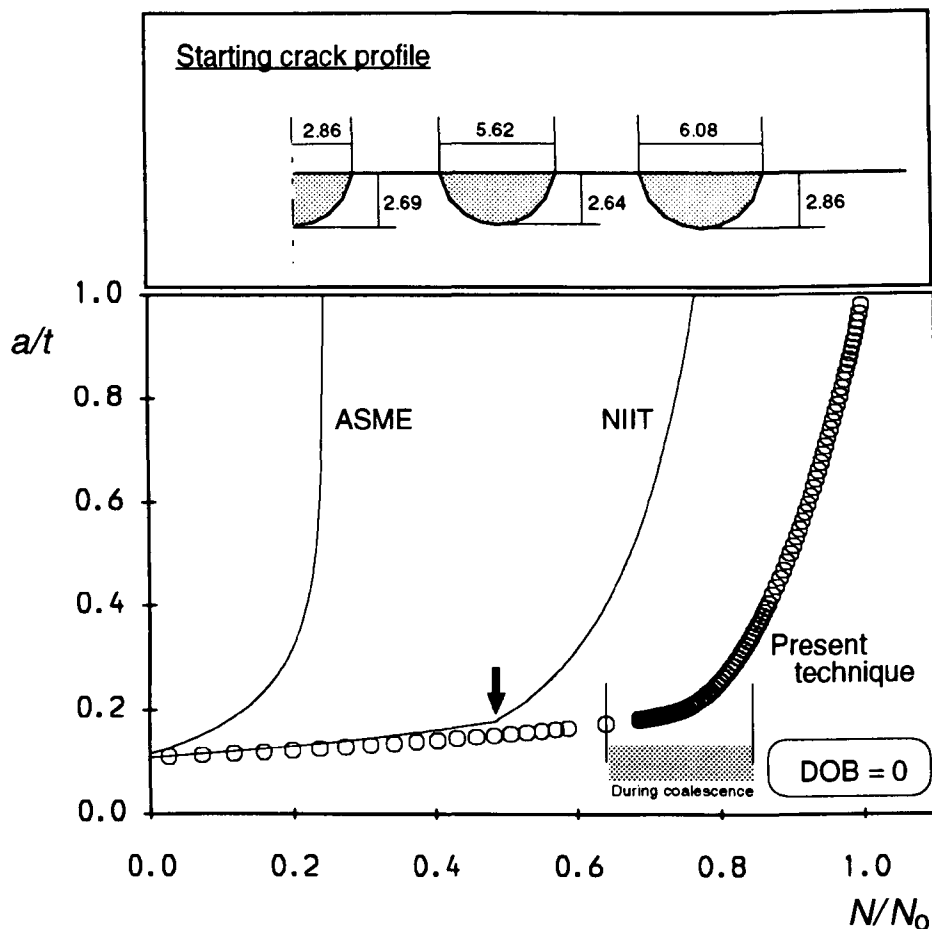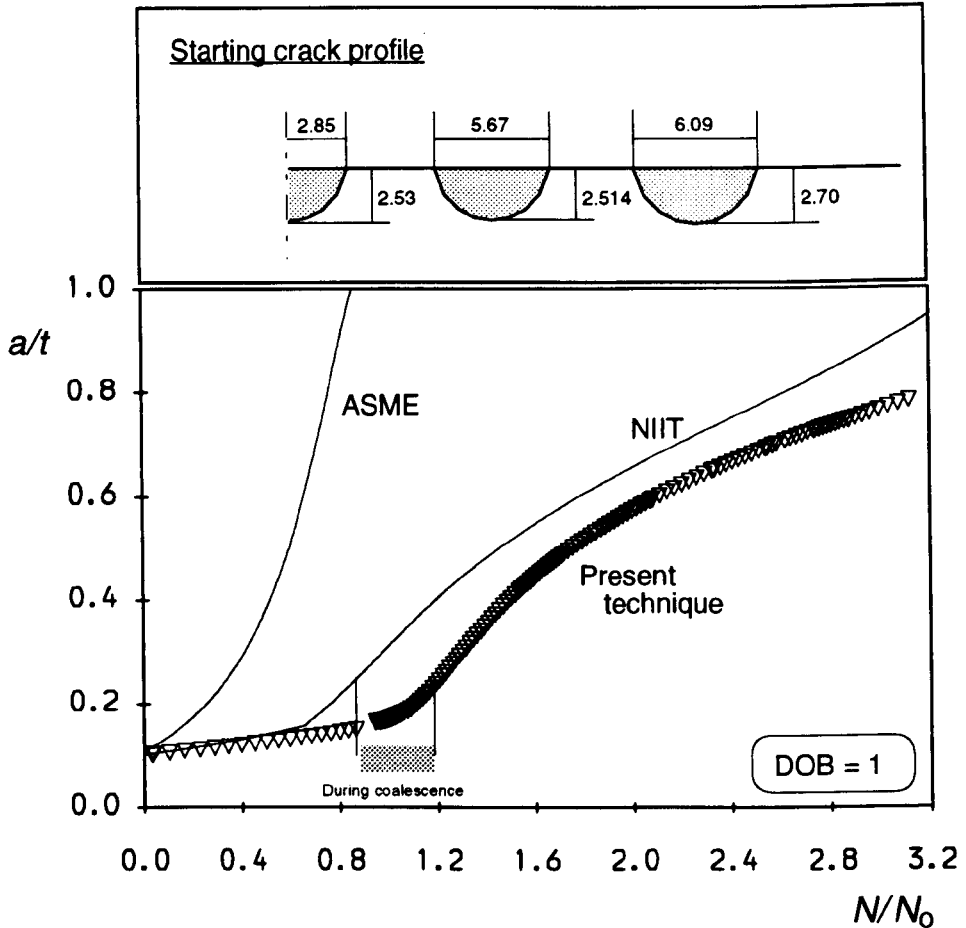
Figure 5.22   Comparison of crack growth curves predicted by the present technique
and by the simplified methods for DOB = 1

It should be indicated that the 'NIIT' simplified method predicts the earlier touching of the adjacent cracks, as marked in Fig. 5.20 by an arrow, than the present FE simulation technique, which is probably because, prior to coalescence, the SIF values along the computed crack front obtained by the present technique are somewhat lower than those around the corresponding semi-elliptical profiles which are assumed in the 'NIIT' simplified method. However, if the difference of the fatigue cycles before coalescence is removed, it can still be found that the 'NIIT' method estimates a slightly larger crack depth than the present simulation method, which can be understood by considering the effect of neglecting the coalescence period in the simplified analysis. It, therefore, appears that the 'NIIT' method is always more conservative than the present technique, but significantly less conservative than the ASME XI code which is usually considered to be too conservative for practical applications.

The fatigue growth predictions for both DOB = 0.5 and 1 cracks obtained by the present simulation technique are also compared, respectively, in Fig. 5.21 and Fig. 5.22 with those obtained by the ASME code and the 'NIIT' simplified method. Similarly, a particular starting configuration is selected for each loading case. This crack configuration is one of the crack profiles predicted by the present technique at the pre-coalescence stage, and should be simplified to a single crack according to the ASME XI code,. It can also be seen that the ASME code predicts quite conservative results, and the 'NIIT' method gives slightly less conservative predictions for both DOB = 0.5 and 1 compared with those by the present simulation technique.

5.6 Conclusions

The fatigue growth of a row of five small initially semi-circular surface defects under different combinations of tension and bending loads, through three different crack growth stages, i.e. pre-coalescence, coalescence and post-coalescence, has been analysed using the step-by-step finite element simulation technique. The following conclusions are drawn:

1) The shape development of initially multiple fatigue cracks has been successfully modelled through the pre-coalescence, coalescence and post-coalescence stages by using the present finite element simulation technique.

2) Fatigue growth of multiple cracks prior to coalescence was compared with that of a single crack. It is shown that these coplanar initially semi-circular surface cracks grow almost independently and the interaction between them is very limited even as they approach each other very closely.

3) During coalescence the stress intensity factor at the concave point where the adjacent cracks touch reaches a high value along the combined crack front, which results in a rapid transition to a single smooth convex crack. As the crack evolves to form a smooth profile, the high SIF value at the coalescence region subsequently decreases. The SIF values remote from the region of coalescence increase monotonically with crack development and are not affected by the significant crack shape changes.

4) Simplified computations according to the ASME XI code and the 'no interaction and immediate transition' method estimate the crack growth more conservatively than the present FE simulation technique. However, the 'NIIT' simplified method is significantly less conservative than the ASME XI code which is usually considered to severely underestimate fatigue lives in practical applications.

5.7 References

A.S.M.E. Boiler and pressure vessel code, section XI (1977) Rules for in-service inspection of nuclear power plant components.

British Standards Institution (1980) *Guidance on some methods for the derivation of acceptance levels for defects in fusion welded joints.* Section 3, BSIPD 6493.

Chang, R. (1982) *On crack-crack interaction and coalescence in fatigue.* **Engng Fract. Mech. 16(5),** 683-693.

Grandt, A. F., Jr. (1986) *An experimental and numerical investigation of the growth and coalescence of multiple fatigue cracks at notches.* ASTM STP **905,** 239-252.

Heath, B. J. and Grandt, A. F. (1984) *Stress intensity factors for coalescing and single corner flaws along a hole bore in plate.* **Engng Fract. Mech. 19(4),** 665-673.

Iida, K. (1983) *Shapes and coalescence of surface fatigue cracks.* Proceedings of ICF International Symposium on Fracture Mechanics, Beijing, China, 22-25, November, 1983, 679-693.

Kishimoto, K., Soboyejo, W. O., Smith, R. A. and Knott, J. F. (1989) *A numerical investigation of the interaction and coalescence of two coplanar semi-elliptical fatigue cracks.* **Int. J. Fatigue 11(2),** 91-96.

Kobayashi, A. S. (1976) crack *opening displacement in a surface flawed plate subjected to tension or plate bending.* Proceedings of 2nd International Conference on Mechanical Behaviour of Materials, ASME, 1073-1077.

Kobayashi, A. S. and Moss, W. L. (1969) *Stress intensity magnification factors for surface flawed tension plate and notched round tension bar.* Proceeding of 2nd International Conference on Fracture.

Lin, X. B. and Smith, R. A. (1994) *Numerical simulation of fatigue crack growth of a surface defect.* submitted to **Fatigue Fract. Engng Mater. Struct.**

McComb, T. H., Pope, J. E. and Grandt, A. F., Jr., (1986) *Growth and coalescence of multiple fatigue cracks in polycarbonate test specimens.* **Engng Fract. Mech. 24**(4), 601-608.

Melin, S. (1983) *Why do cracks avoid each other?* **Int. J. Fracture 23**, 37-45.

Miyoshi, T., Shiratori, M. and Tanabe, O. (1985) *Stress intensity factors for surface crack with arbitrary shapes in plates and shells.* ASTM STP **868**, 521-534.

Morgan, H. G. (1986) *Fatigue crack shape development in cracked plates and welded joints.* Proceedings of International Conference on Fatigue and Crack Growth in Offshore Structures, 7-8, April, 1986, Proc. Inst. Mech. Eng.

Murakami, Y. and Nisitani, H. (1981) *Stress intensity factors for interacting two equal semi-elliptical surface cracks in tension.* Trans. Japan Soc. Mech Engrs., Ser. A. **47**(415), 295-303.

Murakami, Y., and Nemat-Nasser, S. (1982) *Interacting dissimilar semi-elliptical surface flaw under tension and bending.* **Engng Fract. Mech. 16**, 373-386.

Murakami, Y. and Nemat-Nasser, S. (1983) *Growth and stability of interacting surface flaws of arbitrary shape.* **Engng Fract. Mech. 17**, 193-210.

Newman, J. C., Jr. and Raju, I. S. (1981) *An empirical stress intensity factor equation for the surface crack.* **Engng Fract. Mech. 15**, 185-192.

O'Donoghue, P. E., Nishioka, T. and Atluri, S. N. (1984) *Multiple surface cracks in pressure vessels.* **Engng Fract. Mech. 20**, 545-560.

O'Donoghue, P. E., Nishioka, T. and Atluri, S. N. (1985) *Multiple coplanar embedded elliptical cracks in an infinite solid subject to arbitrary crack face tractions.* **Int. J. num. Meth. Engng 21**, 437-449.

Soboyejo, W. O., Kishimoto, K., Smith, R. A. and Knott, J. F. (1989) *A study of the interaction and coalescence of two coplanar fatigue cracks in bending.* **Fatigue Fract. Engng Mater. Struct. 12**(3), 167-174.

BLANK PAGE
IN
ORIGINAL

Chapter 6

EXTERNAL SURFACE CRACKS IN INTERNALLY PRESSURISED CYLINDERS

In this chapter, the fatigue growth characteristics of external surface cracks in internally pressurised cylinders were numerically studied by the finite element step-by-step technique. A new method of stress linearisation through the wall was proposed and combined with Newman and Raju's flat plate SIF equation to produce a simplified assessment for external surface cracks. An investigation of the SIF accuracy for the present finite element analysis was made by comparing with existing SIF solutions. The deviation of fatigue crack shape from the semi-ellipse was also studied. It is shown that the external surface crack during the growth process basically can retain an approximate semi-ellipse. A variety of results, such as aspect ratio changes, stress intensity factor variations and relations between the fatigue crack depth and fatigue cycles, were also obtained by both the simulation technique and the simplified method, and compared with each other. The comparison shows that the simplified method can predict aspect ratio changes nearly as well as the present finite element simulation does, but generally overestimates the stress intensity factors and the fatigue crack depth, compared with the present numerical technique. These results presented in this chapter are of great significance for the assessment of practical external surface cracks.

6.1 Introduction

External surface cracks are probably found in pressure vessels, particularly at welds. How to assess effectively the external surface cracks subjected to static or fatigue loading, obviously, is of great engineering significance.

An internally pressurised cylindrical vessel with no attachments at both ends, as shown in Fig. 6.1, has a non-linear circumferential stress distribution (*normal to the crack plane*) through the wall thickness, and the maximum stress occurs at the inner surface of the vessel and the minimum at the outer surface. The well known Lame equation (Timoshenko, 1956) has analytically described the stress variations along the wall thickness. It can be seen that if the curvature of a cylinder is neglected, an external surface crack in an internally pressurised cylinder is similar to a surface crack in a flat plate that has the same thickness and is subjected to the same non-linear tension stress as the cylinder has. Therefore, the external surface is often treated as a surface crack in a flat plate which has been extensively studied.

However, due to the unavailability of SIF solutions for a general non-linear load, the linearisation of the stress distribution along the wall is required, if the stress intensity factor equations for surface cracks in plates subjected to tension or bending are used. Both ASME XI (1977) and BSIPD 6493 (1980) have also recommended such a linearisation to make the analysis simplified. Both documents indicated that all stresses at the flaw location should be taken into account, and a non-linear stress distribution should be "conservatively" approximated by a linear one, and then the linear stress distribution obtained should be resolved into a tensile stress and a bending. The accuracy of the simplified analytical method depends principally on the effect of the curvature of the cylinder and the degree of the linear stress approximation to the actual non-linear stress distribution.

Connors (1984) suggested that the Lame stress variation along the wall should be linearised in the way that the same resultant force and bending moment are maintained. Using his stress linearisation criterion and Newman and Raju's (1981) SIF equations for surface cracks in flat plates, Connors predicted the shape changes of external surface cracks in thin $(t/R_i = 0.1)$ cylindrical vessels subjected to fatigue inner pressure, and also compared them with experimental results available. The comparison showed that the predictions were in good agreement with the experimental observations.
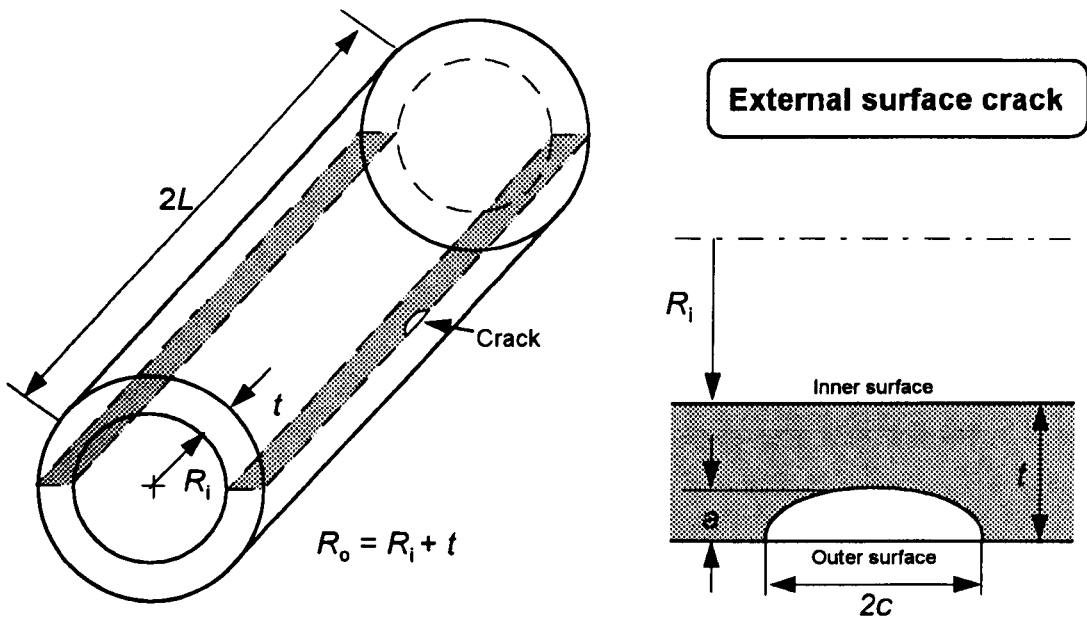
Figure 6.1   Cylindrical vessel with an external surface crack

A specific approach to external surface cracks under static loading was made by Atluri and Kathiresan (1979), Miyazaki *et al.* (1981) and Raju and Newman (1982), who all used 3D finite element methods to calculate stress intensity factors around semi-elliptical external cracks in pressurised cylinders. Atluri and Kathiresan (1979) and Miyazaki *et al.* (1981) only obtained SIF results for a limited range of configuration parameters, but Raju and Newman (1982) reported SIF estimates for a wide range of crack sizes (t/R_i = 0.1, 0.25; a/c = 0.2, 0.4, 1.0 and a/t = 0.2, 0.5, 0.8). These SIF results, obviously, are more accurate than those obtained by approximating a crack in a cylinder to an equivalent crack in a flat plate. Connors (1984) compared some SIF results at the two extremes of a semi-elliptical surface crack estimated by Raju and Newman (1982) using the FE method and those obtained from the flat plate approximation using his stress linearisation. The comparison showed that the SIF values generally agreed well, the disagreement being below 12%.

Conventional fatigue analysis, currently, can also be based on the flat plate approximation plus a stress linearisation combined with the "two-point plus semi-ellipse" method described in Chapter 4. But, specific fatigue analysis for such a crack has been difficult due to the unavailability of analytical SIF equations. It seems that no publications have been related to it.

In this chapter, the present author will perform the specific fatigue analysis for some initially semi-elliptical external surface cracks in two cylinders of different inner radius by using the automatic FE simulation technique. The fatigue growth behaviours, such as crack shape developments and deviations from semi-elliptical profiles, aspect ratio changes, stress intensity factor variations and fatigue growth curves are to be examined. A new method of stress linearisation, which is different from Connors' (1984), is also proposed herein. The results obtained by the present numerical simulation technique are compared overall with those calculated by the flat plate approximation using the present stress linearisation method.

6.2 A New Stress Linearisation Method

It is usually necessary to make a linearisation of the hoop stress through the vessel wall for the simplified assessment using the flat plate SIF equations. Both ASME XI and BSIPD 6493 suggested that the stress linearisation should be "conservatively" made in order to ensure the assessment results obtained to be absolutely conservative. As mentioned previously, Connors (1984) proposed a stress approximate method which assumes that the linearised stress field should have the same resultant force and bending moment as the Lame stress field. Connors' method seems to be a little bit complicated, and the conservative degree of both ASME XI and BSIPD 6493 requirements has not been demonstrated. The present author herein assumes a very simple stress linearisation for an internally pressurised cylinder.

Fig. 6.2 shows the hoop stress variation across the vessel wall obtained by the Lame equation:

$$\sigma_\theta = \frac{PR_i^2}{R_o^2 - R_i^2}\left(\frac{R_o^2}{r^2} + 1\right)$$ (6.1)

where R_i and R_o are the internal and external radii of a vessel, respectively, and P is the internal pressure. From Eq. (6.1) it can be obtained that the maximum and minimum stresses are, respectively,

$$\sigma_{\theta max} = \frac{P\left(R_o^2 + R_i^2\right)}{R_o^2 - R_i^2}; \quad \sigma_{\theta min} = \frac{2PR_i^2}{R_o^2 - R_i^2} \qquad (6.2)$$

where the maximum stress occurs at the inner surface of the vessel, whilst the minimum stress at the outer surface.

It is seen in Fig. 6.2 that using a straight line that connects both the maximum and minimum stress points easily linearises the Lame non-linear stress distribution. Such a stress linearisation is certainly conservative since the actual non-linear stress distribution is entirely below the straight line. The average stress value of the straight line is

Figure 6.2   Stress distribution along the vessel wall

$$\overline{\sigma_\theta} = \frac{P\left(R_o^2 + 3R_i^2\right)}{2\left(R_o^2 - R_i^2\right)} \qquad (6.3)$$

which is higher than the actual average stress

$$\overline{\sigma_\theta} = \frac{PR_i}{t} \qquad (6.4)$$

The linear stress variation through the vessel thickness can then be resolved into a tensile stress and a bending as follows

$$\sigma_t = \overline{\sigma_\theta} = \frac{P\left(R_o^2 + 3R_i^2\right)}{2\left(R_o^2 - R_i^2\right)}; \quad \sigma_b = \frac{\sigma_{\theta max} - \sigma_{\theta min}}{2} = \frac{P}{2} \qquad (6.5)$$
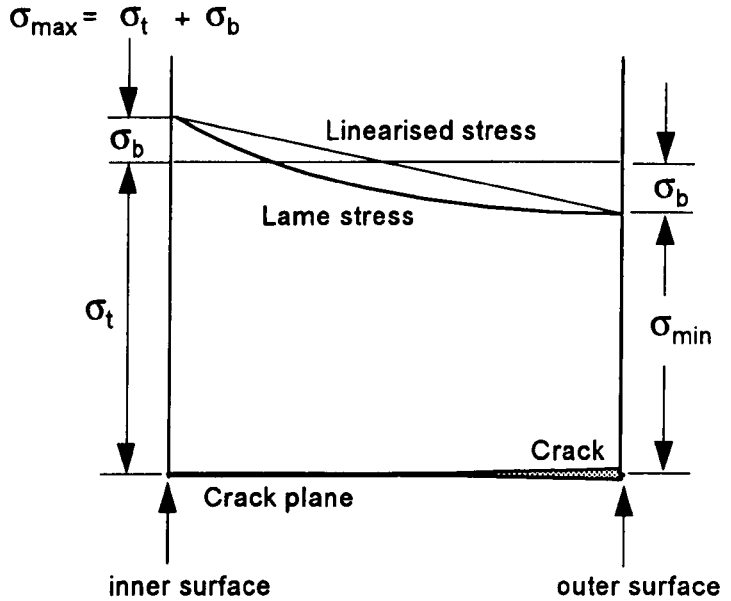
175

If the degree of bending (*DOB*) defined in Chapter 4 is still used, then we have

$$DOB = \frac{\sigma_b}{\sigma_b + \sigma_t} = -\frac{R_o^2 - R_i^2}{4R_i^2} \qquad (6.6)$$

Compared with Connors' (1984) stress linearisation resolution, it is clear that the present method is more conservative. Connors' resolution surely underestimates the actual stress at some locations of the wall, which may lead to a dangerous assessment conclusion.

Once the linearised stress is obtained, it is possible to assess a static or fatigue external surface crack in a cylinder using the flat plate SIF equations proposed by Newman and Raju (1981). If the fatigue assessment is performed, the conservative recommendations made by both ASME XI and BSIPD 6493, or the relatively accurate "two-points plus semi-ellipse" calculation, as described in Chapter 4, is required. This analytical procedure is also suitable for an internal surface crack in an internally pressurised cylindrical vessel.

6.3 Modelling Calculation Details

An external semi-elliptical surface crack in an open cylinder has been depicted in Fig. 6.1. The uniform pressure, *P*, is applied on the internal surface of the cylinder. Two different cylindrical vessels, t/R_i = 0.1 (25mm/250mm) and 0.2 (25mm/125mm), were examined. The length (2*L*) of the two cylinders was selected to be 800mm, which was considered to be large enough for it to have negligible effect on crack growth. Fatigue growth was simulated from six different initially semi-elliptical cracks ((0.2(a/t), 1.0(a/c)); (0.1, 0.5); (0.2, 1.2); (0.4, 0.2875); (0.4, 0.4) and (0.6, 1.2)) for the t/R_i = 0.1 vessel and five initially semi-elliptical cracks ((0.2, 0.2); (0.2, 0.4); (0.2, 0.6); (0.2, 0.8) and (0.2, 1.0)) for the t/R_i = 0.2 vessel.

Due to the symmetry of the geometry and loading, only a quarter of the cylinder was analysed by the FE method. All FE models were also created with the two blocks, i.e. cracked and uncracked blocks. Fig. 6.3 shows two pre-defined uncracked blocks, corresponding to the two cylinders of different size, with the help of the software FEMGV. The two uncracked blocks remained unchanged during the fatigue modelling computations, whilst the cracked

blocks, whose thickness is 6mm, were automatically formed by DUCKPRE from their 2D crack plane meshes and then reassembled to a corresponding uncracked block after each successive increment of crack growth. During the formation of a 3D cracked block, the 3D cracked block mesh was expanded in the same way as that for a flat plate and was then deformed into a part of the cylinder. A typical deformed 3D cracked block mesh is shown in Fig. 6.4. The total number of degrees of freedom for the 3D FE models created was between 9408 and 9675.
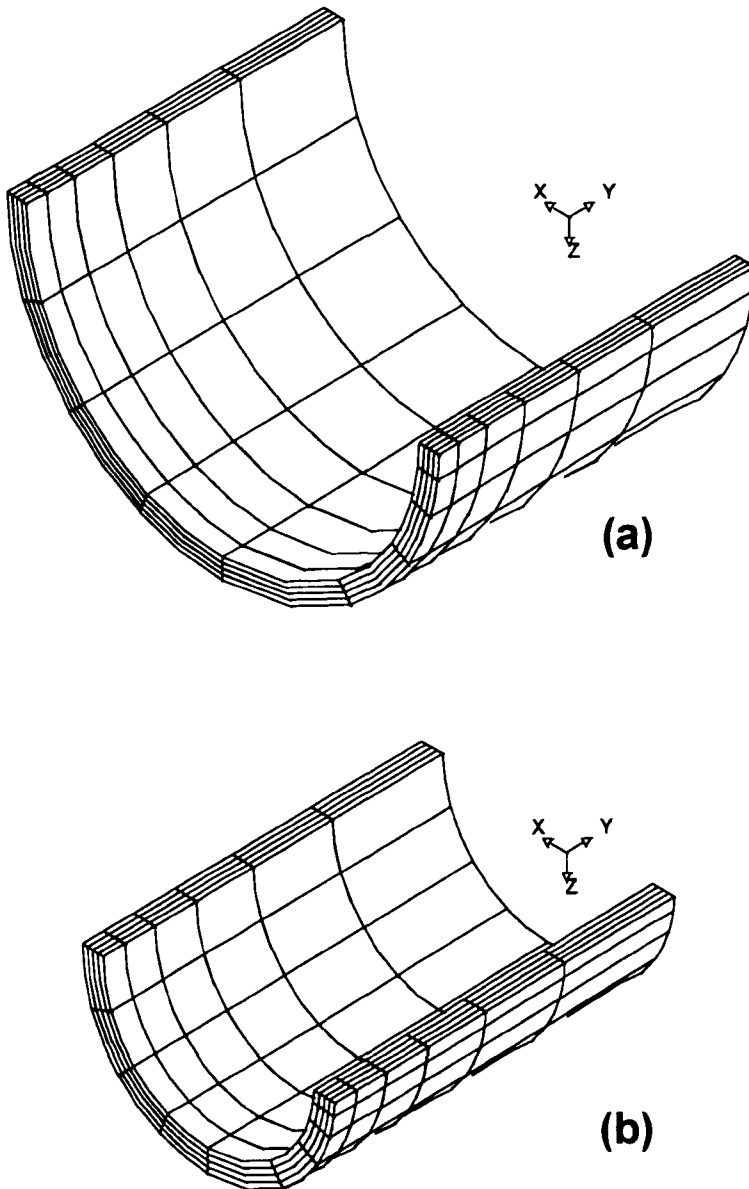
Figure 6.3   Two uncracked blocks used in modelling computations;
(a) t/R_i = 0.1, (b) t/R_i = 0.2
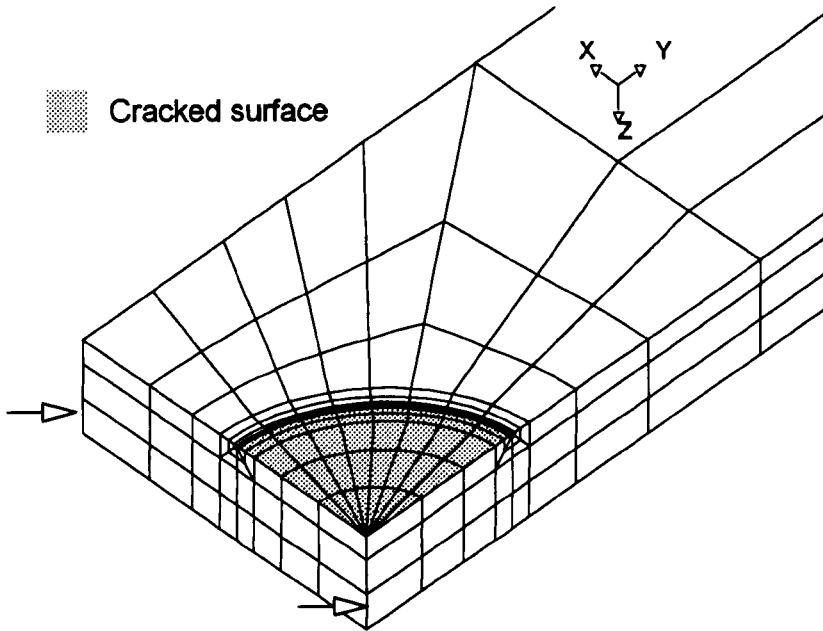
Figure 6.4   A typical cracked block mesh

Similarly, the formation of a 2D cracked plane mesh was completely automatic after the crack had advanced to a new position. These FE configurations of 2D cracked planes were similar to those shown in Chapter 4. There were seventeen nodes defining the crack front. The cubic spline curve approximation described in Chapter 2 was used to create a new crack front.

The material constants employed in this chapter were the same as assumed in the previous chapters, i.e. the Poisson's ratio $\nu = 0.3$; the Paris coefficients $C = 1.83 \times 10^{-13}$ (the units: da/dN ~ mm/cycle and ΔK ~ MPa$\sqrt{\text{mm}}$) and the Paris exponent $n = 3$. The maximum crack growth increment, Δa_{max}, along the crack front was confined to less than $t/100$, which has proven to be sufficiently small in Chapter 4 for the convergence of both the aspect ratio change and fatigue growth curve. For each initial crack, the fatigue growth simulation had been performed until the internal surface of the cylindrical vessel was reached. All calculations were completed on an UNIX-based Silicon Graphic Workstation.

6.4 Shape Change of Fatigue Defects

Figs. 6.5 and 6.6 present, respectively, the shape developments of initially semi-elliptical external surface cracks for both cylindrical vessels. It can be seen that the crack shape developments, similar to those of flat plate surface cracks obtained in Chapter 4, also tend asymptotically towards a preferred propagation path.

By carefully examining the relative residual distribution and the relative standard deviation, Chapter 4 concluded that an initially semi-elliptical surface crack in a flat plate can basically maintain an approximate semi-elliptical shape during the crack growth through the plate thickness for tension and DOB = 0.5 cases. Similar results can also be found in Figs. 6.7 and 6.8 for external surface cracks in internally pressurised cylinders. Fig. 6.7 shows the distribution of the relative residual, E_i, around several crack profiles for two particular initial cracks. The definition of the relative residual is the same as that used in Chapter 4 (*see Eq. (4.4)*). It can be seen in Fig. 6.7 that all E_i values are negative, which means that the predicted crack profiles are always on the inside of their corresponding semi-ellipses. However, different initial cracks have different crack shape deviations around the crack front. The analysis of E_i variations for all initial cracks shows (*not presented here*) that all obtained E_i distributions are negative, and the maximum E_i value is below 5%. Fig. 6.8 shows the variations of the relative standard deviation, S_r, with the crack growth for all initial cracks, where Fig. 6.8(a) corresponds to the cylinder of $t/R_i = 0.1$ and (b) to that of $t/R_i = 0.2$. The S_r was defined by Eq. (4.6) in Chapter 4. Clearly, the S_r variations are different for each initial crack, but a convergence seems to exist when these cracks approach the internal surface of the cylinder. This also implies that the crack growth tends toward a preferred propagation path although the crack shape is not exactly semi-elliptical as indicated in Fig. 6.7. It can also be seen from Fig. 6.8 that all values of the relative standard deviation, S_r, during all crack growth processes are below 3%, which is similar to results obtained in Chapter 4 for the flat plate surface crack. Hence, it is also concluded that for an external surface crack in a cylindrical vessel the semi-elliptical shape can approximately be maintained during the crack growth through the thickness.

The aspect ratio variations of all initial cracks are depicted in Fig. 6.9, where (a) corresponds to $t/R_i = 0.1$ and (b) to 0.2. It is obvious that all cracks asymptotically tend to a preferred path, but for larger ratios of crack depth to vessel wall, such as initial cracks of (0.4,
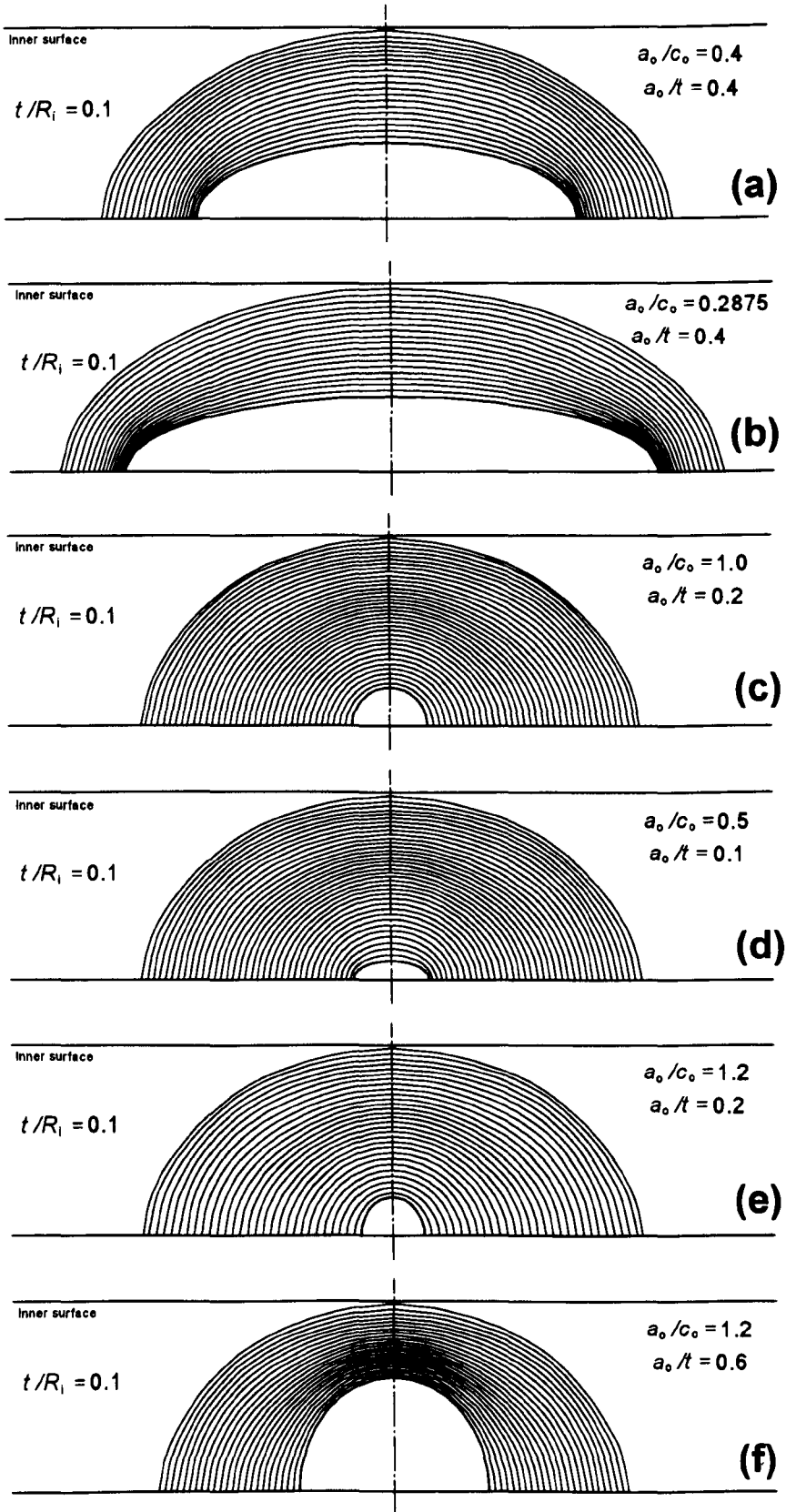
Figure 6.5   Fatigue shape development of initially semi-elliptical external surface cracks in pressurised cylindrical vessels (t/R_i = 0.1)
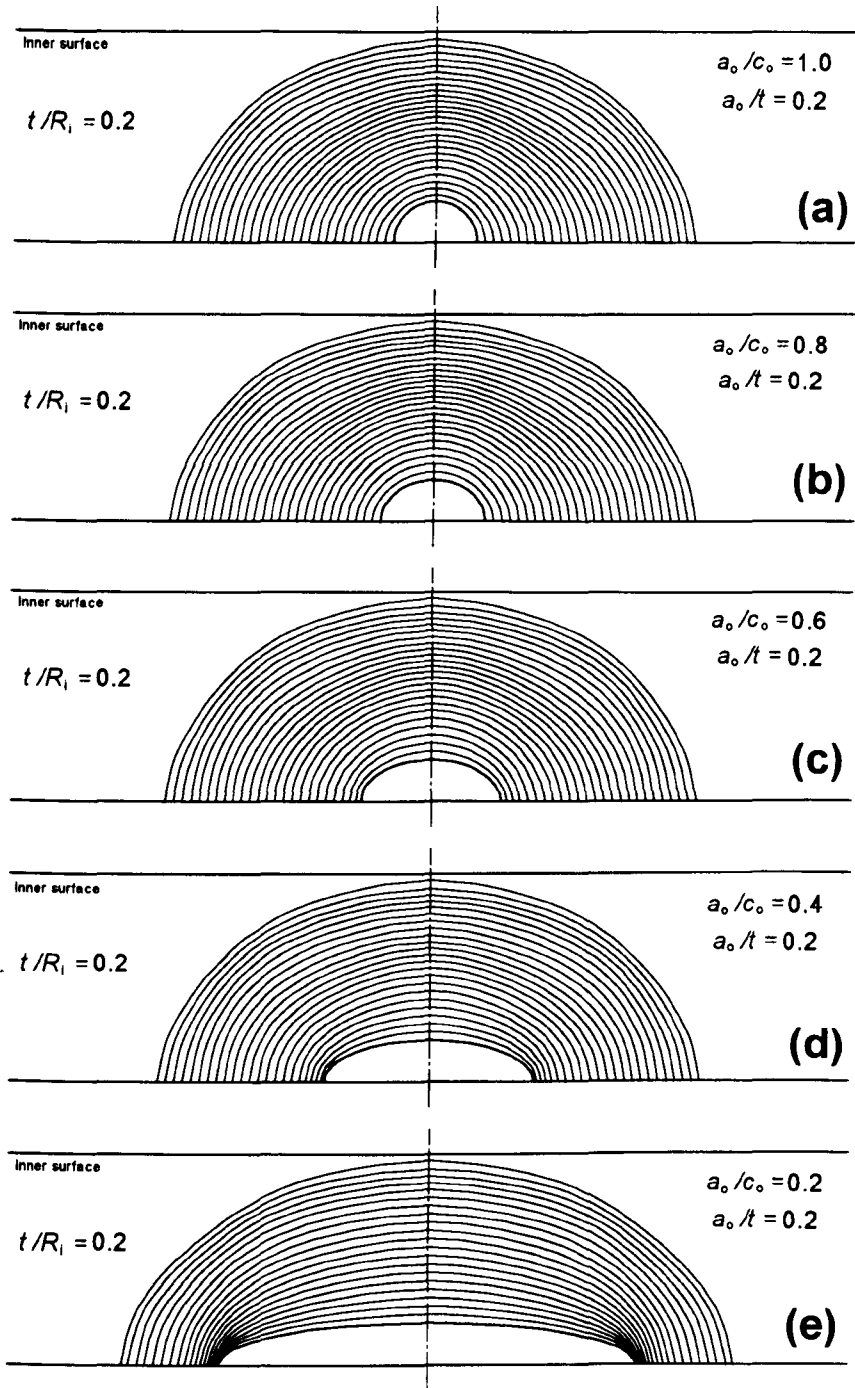
Figure. 6.6   Fatigue shape development of initially semi-elliptical external surface cracks in pressurised cylindrical vessels (t/R_i = 0.2)
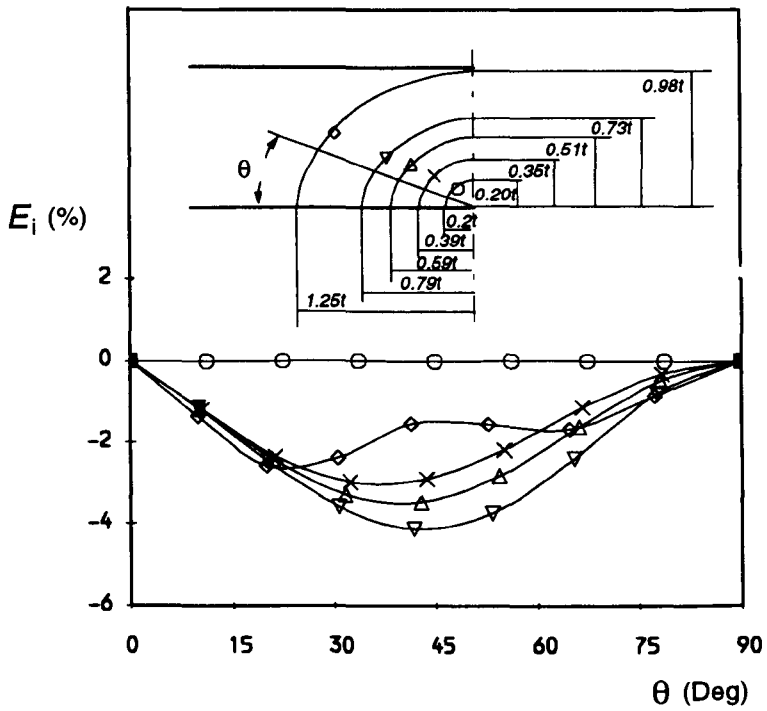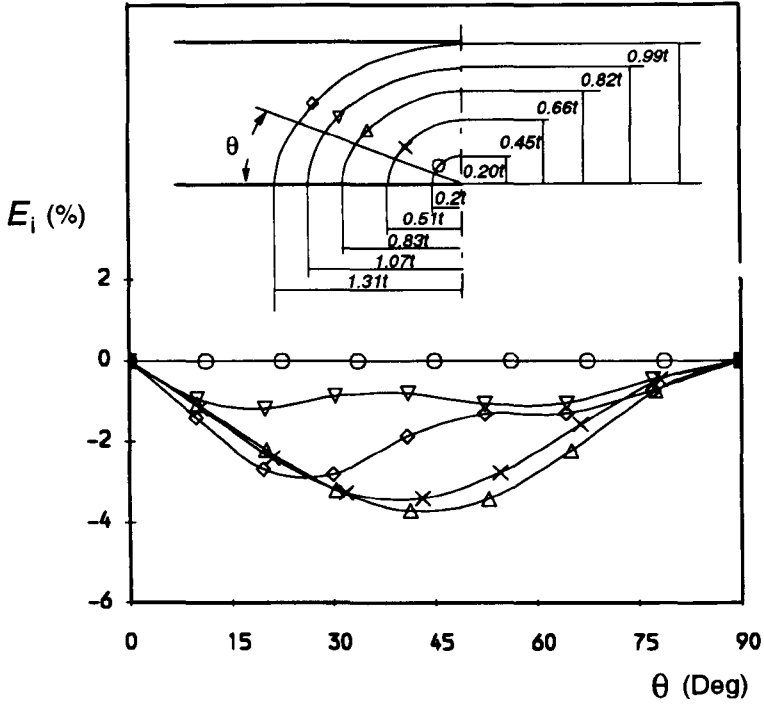
Figure 6.7   Distributions of the relative residual, E_i, around the crack front during crack growth (a_0/c_0 = 1.0, a_0/t = 0.2); (a) t/R_i = 0.1, (b) t/R_i = 0.2
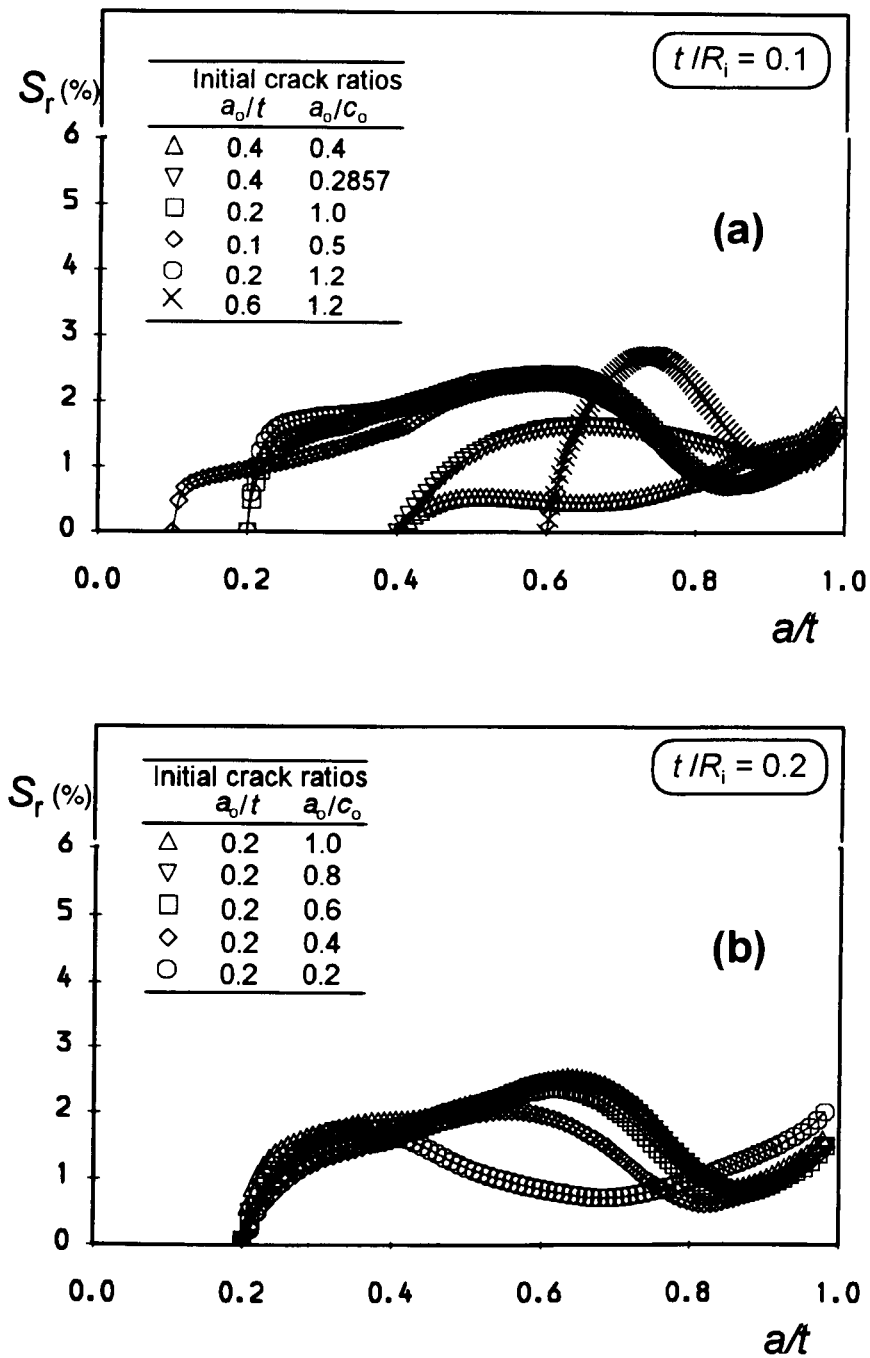
Figure 6.8   Variations of standard residual deviation during crack growth

0.2875) and (0.4, 0.4) in Fig. 6.9(a), it is more difficult for them to converge to the preferred propagation path when the cracks reach the internal surface of the vessel.   It should be true that for different t/R_i cylinders, there are different aspect ratio variations due to different stress distributions through the wall.   However, a difficulty arises in demonstrating the difference of
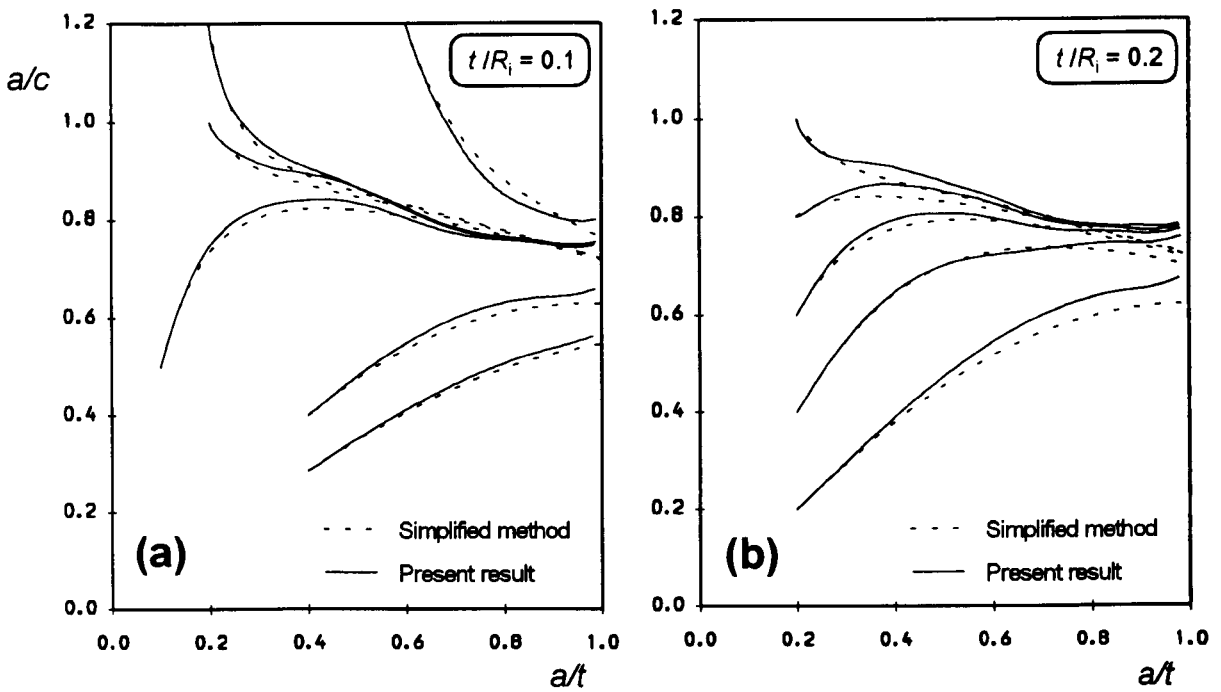
Figure 6.9 Aspect ratio changes predicted by both the present numerical
technique and simplified method

aspect ratio changes between the two cylinders analysed, since different initial crack aspect ratios were used for both cylinders, as shown in Fig. 6.9(a) and (b). If Fig. 6.9 is closely observed, it can still be found that the aspect ratio values at leakage ($a/t = 1$), marked in both (a) and (b), are close, which, to some extent, demonstrates that the difference between both Fig. 6.9(a) and (b) is small. The reason might be that the resultant bending components of the stress field through the wall for the two vessels are very close. Fig. 6.9 also compares the aspect ratio variations obtained by the present simulation technique with those obtained by using Newman and Raju's flat plate SIF equations plus the hoop stress linearisation, which has been suggested in section 6.3. It can be seen in Fig. 6.9 that the agreement is very good between the sophisticated modelling computations and the simplified estimates, except that at near leakage the trend of aspect ratio curves deviate slightly. The aspect ratio curves predicted by the simulation technique ascend a little when the crack approaches the internal surface, whilst those estimated from the simplified method descend continuously. The reason has been discussed in Chapter 4. The comparison in Fig. 6.9 shows that it appears to be acceptable to use the suggested simplified method to estimate the aspect ratio change for an external surface crack in an internal pressure cylindrical vessel.

6.5 Stress Intensity Factor Variations

As mentioned above, the two-block FE models were also used for the cylinders analysed. The cracked blocks designed for the cylinders are similar to those for the flat plates which have been verified to be reliable for achieving a good SIF accuracy in Chapter 4. In this chapter the effect of the mesh mismatch between the cracked and uncracked blocks is not examined further for the cylinder, but a comparison of the SIF result calculated from the two-block model for a particular initial crack ($a/t = 0.2$, $a/c = 1.0$) is made with the result of Raju and Newman (1982). Fig. 6.10 shows this comparison, in which the SIF result estimated by the present stress linearisation method is also included. The SIF variation along the crack front from the model of the present author is generally in fair agreement with Raju and Newman's result. The present result is slightly less than Raju and Newman's result, the maximum difference being below 4%. Raju and Newman (1982) quoted their SIF accuracy as being 90%, thus it can be believed that the present two-block models can obtain a sufficiently good SIF accuracy. In Fig. 6.10 it can also be seen that the SIF estimate from the stress linearisation method is larger than both the present and Raju and Newman's solutions, nearly 10% larger than the present result. The trend should be believable because the present stress linearisation method assumes a larger resultant tensile force through the wall.
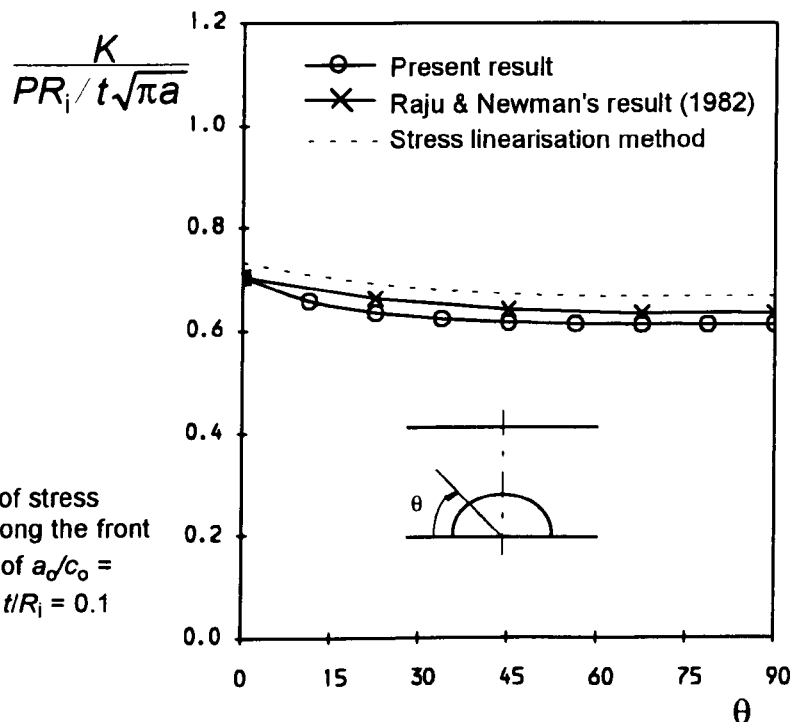
Figure 6.10   Comparison of stress intensity factors along the front of the initial crack of $a_0/c_0 = 1.0$, $a_0/t = 0.2$ and $t/R_i = 0.1$

185

Fig. 6.11 depicts the variations of the ratio of the minimum to maximum stress intensity factor (K_{min}/K_{max}) along each crack front with the normalised crack depth a/t. This can further clarify the change of SIF distributions along the crack front during the fatigue growth process. It can be seen in Fig. 6.11 that most of the curves almost reach unity (iso-K) and subsequently drop as the crack continues to advance, however, several initial cracks are unable to come to their iso-K profiles. Generally speaking, whether to be able to come to an iso-K shape and how early to come depend on the initial crack size and shape, as

Figure 6.11   Variation of ratio of minimum to maximum stress intensity factors along crack front with fatigue growth

concluded in Chapter 4. For a larger crack depth ratio, it usually is more difficult to reach the iso-K shape before leakage. The variations of the ratio of the minimum to maximum SIF in Fig. 6.11, actually, are similar to those obtained for surface cracks in tension plates. In Fig. 6.11(b), a convergence of the K_{min}/K_{max} ratio can also be observed as the cracks approach closely the internal surface of the cylinder, which further demonstrates that the preferred propagation shape does exist.

Figure 6.12   Comparison of stress intensity factor variations with crack growth at both depth and surface points, $t/R_i = 0.1$
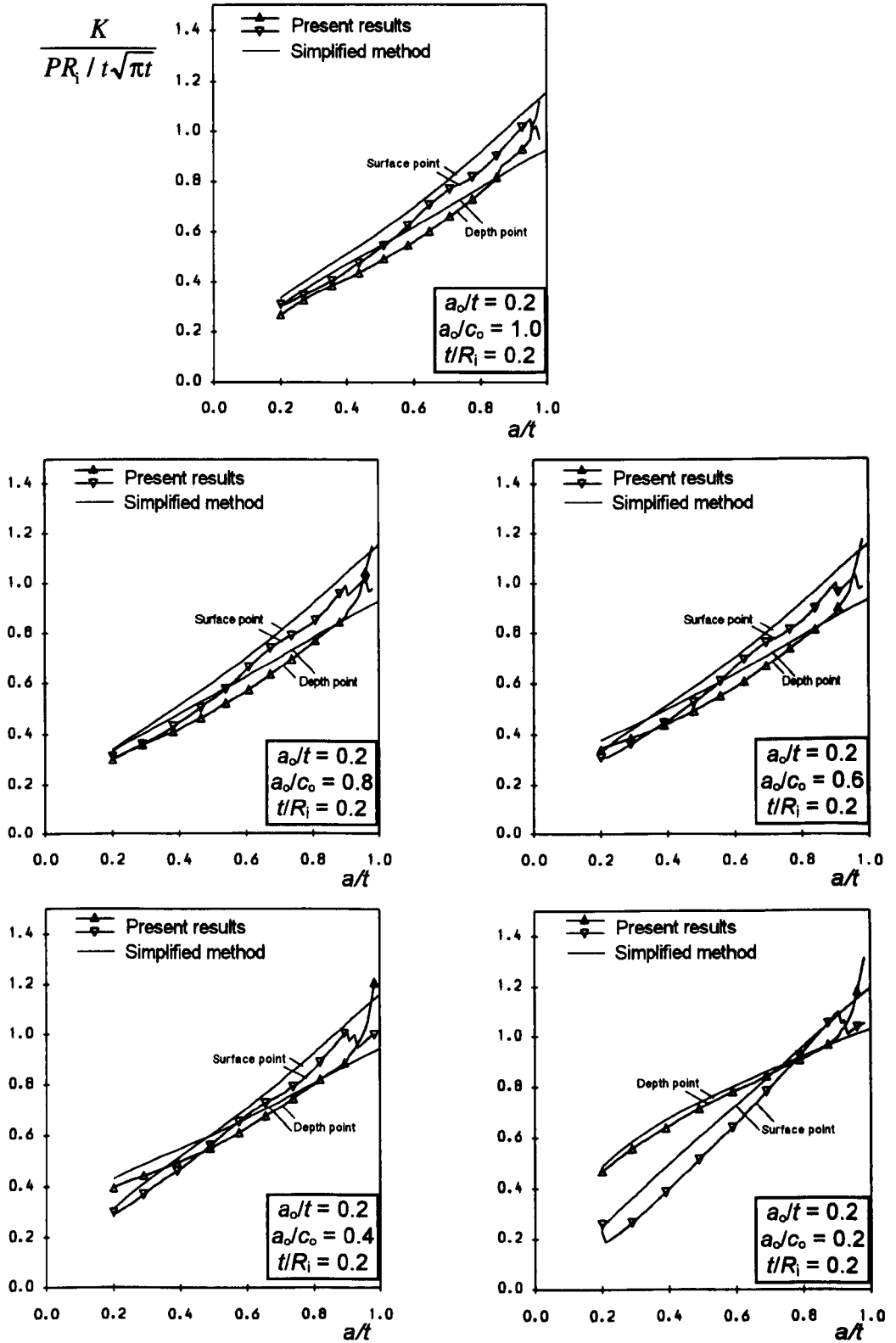
Figure 6.13   Comparison of stress intensity factor variations with crack growth at both depth and surface points, t/R_i = 0.2

$$\frac{K}{PR_i / t\sqrt{\pi t}}$$

Initial crack ratios

	a_0/t	a_0/c_0
△	0.4	0.4
▽	0.4	0.2857
□	0.2	1.0
◇	0.1	0.5
○	0.2	1.2
✕	0.6	1.2

(a) Depth point $t/R_i = 0.1$

Initial crack ratios

	a_0/t	a_0/c_0
△	0.4	0.4
▽	0.4	0.2857
□	0.2	1.0
◇	0.1	0.5
○	0.2	1.2
✕	0.6	1.2

(b) Surface point $t/R_i = 0.1$
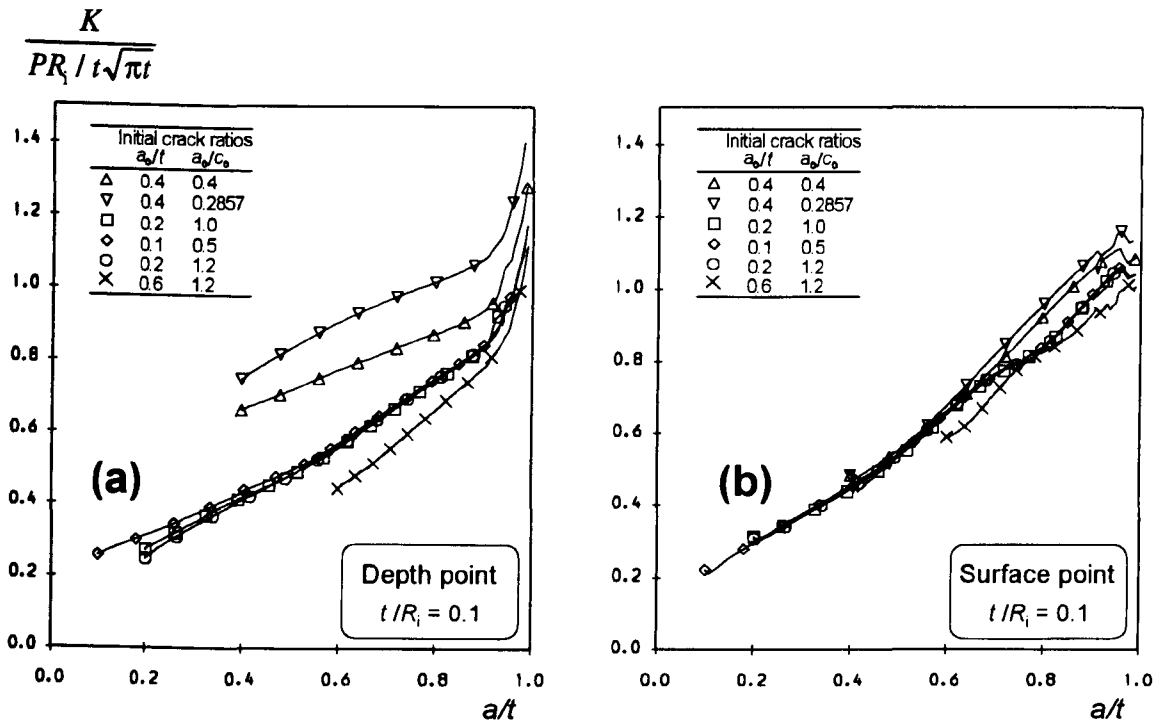
Figure 6.14 Variations of stress intensity factors at the two extremes of a crack front with crack growth for $t/R_i = 0.1$

The SIF variations at both the crack surface and depth positions with the crack growth are shown in Fig. 6.12 and Fig. 6.13, where Fig. 6.12 corresponds to the cylinder of $t/R_i = 0.1$ and Fig. 6.13 to that of $t/R_i = 0.2$. The SIF variation is normalised by $(PR_i/t)\sqrt{\pi t}$. It is seen that when the crack grows to about 90% of the plate thickness the rise in SIF value at the depth point begins to accelerate, and the SIF value at the surface point is even exceeded as the crack approaches the internal surface. Similar results have been obtained and explained in Chapter 4. The predictions made by the present linearisation method are also shown in Fig. 6.12 and Fig. 6.13 for comparison. It appears to be true that the linearisation method usually predict slightly higher SIF results than the FE simulation technique, except near the internal surface of the cylinder, where the SIF acceleration indicated above does not happen. As explained in Chapter 4, this is because the Newman and Raju (1981) plate SIF equation has a relatively larger error for a deep crack ($a/t > 0.9$). Overall, the agreement of SIF variations between them is good. Fig. 6.14 displays together the SIF variations for all initial cracks in the cylinder of $t/R_i = 0.1$ at the depth point (*Fig. 6.14(a)*) and the surface point (*Fig. 6.14(b)*). It is obvious in Fig. 6.14 that the SIF variation at the depth or surface points depends on the initial crack size, but the tendency seems similar for each crack, particularly as the crack

$$\frac{K}{PR_i \,/\, t\sqrt{\pi t}}$$
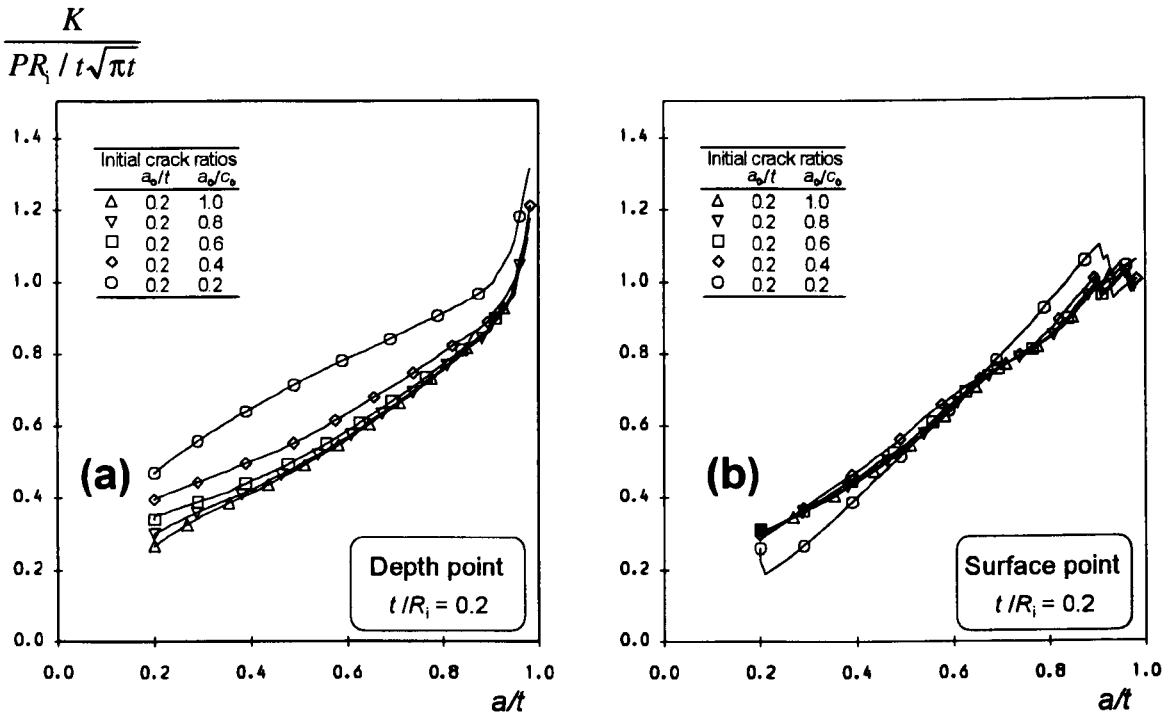
Figure 6.15 Variations of stress intensity factors at the two extremes of
a crack front with crack growth for $t/R_i = 0.2$

approaches the opposite surface. A similar conclusion can also be drawn from Fig. 6.15, which shows the SIF variations for all analysed initial cracks within the cylinder of $t/R_i = 0.2$.

6.6 Predictions of Fatigue Growth Cycles

It has been indicated in Chapter 2 that the selection of maximum crack growth increment in modelling computations affects the prediction of fatigue growth cycles. A sufficient small increment should be used. An investigation of the effect of Δa_{max} on the fatigue growth curve has been made in Chapter 4 for a semi-elliptical surface crack in a flat plate, and concluded that using $\Delta a_{max} = t/100$ can achieve a very good accuracy. For the initial cracks analysed in this chapter, which are similar to those in Chapter 4, the chosen $\Delta a_{max} = t/100$ can also be considered to be satisfactory.
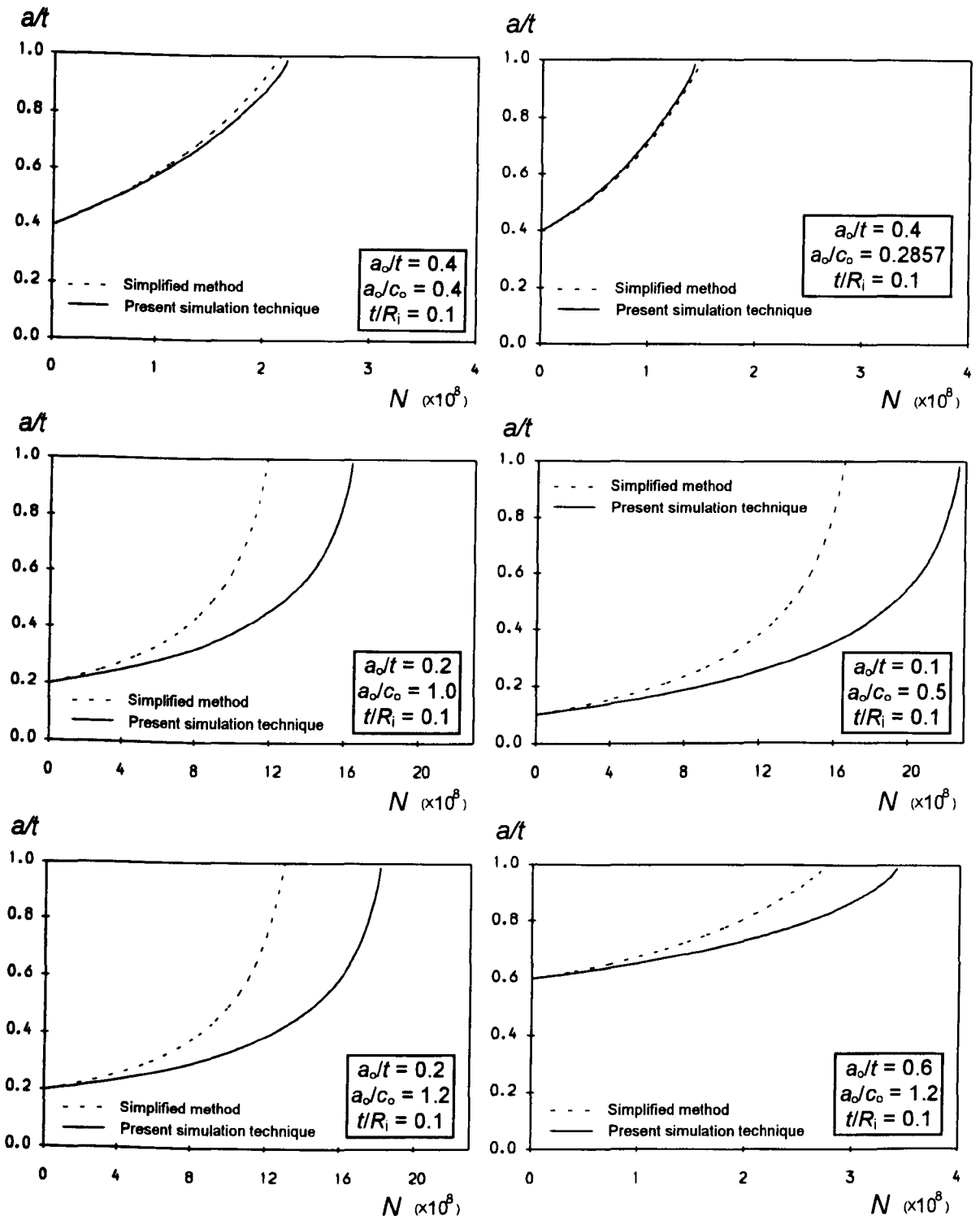
Figure 6.16 Comparison of fatigue growth curves predicted by the present numerical technique and the simplified method for the vessel $t/R_i = 0.1$

Fig. 6.16 presents the relations of the crack depth against the number of spent fatigue cycles for all cracks in the cylinder of $t/R_i = 0.1$. The results obtained using the stress linearisation and Newman and Raju "two-point plus semi-ellipse" method are also plotted
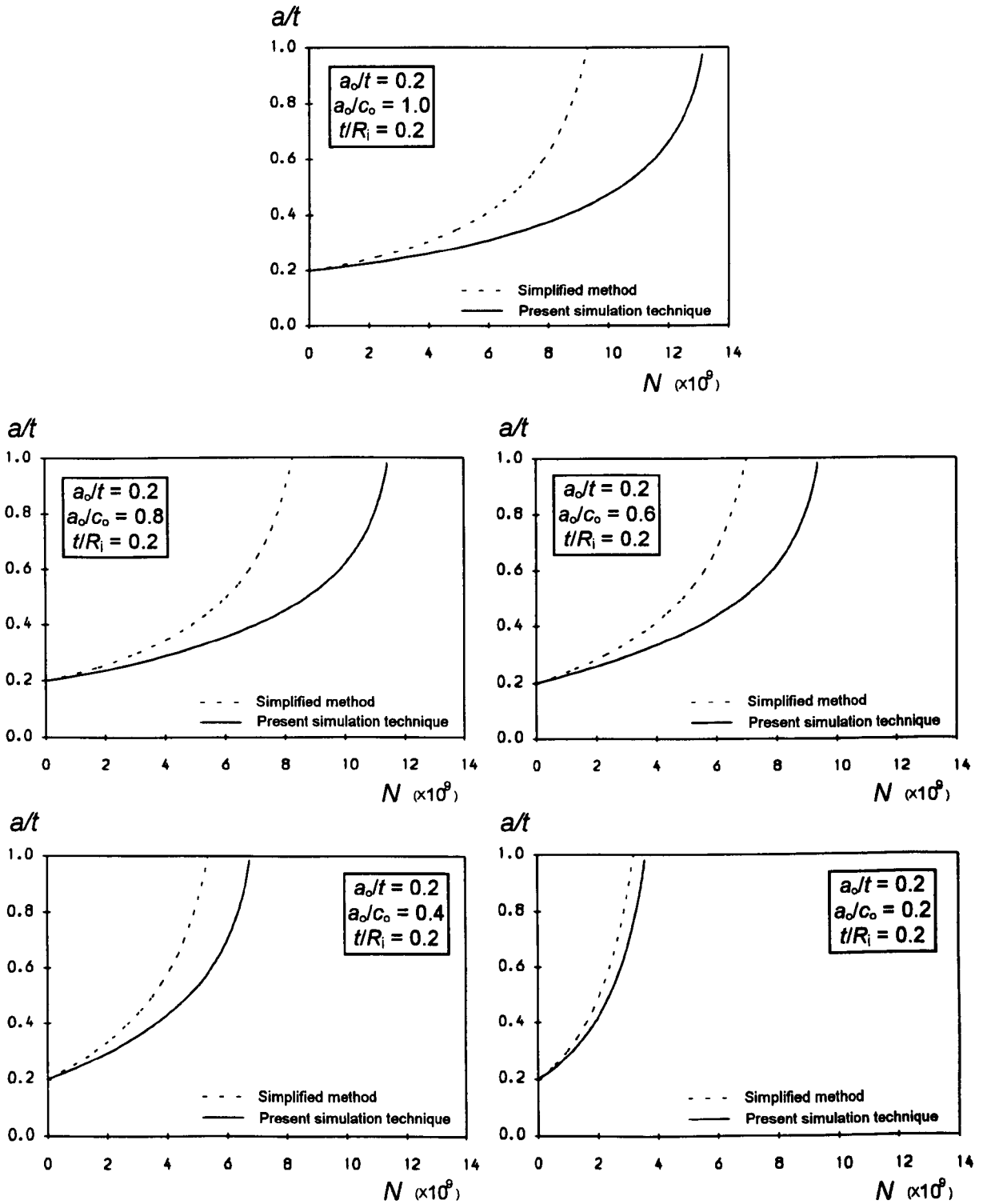
Figure 6.17 Comparison of fatigue growth curves predicted by the present
numerical technique and the simplified method for the vessel $t/R_i = 0.2$

in Fig. 6.16, and compared with those obtained by the present simulation technique. The relation $C_a = C_c$ was used in Newman and Raju's method. Fig. 6.16 shows that the stress linearisation method always overestimates the crack depth for a given number of fatigue cycles for all analysed initial cracks, except the crack of $a/t = 0.4$, $a/c = 0.2857$, for which the agreement between both methods is excellent but the linearisation method seems to underestimate very slightly the crack depth compared with the present simulation technique. Therefore, the simplified calculation using the stress linearisation plus the Newman and Raju flat plate SIF equation is generally conservative, which is mainly because that the linearised resultant stress is larger than the actual stress through the vessel wall. From the point of view of practical use, the present simplified method is reliable and acceptable, although sometimes it might give excessively conservative predictions such as those displayed in Fig. 6.16(c, e).

Fig. 6.17, which displays the fatigue growth curves for the analysed initial cracks in the cylinder of $t/R_i = 0.2$, further demonstrates that the present simplified calculation method is conservative. The maximum difference of the fatigue cycles when the crack grows to the internal wall even reaches nearly 40%. It should be indicated that the difference also includes the error caused by the Newman and Raju SIF equation.

6.7 Conclusions

This chapter has modelled the fatigue growth of various external surface cracks in internally pressurised cylinders by the FE step-by-step technique. A new simplified method that uses the stress linearisation and the Newman and Raju flat plate SIF equation was also proposed for assessing these external surface cracks. The stress intensity factors along an initially semi-elliptical external surface crack obtained by the present FE analyses were compared with existing solutions to examine the SIF accuracy. The deviation of fatigue crack shape from the semi-ellipse was also studied. A wide range of results obtained by both the present numerical simulation technique and the simplified method have been presented and compared, which leads to the following conclusions:

1) The 1/4-point displacement method used in the present simulation technique can achieve an excellent SIF accuracy for external surface cracks in cylinders.

2) The simplified method usually overestimates the stress intensity factor along the crack front, compared with the specific finite element analysis.

3) During the fatigue growth through the wall thickness of a cylinder, the crack can basically retain an approximate semi-ellipse ($S_r < 3\%$). The crack always attempts to tend towards a preferred propagation path, as mentioned in Chapter 4 for a surface crack in a flat plate.

4) The aspect ratio changes estimated by the present simulation technique agree well with those by the simplified method, and are less affected by the ratio of t/R_i within the range analysed in this chapter.

5) The fatigue crack depth is generally overestimated by the simplified method for a given number of fatigue cycles, compared with the result obtained by the present simulation technique, which demonstrates that the simplified method is conservative.

6.8 References

Atluri, S. N. and Kathiresan, K. (1979) *3-D analysis of surface flaws in thick-walled reactor pressure-vessels using displacement-hybrid finite element method.* **Nuclear Engng and Design 51**, 163-176.

A.S.M.E. Boiler and pressure vessel code, section XI (1977) *Rules for in-service inspection of nuclear power plant components.*

British Standards Institution (1980) *Guidance on some methods for the derivation of acceptance levels for defects in fusion welded joints.* Section 3, BSIPD 6493.

Connors, D. C. (1984) *The shape development of surface defects in plates and cylinders under cyclic loads.* TPRD/B/0469/N84, CEGB Technology Planning and Research Division, Berkeley Nuclear Laboratories, Berkeley, UK.

Miyazaki, N., Watanabe, T., and Yagawa, G. (1981) *Calculation of stress intensity factors of surface cracks in complex structures: application of efficient computer program EPAS-J1.* **Nuclear Engng and Design 68**, 71-85.

Newman, J. C., Jr. and Raju, I. S. (1980) *Stress intensity factors for internal surface cracks in cylindrical pressure vessels*. ASME **J. Pres. Ves. Tech. 102**, 342-346.

Raju, I. S. and Newman, J. C., Jr. (1982) *Stress intensity factors for internal and external surface cracks in cylindrical vessels*. ASME **J. Pres. Ves. Tech. 104**, 293-298.

Timoshenko, S. (1956) Strength of Materials, Advanced Theory and Problem,. D. Van Nostrand Company, New York.

BLANK PAGE
IN
ORIGINAL

Chapter 7

SHAPE GROWTH SIMULATION OF SURFACE CRACKS IN TENSION FATIGUED ROUND BARS

The 3D step-by-step finite element technique described in Chapter 2 was used to simulate the fatigue shape development beginning from several elliptical-arc cracks with different aspect ratios and an irregular crack in round bars under axial tension. A Paris crack growth relation was employed as the basis of the modelling computations. The shape of growing cracks was quantitatively examined by both the proposed relative residual and relative standard deviation to reveal the shape difference between the numerically predicted crack profile and the widely assumed circular-arc. The aspect ratio changes for the initially part-elliptical cracks were predicted, and compared with some published experimental results. Moreover, the effect of the exponent in the Paris law on the aspect ratio variation was investigated.

7.1 Introduction

Fatigue cracks initiating and propagating in components with circular cross sections, such as shafts, bolts, screws, or wires, have been receiving a great deal of attention, since these components have wide and important applications in engineering practice.

Experimental results for smooth round bars subjected to tension or bending fatigue loads (Nezu *et al.*, 1982; Forman and Shivakumar, 1986; Athanassiadis *et al.*, 1981; Wilhem *et al.*, 1982; Mackay and Alperin, 1985; Lorentzen *et al.*, 1986; Caspers *et al.*, 1990) have shown that propagating surface cracks through the cross section before final failure have a so-called "almond" shape. Some investigators (Nezu *et al.*, 1982; Forman and Shivakumar, 1986; Wilhem *et al.*, 1982; Mackay and Alperin, 1985; Caspers *et al.*, 1990; Caspers and Mattheck, 1987; Salah and Lovegrove, 1981; Fan *et al.*, 1982; Daoud and Cartwright, 1985; Ng and Fenner, 1988) thought that the "almond" shaped crack front may be well described by a circular arc, and some others (Athanassiadis *et al.*, 1981; Lorentzen *et al.*, 1986; Levan and Royer, 1993; Astiz, 1986; Nord and Chung, 1986; Raju and Newman, 1986; Carpinteri, 1992a, 1993; Nisitani and Chen, 1984) thought that a part-ellipse might also approximate to these observed crack profiles. According to the experimental fact, many stress intensity factor solutions have been published relating to part-circular, part-elliptical, or straight fronted (Salah and Lovegrove, 1981; Levan and Royer, 1993; Ng and Fenner, 1988; Bush, 1976; Daoud *et al.*, 1978; Ouchterlony, 1981; Astiz and Elices, 1980; Blackburn, 1976; Daoud and Cartwright, 1984; Bush, 1981; Carpinteri, 1992b) surface cracks as well as actual shape cracks (Forman and Shivakumar, 1986; Athanassiadis *et al.*, 1981; Wilhem *et al.*, 1982; Salah and Lovegrove, 1981; Astiz, 1986). The straight-fronted crack, despite being unlikely to occur when the crack is small, is approached as the crack advances to half the diameter of the bar, and can be considered as an extreme shape of either the part-circle or part-ellipse. The SIF results were obtained by using either numerical methods, such as finite element (Nezu *et al.*, 1982; Caspers and Matteck, 1987; Salah and Lovegrove, 1981; Fan *et al.*, 1982; Daoud and Cartwright, 1985; Astiz, 1986; Nord and Chung, 1986; Raju and Newman, 1986; Carpinteri, 1992a, 1992b, 1993; Ng and Fenner, 1988; Daoud *et al.*, 1978; Blackburn, 1976; Daoud and Cartwright, 1984), boundary integral equation (Athanassiadis *et al.*, 1981; Levan and Royer, 1993) and weight function (Caspers *et al.*, 1990; Caspers and Mattheck, 1987) methods, or experimental approaches including photoelasticity (Lorentzen *et al.*, 1986; Astiz and Elices,

1980), compliance measurement (Athanassiadis *et al.*, 1981; Bush, 1976; Daoud *et al.*, 1978; Ouchterlony, 1981; Bush, 1981) and fatigue tests (Nezu *et al.*, 1982; Forman and Shivakumar, 1986; Athanassiadis *et al.*, 1981; Wilhem *et al.*, 1982; Mackay and Alperin, 1985; Salah and Lovegrove, 1981; Astiz, 1986). Some of the SIF solutions have been summarised and compared by James and Mills (1988), and Si (1990).

Several attempts to predict the fatigue growth of surface cracks in round bars under tension or bending have also been reported. Most of them based their calculations on a certain shape assumption for propagating crack fronts in order to apply an appropriate crack growth law to the crack depth point, or to both the depth and surface points, which reduced the fatigue calculations to one- or two-dimensional problems. Salah and Lovegrove (1981) employed a circular arc whose centre is fixed at the boundary of the round bar (*see Fig. 7.1(a)*), while Forman and Shivakumar (1986) assumed the actual cracks to be always part-circles that intersect the free surface of the bar at right angles (*see Fig. 7.1(b)*). The two shape assumptions enabled the fatigue life to be predicted by only applying a fatigue crack growth law to the crack depth position. However, Lorentzen *et al.* (1986), Carpinteri (1993) and Caspers *et al.* (1990) considered both the crack depth and surface points, which permitted actual crack profiles to be better approximated. Both Lorentzen *et al.* (1986) and Carpinteri (1993) assumed the part-elliptical shape, as shown in Fig. 7.1(d), whilst Caspers *et al.* (1990) used the part-circle whose centre was allowed to vary along the vertical axis, as shown in Fig. 7.1(c). The shape assumption method, as mentioned previously, can simplify the fatigue calculations, but it is also certain that improvements should be achieved if the shape restraint can be removed. Thompson and Sheppard (1992a, b) recently reported their attempt to avoid such a shape assumption in investigating the fatigue growth of surface cracked round bars by using a finite element following technique.

This chapter aims to employ the versatile numerical technique described in Chapter 2 to predict the fatigue shape development of surface cracks in round bars subjected to tension. The crack shape developments, starting from several initially elliptical-arc cracks and an initially irregular defect, are revealed and also quantitated through both the proposed relative residual and relative standard deviation in order to examine the deviation of the predicted crack profiles from the part-circular shape shown in Fig. 7.1(c). The predicted aspect ratio changes are compared with the experimental results of Caspers *et al.* (1990). The influence of different crack growth laws on the crack shape change is also investigated in this chapter.
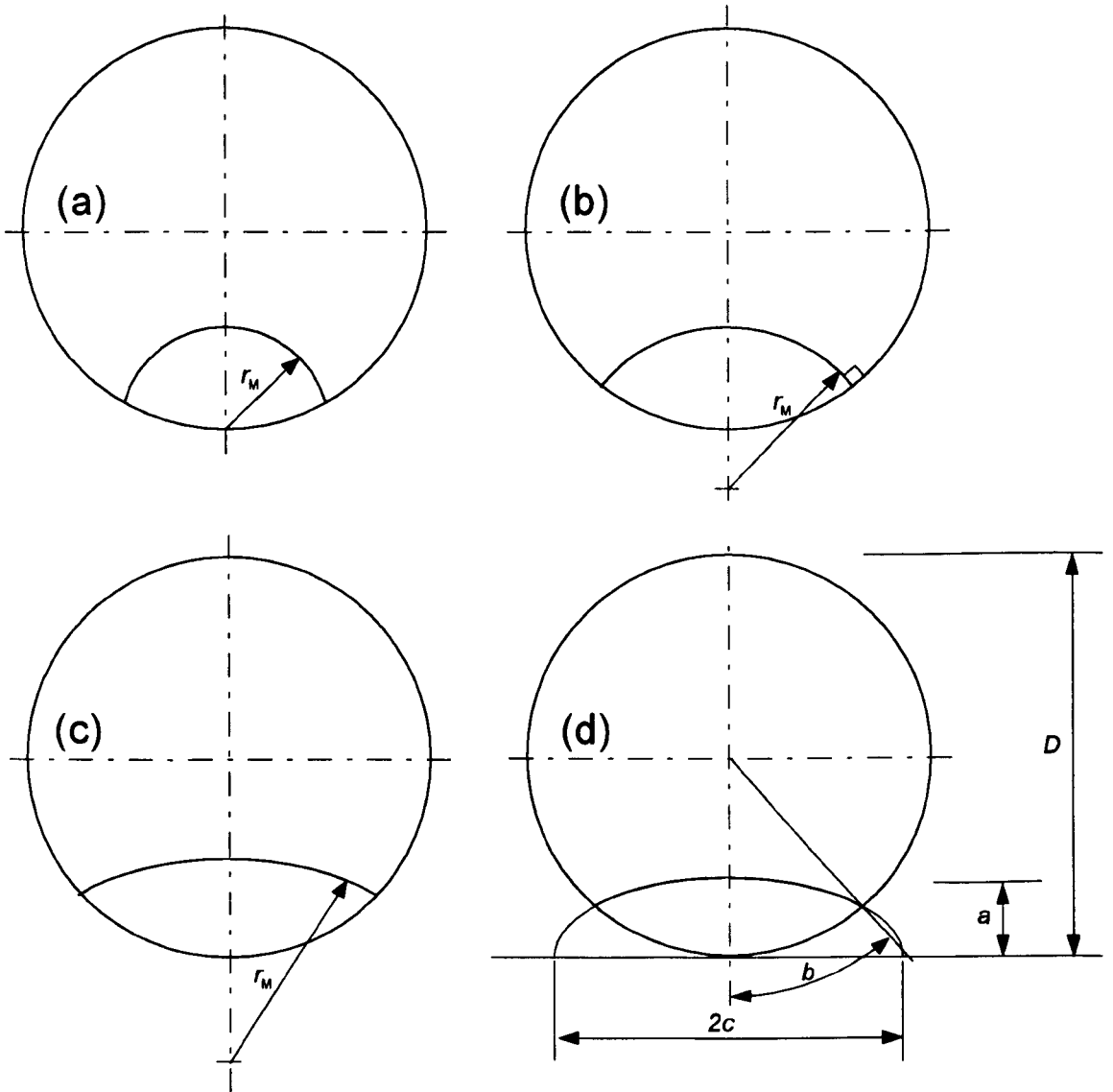
Figure 7.1   Different shape assumptions for surface crack in round bar

7.2 Numerical Calculation Details

Surface cracks in smooth cylindrical bars subjected to fatigue tension are considered.   The crack shape was initially assumed to be part-elliptical, as shown in Fig. 7.1(d).   Six different crack configurations were analysed.   The initial aspect ratios were, respectively, $a_o/c_o = 0$

(straight-fronted), 0.2, 0.4, 0.6, 0.8, and 1.0; and the initial depth was 20% diameter of the bar, i.e. $a_o/D = 0.2$, for all initial cracks. The height of the bar was taken to be 16D.
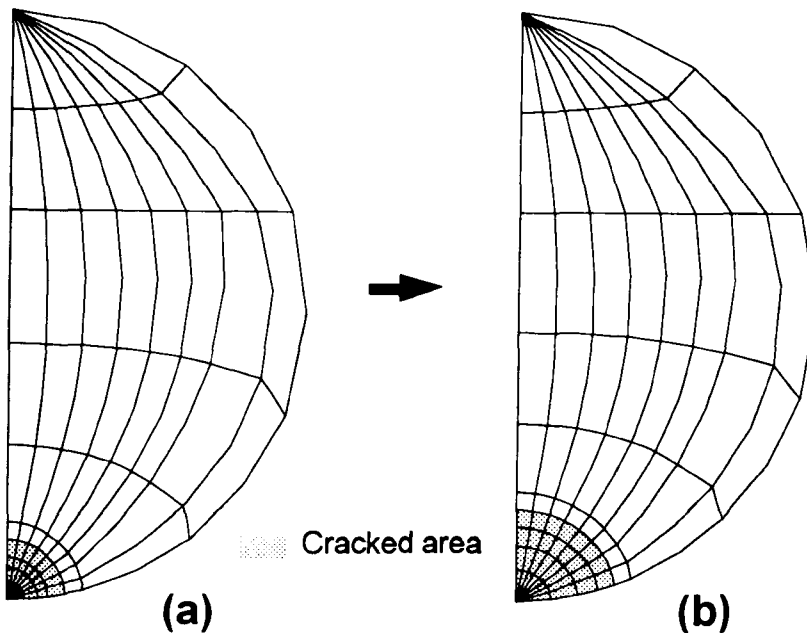
Figure 7.2 Advance of finite element mesh with crack growth

The details of the step-by-step FE technique have been described in Chapter 2. Here only a brief description associated with the cracked bar is given as follows:

a) *Define a 2D finite element mesh for the initial crack*   This was done with the help of the mesh generator FEMGV (*see Fig. 7.2(a)*). The 2D mesh, consisting of 8-noded iso-parameteric elements, was only created for a half of the cross section of the bar, due to the symmetry of its geometry and loading. The crack front was constructed by a set of nodes (*nine corner nodes and eight midside nodes*). The edges of the elements abutting the crack front intersected the crack front orthogonally except at the free boundary. The normal intersection is usually required by the displacement method for estimating the stress intensity factor along the crack front. The cracked surface shaded in Fig. 7.2(a) had thirty-two elements.

b) *Expand the 2D FE mesh into a 3D mesh*   This was completed automatically by DUCKPRE. The expanded 3D mesh, which comprised 20-noded isoparameteric elements with nine Gauss points, is shown in Fig. 7.3. It can be seen that there were three rings of elements arranged surrounding the crack front, each ring having four elements. The wedge
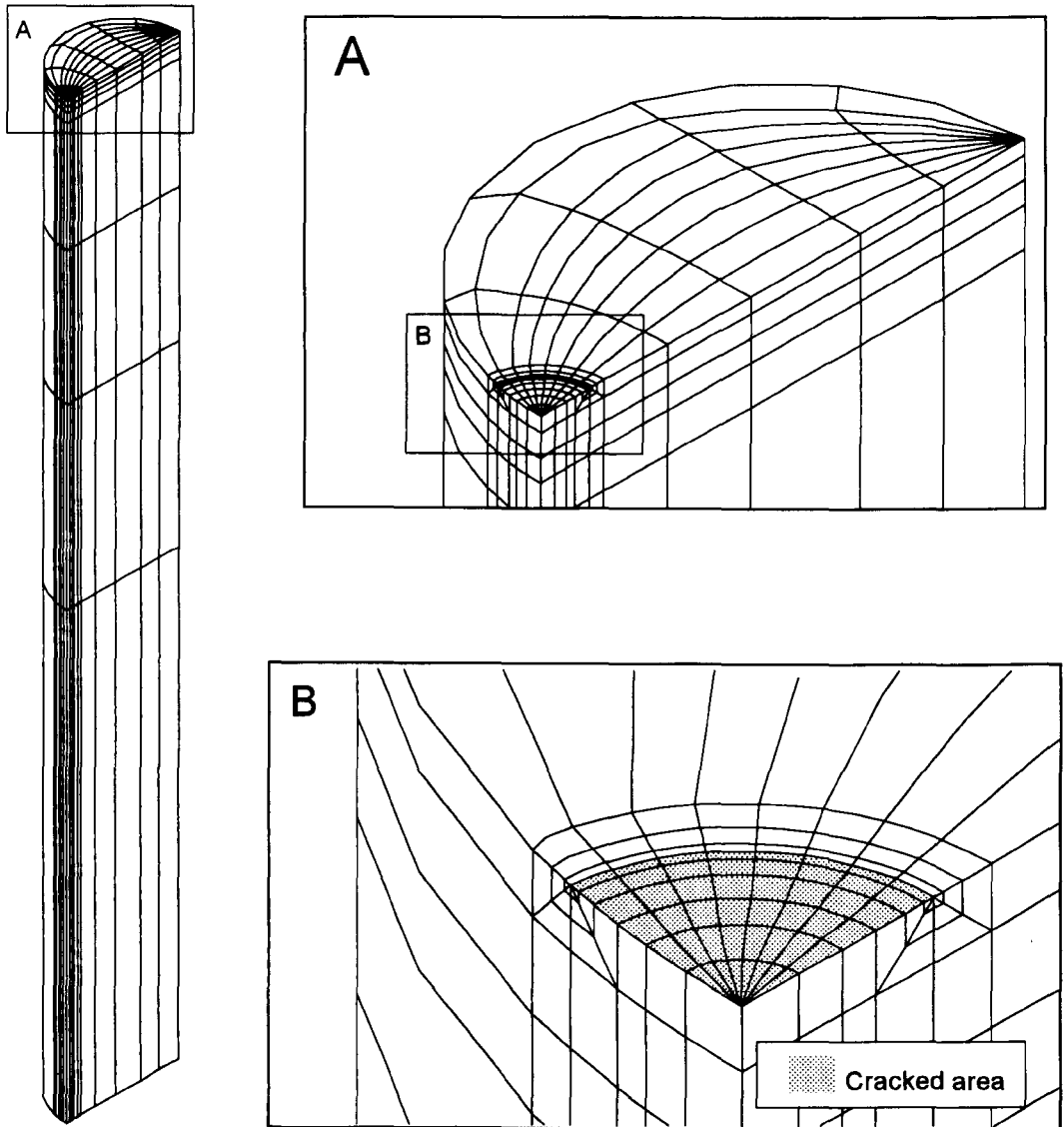
Figure 7.3 Typical 3D finite element configuration for edge cracked cylindrical bar

element in the first ring was formed by collapsing one side of the brick element. The midside nodes of the wedge elements were moved to 1/4-point positions in order to simulate the square-root singularity of the stresses and strains near the crack tip. The 3D FE model had 720 elements with about 3330 nodes.

c) *Calculate the crack face displacements at 1/4-points*   The FE code ABAQUS was used to calculate these displacement values at the 1/4-points on the crack face. Meanwhile,

the 3D *J*-integral values, based on the virtual crack extension principle, along the crack front were also obtained.

d) *Estimate SIFs and apply a Paris law to corner nodes* The stress intensity factors at corner nodes were computed using the 1/4-point displacement method, with the plain strain condition assumed for all positions. It should be indicated here that the plane stress state may prevail at the free boundary, as mentioned previously, but its influence on the fatigue crack growth of the whole crack front is slight since the plane stress state is usually localised in a very thin layer near the free surface. The material Poisson's ratiov was taken as equal to 0.3. Once these SIFs were obtained, an appropriate fatigue crack growth law can be employed to obtain the local increments, Δa_i, of the crack growth at the corner nodal positions. In this chapter the fatigue crack growth law was assumed to obey:

$$\frac{da(\text{mm})}{dN(\text{cycle})} = 1.83 \times 10^{-13} [\Delta K(\text{MPa}\sqrt{\text{mm}})]^3$$

related to a steel, and the maximum crack growth increment was confined to *D*/250, which will be demonstrated later to be small enough for the prediction of crack shape changes. It should be noted that the crack growth increment at the free surface was first calculated along the tangential direction (to the point B′), as shown in Fig. 7.4. The calculation process described in this stage was executed by DUCKPOST.

e) *Advance the crack front to a new position and regenerate a new 2D mesh* According to these Δa_i values, a set of new points (*solid circles in Fig. 7.4*) can be obtained, where the

Figure 7.4 Calculation of crack growth increment along crack front

point B′ was forced to move horizontally to the point B at the circular boundary. DUCKPOST re-established a new crack front using a cubic spline approximation through these new points, rearranged subsequently the position of both corner and midside nodes along the smooth spline curve, and finally recreated automatically a 2D crack plane FE mesh corresponding to the new crack front with the aid of FEMGV.

f) *Go to stage (b)* The crack front can propagate further through the stages from (b) to (e).

The above calculation loop was automatically executed by the software DUCKCONN. All initial cracks were grown by the simulation technique to through the centre of the round bar on a Silicon Graphic Workstation.

7.3 Fatigue Shape Development

Fig. 7.5 exhibits the fatigue shape evolution of six different initially part-elliptical surface cracks in round bars subjected to tension. The crack profiles displayed are those extracted from a range of 144 ~ 170 analysis steps in order to provide a good observation. The initial cracked surfaces were marked as shaded areas. It can be generally seen that at the early stage of crack growth the shape development depends strongly upon the initial crack configuration. For the initial cracks of $a_o/c_o = 1.0$ and 0.8, the crack advances along the front are almost balanced, while for the straight ($a_o/c_o = 0.0$) or near- straight ($a_o/c_o = 0.2$) front cracks the crack grows much more rapidly in the depth direction than along the free surface. As the crack develops further, the shape of the cracks grown from different initial cracks is seen to become similar. Roughly speaking, either the part-circular (*Fig. 7.1(c)*) or part-elliptical (*Fig. 7.1(d)*) arc appears to be able to approximate the propagating cracks. It can also be found that as the crack propagates the crack front gradually becomes flat.

Fig. 7.6 shows the fatigue shape development starting from an irregular shape surface crack in a round bar under tension. It can be seen that the initially irregular crack front grows to a smooth "almond" shape very quickly, resulted from a larger crack growth increment at the concave point and a smaller increment at the convex position. Such a crack growth behaviour is particularly obvious as seen in the coalescing process of multiple cracks in Chapter 5. Once the crack front becomes the "almond" shape, the crack actually behaves as these cracks in Fig. 7.5, and also tends to grow towards a preferred propagation path.
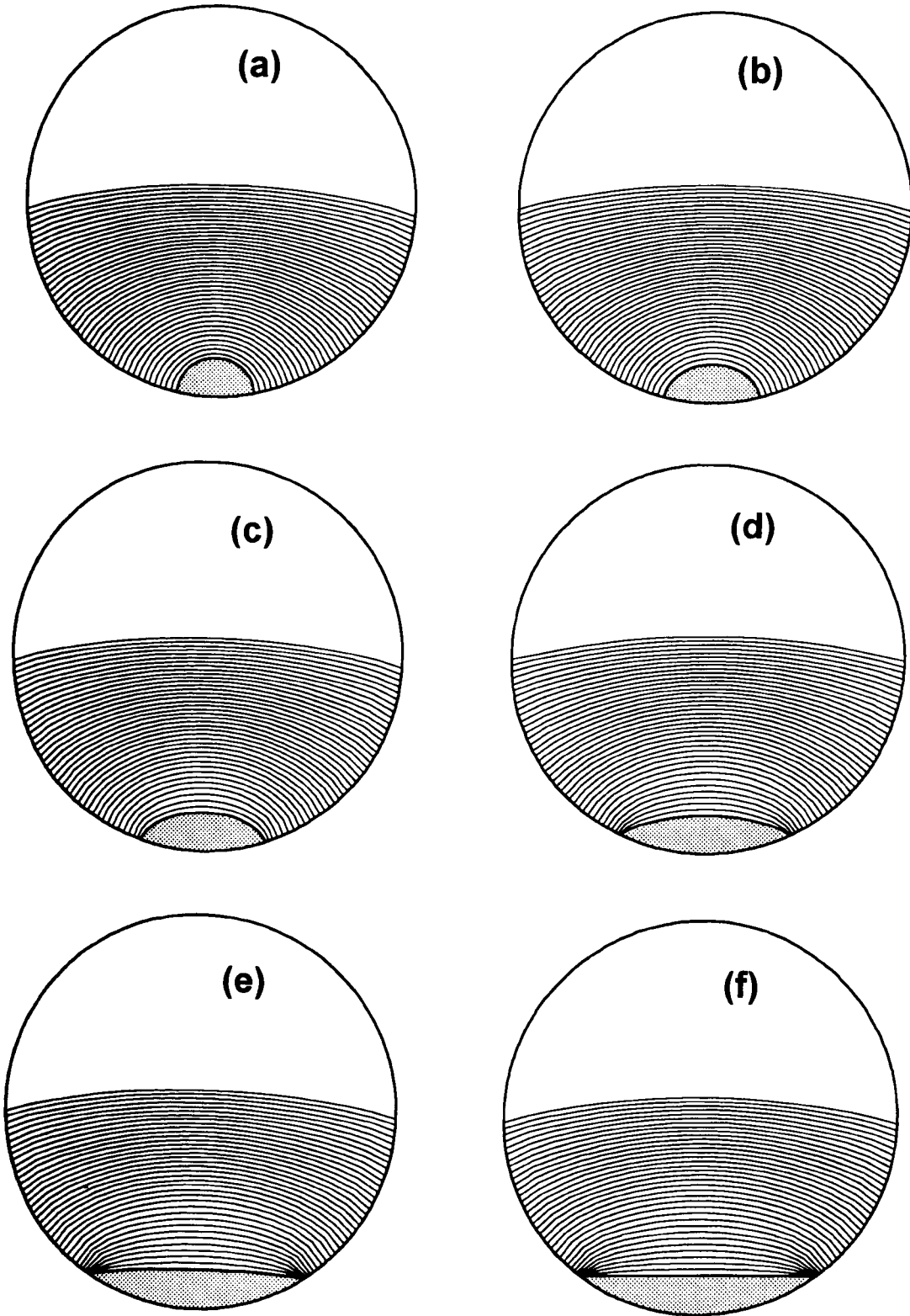
Figure 7.5   Shape development of initially semi-elliptical surface cracks in round bars under tension fatigue; (a) a_o/c_o = 1.0, (b) 0.8, (c) 0.6, (d) 0.4, (e) 0.2, and (f) 0.0

205
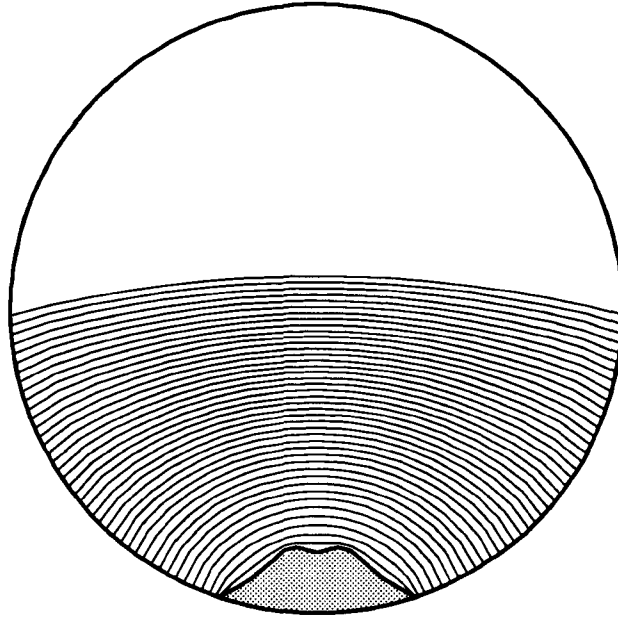
Figure 7.6   Shape development of an initially irregular surface
crack in round bar under tension fatigue

7.4 Fatigue Shape Deviation

As mentioned previously, different shapes for the propagating crack profiles have been
assumed in order to simplify the fatigue prediction process. It is certain that different shape
assumptions will lead to different results, and all numerically include a factor causing an
uncertain error. It has become apparent that the present simulation technique has explicitly
considered the variation of stress intensity factors along the crack front, thus avoiding
employing a shape assumption. Meanwhile, it has also become possible to investigate the
shape development characteristics for the growing cracks numerically. In this chapter, the
present author also proposed both the relative residual, E_i, and the relative standard deviation,
S_r, for the cracked bar. The relative residual was herein defined as follows:

$$E_i = \frac{\overline{PQ}}{\overline{QM}} = \frac{\overline{PM} - \overline{QM}}{\overline{QM}}$$

which, as shown in Fig. 7.7, represents a relative error at the *i*th point P (*corner node*) of the predicted crack front to a corresponding circular arc that passes through both the depth point A and the free surface point B and centres at the point M.

The relative standard deviation was intended to quantitate the total relative error of the predicted crack front to the part-circular shape, and defined in the following equation:

$$S_r = \sqrt{\frac{1}{n}\sum_{i=1}^{n}(E_i)^2}$$

where n is the number of the corner nodes used to construct a crack front in FE models. Obviously, the smaller S_r

Figure 7.7 Comparison of predicted crack front with assumed circular arc

means the better approximation to the assumed circular arc.

Fig. 7.8 shows the distribution of the relative residual around five different selected crack fronts, (a) corresponding to the initial crack of $a_o/c_o = 1.0$ and (b) to $a_o/c_o = 0.2$. The relevant crack fronts are also displayed in the plot. It is seen in Fig. 7.8(a) that there is a zero distribution along the initial crack marked by symbol (O), which is because the initial crack shape is an exactly circular arc. All curves have a zero value at both the depth ($\theta_i/\theta_B = 0$, *see Fig. 7.7*) and surface ($\theta_i/\theta_B = 1$) positions. This is caused by the E_i definition, i.e. the assumed shape is required to be through the two extremes of the predicted crack profile. Fig. 7.8(a) also demonstrates that the predicted crack profiles always deviate outwardly from the assumed part-circles, the maximum relative residual occurring between $\theta_i/\theta_B = 0.7$ and 0.9 and being less than 1.5%. Fig. 7.8(b) shows similar distributions to those in Fig. 7.8(a), but the maximum E_i value reaches 3%. As for other initial cracks, the E_i distributions can also be found to be similar (*not presented in this chapter*).
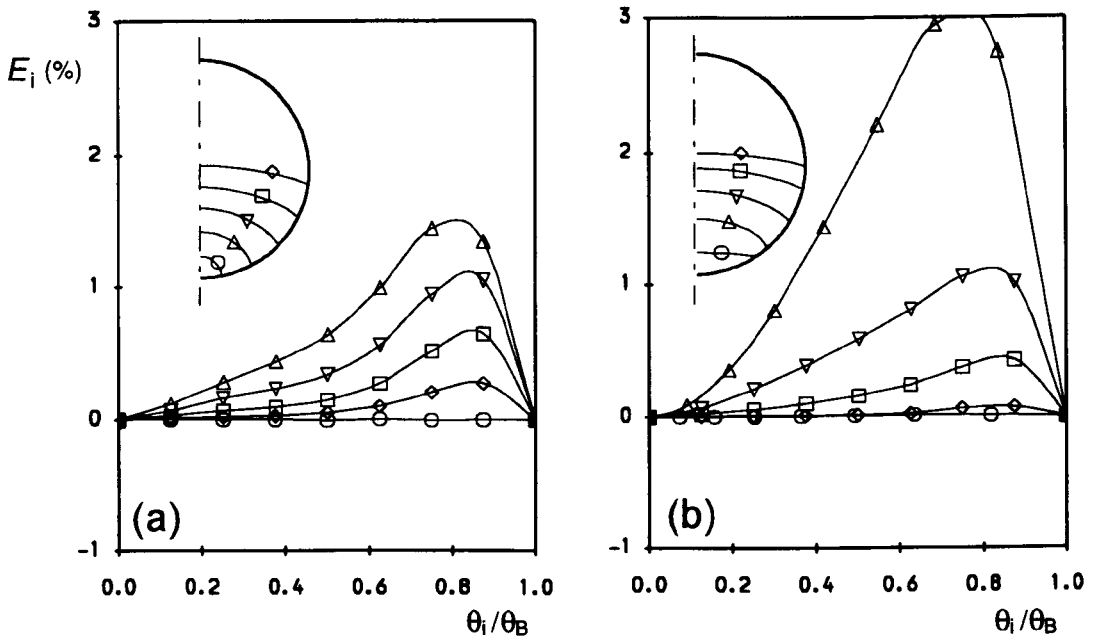
Figure 7.8   Distributions of the relative residual, E_i, around the
crack front during crack growth

The variations of the relative standard deviation with crack growth are shown in Fig. 7.9 for initially elliptical arc cracks. It can be observed that during the early stage of crack growth the S_r value is relatively higher, the maximum being below 2.5%, partly due to the initial difference between the chosen part-elliptical shape and the compared part-circle. However, as the crack grows, the S_r values tend to converge and almost approach zero when the crack reaches the centre of the round bar. This strongly implies that the crack growth always attempts to follow a preferred propagation pattern, no matter what initial crack shape it is.

Both the above E_i and S_r analyses demonstrate that the part-circular shape, as shown in Fig. 7.1(c), has been numerically confirmed to be a good approximation for the developing crack fronts.

Fig. 7.10 shows the variation of the dimensionless radius, r_M/D, of the assumed part-circle against the dimensionless crack depth, a/D. It is seen that for the initially straight ($a_o/c_o = 0.0$), or near-straight ($a_o/c_o = 0.2$) front cracks, big circles are initially needed to approximate the two cracks. However, as the crack advances the radius of the circle decreases rapidly, and subsequently increases gradually as the crack continues to grow. Fig. 7.10 also shows an intense convergence, nearly starting from $a/D = 0.3$, for all different initial crack configurations. When the crack propagates to the bar centre, the r_M/D value is equal to about 1.3.
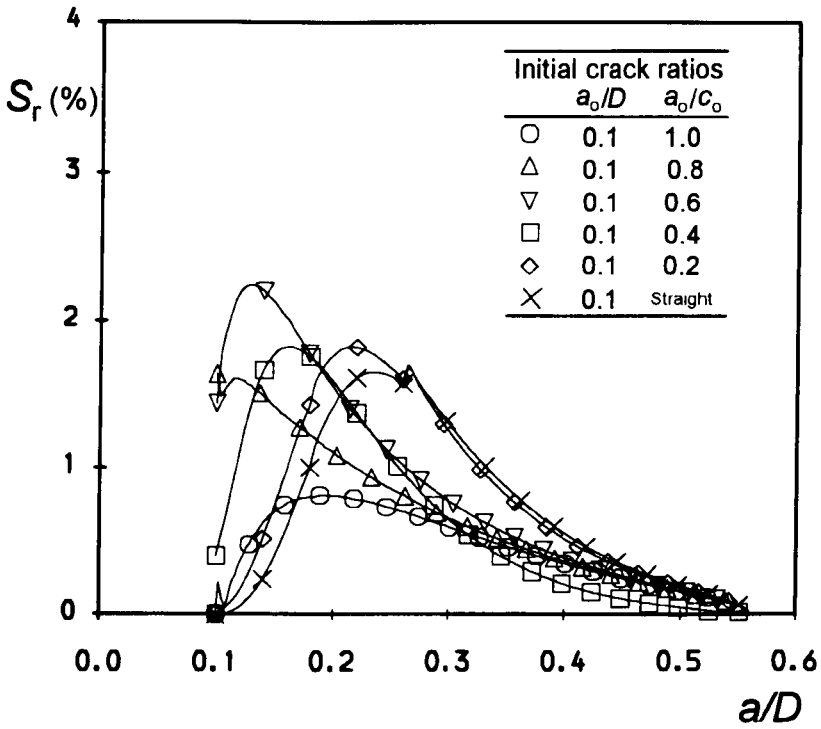
Figure 7.9   Variations of standard residual deviation during crack growth
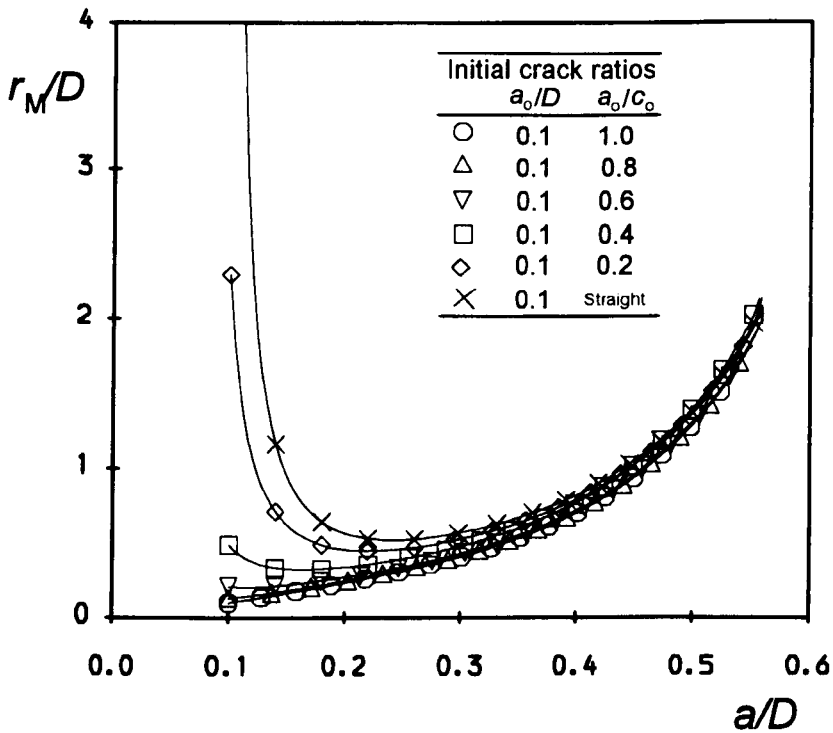
Figure 7.10   Variations of radius of crack front during crack growth

7.5 Aspect Ratio Changes

The crack aspect ratio was defined in this chapter as the ratio of the crack depth, a, to the surface arc half-length, b, as shown in Fig. 7.1(d). Knowledge of the aspect ratio change with crack growth is important in predictions of fatigue lives, although it is still incomplete to be used to fully describe the actual crack profile due to the existence of the shape deviation.

The aspect ratio variation predicted by the present simulation technique is likely affected by the use of different maximum crack growth increments, Δa_{max}, along the crack front during the modelling computations. In order to confirm that the value $\Delta a_{max} = D/250$ employed in the calculations is small enough for the aspect ratio prediction, two larger values, $\Delta a_{max} = D/167$ and $D/100$ were also used in modelling the fatigue growth of the initially elliptical arc crack of $a_o/c_o = 0.8$. Fig. 7.11 shows the effect of the maximum crack growth increment on the aspect ratio change. Clearly, there is an excellent agreement among the three predictions obtained, respectively, from $\Delta a_{max} = D/250$, $D/167$ and $D/100$, which convinces us that taking $\Delta a_{max} = D/250$ can ensure good predictions of aspect ratio changes.

Fig. 7.12 presents the aspect ratio variation obtained by the present numerical technique with the crack depth ratio, a/D. It can be seen that the aspect ratio change is intensely dependent on the initial crack geometry during the early period, but such a dependency is gradually weakened and the cracks asymptotically tend to grow towards a preferred propagation path as the crack extends. The aspect ratios have nearly converged at the value of $a/D = 0.4$ to the value of $a/b = 0.75$, and subsequently decrease slowly to $a/b = 0.71$ at $a/D = 0.55$. In Fig. 7.12 the experimental results obtained by Caspers *et al.* (1990) using the beach marking method are also included for comparison. Caspers *et al.* (1990) performed the tension fatigue tests with a stress ratio $R = 0.5$ on the cylindrical bars made of a chromium-molybdenum steel (*German designation 42CrMo4*). The experimental aspect ratio changes were represented by four different symbols ($\triangle \triangledown \bigcirc \square$) corresponding to four different initial crack configurations, which are identified with the solid symbols. The comparison in Fig. 7.12 shows that the experimental results have a similar tendency of aspect ratio variation to the calculated results. Particularly, when the crack becomes large, the experimental data also show a clear convergence which is in close agreement with the predicted results. Athanassiadis *et al.* (1981) also tested some plain carbon steel wires by fatigue, and obtained the crack shape after the final fracture of specimens. They observed that the aspect ratios at

specimen fracture, occurring between $a/D = 0.28$ and 0.34, ranged from 0.71 to 0.79. Obviously, the results from the experiments of Athanassiadis *et al.* (1981) agree well with the present predictions if the initial aspect ratios of their initial cracks are considered to be about 1.0.
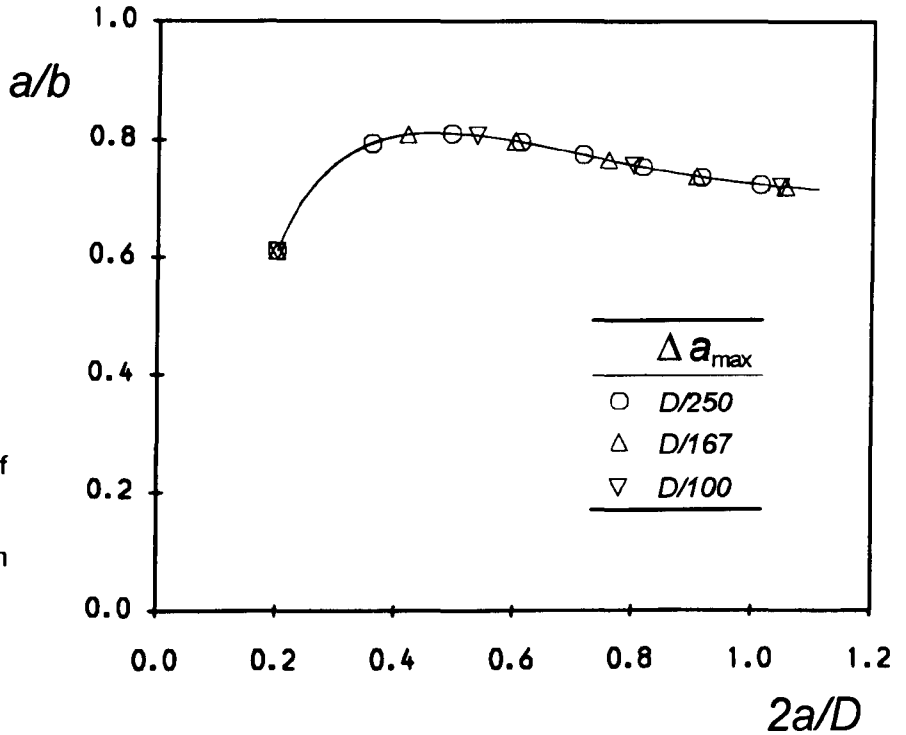
Figure 7.11 Convergence of aspect ratio changes predicted by different maximum crack growth increment, Δa_{max}
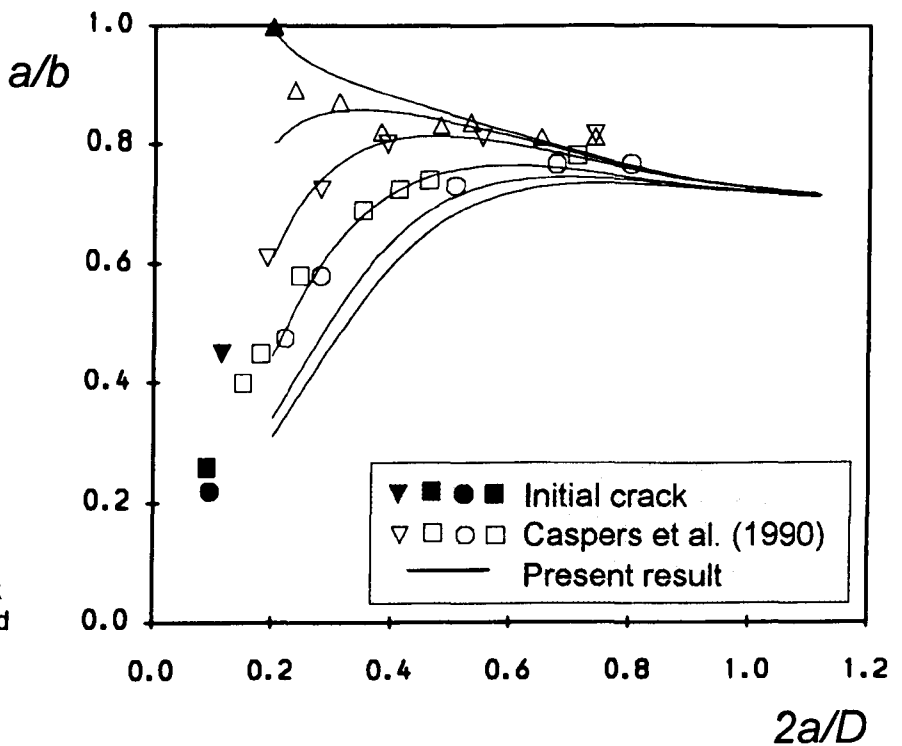
Figure 7.12 Aspect ratio change of edge crack in round bar subjected to tension fatigue
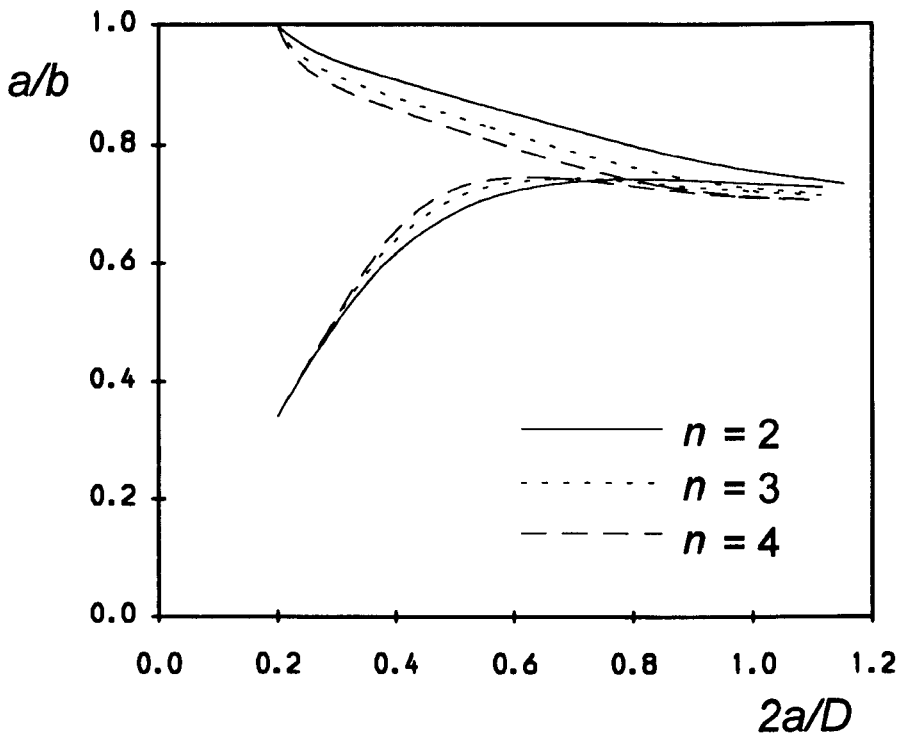
Figure 7.13   Influence of exponent, *n*, in Paris crack growth
law on aspect ratio change of edge crack in round bar
subjected to tension fatigue

Fig. 7.13 reveals the effect of the Paris crack growth law exponent, *n*, on the aspect ratio change for the cracks of $a_o/c_o = 0.2$ and 1.0. Three different values, $n = 2$, 3, and 4 were considered. The results in Fig. 7.13 show that the effect can be seen: a larger *n* always makes the aspect ratio change more intense due to its exponential nature, and reaches a smaller aspect ratio value when the crack grows to the centre of the bar.

7.6 Conclusions

The fatigue shape development of several initially part-elliptical and an initially irregular surface crack in round bars under axial cyclic loading has been studied by the step-by-step FE simulation technique. The main conclusions can be drawn as follows:

1) Surface cracks, of either regular or irregular shapes, in cylindrical bars subjected to tension fatigue loading always attempt to develop asymptotically to preferred propagation paths. The aspect ratio change, despite varying with the initial crack configuration, usually converges to a stable range, $a/b = 0.71 \sim 0.75$, as the crack grows to $a/D \geq 0.4$. The present numerical predictions generally agree well with experimental results.

2) The shape characteristic of propagating cracks has been studied by both the proposed relative residual and relative standard deviation. It is shown that the circular-arc whose centre is allowed to vary along the vertical axis (*Fig. 7.1(c)*) seems to approximate the predicted crack front well ($S_r < 1.5\%$), and the predicted crack profile appears to deviate a little outwardly ($0 \leq E_i \leq 4\%$) from its corresponding circular-arc.

3) The influence of the material constant, n, contained in the Paris crack growth law, can be seen. A larger value of n always causes a more intense change of the aspect ratio due to its exponential nature, and reaches a relatively smaller aspect ratio when the crack advances to the bar centre.

7.7 References

Astiz, M. A. and Elices, M. (1980) *On the application of stiffness derivative method to two- and three-dimensional fracture problems.* Proceedings of 2nd International Conference Numerical Method in Fracture Mechanics, 93-106.

Astiz, M. A. (1986) *An incompatible singular elastic element for two- and three-dimensional crack problems.* Int. J. Fracture 31, 105-124.

Athanassiadis, A., Boissenot, J. M., Brevet, P., Francois, D. and Raharinaivo, A. (1981) *Linear elastic fracture mechanics computations of cracked cylindrical tensioned bodies.* Int. J. Fracture 17, 553-566.

Blackburn, W. S. (1976) *Calculation of stress intensity factors for straight cracks in grooved and ungrooved shafts.* Engng Fract. Mech. 8, 731-736.

Bush, A. J. (1976) *Experimentally determined stress-intensity factors for single-edge-crack, round bars loaded in bending.* **Exper. Mech. 16**, 249-257.

Bush, A. J. (1981) *Stress intensity factors for single-edge-crack solid and hollow round bars loaded in tension.* **J. Test Eval. 9**, 216-223.

Carpinteri, A. (1992a) *Elliptical-arc surface cracks in round bars.* **Fatigue Fract. Engng Mater. Struct. 15**, 1141-1153.

Carpinteri, A. (1992b) *Stress-intensity factors for straight-fronted edge cracks in round bars.* **Engng Fract. Mech. 42**, 1035-1040.

Carpinteri, A. (1993) *Shape change of surface cracks in round bars under cyclic axial loading.* **Int. J. Fatigue 15**, 21-26.

Caspers, M. and Mattheck, C. (1987) *Weighted averaged stress intensity factors of circular-fronted cracks in cylindrical bars.* **Fatigue Fract. Engng Mater. Struct. 9**, 329-341.

Caspers, M., Mattheck, C. and Munz, D. (1990) *Propagation of surface cracks in notched and unnotched rods.* Surface-crack Growth: Models, Experiments, and Structures. ASTM STP **1060**, 365-389.

Daoud, O. E. K., Cartwright, D. J. and Carney, M. (1978) *Strain-energy release rate for a single-edge-cracked circular bar in tension.* **J. Strain Analysis 13**, 83-89.

Daoud, O. E. K. and Cartwright, D. J. (1984) *Strain energy release rates for a straight-fronted edge crack in a circular bar subject to bending.* **Engng Fract. Mech. 19**, 701-707.

Daoud, O. E. K. and Cartwright, D. J. (1985) *Strain energy release rate for a circular-arc edge crack in a bar under tension or bending.* **J. Strain Analysis 20**, 53-58.

Fan, Y. X., Fan, Y. T. and Fan, D. J. (1982) *The approximate analytical solution for both surface and embedded cracks in cylinder with finite size.* **Engng Fract. Mech. 16**, 55-67.

Forman, R. G. and Shivakumar, V. (1986) *Growth behaviour of surface cracks in the circumferential plane of solid and hollow cylinders.* Fracture Mechanics. ASTM STP **905**, 59-74.

James, L. A. and Mills, W. J. (1988) *Review and synthesis of stress intensity factor solutions applicable to cracks in bolts.* **Engng Fract. Mech. 30**, 641-654.

Levan, A. and Royer, J. (1993) *Part-circular surface cracks in round bars under tension, bending and twisting.* **Int. J. Fracture 61**, 71-99.

Lorentzen, T. K., Kjaer, N E and Henriksen, T (1986) *The application of fracture mechanics to surface cracks in shafts*. **Engng Fract. Mech. 23**, 1005-1014

Mackay, T. L. and Alperin, B J (1985) *Stress intensity factors for fatigue cracking in high-strength bolts.* **Engng Fract. Mech. 21**, 391-397

Nezu, K. Machida, S and Nakamura, H (1982) *SIF of surface cracks and fatigue crack propagation behaviour in a cylindrical bar*. 25th Japan Cong Mater Res Metall Mater. 1982, 87-92

Ng, C. K. and Fenner, D N (1988) *Stress intensity factors for an edge cracked circular bar in tension and bending*. **Int. J. Fracture 36**, 291-303

Nisitani, H. and Chen, D H (1984) *Stress intensity factor for a semi-elliptic surface crack in a shaft under tension*. **Trans Japan Soc Mech Engrs 50**, 1077-1082

Nord, K. J. and Chung, T J (1986) *Fracture and surface flaws in smooth and threaded round bars*. **Int. J. Fracture 30**, 47-55

Ouchterlony, F (1981) *Extension of the compliance and stress intensity formulas for the single edge crack round bar in bending*. Fracture Mechanics for Ceramics, Rocks and Concrete. ASTM STP 745, 237-256.

Raju, I. S. and Newman, J C (1979) *Stress intensity factors for a wide range of semi-elliptical surface cracks in finite thickness plates*. **Engng Fract. Mech. 11**, 817-829

Raju, I. S. and Newman, J C (1986) *Stress intensity factors for circumferential surface cracks in pipes and rods*. Fracture Mechanics. ASTM STP 905, 789-805.

Salah el din, A. S. and Lovegrove, J. M. (1981) *Stress intensity factors for fatigue cracking of round bars*. **Int. J. Fatigue 3**, 117-123.

Si, E. (1990) *Stress intensity factors for edge cracks in round bars*. **Engng Fract. Mech. 37**, 805-812.

Thompson, K. D. and Sheppard, S. D. (1992a) *Stress intensity factors in shafts subjected to torsion and axial loading*. **Engng Fract. Mech. 42**, 1019-1034.

Thompson, K. D. and Sheppard, S. D. (1992b) *Fatigue-growth in notched and plain shafts subjected to torsion and axial loading*. **Engng Fract. Mech. 43**, 55-71.

Wilhem, D., FitzGerald, J., Carter, J. and Dittmer, D. (1982) *An empirical approach to determining K for surface cracks*. Proceedings of 5th International Conference on Fracture Research, Cannes, France, 1982, Advances in Fracture research - Fracture 81, 11-21.

BLANK PAGE
IN
ORIGINAL

Chapter 8

CONCLUDING REMARKS

This chapter summarises some principal conclusions reached in this research and briefly outlines some possible directions for further studies.

8.1 Conclusions

1) Significant improvements have been made to a step-by-step finite element technique. Its successful application to various cracked geometries of either theoretical or engineering significance, such as internal cracks in infinite solids, surface cracks in plates, round bars and pressure vessels, and multiple crack configurations, demonstrates that the technique enables direct modelling of the fatigue propagation of initially irregular shaped cracks within practical complex structures, and also provides more accurate estimates of both crack shape changes and fatigue lives compared with the widely used shape assumption method. The stress intensity factor accuracy of the present technique has been verified to be excellent by comparing stress intensity factor results of a variety of crack configurations with either existing analytical or recognised numerical solutions, which essentially ensures the accuracy of fatigue growth modelling. The automatic remeshing capability of the simulation technique makes it possible to apply this technique to practical cracked components.

2) Three important findings in the calculation of stress intensity factors using 3D finite element analyses are: (a) the cubic spline curve should be used to define the front of propagating cracks, in order to effectively eliminate the error of stress intensity factor due to the inadequate position of midside nodes along the crack front; (b) the *J*-integral should be used with caution since its path independence is readily lost near the free surface if the crack front does not intersect the free edge orthogonally; (c) the mesh abutting the crack front is required to be orthogonal for the 1/4-point displacement but unnecessary for the *J*-integral method.

3) The numerical study of fatigue shape changes in this thesis shows that an initially irregular embedded crack in an infinite solid subjected to remote uniform tension will grow to a circle (*iso-K configuration*) and subsequently maintain a circular front, in accord with expectation. The surface crack in a plate can basically maintain an approximate semi-ellipse during the fatigue growth process from the initial defect up to the plate back surface for both pure tension and DOB = 0.5 loads. Such a conclusion can also be reached for an external surface crack in an internally pressurised cylinder. However, for the surface crack in a plate subjected

to pure bending, a greater shape deviation from the semi-ellipse commences to appear when the crack grows to nearly $a/t = 0.75$, and subsequently the deviation increases continuously and very quickly. The shape investigation of a surface crack in a round bar under tension fatigue shows that the crack front can be well approximated by the circular-arc whose centre is allowed to vary along the vertical axis.

4) The shape development of initially multiple fatigue cracks has also been successfully modelled through the pre-coalescence, coalescence and post-coalescence stages by the simulation technique. The results obtained show that the interaction between two adjacent cracks is very limited even as they approach very closely to each other.

5) The aspect ratio variations for either plate or bar surface cracks predicted by the present technique are generally in quite good agreement with experimental results from the literature, further demonstrating that the present numerical technique is reliable. The influence of the material constant, n, contained in the Paris crack growth law, on the aspect ratio change can be demonstrated. A larger value of n always causes a more intense change of the aspect ratio because n is a measure of the strength of the exponential nature of the crack growth law.

6) The effect of different maximum crack growth increments, Δa_{max}, employed in practical computations on the predictions of aspect ratio changes and fatigue cycles has been examined in several chapters. It is shown that a good convergence can be achieved by reducing the Δa_{max} value to a small value.

7) The lagging of the crack growth along the free surface, which is often observed in experiments, due to the 2D plane stress state might be able to be neglected during the fatigue modelling calculations if its locality is considered, which has been demonstrated by an investigation of boundary layer correction in Chapter 4, in which the plane stress state at the free surface point of the crack front and the plane strain state at interior positions are assumed. The result shows that using the stress state correction at the surface point predicts slightly different fatigue lives compared with those obtained without using such a correction.

8.2 Future Directions

The present numerical technique has been shown to be a powerful tool to model the fatigue growth of practical fatigue cracks. Its accuracy, efficiency and flexibility as well as ease of use have been demonstrated for a limited class of problems, the purpose of this section is to consider how its applicability might be widen.

As indicated in Chapter 1, the simulation technique at present is confined to the analysis of planar cracks under Mode I fatigue loading, for which the crack extension is retained within the initial crack planes, i.e. cracks cannot be allowed to change their initial orientation. This greatly restraints its scope of application. Cracks contained in practical complex structures and components often are of non-planar form, and situated in complex stress states which may cause them to change directions during the propagation process. The fatigue growth modelling of such cracks needs to consider mixed mode stress/strain distributions near the crack tip, and to introduce a fatigue crack growth law containing an appropriate mixed mode criterion, such as the maximum tangential stress or the minimum strain energy density criteria. It appears to be not difficult to calculate mixed mode stress intensity factors using the 3D finite element method, but the problem is how to create finite element models conveniently or even automatically, particularly during the crack growth process. Therefore, great effort would be required to develop such an automatic remeshing technique.

More experimental verifications of this technique are needed. In this thesis the comparisons between numerical modelling results and experimental data from the literature have been concentrated on the crack shape change. It is felt that it is necessary and important to compare the fatigue life between both numerical and experimental results for a wide range of practical cracks in order to provide further support for the applicability of the technique.

The fatigue crack growth relation currently used in the technique is the well-known Paris law. This could be readily extended to consider the threshold stress intensity factors and fracture toughness values, thus allowing both crack arrest and rapid growth stages to be predicted. The applied fatigue load throughout this thesis has been assumed to be a constant amplitude one with stress ratio being zero. It obviously is of significance to analyse variable amplitude fatigue growth problems of varying stress ratio during crack growth. More work should be done on this matter.

The simulation technique is likely to be developed further to model the fatigue crack growth in non-metallic materials, and some other crack growth phenomenon, such as creep and corrosion by including certain crack growth relations appropriate to characterise these crack growth mechanisms.

Residual stresses often exist in engineering structures and components, such as in welds and autofrettaged pressure vessels, and near fastener hole edges after cold-working, stress coining, or shot peening there. The fatigue growth of cracks in the material with residual stresses is a complex, but important, problem. The existence of residual stresses alters the stress distribution due to a remote alternating load, and may cause partial closure of the crack faces where an overlapping of crack faces occurs according to the superposing calculation of the normal displacements on the crack plane caused by both the residual stress and the fatigue load. Complex stress variations around the crack front may make the crack experience so complicated shape changes during the fatigue propagation process that the widely used "shape assumption method" mentioned before would be incapable of dealing with them. However, the present technique can take advantage of being able to trace the crack shape change directly. By superposing the static residual stresses to the stresses caused by the alternating loads and further considering the stress redistribution due to possible partial crack face touching, the fatigue crack growth in a residual stress field can be investigated.

APPENDIX A

Some Details about the execution of DUCK

The software DUCK, mainly for simulating the fatigue growth of planar cracks of initially irregular shape, has been written by the present author in the standard computer language FORTRAN 77, and developed in the environment of an UNIX operating system. The software is actually a package including several main programs and many subroutines, each being saved as an individual file and responsible for a unique function. These subroutines are usually small in length in order to increase the convenience of developing the package and the readability of the source codes. These files can be well organised by the "make" tool planted in the UNIX operating system and easily compiled.

Chapter 2 has described the theoretical principles used by the present simulation technique and some technical details. This appendix will give more details, especially for the practical execution of the present software through a typical example. It also explains several other important aspects, such as designing the mesh and choosing the parameters required by the software.

The example selected here is a surface crack in a finite thickness plate subjected to remote tension, as shown in Fig. A.1. The initial crack is assumed to have a semi-elliptical front, and to have a depth ratio (a/t) of 0.2 and an aspect ratio (a/c) of 0.6. The thickness, height and width of the plate are chosen to be 25 mm, 800 mm and 800 mm, respectively. The material is assumed to have a Poisson's ratio v of 0.3 and a Young's modulus of 210 GPa. The Paris crack growth law is assumed to be $da/dN = 1.83 \times 10^{-13} \Delta K^3$, where the units of da/dN and K are mm/cycle and MPa·mm$^{1/2}$, respectively. The load applied on both the outer end surfaces is a cyclic constant load from 0 to 1 MPa, as shown in Fig. A.1.

A.1 Dividing the geometry into two blocks

Before a FE model is created, the symmetry of the problem should be considered in order to reduce the number of degrees of freedom of the analysis model. Obviously, only one-
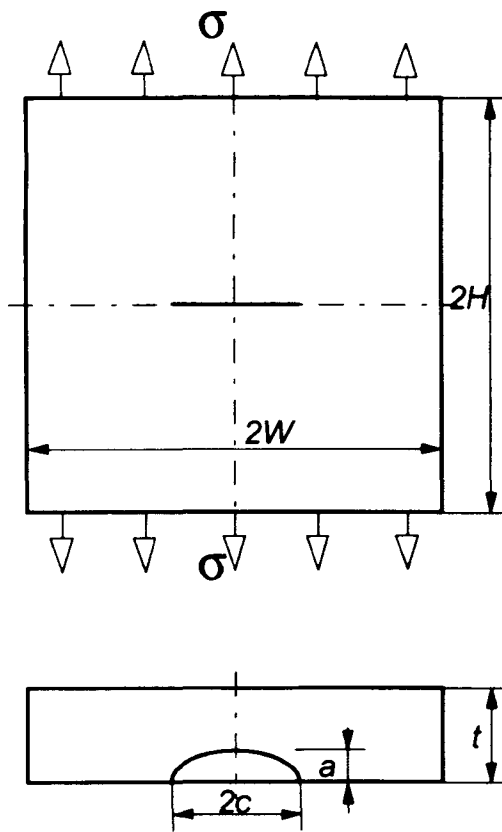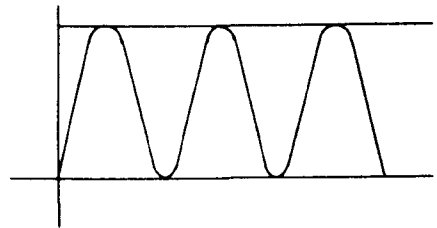
Figure A.1 Simulated surface crack in finite thickness plate

quarter of the plate needs to be analysed by the FE method for the current cracked plate. After that, we should consider whether the two-block model, as explained in Chapter 2 (*see Fig. 2.11*), is necessary for the one-quarter plate. Generally, dividing the geometry into the cracked and uncracked blocks may assist in achieving the automatic remeshing required by the technique, and may also decrease the size of the FE model since a relatively coarse mesh can be used for the uncracked block. Here, we decide to divide the geometry into two blocks, as shown in Fig. A.2. The cracked block has a thickness of 6 mm.

A.2 Create a 3D uncracked block mesh

The 3D FE mesh for the uncracked block should be generated in advance. This mesh defining the bulk of the plate will remain unchanged during the whole modelling analysis. Fig.

A.3 shows the mesh created by using FEMGV, consisting of 256 20-noded brick elements and being saved as the file **plt6c.lod**.
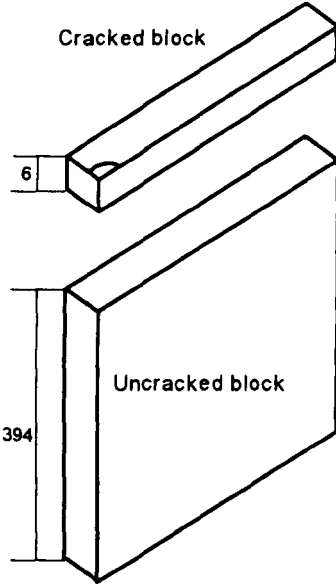
Figure A.2 Two-block model
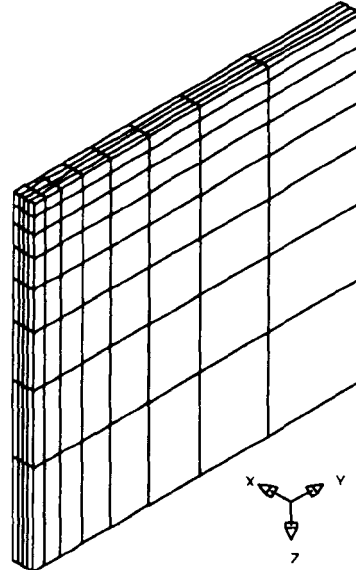
Figure A.3 Uncracked block mesh created by FEMGV

A.3 Create a 2D crack plane mesh

As indicated in Chapter 2, the 3D cracked block mesh is generated by expanding a 2D crack plane mesh. Therefore, the 2D mesh must be established first.

The mesh generator FEMGV has also been employed to define the 2D crack plane mesh. It is first necessary to describe here some principles used by FEMGV for generating a mesh. FEMGV usually creates a mesh first by dividing the geometry into some macro-surfaces (*for 2D*) or bodies (*for 3D*), and then by filling them with a certain type of element. The density of the mesh within a defined surface or body can be controlled by specifying a different number of divisions along the edges of the surface or body. Therefore, the first step is to generate the geometry pattern of the half-section containing the quarter-elliptical crack.

Fig. A.4(a) illustrates the geometry pattern designed by the present author. These small symbols (◊) in Fig. A.4(a) represent the points used to construct the crack front and the boundary, or to assist in the subsequent remeshing as the crack grows. The lines were then established by connecting proper points to form an essential pattern of geometry. It can be seen from Fig. A.4(a) that seventeen points have been arranged to define the quarter-elliptical

225
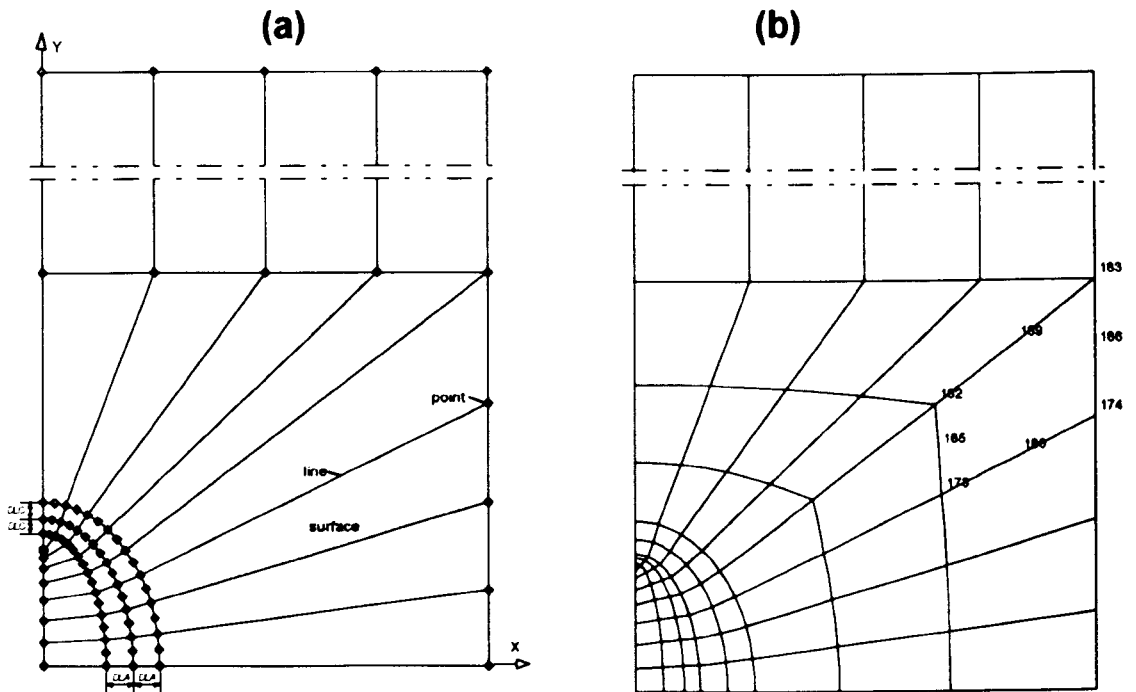
Figure A.4   Designed geometry (a) and mesh (b) patterns for initial
surface crack by using FEMGV

crack front. The same number of points were arranged to situate on each side of the crack front for the purpose of achieving an orthogonal mesh pattern along the crack front. If the crack extends, the position of these points can be adjusted so that the orthogonal pattern may be conveniently retained. Fig. A.4(a) further shows the surfaces constructed by the lines. By specifying an element type, these surfaces can be filled with desired elements finally to achieve a mesh pattern. Fig. A.4(b) shows the created mesh containing 84 8-noded 2D elements, including 32 elements within the cracked region. It should be indicated that the design of a geometry pattern is very important because the automatic remeshing will be dependent upon it. A considerable familiarity with FEMGV is needed for such a design. The geometry pattern, as shown in Fig. A.4(a), will help to achieve the automatic remeshing of the 2D crack section by varying properly the position of most of the points during the crack growth. Both the geometry and mesh patterns are saved as the files **surfcrk0.arc** and **surfcrk0.f2d**, which are of a FEMGV format

A.4 The Execution of DUCKPRE

Once the 2D crack plane and 3D uncracked meshes have been created, a complete 3D FE model can be obtained by DUCKPRE. The execution of DUCKPRE is now explained as follows. Fig. A.5 shows the recorded practical execution.

Lines 0–10: When the command DUCKPRE at line 0 was issued, the first parameter needed to enter is the type of the modelled problem. Obviously, we should select 1 for the surface cracked plate.

Lines 11–13: The model name here is required to include two parts, i.e. a string plus a numeric, where the numeric represents the step of crack growth. We chose **surfcrk** as the identifier of the crack growth simulation and specified **0** for the beginning step.

Lines 14–22: Between these lines, some geometry parameters were required by DUCKPRE, such as the thickness, height and width of the plate, which can be found to be 25

Figure A.6   Mesh pattern near the crack tip

mm, 400 mm and 400 mm from Fig. A.1. Two important parameters, $ZEND\_PLT$ and $FACT\_PLT$ were also demanded. Through them the thickness of the cracked mesh mentioned in Chapter 2 and the mesh pattern around the crack tip can be adjusted. According to the experience of the present author, the cracked block has been designed as having three layers, as shown in Fig. A.6, although it is straightforward to vary the number of the mesh layer, as indicated before. The thickness of each layer is shown in Fig. A.6. The parameter $FACT\_PLT$ is used to control the thickness of the first mesh layer, the value being 0~1. It is suggested that the thickness of the first layer should be close to the size DLA (*also see Fig. A.2*) in the 2D crack plane mesh, in order to obtain a good element shape near the crack tip. For the current example, we selected **6.0** and **0.25** for $ZEND\_PLT$ and $FACT\_PLT$, respectively.

Lines 23–25: The line 23 asked for the name of the **.tip** file which should have been prepared before DUCKPRE is run. Using this file, the software can automatically identify both the crack front and cracked area. The file we have generated is **surfcrk-a.tip**.

Lines 26–28: The name of file that contains the 3D FE mesh of the uncracked block should be entered at this stage. This file is also required to create in advance, as mentioned before. Here, it is **plt6c.lod**.

Lines 29–33: The choice of the loading type offered by DUCKPRE is the uniform or non-uniform load. If a remote non-uniform loading is dealt with, an extra subroutine in which the non-uniform distribution is defined must be provided. This will be read by ABAQUS. Due to a remote tension involved here, we just selected 1 at the line 32.

Lines 34–36: The material properties, such as Young's modulus E, Poisson's ratio v, Paris' coefficient C and Paris' exponent n, were inputted into DUCKPRE.

Lines 37–43: These lines show us some important information associated with the created FE model, including the number of elements and nodes, the number of multiple-point constraint equations on the mismatch plane between the cracked and uncracked blocks. The boundary conditions have been specified directly in the program for the surface cracked plate.

The output of DUCKPRE, finally, is the two files **surfcrk0.inp** and **surfcrk0.f3d**. The former is a complete input file ready for the FE analysis by ABAQUS, and the latter can be fed to FEMGV to check the created 3D mesh, if necessary.

```
0:      silver{me2xl}138: DUCKPRE
1:      ••••••••••••••••••••••••••••••••••••••••••••••••••••••••••••
2:      •••          Enter type of problem analysed >          •••
3:      •••                                                    •••
4:      •••   1) SURFACE CRACK in PLATES                       •••
5:      •••   2) INTERNAL CRACK in INTERNALLY PRESSURIZED CYLINDER •••
6:      •••   3) EXTERNAL CRACK in INTERNALLY PRESSURIZED CYLINDER •••
7:      •••   4) SURFACE CRACK in ROUND BAR                    •••
8:      ••••••••••••••••••••••••••••••••••••••••••••••••••••••••••••
9:      1
10:     •••              1
11:     ••• Enter input model name >
12:     surfcrk0
13:     ••• surfcrk0
14:     ••• Enter geometry of bar >
15:     •••   t --- Thickness of plate
16:     •••   H --- Height of plate
17:     •••   W --- Width of plate
18:     25.0, 400.0, 400.0
19:     ••• Enter parameter of the cracked mesh >
20:     •••   ZEND_FLT --- Thickness of the cracked block
21:     •••   FACT_FLT --- Factor of the mesh
```

228

```
22:    6.0, 0.25
23:    *** Enter file name of crack front >
24:    surfcrk-a.tip
25:    *** surfcrk-a.tip
26:    *** Enter file name of LOADING BLOCK FILE >
27:    plt6c.lod
28:    *** plt6c.lod
29:    *** Enter type of loading >
30:    ***    1 = UNIFORM LOADING
31:    ***    2 = NON-UNIFORM LOADING
32:    1
33:    ***                      1
34:    *** Enter MATERIAL PROPERTIES (E, POISS, C, N) >
35:    210.e3, 0.3, 1.83e-13, 3.0
36:    ***     210000.0       0.3000000    1.8300000E-13   3.000000
37:    *** Reading 2-D mesh ***
38:    *** Reading 2-D crack front information ***
39:    *** Creating cracked block  (element:        344) ***
40:    *** Reading loading block      plt6c.lod ***
41:    *** Merging cracked and loading blocks ***
42:    *** MODEL: 3461 nodes,    600 elements ***
43:    ***  298 points are constrained on surface, Z =   6.00 ***
```

Figure A.5 The execution of DUCKPRE

A.5 The Execution of ABAQUS

Once the file surfcrk0.inp has been obtained, ABAQUS can be started, as shown in Fig. A.7. The current version of ABAQUS is 5.3 installed in a Silicon Graphic computer (_machine name_: silver) at the University of Sheffield. Usually, the ABAQUS run is put into background operation for which a low priority is given.. It took about five minutes to complete the analysis of the present FE model (_10383 degrees of freedom_). As a commercial package, ABAQUS produces many files, such as **surfcrk0.dat**, **surfcrk0.fil**, **surfcrk0.log** and **surfcrk0.sta**, etc. The useful file for us is the file **surfcrk0.dat**, which is a data file containing the out-of-plane displacements at the 1/4-point and the _J_-integral values. The file **surfcrk0.fil** may be converted to FEMGV for inspecting or plotting some quantities, such as stresses, strains and displacements.

229

```
44:   silver{me2x1}142: abaqus
45:   Identifier                              : surfcrk
46:   User routine file                      :
```

Figure A.7 The execution of ABAQUS

A.6 The Execution of DUCKPOSTa

DUCKPOST has been developed mainly for obtaining a new crack front in terms of a Paris fatigue crack growth law, and for regenerating a 2D crack plane mesh for the new crack, as mentioned in Chapter 2.   Both tasks are actually undertaken in the package by the two separate main programs, DUCKPOSTa and DUCKPOSTb.   DUCKPOSTa must be executed first. Fig. A.8 displays a record of the execution of DUCKPOSTa.

Lines 47–89:   The FE mesh for the cracked plate was created again, because the node ordering of the 1/4-points and some other information were required while extracting the displacements at these points.   So, the same parameters of geometry and mesh as those used for DUCKPRE must be fed into DUCKPOSTa, in order to obtain an identical FE mesh.

Lines 90–92:   The value of the maximum crack growth increment, Δa_{max}, along the crack front is required to input so that the crack was advanced. This value, theoretically, should be chosen as small as possible, as indicated in Chapter 2, but during the practical simulation the computing time and resource should be taken into account.   Here, we specified $\Delta a_{max} = 1$.

Lines 93–159: Between these lines, some important results obtained by DUCKPOSTa are displayed. These include some information of the created FE model, the increment of fatigue cycles, ΔN, taken to propagate the crack front with the maximum crack growth increment being 1 mm, the three J-integral results, the displacements at the 1/4-point positions, the stress intensity factors calculated from both these J-integral and displacement values.   The crack growth direction and increment at each corner node as well as the position of the extended crack front are also obtained.   It can be seen that the SIF values obtained by the two methods are very similar.

Lines 160–162: A further parameter was demanded by DUCKPOSTa, and three choices, 80, 280 and 380 were provided. This parameter is used to recreate a cubic spline curve by FEMGV, which will be demonstrated later.   80 represents that the cubic spline curve will be equally divided into 80 segments, whilst 280 and 380 mean, respectively, that this curve is

biassedly divided into 80 segments with a bias factor 2 and 3. More details are available in the manual of FEMGV. For our case, we entered **80**.

A file was produced by DUCKPOSTa, which is the **surfcrk0n_spl.arc** containing the coordinates of these extended corner nodes along the crack front and some FEMGV commands used to instruct the creation of the cubic spline curve.

```
47:     silver{me2x1}174: DUCKPOSTa
48:     ****************************************************************
49:     ***             Enter type of problem analysed >          ***
50:     ***                                                       ***
51:     ***   1) SURFACE CRACK in PLATES                          ***
52:     ***   2) INTERNAL CRACK in INTERNALLY PRESSURIZED CYLINDER ***
53:     ***   3) EXTERNAL CRACK in INTERNALLY PRESSURIZED CYLINDER ***
54:     ***   4) SURFACE CRACK in ROUND BAR                       ***
55:     ****************************************************************
56:     1
57:     ***             1
58:     *** Enter input model name >
59:     surfcrk0
60:     *** surfcrk0
61:     *** Enter geometry of bar >
62:     ***   t --- Thickness of plate
63:     ***   H --- Height of plate
64:     ***   W --- Width of plate
65:     25.0, 400.0, 400.0
66:     *** Enter parameter of the cracked mesh >
67:     ***   ZEND_PLT --- Thickness of the cracked block
68:     ***   FACT_PLT --- Factor of the mesh
69:     6.0, 0.25
70:     *** Enter file name of crack front >
71:     surfcrk-a.tip
72:     *** surfcrk-a.tip
73:     *** Enter file name of LOADING BLOCK FILE >
74:     plt6c.lod
75:     *** plt6c.lod
76:     *** Enter type of loading >
77:     ***   1 = UNIFORM LOADING
78:     ***   2 = NON-UNIFORM LOADING
79:     1
80:     ***             1
81:     *** Enter MATERIAL PROPERTIES (E, POISS, C, N) >
82:     210.e3, 0.3, 1.83e-13, 3.0
83:     ***    210000.0      0.3000000      1.8300000E-13    3.000000
84:     *** Reading 2-D mesh ***
85:     *** Reading 2-D crack front information ***
86:     *** Creating cracked block   (element:        344) ***
87:     *** Reading loading block        plt6c.lod ***
88:     *** Merging cracked and loading blocks   ***
```

```
 89:    *** MODEL:  3461 nodes,    600 elements ***
 90:    *** ??? Enter da step >
 91:    1.0
 92:    ***    1.000000
 93: $$$$$$$$$$$$$$$$$$$$$$$$$$$$$$$$$$$$$$$$$$$$$$$$$$$$$$$$$$$$$$$$$$$$$$$$$$$$$$$$$$$$$$$$$$$$$
 94:
 95:       MODEL :   surfcrk0
 96:
 97:                Number of elements      =   600
 98:                Number of nodes         =  3461
 99:                Increment of cycles , dN  =  0.1484607E+12
100:
101:
102:           J-integral along crack front
103:
104:           x,y  of crack front         J1              J2              J3
105:
106:           5.00000    0.00000    0.49664E-04    0.48032E-04    0.48103E-04
107:           4.90390    1.62570    0.49165E-04    0.47544E-04    0.47604E-04
108:           4.61940    3.18890    0.47731E-04    0.46164E-04    0.46228E-04
109:           4.15730    4.62960    0.45496E-04    0.44016E-04    0.44090E-04
110:           3.53550    5.89230    0.42720E-04    0.41345E-04    0.41423E-04
111:           2.77790    6.92860    0.39869E-04    0.38600E-04    0.38678E-04
112:           1.91340    7.69870    0.37623E-04    0.36451E-04    0.36568E-04
113:           0.97545    8.17290    0.37114E-04    0.36070E-04    0.36440E-04
114:           0.00000    8.33300    0.40495E-04    0.39522E-04    0.39998E-04
115:
116:
117:           Displacement at 1/4 nodes
118:
119:           x,y  of 1/4 nodes                 displacement (w-z)
120:
121:           4.91667    0.00000              0.66402E-05
122:           4.82217    1.61699              0.65624E-05
123:           4.54241    3.17181              0.63353E-05
124:           4.08801    4.60479              0.59769E-05
125:           3.47658    5.86072              0.55207E-05
126:           2.73160    6.89148              0.50256E-05
127:           1.88151    7.65744              0.45765E-05
128:           0.95919    8.12910              0.43193E-05
129:           0.00000    8.28834              0.45260E-05
130:
131:
132:           Stress Intensity Factor along crack front
133:
134:           x,y  of crack front      SIF(dispacement)    SIF(J-integral)
135:
136:           5.00000    0.00000         3.32644             3.34893
137:           4.90390    1.62570         3.31013             3.33182
138:           4.61940    3.18890         3.26242             3.28309
139:           4.15730    4.62960         3.18606             3.20579
140:           3.53550    5.89230         3.08780             3.10692
141:           2.77790    6.92860         2.98336             3.00188
```

232

```
142:              1.91340      7.69870          2.89829          2.91735
143:              0.97545      8.17290          2.88980          2.90390
144:              0.00000      8.33300          3.09730          3.03841
145:
146:
147:            Crack length increment along crack front
148:
149:       direction (Deg.)    increment, da        new crack front, x,y
150:
151:            0.00000        1.00000          6.00000          0.00000
152:            6.08368        0.98536          5.88372          1.73013
153:           12.51483        0.94337          5.54036          3.39332
154:           19.70134        0.87867          4.98453          4.92581
155:           28.18808        0.79985          4.24049          6.27012
156:           38.72172        0.72141          3.34074          7.37987
157:           52.29741        0.66144          2.31791          8.22203
158:           69.63616        0.65564          1.20360          8.78757
159:           90.00001        0.80726          0.00000          9.14026
160:    *** ??? Enter division number (80, 280, 380) >
161:    80
162:    ***              80
```

Figure A.8   Execution of DUCKPOSTa

A.7 The Execution of FEMGV

At this stage, FEMGV was employed mainly to create a cubic spline curve by reading the file **surfcrk0n_spl.arc** produced by DUCKPOSTa.   FEMGV generated a file called **surfcrk0n.spl** in which the spline function is defined.

A.8 The Execution of DUCKPOSTb

The main purpose of DUCKPOSTb is to recreate a geometry pattern for the 2D crack plane with the new crack front just defined in the file **surfcrk0n.spl**, see Fig. A.10.

Lines 163–215: The FE mesh needed to be generated again, as indicated previously.

Lines 216–218: The same Δa_{max} as that used during the execution of DUCKPOSTa should be inputted

Lines 219–222: *DLA* and *DLC* are two geometry parameters that are introduced to control the position of these points on each side of the crack front, as shown in Fig. A.2. We specified **1.5** to either *DLA* or *DLC*.

233

Lines 223–226: DUCKPOSTb further demands the name of a file that contains a basic geometry pattern designed previously, as shown in Fig. A.2. DUCKPOSTb will inherit the geometry pattern except for adjusting the position of some points, so that the remeshing can be readily achieved by the help of FEMGV. For the analysed crack, most of the points will be relocated with minor change of the positions to accommodate the new crack front. Here, the geometry pattern file is **surfcrk-a.arc**.

Finally, DUCKPOSTb produced the two files, **surfcrk0.fat** and **surfcrk0n.arc**. The file **surfcrk0.fat** is a result file, as shown between lines 93 and 159 in Fig. A.8, whilst **surfcrk0n.arc** is a complete FEMGV geometry pattern file. By running FEMGV again, the 2D crack plane mesh for the new crack front can be obtained from the file **surfcrk0n.arc**, and is usually saved as the file **surfcrk1.f2d** ready for the next step calculation.

```
163:   silver{me2x1}177: DUCKPOSTb
164:   ********************************************************
165:   ***         Enter type of problem analysed >         ***
166:   ***                                                  ***
167:   ***   1) SURFACE CRACK in PLATES                     ***
168:   ***   2) INTERNAL CRACK in INTERNALLY PRESSURIZED CYLINDER ***
169:   ***   3) EXTERNAL CRACK in INTERNALLY PRESSURIZED CYLINDER ***
170:   ***   4) SURFACE CRACK in ROUND BAR                  ***
181:   ********************************************************
182:   1
183:   ***              1
184:   *** Enter input model name >
185:   surfcrk0
186:    *** surfcrk0
187:   *** Enter geometry of bar >
188:   ***   t --- Thickness of plate
189:    ***  H --- Height of plate
190:    ***  W --- Width of plate
191:   25.0, 400.0, 400.0
192:   *** Enter parameter of the cracked mesh >
193:   ***   ZEND_PLT --- Thickness of the cracked block
194:   ***   FACT_PLT --- Factor of the mesh
195:   6.0, 0.25
196:   *** Enter file name of crack front >
197:   surfcrk-a.tip
198:   *** surfcrk-a.tip
199:   *** Enter file name of LOADING BLOCK FILE >
200:   plt6c.lod
201:   *** plt6c.lod
202:   *** Enter type of loading >
203:   ***   1 = UNIFORM LOADING
204:   ***   2 = NON-UNIFORM LOADING
```

```
205:  1
206:  ***                    1
207:  *** Enter MATERIAL PROPERTIES (E, POISS, C, N) >
208:  210.e3, 0.3, 1.83e-13, 3.0
209:  ***     210000.0        0.3000000      1.8300000E-13   3.000000
210:  *** Reading 2-D mesh ***
211:  *** Reading 2-D crack front information ***
212:  *** Creating cracked block  (element:           344) ***
213:  *** Reading loading block        plt6c.lod ***
214:  *** Merging cracked and loading blocks  ***
215:  *** MODEL:  3461 nodes,     600 elements ***
216:  *** ??? Enter dastep >
217:  1.0
218:  ***     1.000000
219:  *** Starting to create .ARC file for next mesh ***
220:  *** ??? Enter stable .ARC file name :
221:  surfcrk-a.arc
222:  *** surfcrk-a.arc
223:  *** ??? Enter parameter dla, dlc :
224:  1.5, 1.5
225:  ***     1.500000        1.500000
```

Figure A.9   Execution of DUCKPOSTb

A.9 The loop

The loop of DUCKPRE → ABAQUS → DUCKPOSTa → FEMGV → DUCKPOSTb → FEMGV → DUCKPRE described above can be continuously executed on a UNIX-based Workstation. This has been achieved through a C-Shell batch file called DUCKCONN.

BLANK PAGE
IN
ORIGINAL

APPENDIX B

Newman and Raju's (1981) Stress Intensity Factor Equation

$$K = (\sigma_t + H\sigma_b)\sqrt{\frac{\pi a}{Q}} F\left(\frac{a}{t}, \frac{a}{c}, \frac{c}{W}, \phi\right)$$

The equation is applicable for: $0 \le \dfrac{a}{c} \le 1.0$; $\dfrac{c}{W} < 0.5$; $0 \le \phi \le \pi$

where: σ_t — tensile stress

$\quad \sigma_b$ — bending stress at surface, as shown in Fig. 4.1

$$F = \left[M_1 + M_2 \left(\frac{a}{t}\right)^2 + M_3 \left(\frac{a}{t}\right)^4 \right] g f_\phi f_W$$

$$f_\phi = \left[\left(\frac{a}{c}\right)^2 \cos^2 \phi + \sin^2 \phi \right]^{1/4}$$

$$f_W = \left[\sec\left(\frac{\pi c}{2W}\sqrt{\frac{a}{t}}\right) \right]^{1/2}$$

$$M_1 = 1.13 - 0.09 \frac{a}{c}$$

$$M_2 = -0.54 + \frac{0.89}{0.2 + a/c}$$

$$M_3 = 0.5 - \frac{1}{0.65 + a/c} + 14\left(1 - \frac{a}{c}\right)^{24}$$

$$g = 1 + \left[0.1 + 0.35\left(\frac{a}{t}\right)^2 \right](1 - \sin\phi)^2$$

$$H = H\left(\frac{a}{t}, \frac{a}{c}, \phi\right)$$

$$H = H_1 + (H_2 - H_1)\sin^p \phi$$

$$p = 0.2 + \frac{a}{c} + 0.6\frac{a}{t}$$

$$H_1 = 1.0 - 0.34\frac{a}{t} - 0.11\frac{a}{c}\frac{a}{t}$$

$$H_2 = 1.0 + G_1\frac{a}{t} + G_2\left(\frac{a}{t}\right)^2$$

$$G_1 = -1.22 - 0.12\frac{a}{c}$$

$$G_2 = 0.55 - 1.05\left(\frac{a}{c}\right)^{0.75} + 0.47\left(\frac{a}{c}\right)^{1.5}$$